Nanostructured light weight hydrogen storage materials

Johannes Mlandu Sibanyoni

A thesis submitted in fulfilment of the requirements for the degree of Doctor Philosophiae in the Department of Chemistry, University of the Western Cape

Supervisor: Dr. M. Lototskyy

Co-supervisor: Dr. M. Williams

November 2012

Student Number: 2004065

DECLARATION BY CANDIDATE

I declare that "***Nanostructured light weight hydrogen storage materials***" is my own work and it has not been submitted before for any degree or examination in any other university; all the sources I have quoted have been indicated and acknowledged as complete references.

Johannes Mlandu Sibanyoni **November 2012**

Signature:……..…….....

ACKNOWLEDGEMENTS

The present work was carried out in the South African Institute for Advanced Material Chemistry (SAIAMC) based at University of the Western Cape. I would like to take this opportunity to thank a number of people for their contributions to this work, without which this thesis would not have been possible. Foremost, my warmest thanks go to the Director of SAIAMC, Prof Vladimir Linkov for affording me the opportunity to be a member of the SAIAMC. My sincere gratitude goes to my supervisor, Dr Mykkhalo Lototskyy for giving me the opportunity to work with his research group and for his continuous support during my PhD; for his patience, motivation, enthusiasm, immense knowledge, and guidance throughout my research studies and whilst writing up this thesis. I could not have imagined having a better supervisor and mentor.

To my co-supervisor Dr Mario Williams, thank you for all the effort and time that you dedicated to this work, it has been a very fruitful time working with you.

To the Metal Hydride (MH) team; Dr Wafeeq Davids, Dr Y Klochko, Desmond Modibane, Ncumisa Jonas, thank you all for the support and contribution during my studies.

To all the working staff and colleagues at SAIAMC, I thank you all.

Special thanks go to the Electron Microscope Unit at the University of the Western Cape, Dr S Botha for TEM analysis and S Josephs for SEM analysis and Dr B Remy at iThembaLabs for XRD analysis. A big Thank you goes to the Dr R V Denys for the SR-XRD measurements.

To all my friends that have supported me over the years in my studies, I wish to thank you all.

To the Sibanyoni Family, thanks you all for supporting me during my research studies. And to Dr Paul Mtoloki Sibanyoni, thank you so very much. There are no words that can express how grateful I am to you. To my Mom Betty Nolanga Sibanyoni, I will always remain grateful for everything you have done for me.

I also wish to acknowledge the financial assistance received from the South African Energy Research Institute (Pty) Ltd/The South African Nuclear Human Asset and Research Programme without which this thesis would not have come to fruition.

Above all, praise and thanks be to God for protecting and granting me strength over the years of my studies/ May your love remain the same in me, all the days of my life.

ABSTRACT

The main objective of this study was to advance kinetic performances of formation and decomposition of magnesium hydride by design strategies which include high energy ball milling in hydrogen (HRBM), in combination with the introduction of catalytic/dopant additives. In this regard, the transformation of $Mg \rightarrow MgH_2$ by high-energy reactive ball milling in hydrogen atmosphere (HRBM) of Mg with various additives to yield nanostructured composite hydrogen storage materials was studied using *in situ* pressure-temperature monitoring that allowed to get time-resolved results about hydrogenation behaviour during HRBM. The as-prepared and re-hydrogenated nanocomposites were characterized using XRD, high-resolution SEM and TEM, as well as measurements of the mean particle size. Dehydrogenation performances of the nanocomposites were studied by DSC / TGA and TDS; and the re-hydrogenation behaviour was investigated using Sieverts volumetric technique. The following nanocomposites were investigated in the course of this study:

- Magnesium + sp^2-hybridized carbon (1–10 wt.%), including*:*
    - graphite (G),
    - activated carbon (AC),
    - multi-wall carbon nanotubes (MWCNT),
    - expandable graphite (EG),
    - thermally-expanded graphite (TEG).
- Magnesium + carbon and/or hydride-forming metal alloy, including:
    - Pd-black (0.1–5.0 wt.%).
    - BCC-V alloy (10 wt.%),
    - ZrNi (10 wt.%),
- Magnesium + carbon and/or mixed titanium – iron oxide ($TiFeO_3$, 2–20 wt.%).

The hydrogenation behaviour of Mg-C composites during HRBM was observed to be strongly dependent on the nature and amount of carbon additive. For the composites containing 1 wt.% AC and TEG, and 5 wt.% MWCNT, the hydrogenation kinetics become superior to that for the individual magnesium. For Mg–G and Mg–EG the hydrogenation proceeds slower and, for Mg–G, starts from an incubation period. An increase in the content of EG and TEG above 1 wt.% results in the deterioration of the hydrogenation kinetics. The hydrogenation behaviours associated with carbon additives have roots in their destruction during HRBM to form graphene layers encapsulating the MgH_2 particles and preventing the grain growth. This results in a 2-4 times decrease of the MgH_2 crystalline size in the re-hydrogenated Mg–C composites compared to Mg alone. Because of the presence of carbon layers, the absorption-desorption cycle stability of the Mg–C nanocomposites increases. Dehydrogenation performances of the nanocomposites become very sensitive to their exposure to O_2 and H_2O.

In the case of Mg-M (M = BCC-V, ZrNi, Pd) or Mg-$TiFeO_3$ composites, fast hydrogenation kinetics were observed for the transformation of Mg → MgH_2 to achieve maximum hydrogen capacity in < 1.5 hour. Additional introduction of the carbon materials resulted in the appearance of an incubation period that was dependent on the nature of the carbon additives. The composites prepared with "harder" carbon additive, like AC, showed much faster hydrogenation kinetics rates than those of MWCNT and G. The synergistic effect of carbon with metal was found to be very important as the Mg-C-M composites showed high hydrogen capacity and significantly faster re-hydrogenation rates than those for undoped Mg and Mg-C

composites. They also desorb hydrogen at lower temperatures, and crystalline size growth was minimized as compared to those without carbon materials.

In the case of Mg-$TiFeO_3$ composite, the optimal amount of $TiFeO_3$ added to magnesium was found to be about 10 wt.%, in respect to the amount of the latter. Further improvement of the hydrogenation/dehydrogenation performances of the material was achieved by introducing carbon additives (G, MWCNT, AC, EG, TEG), in addition to $TiFeO_3$. The favourable effect of carbon addition to Mg + $TiFeO_3$ was also associated with the facilitation of reduction of $TiFeO_3$ in the composite to yield TiFe which plays a role of hydrogenation/dehydrogenation catalyst.

LIST OF FIGURES

LIST OF TABLES

LIST OF ABBREVIATIONS

AC	Activated carbon
BCC	Body centered cubic
BPR	Balls-to-powder weight ratio
CNT	Carbon nanotube
DoE	Department of Energy.
DSC	Differential scanning calometry
ECAP	Equal channel angular pressing
EDX	Energy-dispersive X-ray spectroscopy
EG	Expandable graphite
G	Graphite
JMA	Johnson – Mehl – Avrami equation
HRBM	High energy reactive ball milling
HRSEM	High resolution scanning electron microscopy
HRTEM	High resolution transmission electron microscopy
HTP	High pressure torsion process
LOH	Liquid organic hydrides
MH	Metal hydride
MM	Mechanical milling
MWCNT	Multi-wall carbon nanotube
RS	Rapid solidification
SAD	Selected area diffraction pattern
SEM	Scanning Electron Microscopy.
SR-XRD	Synchrotron radiation X-ray powder Diffraction.
TDS	Thermal desorption spectroscopy.

TEG	Thermally expanded graphite
TEM	Transmission electron microscopy.
TGA	Thermal gravimetric analysis.
TM	Transition metal.
RT	Room temperature.
XRD	X-ray diffraction.

CHAPTER 1:Introduction

1.1. General background

The parallel increase in energy demand with population growth and modernization has put an enormous strain on the current available energy resources. The current available energy sources (fossil fuels) are getting lesser every year and it is predicted that in the near future there will be depleted. Combustion of these fossil fuels is considered to be the largest contributing factor to the release of greenhouse gases into the atmosphere. In fact, it is believed that energy providers are the largest source of atmospheric pollution today. There are many types of harmful outcomes which result from the process of converting fossil fuels to energy. Some of these include: air and water pollution, accumulation of solid waste, not to mention land degradation and human illness. Therefore, the need for sustainable, environmental friendly, safe, easy conversion and very convenient energy carrier is of high importance [1].

One of the most challenging and exciting candidates to fulfil these demands is hydrogen. This element is the most abundant in nature but it exists almost exclusively in a bonded form in different chemical compounds. Hydrogen has chemical energy per unit mass of 142 MJ/kg, that is, three times more than those of other chemical fuels (e.g., equivalent value for liquid hydrocarbons is 47 MJ/kg), it is a clean burning fuel and is also renewable [2-7].

Hydrogen storage, along with hydrogen production and the lack of infrastructure remains a major stumbling block in efforts to usher in hydrogen as a replacement for hydrocarbon-based fuels in cars, trucks and homes. But with the multiple advantages hydrogen offers, developing hydrogen storage solutions has been the focus of a great deal of research.

1.1.1. Energy value chain and primary energy sources

The energy value chain begins with a source of energy. First of all, these are hydrocarbon fuels, like coal, natural gas, and petroleum, as well as biomass-based organics like wood, straw, and municipal wastes. The non-organic energy sources include renewables like wind, solar, hydro and nuclear fuels based on uranium. The organic fossil fuels are transported through vast truck, rail, and pipe lines to conversion facilities like refineries and power stations, industrial facilities where they are consumed as raw materials, or in the case of natural gas, to distributors who sell it directly to consumers. Most of the renewable and nuclear sources are used to produce electricity. So, in the case of electricity, the value chain is fuel/energy source, power generating station, transmission, distribution, and consumption. Unlike gasoline or crude oil, both of which are liquid fuels and have similar networks, electricity cannot be stored [8, 9]. Figure 1.1 below illustrates the energy value chain.

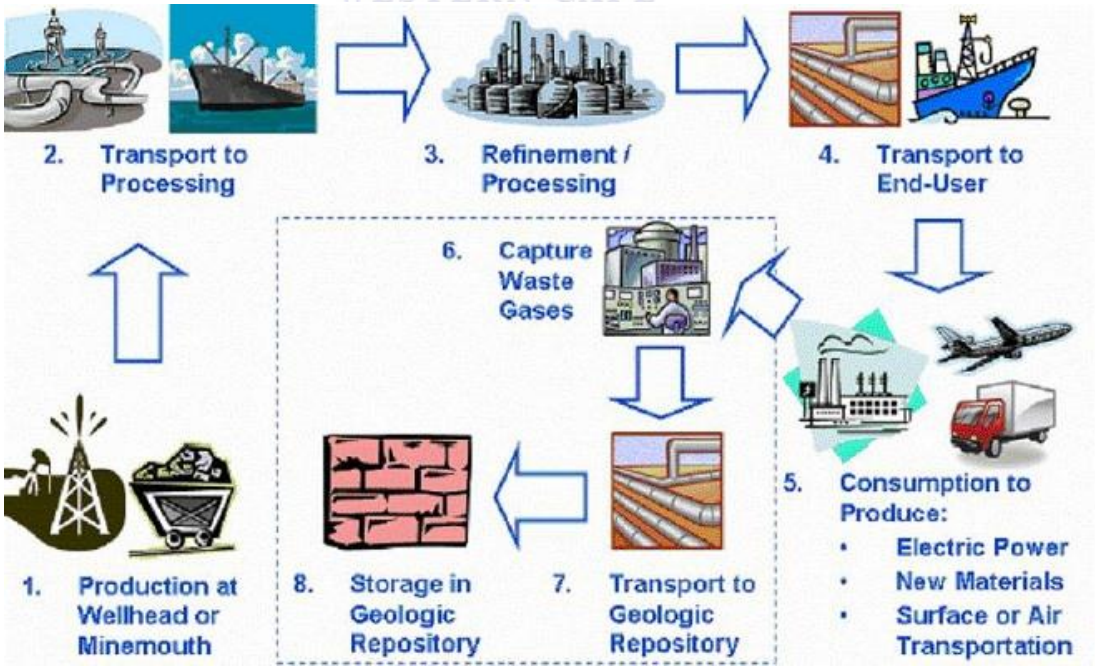

Figure 1-1: Energy value chain diagram

Renewable energy technologies convert primary energy such as wind and solar to energy forms that humans can readily use, including heat and electricity. On the other hand, hydrogen is an energy carrier that can be produced from the above mentioned energy sources. However, there is more that still needs to be done in the fields of research and development in order to make a transition across to the energy gained from these resources. As pointed out above, Figure 1.1 shows the energy value chain, previously defined as five segment model spanning extraction, processing, wholesale, delivery and retail which continues to evolve, with new segments emerging via the combination of previously separate segments and the splitting of previously single segment into multiple segments [8, 9].

1.1.2. Fossil fuels challenges

Fossil fuels are worldwide used as an energy source but there are a number of problems associated with burning these fuels to provide energy. These can cause significant damage to the natural and built environments, and to the health of people exposed to the chemicals released when these fuels are burnt. The burning fossil fuels for energy releases a number of chemicals into the atmosphere and these include; carbon dioxide, nitrogen oxides, heavy metals, sulphur dioxide and volatile organic compounds. The chemicals can further lead to the release of nitric, carbonic and sulphuric acids into the environment. This can create acid rain, which in turn has potential to cause damage to plants and buildings. Some of the chemicals that are released by the combustion of fossil fuels have been attributed as major contributors to climate change. By changing the proportion of carbon dioxide in the atmosphere, the use of fossil fuels can alter the way heat is absorbed and stored in the atmosphere. This can lead to climate changes, which could affect the weather patterns and sea level.

The soot and particles that are released when fossil fuels are used can also cause environmental problems. Toxic chemicals such as lead and small amounts of radioactive materials can be released into the atmosphere, but these are not believed to have any significant environmental effects. The production and transport of fossil fuels can also lead to environmental damage, particularly if there are any accidents such as oil spills. Mining and drilling can also lead to the release of toxic chemicals that may have negative impacts on the areas surrounding mines [8, 9, 10, 11].

Another problem with the use of fossil fuels is that, they are becoming increasingly expensive. Part of the reason for this is that governments are taxing them higher, and also because fossil fuels are what are termed "non-renewable" source of energy, meaning that they cannot replenish themselves once used. The implication is that the supply of fossil fuels is limited and will one day, run out [10, 11].

It is this type of problems that have made alternative, renewable sources of energy a more attractive and lucrative option.

1.1.3. Hydrogen Economy as a strategic way for the problem solution

A clean way to use hydrogen as fuel is envisaged as a linked network of chemical processes that produce hydrogen and convert the stored hydrogen to electrical energy and heat for end use, this is termed as “hydrogen economy”. This would address the major energy challenges at the current moment. In order for hydrogen economy to become a reality, the following challenges need to be addressed:

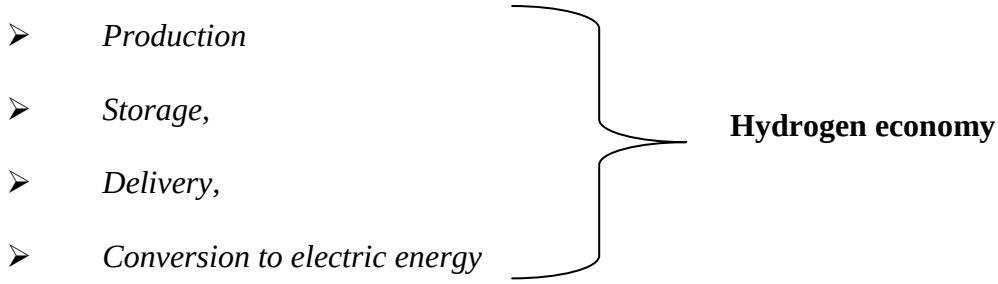

Currently, hydrogen production and conversion are technologically feasible but the main drawback for the implementation of hydrogen economy is hydrogen storage, particularly for on-board vehicle applications. Hydrogen storage is a key enabling technology for the use of this element as a future energy carrier and for the mass market entry of hydrogen fuelled vehicles. Therefore, for sustainable energy technologies and a sustainable energy economy, hydrogen storage is a key link for hydrogen economy. Currently, many countries are now compiling roadmaps, in many cases with specific numerical targets for the advancement of fuel-cell and hydrogen technologies.

1.2. Hydrogen as a future energy carrier: perspectives and challenges

1.2.1. The concept of Hydrogen Energy Systems: an overview

Hydrogen can be produced from many sources, including fossil fuels, renewable resources, and nuclear energy. Hydrogen and electricity can be converted from one to the other using electrolyzers (electricity to hydrogen) and fuel cells (hydrogen to electricity). Hydrogen is an effective energy-storage medium, particularly for distributed generation. Therefore, implementation of hydrogen energy systems could play a major role in addressing climate challenges and national energy security issues. Today, hydrogen is produced primarily from natural gas using widely known commercial thermal processes. In the future, it could be produced directly from renewable sources. In the meantime,

current technologies can be adapted to produce hydrogen with significantly reduced CO_2 emissions through carbon capture and sequestration processes and by using renewable and nuclear electricity to produce hydrogen with no production-side CO_2 emissions. Using hydrogen in combustion devices or fuel cells result in few, if any, harmful emissions [2, 12-14].

The vision for a hydrogen economy is based on a clean and simple cycle: separate water into hydrogen and oxygen using renewable energy such as solar, use the hydrogen to power a fuel cell where hydrogen and oxygen (from air) recombine to produce electrical energy, heat, and water to complete the cycle. This process produces no particulates, carbon dioxide and no pollution.

In the coming years, hydrogen systems used for stationary and vehicular applications could solve many of our energy and environmental security concerns. Hydrogen is likely to be affordable, safe, domestically produced, and used in all sectors of the economy and in all regions of the country. These properties are considered to enable hydrogen to compete with established fuels and make it an ideal cleaner energy carrier [2, 6, 13, 14].

1.2.2.. Hydrogen and fuel cell activities in South Africa (HySA program)

The hydrogen economy is undergoing serious consideration in South Africa in an effort to develop safe, clean and reliable alternative energy sources to fossil fuels. As pointed out above, hydrogen is an energy carrier and is used to store and distribute energy and can be combined with the use of fuel cell technologies to produce electricity. Another driving force behind this technology is the prevalence of platinum reserves found in South Africa. Platinum Group Metals (PGMs) are the key catalytic materials used in most

fuel cells, and with more than 75% of the world's known platinum reserves found within South African borders, there is great potential for socio-economic benefits to be obtained from these natural resources. Fuel cells were invented about 150 years ago and directly convert chemical energy into electrical energy in a clean, environmentally friendly way, with no harmful carbon dioxide (CO_2) emissions at the point of use. Thus, converting hydrogen gas to electricity in fuel cells does not "destroy" the hydrogen, but transforms it into water. Hydrogen can be produced from any hydrocarbon compounds, including fossil fuels, but the emphasis in South Africa is upon developing hydrogen from renewable energy sources in the long term. Fuel cell technology is more efficient, reliable, quieter and compact, and if the hydrogen used is from a renewable source, this technology is also cleaner and better for the environment.

The commitment to energy security is identified as one of the five priority areas or "grand challenges" in the Department of Science and Technology's (DST) Ten-Year Innovation Plan. Reflecting the shift in national priorities from the extraction of natural resources to the development of a knowledge based economy, these strategic outcomes indicate where South Africa wants to be in 2018. Within the DST's grand challenge on energy security, this interest in hydrogen falls under the National Hydrogen and Fuel Cell Technologies Research, Development and Innovation strategy, branded as Hydrogen South Africa (HySA) in 2008.

The strategy stimulates and guides innovation along the value chain of hydrogen and fuel cell technologies in South Africa, aiming to position the country to drive and optimise local benefits from supplying high value-added products (i.e. PGMs) to the potentially increasing international markets. These local benefits should include economic benefit,

through job, wealth and new industries creation; the development of appropriate skills and human resources capital; and an improved quality of life for all South Africans. Three Centres of Competence (CoC) have been established by DST to implement the HySA strategy, and are charged with unique responsibilities collectively geared towards attaining the goal of supplying 25% of global PGM based catalyst demand by 2020. The three CoCs are:

- HySA Catalysis, Catalysis Competence Centre (hosted by UCT and Mintek);
- HySA Infrastructure, Hydrogen Infrastructure Competence Centre (hosted by NWU and CSIR);
- HySA Systems, Systems Integration & Technology Validation Competence Centre (hosted by UWC).

The combined efforts of these three CoCs are aiming towards the research and development (R&D) of a variety of hydrogen fuel cell technologies so that fuel cells can be "tailor-made" for specific uses and applications.

Potential products being developed with the contribution of HySA Systems include a portable power source for use as a back-up power source as a quieter and cleaner alternative to generators. The second potential product is a combined heat and power (CHP) source based on fuel cells to supply decentralised power and heating for buildings and industries. Popular in colder countries, these CHP systems offer high efficiency and low emissions, and can operate from existing natural gas distribution networks providing up to 10 kW power for domestic and up to 150 kW for industrial buildings. South African R&D is focusing on developing internationally competitive and marketable CHP systems and critical CHP system components to meet the needs of the international

market. The third potential product is fuel cell powered vehicles that could provide another alternative to hybrid and pure electric vehicles. Using Proton Exchange Membrane (PEM) technology, research over the next 20 years will focus on hydrogen storage density and extending fuel cell life. A more immediate possibility is utility vehicles, which require lower energy dense storage, making these a real possibility.

South Africa is also exploring other energy options, and it is envisaged that by 2018, from the total national energy produced, 5% would be from renewables, 20% from nuclear and 70% from coal (of which 30% based on clean coal technologies, where the harmful environmental effects can be reduced and the emissions contained). HySA also aims to demonstrate hydrogen production by splitting water at a pilot scale, using nuclear or solar power as the primary power source. Key challenges facing HySA include the high cost of producing fuel cells and components which will need to be considerably reduced if this technology is to be competitive. South Africa has a strong potential to achieve this cost reduction through development of local PGM-based technology. Making this technology truly "green and clean" is the other main challenge, as "hydrogen is only as clean as it is made". Issues around the storage and distribution of hydrogen also need to be resolved before the technology can be scaled up and commercialised [15]

1.3. Hydrogen storage as a key enabling technology for the implementation of Hydrogen Economy

1.3.1. Goals for hydrogen storage: role of application requirements to hydrogen storage systems

In order to use hydrogen as an energy carrier, hydrogen storage and transportation should be efficient, safe and economical. However, this depends on diverse factors like: (i) its final stage application, (ii) energy density required, (iii) length of storage time, (iv) costs, (v) necessities of maintenance, and other related problems. At present, there are different ways (compressed gas, liquid form, solid-state) of storing hydrogen for both stationary and mobile applications. In stationary applications, the storage method will be well suited for operation at high temperature and pressure with extra capacity. In case of mobile applications such as portable devices and vehicles, high hydrogen volume density and weight density are of importance. For instance, in vehicle hydrogen storage, a method that occupies the minimum space supplies enough hydrogen to enable a drive range comparable to gasoline powered vehicle, charge/recharges near room temperature and fast hydrogen supply to the fuel cell. Hydrogen storage requirements for vehicle applications are far more stringent than those of stationery applications.

1.3.2. Requirements and technical targets for on-board hydrogen storage systems for mobile applications

The requirements for hydrogen as a fuel on-board vehicle are that it should be transparent to the consumer in terms of vehicle drive range, refuelling cost and time. However, increasing the hydrogen storage weight and volume beyond that of the gasoline tank adversely affects the vehicle design in a number of ways. The direct effects of increasing

volume of the fuel storage system are changes in the packaging of all the components of the vehicle. In fact, if the increase is large enough, it makes packaging impossible and the mass of the hydrogen stored on the vehicle must be reduced with the resultant decrease in vehicle drive range. Hence in any analysis of hydrogen storage on-board vehicles, it is convenient to reference weight and volume limits in terms of the weight fraction of a conventional internal combustion engine (ICE) vehicle and the space available under the vehicle to store hydrogen [16].

In hydrogen-fuelled vehicles, 4-5 kg (130-160 kWh) H_2 must be stored in a small, preferably lightweight tank in order to achieve a drive range of 500 km (i.e. 80-125 km/kg H_2). However, whereas the gravimetric energy density of hydrogen is extremely high, the volumetric storage density of the lightweight gas is low. Consequently, the most important technical and economic challenges to be overcome in a practical hydrogen-storage system are the storage density related to the system; its safety, short refuelling time and the ability to deliver enough hydrogen during the driving cycle [17].

United State Department of Energy (US DoE) in collaboration with car manufacturers has developed technical and economic targets for hydrogen storage system goals in fuel cell powered light duty vehicles and current technical targets for on-board hydrogen storage are given in Table 1.1. These goals, which have been developed in consultation with automotive companies, are used by hydrogen storage technology developers as targets to be met in their programs. As is often the case in the development of new technologies, the goals become increasingly demanding over a period of time. The set goals for development of hydrogen storage systems with primary consideration given to the weight and volume of the systems to store sufficient hydrogen for a vehicle drive range approaching that of conventional ICE using petroleum fuel [17].

Table 1.1: Technical hydrogen storage targets for on-board hydrogen storage systems [17]

Storage parameters	Units	2010	2015	Ultimate
System gravimetric capacity	$Kg(H_2)$/ kg(system)[b]	0.045	0.055	0.075
	kWh/kg	(1.5)	(1.8)	(2.5)
System volumetric capacity	kg/m^3	28	40	70
	kWh/m^3	(900)	(1300)	(2300)
Cycle life	cycles	1000	1500	1500
Min/Max delivery temperature	K	233/358	233/358	233/358
Min H_2 delivery pressure	atm	4 FC/35 ICE [(a)]	3 FC/35 ICE [(a)]	4 FC/35 ICE[C]
Max H_2 delivery pressure	atm	100	100	100
System fill time	kg/min	1.2	1.5	2.0
Safety	meets or exceeds applicable standards			
Toxicity	meets or exceeds applicable standards			
Fuel purity	percentage H_2		99.99 (dry basis)	

(a) FC = fuel cell, ICE = internal combustion engine.

1.3.3. Challenges and constrains

The challenge with the use of hydrogen in automotive vehicle is the discovery and development of materials and compounds capable of storing enough hydrogen on-board to enable > 500 km drive range without adding significant weight or volume to today's vehicle. A minimum of 5 kg hydrogen would need to be stored on-board to drive even the most fuel-efficient vehicle > 500 km. At standard temperature and pressure (STP), 5 kg of hydrogen requires a volume of nearly 54 m^3. Unfortunately, even highly compressed hydrogen gas is unlikely to be of sufficient volumetric density (40 g/L at 700

bar) to enable a fuel system to meet the > 500 km drive range target. Liquefied hydrogen also falls short of reasonable volumetric system targets and high amount of energy is consumed to keep hydrogen liquefied (b.p. –253°C).

1.3.4. Methods of hydrogen storage

The physical and chemical properties of hydrogen impose technical boundary conditions on standard methods of storing H_2 in pure form such as pressurized gas or cryogenic liquid. Currently, the following methods of storing hydrogen on-board vehicles have been proposed: pressurized hydrogen, liquid hydrogen, storage in solids, hybrid storage systems and regenerative off-board systems. Of the various options, the two convectional and technically most advanced storage systems are based on the storage of pure hydrogen in pressurized or liquid form. However, both methods exhibit principal drawbacks or limitations and optional method such as storage in solids and in the form of regenerative off-board systems have been proposed as alternatives and are under development. The following section outlines some of the advantages, drawbacks and limitations of the various methods currently considered as storage options in vehicles.

1.3.4.1. Physical; H_2 compression, liquefaction, cryogenic compression

Hydrogen gas has poor volumetric capacity and, for transportation applications, requires storage containers that are too large (occupy large internal vehicle volume) for most applications. Typically, ~350 bar H_2 at room temperature has a density of 23.4 g/L, so to store 5 kg H_2 would require a volume of 214 litres for gaseous H_2, not including the vessel, components and mounting devices [18]. Thus, it is difficult to package a compressed hydrogen system in a vehicle without compromising its utility. And, if the

tank is designed to occupy the volume of a conventional gasoline tank, vehicle driving range is strongly reduced.

Due to the nature of hydrogen, its compression is much more energy intensive than other gas fuels, such a methane. Compressing hydrogen from 1 bar to 350 bars requires about 8-10% of the energy content of the fuel in terms of its high heating value. Compressing it to 700 bars would require about 11-13% of the energy content [19]. Filling times of compressed gas systems are not a problem; however, due to temperature increase during rapid filling, the process must be monitored. In order to obtain temperatures around room temperature within the tank after rapid filling, supply gas cooling in the filling station is required if the tank is not equipped with a heat exchanger. Since no heat supply is required during discharge, discharge rates are not limited. Thus, storage of hydrogen as a compressed gas is a mature technology, for example,700 bar tanks are already certified [20]. These tanks use lightweight composite materials such as carbon-fibre reinforced plastics. Several hydrogen-powered vehicle prototypes utilise this technology for fuel storage [21]. However, the low gravimetric density of hydrogen and problems associated with handling high pressure are some of the challenges that makes high pressure hydrogen storage not to be a good candidate [3].

Alternative to high pressure hydrogen storage is to store in a liquid form. Liquid hydrogen storage has high volumetric density. Nevertheless, the system has to be maintained at -253°C for hydrogen to be in the liquid state and this requires super-insulation in order to reduce heat leakage and consequently boil-off of hydrogen. In addition, the high consumption of power during cooling (approximately 30% of the stored energy) causes this option to be economically non-viable except in cases where the hydrogen cost is not a critical factor and the fuel is consumed in a short period of time after being stored (for example, in aerospace applications). The volumetric density of

liquid hydrogen is 70.8 kg·m^3 and slightly higher than that of solid hydrogen (70.6 kg·m^3) [22].

Considering that a standard gasoline station needs only a couple of steel tanks, liquid hydrogen fuelling station, on the other hand needs expensive and energy intensive support equipment to achieve or maintain cryogenic temperatures. The potential failure of cryogenic support equipment at a LH_2 refuelling station could lead to a potentially dangerous expansion of gaseous hydrogen. While the latter may offer benefits over the other technologies with regard to safety aspects, it has its own set of associated drawbacks [3, 23]. The support equipment to maintain a tank of hydrogen at nearly absolute zero is very expensive and requires an outside energy source, and/or need to continually allow the hydrogen to vent. Even with some of the best cryogenic tanks built, it would only take a few days before a large percentage of the hydrogen would evaporate. The hydrogen venting concerns are also a problem for civilian applications considering that many undercover parking areas and garages are nearly air tight, it may be harder for the vented hydrogen to escape, leading to a potential hazard [18].

1.3.4.2. Physical-chemical and chemical hydrogen storage methods

Another alternative to H_2 compression is to store hydrogen in a bound state. This form of hydrogen storage can yield high volumetric capacity. The first group of the physical-chemical hydrogen storage methods uses the process of H_2 physisorption on the surface of a solid hydrogen storage material. In this method, non-dissociated hydrogen molecules are held on the surface of the solid by van der Waals forces. The bond strength of this interaction is weak, and the enthalpy of this process is less than 10 kJ/mol. Therefore,

hydrogen gas physisorption (adsorption) on the surface needs very low temperatures close to nitrogen boiling point. Materials such as zeolites, metal organic frameworks (MOF's) and carbons are of interest for this purpose because of their high surface areas.

1.3.4.2.1. Zeolites

Zeolites are cheap, easily available and safe to use as hydrogen storage materials. They are crystalline alumosilicates which contain networks of pores and channels of molecular dimension usually accommodating a wide variety of cations, such as Na^{+}, K^{+}, Ca^{2+}, Mg^{2+} and others [24]. The positive ions are rather loosely held and can readily be exchanged in a contact solution. Zeolites are of interest as hydrogen storage candidates because the diameter of the cages and the channels can be controlled by exploiting their ion-exchange property to modify the valence state and the size of the exchangeable cations [25, 26]. At ambient temperatures, zeolites can store small amounts of hydrogen (~ 0.3 wt.%). However, under cryogenic conditions, hydrogen storage capacities of ~1.0 wt.% can be achieved. Zeolite-Y partially exchanged with magnesium cations (Mg^{2+}) has an unprecedented high adsorption enthalpy of -17.5 kJ/mol which is closer to the US DoE's hydrogen storage requirements [27]. However, from the capacity point of view, hydrogen storage in zeolites is not yet promising in stationary and automotive applications.

1.3.4.2.2. Metal organic frameworks (MOF's)

Metal organic frameworks (MOF's) sometimes referred to as "crystal sponges", are made of network of transition metal ions linked by organic donor molecules called ligands.

These materials are of interest for hydrogen storage applications as they have large overall pore volume, large surface areas, high gravimetric hydrogen absorption, and adjustable pore sizes and are amenable to being designed [28-30]. During hydrogen sorption in MOF's, the materials retain its form without changes. However, MOF's require cryogenic temperatures to absorb large quantities of hydrogen, and at ambient temperature, storage capacities achieved so far are below 2.0 wt.% H_2. This is a direct result of the weakening of the van der Waals forces which bind hydrogen to the MOF's. Improved hydrogen storage capacities were observed when introducing catalytic additives [31-33].

The temperature dependence of hydrogen adsorption in MOF's is a major impediment for storage applications [34]. The adsorption capacity decreases rapidly with increase in temperature and is hard to detect above 193K. From the current available results, it is not clear if increasing pressure will be sufficient to increase the adsorption capacity at ambient temperatures similar to results achieved at 77K. The challenge with the use of MOF's as hydrogen storage material is the low hydrogen capacity at ambient operating temperatures that need to be overcome before MOF's can be applicable for stationary and on-board hydrogen storage systems.

1.3.4.2.3. Carbon materials

Carbonaceous materials are attractive candidates for hydrogen storage because most of them have high surface area and porosity, and low-mass density. The reported hydrogen uptake capacities vary from 0.1 to 10 wt.% [35-37]. The capacity of ~10 wt.% has not yet been reproduced. However, there is room for development as there are theoretical

studies predicting that high storage capacity in carbon nanomaterials is possible [38]. Carbon aerogels have shown that they can be employed for hydrogen storage. This is so because storage capacity of ~5.0 wt.% could be achieved in carbon aerogels possessing high porosity and surface area above 3000 m^2/g [39].

1.3.4.2.4. Chemical interaction: an overview

The other option to overcome the volumetric density challenge is to store hydrogen using chemical interactions with other elements: chemical hydrogen storage. This storage method is similar to complex hydrides. These compounds can contain large quantities of hydrogen by mass and volume. They can appear in either solid or liquid form, and can be heated directly, passed through a catalyst-containing reactor, or combined with water (i.e. hydrolysis) or other reactants to produce hydrogen. Nevertheless, unlike reversible complex hydrides, chemical hydrides are intended as ‘‘one-way’’ single-use fuels. The spent material can then be reprocessed or regenerated off-board. A few prominent examples of chemical hydride reactions include thermal decomposition of ammonia borane (NH_3BH_3) [40], hydrolysis of sodium borohydride ($NaBH_4$) [41, 42] and off-board reversible liquid organic carriers (e.g. N-ethyl carbazole) [43]. The appeal of some chemical hydrides originates from their high gravimetric and volumetric capacities and near-ambient operating conditions which are often less than 80°C (at 0.1 MPa hydrogen pressure). For example, ammonia borane (NH_3BH_3) contains over 19 wt.% H_2 and 150 g H_2/L of hydrogen by weight and volume (materials basis), respectively, and practically releases over one equivalent of H_2 rapidly at 70°C using a transition metal catalyst [44]. Likewise, materials related to ammonia borane, for example, ammonia-triborane ($NH_3B_3H_7$), are being actively pursued as candidate hydrogen storage materials [45].

While chemical hydrides are capable of operating within temperature–pressure conditions which exist on-board FC vehicles (i.e. utilizing fuel cell waste heat), they suffer from a few drawbacks which could limit their practicality. In particular, many chemical hydride reactions are exothermic and can result in the formation of very stable dehydrogenated products (e.g. the hydrolysis of $NaBH_4$ results in the formation of $NaBO_2$). Thus, the reconstitution of these stable products back into the hydrogen-containing fuel generally involves energy-intensive reaction steps, for example, B–N or B–O bond breaking reactions which contribute to an overall energy inefficient process. This, coupled with complex fuel system components that are often high-cost, such as dehydrogenation reactors, multiple (compartment) tanks, phase separators and pumps for addition (removal) of fuel (spent material), complicates the implementation of chemical hydrides as on-board storage media. In fact, these cumulative challenges have contributed to discontinuation (no-go decision) of research on hydrolysis of sodium borohydride by the DoE. Additionally, some by-products of the decomposition of similar compounds are either very toxic (B_2H_6), or can poison the LT PEM FC (NH_3).

Nevertheless, the positive attributes—high capacity and near ambient operation make many chemical hydrides compelling candidates for hydrogen storage. More detailed reviews of the properties of chemicals hydrides with an emphasis on ammonia borane are available elsewhere [46, 47].

1.3.5. Comparison of hydrogen storage methods: weight and volume efficiency, energy consumption and safety

Current research is focused on achieving the targets of volumetric and gravimetric capacity, while also meeting the energy and temperature requirements for hydrogen release and the kinetics of hydrogen charging and discharging. A number of high

volumetric and/or gravimetric hydrogen densities materials have been studied over the past years, especially those composed of light weight elements on the periodic table. It is important to remember that the DoE targets include not just the material but the entire *storage system*. The storage system is all storage and hydrogen conditioning components leading up to the fuel cell.

Figure 1-2 summarizes the volumetric and gravimetric storage capacities for the various hydrides. Physisorption materials are represented by a curve depicting the relationship between gravimetric and volumetric storage capacity for physisorbed hydrogen on carbon materials. It should be noted that the values in the diagram are material properties and not system values, for instance, storage tank is not included.

An ideal hydrogen storage material should meet the targets at high hydrogen capacity, low desorption temperature, moderate dissociation pressure, low heat dissipation during the exothermic hydride formation, good reversibility, fast kinetics, low sensitivity to O_2 and moisture for long cycle life [18].

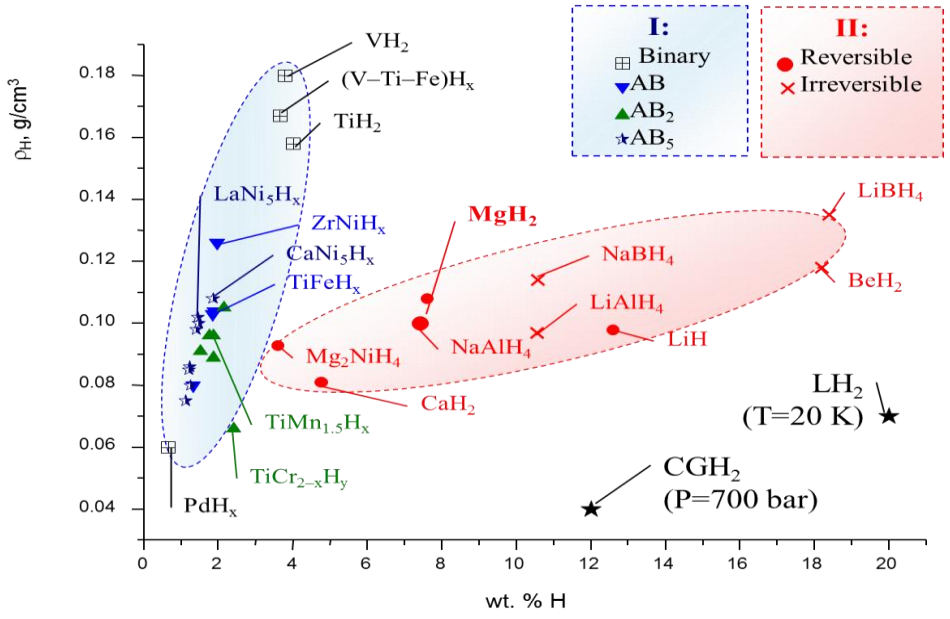

Figure 1-2: Volumetric and gravimetric hydrogen storage densities of different hydrogen storage materials [3]. Reported values for hydrides are excluding tank weight.

The mass of fuel required for a certain drive range can be devised directly from specific energy consumption of the vehicle. Most fuel cell vehicles have been specific energy consumption in order 1-12 MJ/km which corresponds to roughly 1 kg of hydrogen per 100 km. Apparently, high pressure systems have by far the best gravimetric capacity, a factor of crucial importance in vehicle engineering. Hence high pressure storage has been used in more than 90% of fuel cell vehicle in the past years [48]. Although 70 MPa high pressure storage can be regarded as the best state-of-the-art in hydrogen storage, the volumetric capacity of this technology is still significantly below design targets stated, for example, by DoE [18]. Due to the low hydrogen density, storage of hydrogen under ambient conditions requires a huge volume (11.2 L for 1.0 g of hydrogen). High pressure storage is widely discarded since it is risky, cost-intensive and highly in-effective.

In the case of cryogenic storage, low temperature requirements (< -253°C) for liquefaction and the requirement of super insulated containers makes this mode of storage very expensive. Handling and distribution of liquid hydrogen is also a difficult task. Liquid hydrogen cannot easily be moved via underground pipelines and it is necessary to use special vacuum insulated hoses for moving liquid hydrogen from one container to the other [23]. The reversible hydrogen storage in metals, alloys or intermetallic compounds is considered as a convenient way to store hydrogen [49]. This is due to the fact that, unit volume of metal hydride holds more hydrogen than liquid hydrogen does.

1.4. Problem statement

The use of magnesium hydride, MgH_2, as a very promising hydrogen storage material is of interest due to its high hydrogen capacity of 7.6 wt.% / ~110 kg H/m^3 (see Figure 1-2), low cost, light weight, good reversibility and its abundance. However, the application of magnesium hydride is hindered by its unfavourable thermodynamic properties (high desorption temperature of 300°C at 1 bar H_2) and slow hydrogenation-dehydrogenation kinetics. Several factors significantly reduce the rates of magnesium hydrogenation and dehydrogenation of the magnesium hydride. One of them is the oxidation of magnesium surface resulting in the formation of magnesium hydroxide [50]. Magnesium oxide forms easily when Mg surface is exposed to air (water and /or oxygen) as the MgO layer hinders hydrogen molecules from penetrating into the material [51]. Hence, to initiate hydrogen absorption, the oxide layer should be broken down by activation process to eliminate or crack the MgO layer [52, 53]. The activation may consist of cyclic heating and cooling in a vacuum or hydrogen atmosphere. But even after such activation process, magnesium hydride formation takes several hours at 400°C. This also includes deterioration of H_2 sorption properties during

dehydrogenation/hydrogenation cycling [54]. The other reason for the slow hydrogenation rate of magnesium (even after activation) is low dissociation rate of hydrogen molecules on the surface of magnesium [55]. Finally, the hydrogenation of magnesium is significantly impeded by the slow diffusion of H atoms through the grown layer of MgH_2 [56].

Many studies have been conducted in an attempt to improve the reaction kinetics of magnesium with hydrogen by adding some catalytic materials and performing mechanical treatment and/or alloying. Mechanical treatment promotes reduction of particle size for Mg/MgH_2 that results in shortening paths for H diffusion and for movement of phase transition interface. The dissociation rate of hydrogen molecules, which indicates the degree of surface activity, can be improved by adding catalysts to reduce the activation energy of hydrogen dissociation and recombination processes. The corresponding general approach to the solution of the problem is shown in Figure 1-3 [57].

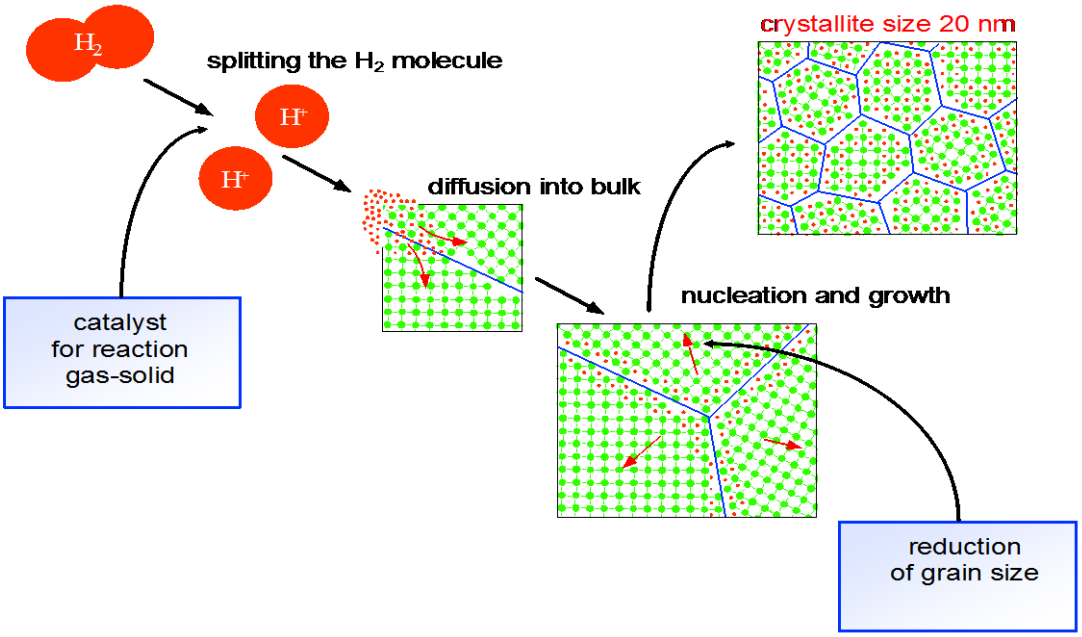

Figure 1-3: Improvement of H sorption kinetics of Mg-based materials by reducing their grain size, in combination with a catalyst

1.5. Research aims and objectives

In this study, the main objective was to advance kinetic performances of formation and decomposition of magnesium hydride by design strategies which include high energy ball milling in hydrogen (HRBM), in combination with the introduction of catalytic/dopant additives. Therefore, in order to improve the properties of Mg-based hydrogen storage materials, the present study focused on the following specific objectives:

- To radically improve the hydrogenation/dehydrogenation performance of Mg by nanotechonology routes, including reactive ball milling in hydrogen atmosphere;
- To develop weight efficient hydrogen storage materials (> 6 wt.%) characterized by fast hydrogenation/dehydrogenation at mild conditions;
- To outline promising ways of usage of the developed materials for hydrogen storage and related applications.

1.6. Thesis outline

Chapter 1 gives a general introduction to the thesis. The importance of the hydrogen economy is discussed and the criteria for a material to be considered for hydrogen storage are elucidated. General overviews of different types of materials that are currently studied for hydrogen storage are noted.

Chapter 2 gives an overview of different hydrogen storage materials with more details emphasised on MgH_2 and other Mg-based hydrogen storage materials. A brief overview of MgH_2, i.e. crystal structures, preparation methods, thermodynamics properties, hydrogen storage properties, kinetic limitations, introduction of additives and other modification approaches are discussed.

Chapter 3, gives the experimental details on the preparation of Mg-based nanocomposites by high-energy reactive ball milling of magnesium metal with various additives, and characterization of both preparation process (hydrogenation kinetics) and the produced materials studied in this work, along with the explanation of the different characterization techniques used in studying the prepared materials.

Chapter 4 presents the experimental results detailed in the following subsections:

4.1 presents the detailed results of HRBM, TDS/re-hydrogenations studies, microstructure and morphology for magnesium – carbon hybrid materials;

4.2 presents the detailed results of HRBM, TDS/re-hydrogenations studies, microstructure and morphology for magnesium-based hybrid materials containing additives of metallic catalysts;

4.3 presents the detailed results of HRBM, TDS/re-hydrogenations studies, microstructure and morphology for magnesium-based hybrid materials containing the additives of carbon in combination with the metallic catalysts, including Mg–C–BCC-V (4.3.1), and Mg–C–ZrNi (4.3.2);

4.4. presents the detailed results of HRBM, TDS/re-hydrogenations studies, microstructure and morphology for magnesium-based hybrid materials containing the additives of carbon in combination with the oxide catalyst ($TiFeO_3$).

The study is concluded in **Chapter 5** with a concise discussion of the objectives achieved pertaining to the study of phase composition, structure, morphology and hydrogenation/dehydrogenation behaviours of Mg-based hybrid materials prepared and characterised in this work. Recommendations are made, anomalies noted, and the greater relevance and implications of the study are discussed.

CHAPTER 2: Literature Review

Interest in the use of clean and renewable energy system on-board vehicle and in stationary applications has received a lot of attention over the past years. This can be seen from the increase of a number of published articles and patent reports by different researchers. The inevitable socio-economic impact of recurring fuel crises, the treat of early end to fossil fuels in the coming years, increased environmental pollution and anthropogenic climate change have been the catalyst for use of clean and renewable energy resources [58-60]. In vehicle applications, the idea to produce and store energy is of great interest. There are two main groups of zero-emission energy carriers that are being considered for vehicle applications: (i) batteries and (ii) hydrogen [61]. Batteries have the advantage that they only need an electric system in order to "refuel" the vehicle. However, the amount of energy that can be stored in today's batteries is limited, and this limits the driving range of the vehicle, and also the battery charging time is also too long, usually more than 4 hours.

The use of hydrogen as an energy carrier for on-board vehicle application is of interest because it has high energy density by weight, can be produced in large quantities from diverse array of primary energy sources, is clean burning, reducing greenhouse gas and also reducing the dependence on fossil fuels for energy supply [62]. However, when split from these primary sources of energy to form molecular hydrogen, a process requiring another source of energy, it becomes an environmentally attractive fuel. It can be burned or combined with oxygen in a fuel cell without generating CO_2, producing electricity, heat and water as a by-product as shown by equation 2.1 [63]. Like electricity it is a very

clean energy at the point of use, but like natural gas, it can form explosive mixtures with air.

$$H_2 + ½\ O_2 \rightarrow H_2O + 241.1\ kJ \qquad (\mathbf{2.1})$$

Hydrogen conversion in fuel cell into electrical energy is an efficient process that is enhanced by a factor of ~ three compared to conventional internal combustion engine where most of the energy is wasted as heat [64]. The challenge with the use of hydrogen on-board vehicle is the lack of suitable storage system, a combination of both volume and weight for drive range > 400 km. The development of an effective hydrogen storage medium that is safe, efficient, and light-weight has been a major impediment to the advent of a hydrogen-based industry and economy [65-67].

Considering the above, this chapter examines various hydrogen storage technologies and their advantages and limitations for on-board vehicle application.

2.1. Analysis of the present activities in weight-efficient solid- and liquid-state hydrogen storage technologies

2.1.1. Hydrides

Numerous metals and their alloys can be used to store hydrogen in the form of metal hydrides with selected materials shown in Table 2.1. These hydrides are formed by the reaction of metals or alloys with hydrogen. Hydrogen storage in metal hydrides can be grouped into: (i) low temperature hydrides which release H_2 at 1 bar around 70-100°C but with hydrogen storage capacity restricted to < 2.5 wt.% H e.g. $FeTiH_{1:8}$ [68, 69] and

$LaNi_5H_6$, [70-72], and (ii) high temperature hydrides require higher heating input and heating above 300°C for hydrogen desorption e.g. NaH, LiH [16] and MgH_2 [73].

Another sub-class of solid state hydrogen storage materials are complex hydrides which are ionic compounds of complex $[MH_n]^{m-}$ anions (e.g., $[AlH_4]^-$ or $[BH_4]^-$) and cations, usually the alkali or the alkaline earth metals, for example, $NaAlH_4$, $Mg(BH_4)_2$, $Ca(AlH_4)_2$ and $LiBH_4$. In contrast to metal hydrides, some complex hydrides combine high hydrogen storage capacities with a hydrogen release temperature down to ~100°C, thus, potentially meeting the DOE hydrogen storage criteria. The main issue with the complex hydrides so far is their reversibility [74-76].

Table 2.1: Gravimetric and volumetric hydrogen content in various materials

Material	**wt.% Hydrogen**	**H-atom/cm^3 (x 10^{22})**
H_2 (solid), 2.4K (-269°C)	100	5.3
MgH_2	7.6	6.5
Mg_2NiH_4	3.6	5.9
$FeTiH_{1.95}$	1.89	6.0
$LaNi_5H_{6.7}$	1.37	5.5
$ZrMn_2H_{3.6}$	1.75	6.0
VH_2	2.10	11.4

From the above, all hydrides release large amounts of energy during their formation, i.e., when hydrogen is absorbed in the material. The same amount of energy is required to release the hydrogen stored. Low and high-temperature hydrides have a heat of absorption of about 12-15 MJ/kg H_2 and 25-35 MJ/kg H_2, respectively. This makes rapid filling of a storage unit extremely difficult because high energy removal rates are required. For instance, if a hydride unit with a storage capacity of 5 kg of H_2 is to be refuelled in 5 minutes, a heat removal rate of 250 kW is required (hydride heat of

absorption of 15 MJ/kg). If this is waste heat, the impact on the overall efficiency of the system is high. During driving, the heat of absorption has to be supplied to the system in order for hydrogen to be released. However, the energy is to be supplied over longer periods of time and might be obtained from the waste heat of the engine or fuel cell. Because of their compactness, metal hydride storage systems are proposed for mobile applications. Nonetheless, the value of the heat of absorption of such systems probably hinders its application. Moreover, such systems are heavy. Prototype vehicles have already been operated using low-temperature hydrides. Liquid coolant from an external source is circulated through the storage system during refuelling in order to remove the energy released by the absorption process. During vehicle operation, the storage system is warmed by waste heat from the engine or fuel cell. Hence, at least from a vehicle operation point-of-view, the application of hydrides for hydrogen storage is feasible.

2.1.1.1. Light weight binary hydrides

The alkali earth metals form hydrides with a high degree of ionic bonding character. Thus the bonding between hydrogen and metal is strong resulting in high decomposition temperatures though in MgH_2 some covalent contribution presents [77]. In MgH_2 with its mixed bonding character, the electronic density is located around the atoms with a net charge of Mg close to +2 and negatively charged H atoms with a charge of -0.94-(-0.26). The remaining electron density is distributed evenly in the interstitial region, although recent experiments have revealed regions with increased electron density between Mg and H atoms clearly suggesting a partial covalent bonding character [78, 79]. Beryllium and magnesium have hexagonal close packed (*hcp*) structure but transforms into an orthorhombic structure and a tetragonal structure, respectively, for their corresponding

hydrides. Due to lower atomic packing density compared to the close packed hosts, the density of the hydrides of Be and Mg are lower than the metals. Ca, Ba, and Sr all have *bcc* structures and orthorhombic structures for their corresponding hydrides [77]. The alkaline earth metal hydrides are quite stable and require heating to elevated temperatures for decomposition into hydrogen and metal. Beryllium seems to deviate from the others with a remarkable low decomposition temperature which may rationalized in terms of a large cohesive energy of Be thereby reducing the stability of BeH_2. The use of light-weight metal for hydrogen storage is challenging because of both kinetic and thermodynamic limitations [80, 81].

2.1.2. Complex hydrides

The use of group I and group II salts of $[AlH_4]^-$, $[NH_2]^-$ and $[BH_4]^-$ (alanates, amides, borohydrides) has received considerable attention over the past years as potential hydrogen source. A summary of some widely investigated complex hydrides including amide/imide systems is given in Table 2.2. All these materials have high kinetic barrier to dehydrogenate and/or re-hydrogenate in the solid state. Over the past years, it was thought to be impractical to reduce the kinetics barrier to an extent that would give reaction rates that are approaching automotive requirements applications. Bogdanovic *et.al*. [74] demonstrated that, upon metal doping, the dehydrogenation of anionic alumohydrides could be kinetically enhanced and render the materials reversible under moderate conditions in the solid state. Following these findings, a number of complex hydrogen storage materials including amides and borohydrides have been studied. It has been demonstrated that amide/imide system reversibly stores hydrogen under moderate reaction temperatures. Lithium amide system motivated extensive studies and

subsequently a series of amide/imide system has been investigated by various researchers [82-84].

Table 2.2: Complex Hydrides hydrogen storage properties [87]

Material	Density (g/mol)	Density (g/cm^3)	Hydrogen (wt.%)	Hydrogen (kg/m^3)	T_m (C)*	$\Delta H_f°$ (kJ/mol)
$LiAlH_4$	37.95	0.917	10.54		190[d]	-119
$NaAlH_4$	54.00	1.28	7.41		178	-113
$KAlH_4$	70.11		5.71	53.2		
$Mg(AlH_4)_2$	86.33		9.27	72.3		
$Ca(AlH_4)_2$	102.10		7.84	70.4	>230[d]	
$LiNH_2$	22.96	1.18	8.78	103.6	372-400	-179.6
$NaNH_2$	39.01	1.39	5.15	71.9	210	-123.8
KNH_2	55.12	1.62	3.66	59.3	338	-128.9
$Mg(NH_2)$	56.37	1.39	7.15	99.4	360	
$Ca(NH_2)_2$	72.13	1.74	5.59	97.3		-383.4
$LiBH_4$	21.78	0.66	18.36	122.5	268	-194
$NaBH_4$	37.83	1.07	10.57	113.1	505	-191
KBH_4	53.94	1.17	7.42	87.1	585	-229
$Mg(BH_4)_2$	53.99	0.989	14.82	146.5	320[d]	
$Ca(BH_4)_2$	69.76		11.47		260[d]	
$Al(BH_4)_3$	71.51	0.7866	16.78	132	-64.5[d] 44.5[b]	

*(**b**) and (**d**) represent boiling and decomposition temperatures.

Magnesium borohydride is another attractive material with hydrogen gravimetric capacity of 14.8 wt.% and volumetric densities of 112 g/L, and favourable decomposition enthalpy of ~40 kJ/mol H_2 [86-90]. $Mg(BH_4)_2$ can be prepared by different methods but almost all of them produce solvates $Mg(BH_4)_2$ xL where x = 1-6, and L is a Lewis base . The first known synthesis of $Mg(BH_4)_2$ was prepared by the wet exchange reaction (metathesis) of

sodium borohydride ($NaBH_4$) with anhydrous magnesium chloride ($MgCl_2$) in diethyl ether as in equation 2.3 [91]. A direct wet chemical synthesis of $Mg(BH_4)_2$ was reported by Chłopek *et.al*.[88] in which magnesium hydride reacts with aminoborane as a BH_3 donor was found to be the only method capable of yielding the α-phase of $Mg(BH_4)_2$ and other tetrahydroborates in high purity without any solvents.

$$MgCl_2 + 2NaBH_4 \rightarrow Mg(BH_4)_2 + 2NaCl \qquad (\mathbf{2.2})$$

Following the above findings, $Mg(BH_4)_2$ was prepared by mechanochemical ball milling of $MgCl_2$ and $LiBH_4$ under argon atmosphere. However, product separation was not mentioned in this method [86]. Mechanochemical ball milling gives unsolvated $Mg(BH_4)_2$ but its separation from the reaction mixture requires extraction with a donor solvent that also yields a solvated product [87-90]. $Mg(BH_4)_2$ was postulated to decompose in two separate stages: release of hydrogen, and formation of boron (presumably amorphous) and magnesium hydride, which then further decompose to metallic Mg. Soloveichik *et.al*. reported attempts to rehydrogenate the decomposed $Mg(BH_4)_2$, with only Mg metal that could be rehydrogenated to MgH_2. Rehydrogenated products produce only 2.7-3.1 wt.% H_2 depending on the rehydrogenation conditions, which corresponds to the hydrogen desorbed from MgH_2 [92].

Matsunaga *et.al*. [87] reported the hydrogen storage properties of $Mg(BH_4)_2$ in detail and confirmed the presence of two flat plateaus in the desorption isotherm. The first decomposition enthalpy was obtained to be −39.3 kJ/mol H_2. A different value of enthalpy change for $Mg(BH_4)_2 \rightarrow MgH_2$ i.e. 57 ± 5 kJ/mol H_2 is reported by Li *et.al*. [92], but the reason for the observed differences in decomposition enthalpy measurement is not mentioned. The re-hydrogenation studies of this complex was able to reversibly

absorb 6.1 wt.% H_2 which is probably due to the re-hydrogenation of Mg into MgH_2. Soloveichik *et.al*. [93] proposed a four-stage pathway for thermal decomposition of $Mg(BH_4)_2$ with formation of intermediate magnesium polyboranes that eventually transformed to the most stable magnesium dodecarbonate, and ultimately ends with formation of MgB_2.

However, the above mentioned hydrides systems have practical limitations that must be overcome: (i) alanates have insufficient reversible capacity; (ii) borohydrides suffer from unacceptable slow kinetics and also from undesirable evolution of diborane, and amides are plagued by capacity and kinetic limitations as well as undesired evolution of ammonia. Additionally, the problem of thermal management on recharging is common to all complex hydrides.

2.1.3. Liquid (organic) hydrides

Liquid organic hydrides (LOH) have also attracted special attention. These liquid hydrides have several practical advantages with regard to system design, handling, etc. Hydrogen can be reversibly stored in unsaturated hydrocarbons through a catalytic reaction pair of dehydrogenation of cycloalkanes such as methylcyclohexane, cyclohexane and decalin. Hydrogenation of corresponding aromatics is a useful process for supplying hydrogen to PEMFC [99-103]. This is one of the most promising methods to store, transport and supply with *in-situ* generation of hydrogen. The advantages of this system are: CO free hydrogen at fuelling stations, reversible catalytic reactions, recyclable reactants and products and relatively high hydrogen contents (6-8 wt%) [94]. Due to high boiling points of cycloalkanes, the present infrastructure such as oil tankers and tank lorries can be used for the long-term storage and long-distance transportation of hydrogen in the form of LOH. The proposed system of hydrogen storage using liquid

organic hydrides will serve the transportation of hydrogen from production facility to fuelling stations. Whereas for on-board storage of hydrogen other methods such as gas cylinders or systems based on metal hydrides would be useful.

Hodoshima *et.al*. have shown that decalin ↔ naphthalene system can afford sufficient hydrogen content (7.3 wt.%; 64.8 kg-H_2/m^3) [99]. The >500 km drive range for PEMFC vehicle would be managed by 50 litres of decalin on the basis of its high volumetric hydrogen content. In addition, evaporation loss during storage is negligible because of their high boiling points: 187°C (*trans*-decalin), 196°C (*cis*-decalin) and 218°C (naphthalene). Decalin dehydrogenation is highly endothermic (the enthalpy change is 297.3 kJ/mol at 298.15 K) and thermodynamically restricted at low temperatures [95]. The conventional heterogeneous catalysis of dehydrogenation in the solid–gas phase is therefore performed at high heating temperatures of more than 400°C which might result in the formation of by-products or carbonaceous deposit over catalyst in addition to thermal energy loss.

Furthermore, cyclohexane and methylcyclohexane are the other widely studied liquid hydrides systems for hydrogen storage. The reactions routes of cyclohexane ↔ benzene and methylcyclohexane ↔ toluene have ~ 6.0 wt.% reversible hydrogen capacity [100].

$$C_6H_{12} \leftrightarrow C_6H_6 + 3H_2 \qquad (\Delta H = 206 \text{ kJ/mol } H_2) \qquad \textbf{(2.3)}$$

$$C_7H_{14} \leftrightarrow C_7H_8 + 3H_2 \qquad (\Delta H = 215.3 \text{ kJ/mol } H_2) \qquad \textbf{(2.4)}$$

However, these reactions are not quite amenable towards dehydrogenation for practical application conditions. High temperature of dehydrogenation and in some, the undesired carbonaceous deposits on the catalyst and catalyst poisoning makes this system not suitable for automotive application.

2.1.4. Hydrolysis systems utilizing water-reacting alloys or hydrides

An attractive source of hydrogen for mobile proton exchange membrane fuel cells is aqueous hydrolysis of chemical hydrides. However, challenge with this method of hydrogen production is the control of the hydrolysis reaction. The reaction is either too fast or even explosive for some chemical hydrides such as $LiAlH_4$ or it is too slow for practical applications in some cases [106]. Hydrolysis of chemical hydrides can be represented as follows:

$$2\ MH_n + nH_2O \rightarrow M_2O_n + nH_2 \qquad (\mathbf{2.5})$$

One of the chemical hydrides that could be used is sodium borohydride (NaBH4); its hydrolysis could be used to generate hydrogen gas and water-soluble sodium metaborate ($NaBO_2$) in the presence of suitable catalyst [102], in this way hydrogen can be generated safely for fuel cells applications. Generating H_2 catalytically from $NaBH_4$ solutions has many advantages in that NaBH4 solutions are non-flammable, reaction products are environmentally friendly, rate of H_2 generation is easily controlled, the reaction product $NaBO_2$ can be recycled, H_2 can be generated even at low temperatures. Such hydrolysis of sodium borohydride can be accelerated by catalysts, acid addition, or under elevated temperature [103]. All of the catalysts used in hydrolysis of NaBH4 so far are bulk metals and they act as heterogeneous catalysts [104, 105]. This can be represented in the equation as below:

$$NaBH_4 + 2H_2O \rightarrow NaBO_2 + 4H_2 \quad (\mathbf{2.6})$$

The hydrolysis reaction of MgH_2 results in an incomplete and very slow reaction because of the magnesium hydroxide $Mg(OH)_2$ layer formed and the reaction can be expressed by equation 2.7 [101]:

$$MgH_2 + 2H_2O \rightarrow Mg(OH)_2 + 2H_2 \quad (\mathbf{2.7})$$

The hydrogen yield for this reaction is 6.5 wt.% when water is taken into account. In fuel cell applications, if the water produced by the fuel cell is redirected to the chemical hydride, then the yield increases to 15.4 wt.%. The yield for this reaction compares well with the hydrolysis of sodium borohydride which produces 7.3 wt.% if the weight of water is accounted and 21.2 wt.% if water is not accounted. Moreover, the reacted product (magnesium hydroxide) is environmentally benign [101] with -160 kJ/mol heat of hydrolysis and this makes it the least suitable hydride for hydrogen production in terms of reaction controllability. Table 2.3 shows the summary of the primary reaction equation and associated hydrogen storage properties of some well-known chemical hydrides.

Table 2.3: Chemical hydride hydrolysis and their hydrogen storage properties

Hydride and reaction	Fraction -H	H_2 specific Mass (kg H_2/kg)	H_2 Density (kg H_2/L)
$LiH + H_2O \rightarrow LiOH + H_2$	0.126	0.252	0.122
$NaH + H_2O \rightarrow NaOH + H_2$	0.042	0.083	0.106
$CaH_2 + 2H_2O \rightarrow Ca(OH)_2 + 2H_2$	0.048	0.095	0.121
$MgH_2 \rightarrow Mg + H_2$	0.076	0.076	0.110
$LiAlH_4 + H_2O \rightarrow LiOH + Al + 2.5\ H_2$	0.105	0.132	0.121
$TiH_2 \rightarrow Ti + H_2$	0.040	0.040	0.152
$LiBH_4 + H_2O \rightarrow LiOH + HBO_2 + 4H_2$	0.184	0.367	0.235
$NaBH_4 + H_2O \rightarrow NaBO_2 + 4H_2$	0.105	0.211	0.226

2.1.5. Methanol (on-board reforming)

On-board methanol reforming to produce hydrogen is considered to be a practical solution for automotive fuel cell applications [106]. Methanol has high volumetric energy density and is one of the promising candidate fuels for producing hydrogen. Methanol reforming reaction is endothermic and run sufficient at 250-300°C on copper-based catalysts. Usually the reaction is operated under pressure (3-15 bar) and heat is supplied to drive the reaction to produce hydrogen. The heat may be supplied by an external burner or by associating an exothermic oxidation reaction within the reformer (autothermal process). *In-situ* combustion with air can supply the necessary heat and ideally the reforming and combustion reactor would occur simultaneously [107, 108]. The steam reforming of methanol can be simplified to the following overall reactions (equation. 2.8 and 2.9):

$$CH_3OH + H_2O \rightarrow CO_2 + 3H_2 \qquad \Delta H_{298} = 49.4\ kJ/mol \quad (\mathbf{2.8})$$

$$CO + H_2O \rightarrow CO_2 + H_2 \qquad \Delta H_{298} = -\ 41\ kJ/mol \quad (\mathbf{2.9})$$

In autothermal reforming of methanol, an extra exothermic step is added to the steam reforming to generate the necessary heat to complete the reformation. Using oxygen as the oxidiser, the exothermic step is (eq. 2.10):

$$CH_3OH + 1.5\ O_2 \rightarrow CO_2 + 2H_2O \qquad \Delta H_{298} = 675.4\ kJ/mol \quad (\mathbf{2.10})$$

Methanol reforming may bridge the current hydrogen gap because the existing energy network is well established for transporting liquid fuels.

2.1.6. Ammonia (on-board storage and decomposition)

Ammonia (NH_3) has a theoretical hydrogen storage content of 17.6 wt.% and it seen as the potential fuel source for fuel cell application. Pure ammonia has an energy density of 8.9 kWh/kg which is higher than methanol (6.2 kWh/kg), but less than diesel (13.2 kWh/kg). Proponents quickly point out that ammonia's strong odour makes leak detection simple, reducing some of the risk. Another challenge is that PEMFC require ammonia levels to be reduced below ppb levels to ensure long life, since exposure of ammonia to the acidic PEMFC electrolyte causes severe and irreversible loss in performance. The losses are cumulative since the ammonia will build up in the electrolyte [109, 110].

While the material would not be regenerated "on-board" it could potentially meet many US DoE targets. The toxicity and hazardous effect of ammonia on health puts a drawback on the use of ammonia as fuels for on-board automotive applications.

2.2. Thermodynamics and Kinetics of metal hydrides

Metal hydrides provide a possibility to store and extract hydrogen via the hydride formation and decomposition reaction, respectively. When hydrogen absorbing metal is exposed to hydrogen atmosphere, a chemical reaction occurs between the metal and hydrogen. During the process of hydrogenation, first the hydrogen molecules are adsorbed onto the metal surface, where H_2 molecules are split into H-atoms [3]. The first hydrogen atoms that penetrate the bulk phase occupy mainly interstitial positions. This phase in which the H-atoms are in dilute solid solution is the so-called α-phase. As the amount of hydrogen atoms in the metal increases, a phase transition is induced. The resulting hydride often has a different structure to that of corresponding metal. As this β-phase has larger volume than the metal. The transition can be accompanied by stress in the material and significant transition- and activation-energies [111]. Since a such phase has to grow or shrink, the difference in structural and volume change may also cause a barrier for hydrogen charging or discharging [112, 113]. Upon absorption of hydrogen into a metal, the metal undergoes a structural changes depicted in Figure 2.1.

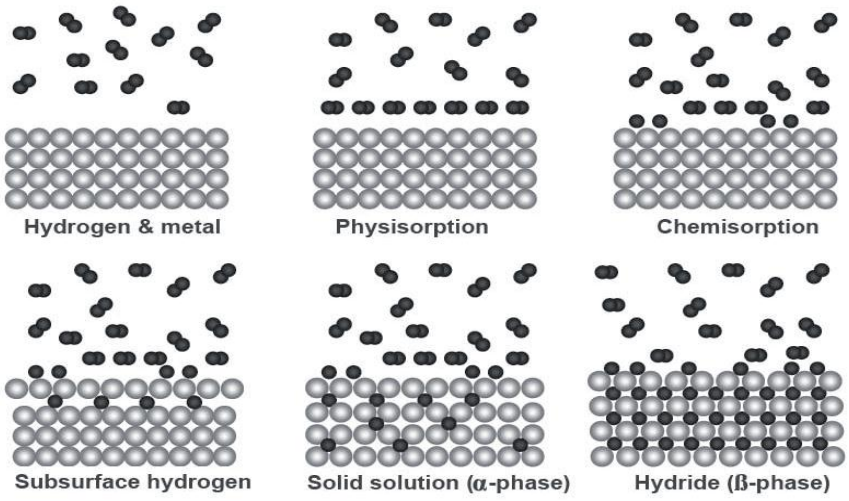

Figure 2-1: Schematic mechanism of hydrogen absorption of metal [3, 114]

The thermodynamic behaviour as well as the capacity of metal hydrides can be described by pressure-composition isotherms (P-C-I). Figure 2.2 (**left plot**) depicts an ideal P-C-I curve of a typical metal hydride at constant temperature. In Figure 2.2, P_{eq} is the hydrogen equilibrium pressure, H/M the hydrogen to metal ratio (concentration), α represent interstitial solid solution of H in the metal phase, β the hydride phase. At temperatures below the critical temperature (T_c), two phase region exist between the solid solution (α-phase) and the (β-phase). At temperature above the critical temperature this two-phase region no longer exists. In the first step of the curve, the hydrogen absorbed by the metal is increased by increasing the hydrogen pressure, and the metal forms solid solution with hydrogen called the α-phase. The hydrogen is then dissolved interstitially. Sievert's law can often be applied in this particular region:

$$\frac{M}{H} = k_S \sqrt{p} \qquad (\mathbf{2.11})$$

where M/H is the hydrogen concentration, Ks is the equilibrium constant, P is the partial pressure of H_2 in the atmosphere.

When the hydrogen content in the metal increases, the hydrogen atom interacts via elastic strain introduced in the metal lattice, and the pressure/composition departs from ideality. This is reflected by the decrease in the slope of the isotherm compared to the ideal Sievert law behaviour. There is, however, a limit in the amount of hydrogen the α-phase can store. Once the α-phase is saturated, then the formation of β-phase commences. At equilibrium pressure (P_{eq}), the transformation from α-phase to β-phase becomes complete. When the solid solution and hydride phases coexist, there is a plateau in the isotherm, the length of which determines the amount of hydrogen stored. In the β-phase,

the hydrogen pressure rises steeply with concentration. The two phase region end in a critical point, (T_c) above which the transition from the α-phase to β-phase is continuous. The plateau pressure will rise with temperature according to the van't Hoof equation (eq. 2.13) and disappear at the critical temperature T_c:

$$\Delta G° = -RT\ ln\ Keq = RTln\left[P / P_\circ\right] = \Delta H° - T\Delta S° \qquad \textbf{(2.12)}$$

$$ln\left[P / P_\circ\right] = +\Delta H° / RT - \Delta S° / R \qquad \textbf{(2.13)}$$

where, ΔG° is the standard change of Gibbs free energy, ΔH° is the standard enthalpy change and ΔS° is the standard entropy change during the phase transformation. P_o is standard pressure, i.e. P_o = 1.01 x 10^5 Pa. K_{eq} is the equilibrium constant at absolute temperature T. R is the universal gas constant. With the equilibrium conditions, thermodynamics characteristics of hydrogen sorption can be derived from the plot $ln[P/P_o]$ vs 1/T depicted in Figure 2.2 (**Right plot**). The intercept with the $ln[P/P_o]$ axis yields the sorption entropy, which amounts approximately to the standard entropy of hydrogen [3, 114]. The slope is a measure of the sorption enthalpy, which is independent on the isothermal desorption temperature.

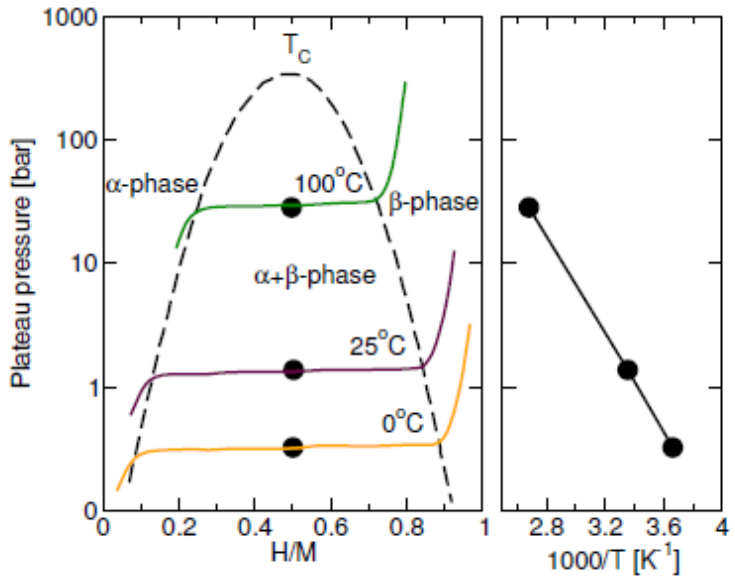

Figure 2-2: (Left) Hypothetical representation of pressure-composition-isothermal (PCI) diagram metal hydride. (Right) van't Hoff plot for hypothetical metal hydride derived from the measured pressures at plateau midpoints from PCI [3]

For practical applications of hydrogen on-board the vehicle, the pressure at which the transition from α to β-phase takes place must be close to 1 bar at relatively low temperature (~100°C). Assuming that ΔS is the entropy of gaseous hydrogen (130 J/mol K), the enthalpy of formation of the hydride ΔH should be between -30 and -55 kJ/mol H_2 to achieve 1 bar H_2 equilibrium between 40°C and 150°C, based on van't Hoff equation.

The hydrogen sorption kinetics is of important consideration for practical applications of metal hydrides. It has been shown that the hydrogenation is composed of several steps, including:(i) dissociation of hydrogen molecules to hydrogen atoms, (ii) surface penetration of hydrogen atoms, (iii) diffusion of hydrogen atoms through the hydride layer by a vacancy mechanism (α-phase) or interstitially (β-phase), (iv) nucleation of the

α- or β-phase and (v) movement of the α/β-phase [115, 116]. For hydrogen desorption, the steps includes: (i) hydride decomposition at the hydride/metal interface, (ii) diffusion of hydrogen atoms through α-phase, (iii) surface penetration of hydrogen atoms, (iv) recombination of chemisorbed hydrogen atoms and physisorption and (v) desorption to the gas phase [116].

To acquire detailed information about the kinetics of the reactions, the apparent activation energy (E_A) for the reaction can be calculated by Arrhenius equation (eq. 2.14) based on the isothermal dehydrogenation/re-hydrogenation as follows:

$$K(T) = A\exp\left(-\frac{E_A}{RT}\right) \qquad (\mathbf{2.14})$$

where K is the temperature-dependent reaction rate constant, A is a pre-exponential factor, E_A is the apparent activation energy, R is the gas constant, and T is the absolute temperature. Therefore, it is necessary to determine the value of K before calculating the activation energy. Usually K can be determined by analyzing the isothermal hydrogen sorption curves with appropriate solid state kinetics rate expressions, which are derived from the corresponding solid-state reaction mechanism model such as nucleation, geometrical contraction, the diffusion and the reaction order models, which are based on the different geometric of the particles and the driving forces [3, 111-116]. Many different rate expressions have been derived from these mechanisms.

The kinetics rate-limiting step for metal hydrides is typically either the dissociation/recombination (chemisorption) transition between hydrogen gas and

hydrogen atoms on the materials surface or the nucleation and growth (NG) of the hydride during absorption or the metal phase during desorption. When the hydriding involves a phase transformation from α to β, nucleation and growth is usually the dominant kinetics process. The most frequently applied model of kinetics of phase transformation relevant to the process of H-desorption was proposed by Avrami [117] and Johnson and Mehl [118], which is typically referred to as the JMA. The model is based on the approach describing the kinetics as nucleation and growth of the nuclei of a new phase within the bulk of the matrix phase as the rate-liming step. The JMA model describes the nucleation of randomly dispersed second phase particles independently from location, i.e. surface or bulk. The growth rate *k* of new phase is controlled by temperature and is independent of time [119, 120] shown by equation 2.15.

$$\left[-\ln(1-\alpha)\right]^{1/n} = kt \qquad \textbf{(2.15)}$$

where *n* depends on the dimensional growth of new phase, e.g. $n = 2$ or $n = 3$ correspond to two- or three-dimensional growth of the existing nuclei, respectively. It is only valid when the nucleation rate is not time dependent. Under both situations, the rate-limiting step is the moving of the metal/metal hydride interface [120] under the assumption that the hydrogen diffusion is quick enough.

2.3. Synthesis and properties of magnesium hydride

Magnesium hydride (MgH_2) can be synthesized both by chemical methods, starting from magnesium-organic compounds and by direct synthesis from magnesium metal and hydrogen gas as shown in equation 2.16:

$$Mg + H_2 \leftrightarrow MgH_2 + 74.5\ kJ \qquad (\mathbf{2.16})$$

The first report on MgH_2 preparation by pyrolysis of ethyl-magnesium-iodide was published in 1912 [122].

Following the above findings, the direct synthesis of MgH_2, according equation 2.16, at P_{H2} = 200 bar and T = 567°C, using MgI_2 as a catalyst was reported [122] with the yield of 69% obtained under these conditions. Later, by combined use of iodine catalyst (0.5 – 1%) and ball milling of the charge, the yield of MgH_2 was increased, and synthesis conditions were softened (P_{H2} = 100 – 200 bar, T = 350 – 450°C). Some other organic catalysts, like allyl-iodide, multiring aromatic compounds of transition metals, etc., were successfully used as well [123, 124]. Further improvements of the experimental technique allowed to carry out the direct synthesis of MgH_2 without catalysts [128-131]. In contrast to chemically synthesized MgH_2 being very active substance, which self-ignites when exposed to air and intensively reacts with water, magnesium hydride obtained by hydrogenation of metallic Mg is rather inert and safe in handling material.

Figure 2.3 shows the structures of Mg (A) together with α- (B) and γ- (C) allotropic modifications of MgH_2. MgH_2 is stoichiometric hydride having ionic type of chemical bond, with some covalent contribution. α-MgH_2 has tetragonal, rutile-type, crystal structure (Figure 2.3(**B**); space group #136; a = 4.517Å, c = 3.020 Å) and bulk density of 1.45 g/cm^3 [127, 128]. So, the transformation of hexagonal magnesium (Figure 2.3(**A**); space group #194; a = 3.209 Å, c = 5.211 Å; bulk density 1.74 g/cm^3) to α-MgH_2 is accompanied by 20% increase in volume and the volumetric hydrogen density in magnesium hydride is about 0.11 g/cm^3. Under high pressures (up to 80 Kbar) and temperatures (up to 900°C) this modification of magnesium hydride (α-MgH_2) transforms

to a hexagonal (pseudocubic) β-MgH_2 (fluorite type form with an eight-coordination for Mg, *a* = 4.53Å, *c* = 10.99 Å, ρ = 1.79 g/cm^3) and, further, to γ-MgH_2 having the α-PbO_2 type structure with a six-coordination for Mg (Figure 2.3 (**C**); space group *Pbcn* / # 60, *a* = 4.526Å, *b* = 5.448Å, *c* = 4.936 Å, ρ = 1.43 g/cm^3). γ-MgH_2 is stable on air, does not interact with water at room temperature; at atmospheric pressure and T~350°C the reverse transformation of γ-MgH_2 → α-MgH_2 takes place [129-130].

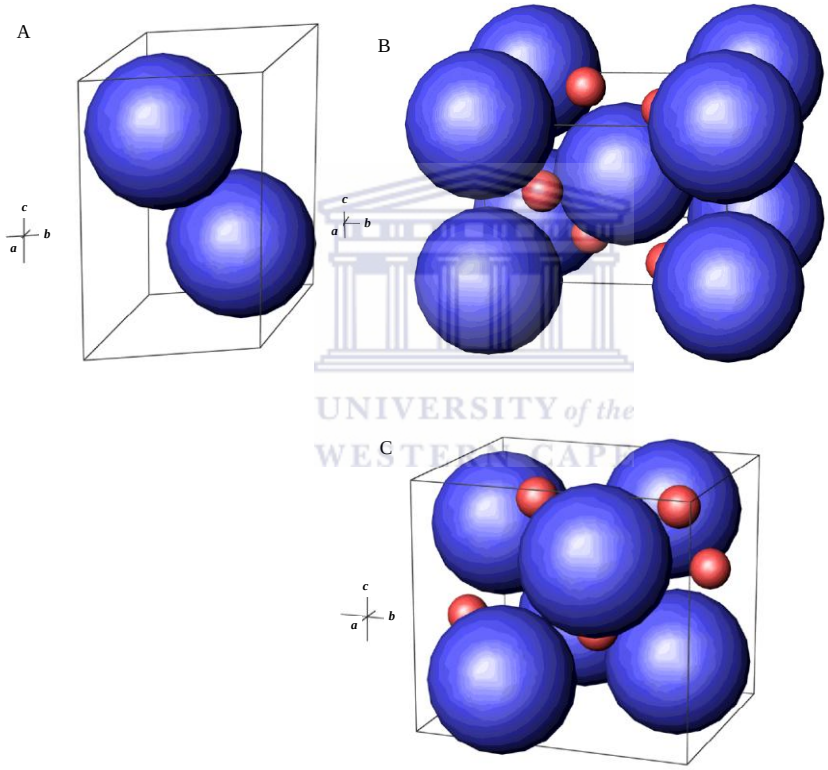

Figure 2-3: Unit cells of Mg (A**), α-MgH_2 (**B**) and γ-MgH_2 (**C**). Magnesium atoms are shown as blue spheres (R~1.45 Å), H atoms as red ones**

The main disadvantage of the individual magnesium as a hydrogen storage material is the low rate of its interaction with hydrogen gas, especially in the course of the first hydrogenation. According to data by different authors surveyed in [131], the first

hydrogenation of Mg at T=340–350^{o}C and hydrogen pressure up to 30 bar can be completed within 6 to 336 hours. Such great discrepancies are caused by high sensitivity of the reaction rate to the purity, particle size and surface state of the parent metal, activation conditions, purity of hydrogen gas, etc. The reaction can be accelerated by the increase of the temperature to 400–450^{o}C and hydrogen pressure to 100–200 bar, in combination with some gas-phase catalysts, like iodine vapours, CCl_4, etc. The mechanical treatment (ball milling) of the charge during hydrogenation improves hydrogen sorption performances as well [132].

Data from different authors concerning kinetics of the second and the following hydriding cycles of pure magnesium are in relative agreement, but the discrepancies are still significant. At hydrogen pressure P=20–40 bar and temperature of 300–400°C, the 80–90% hydrogenation can be reached in 2–20 hours, whereupon the reaction practically stops [133, 134, 135]. The reasons of such behaviour, most probably, in the following features of magnesium – hydrogen system could be (i) very low hydrogen solubility in magnesium and (ii) precise stoichiometry of magnesium hydride. Therefore, at the first stage of MgH_2 formation (conversion fraction up to ~0.3), the reaction, most likely, is controlled by nucleation and growth, and at the final stage (conversion fraction more than 0.8) the hydrogenation is controlled by slow diffusion of H atoms through hydride layer [131]. Since 1960-th there were attempts to improve the hydrogen sorption properties of magnesium, through the development of alloys and multiphase polymetallic compositions on its basis. Thus as early as 1963 Mikheeva *et.al*. [136] had shown the possibility of gas phase hydrogenation both for magnesium at room temperature and atmospheric pressure, using Ce–Mg alloys. Later, the works by Reilly and Wiswall showed the improvement of

hydriding kinetics of magnesium by hydride-forming intermetallides (Mg_2Ni and Mg_2Cu) [137, 138], which stimulated intensive activities in this field.

An overview of the studies aimed at the improvement of hydrogenation/dehydrogenation performances of Mg-based hydrogen storage materials is presented in the next section.

2.4. Methods of improvement of hydrogen sorption performances of magnesium hydride

2.4.1. Bulk modification (alloying with additives)

Efforts to improve the absorption/desorption process of hydrogen for Mg/MgH_2 involve modification of both composition and structure of the subject materials to lower the operation temperature, increase hydrogenation/dehydrogenation rates and possibly, to destabilise the hydrides. First principles investigation into ways of destabilizing MgH_2 demonstrated the influence of different alloying elements on the stability of rutile-type α-MgH_2. It was found that Al, Ti, Ni, Cu and Nb destabilize it to a large extent, ranging from 22.9 kJ/mol H_2 for Ti to 69.1 kJ/mol H_2 for Cu [139]. Calculations of total energy and heat formation of magnesium hydride alloyed with aluminium indicate that the bonding between magnesium and hydrogen is weakened by the addition of aluminium [140]. Furthermore, Al is a light-weight metal, it reduces the affinity towards oxidation and enhances heat transfer during the hydrogenation process. MgH_2/Al alloys (Al composition ranging from 10 to 80%) synthesis via ball milling have been reported. The amount of Al incorporated into the Mg and the formation of the intermetallic γ-phase ($Mg_{17}Al_{12}$) is reported to depend on the ball milling time as well as the initial ratio of the Mg and Al powders. When 10% Al powder was mixed with Mg powder, no intermetallic

phase was observed even after long milling times [141]. In addition to alloying, ball-milling for longer times results in the development of nanocrystalline structure in Mg-Al alloy powders [142]. Hydrogenation of Mg-10% Al alloy at 400°C by ball-milling produce β-MgH_2 as the final product.

The hydrogenation of Mg-containing intermetallic compounds was at first experimentally observed by Reilly and Wiswall in 1967 [137], who have found the reaction of Mg_2Cu with hydrogen gas according to the scheme:

$$2Mg_2Cu + 3H_2 \leftrightarrow 3\ MgH_2 + MgCu_2 + 218.4\ kJ \qquad (\mathbf{2.17})$$

Reaction (2.17) proceeds rapidly at T~300°C and P_{H2}~20 bar. It can be formally classified as a hydrogen disproportionation of starting intermetallide Mg_2Cu, but unlike majority of the disproportionation reactions, it is reversible and allows to reversibly absorb up to 2.6 wt.% H at the temperatures lower than for Mg-H systems (reaction 2.16). The absolute value of the corresponding reaction enthalpy (–72.8 kJ/mol H_2) is lower than one of the enthalpy of formation of MgH_2 (–74.5 kJ/mol H_2).

Further destabilization of Mg-based hydrides was achieved for Mg_2Ni to reversibly form a ternary hydride, Mg_2NiH_4 [138]:

$$Mg_2Ni + 2H_2 \leftrightarrow Mg_2NiH_4 + 128\ kJ \qquad (\mathbf{2.18})$$

Reaction (2.18) proceeds rapidly at T~325°C and P_{H2}~20 bar allowing to reversibly absorb up to 3.7 wt.% H; the specific heat of formation of the Mg_2NiH_4 hydride (64

kJ/mol H_2) is lower than one for MgH_2. The presence of Mg_2Ni in Mg–Ni alloys catalyses the hydrogenation of magnesium and dehydrogenation of MgH_2 thus improving the hydrogenation/dehydrogenation kinetics. Among Mg-containing intermetallic compounds, the numerous group of magnesium-rich intermetallides with rare-earth metals, R (e.g. RMg_2, R_2Mg_{17}, R_5Mg_{41}, etc), are of practical importance. Independently of their composition and structure, these intermetallides irreversibly disproportionate in the course of their interaction with hydrogen gas to yield a homogeneous mixture of magnesium and rare-earth hydrides [143]. Due to fine microstructure of the material and catalytic properties of the hydrides of rare-earth elements towards hydrogen transfer reactions, the hydrogenation/dehydrogenation kinetics in these materials is significantly improved. Further improvement of the hydrogenation/dehydrogenation performances was achieved in Mg–RE–Ni ternary alloys prepared either by conventional metallurgical routes [144], or using powder metallurgy [145]. After hydrogenation, these materials contain MgH_2, RH_{3-x} (R – rare earth element) and Mg_2NiH_4 where the latter two catalyse hydrogenation of Mg and dehydrogenation of MgH_2.

Table 2.4 summarizes the information about hydrogen sorption performances of magnesium and Mg-based alloys important from application point of view. It can be noted that the alloying allows only limited opportunities to reduce operating temperature ranges. The price for that is a significant reduction of hydrogen storage capacity of the material.

Table 2.4: Hydrogen storage properties of magnesium and some alloys/intermatallides on its basis

Parent material	H storage capacity		Density, g/cm^3		Thermodynamic parameters of H sorption / desorption		
	wt.%H	g H /L	Parent material	Hydride	ΔH° [kJ/mol H_2]	ΔS° [J/(mole H_2 K)]	T [$^\circ$C]
Mg	7.6	110	1.74	1.45	–74.5	–135.0	250–400
Mg_2Cu	2.6	66	3.40	2.53	–72.8	–142.1	200–400
Mg_2Ni	3.7	100	3.40	2.70	–64.0	–122.5	200–400
Mg–Ni (eutectic alloy)	5.8	104	2.20	1.80	–75 –70	–130 –120	300–350
Mg–Mm–Ni (eutectic alloy)	5.5	115	2.50	2.10			

2.4.2. Nanostructuring (Equal Channel Angular Pressing, Rapid Solidification)

Equal channel angular pressing (ECAP) is a technique used to improve the mechanical properties of commercial structural alloys [152]. ECAP belongs to the family of severe plastic straining deformation methods in which an intense plastic straining is imparted on a material, chiefly through simple shear. Efforts have been made to improve the mechanical properties of light weight-structural alloys. ECAP is the most efficient one, where heavy strain is imposed by simple shear to the alloy processed, resulting in an ultrafine microstructure and ameliorated properties. ECAP enables the production of porosity-free materials with average crystallite sizes between 2 μm and 100 nm in

substantial quantities with lower concentration of impurities and at a lower cost than conventional ball milling [147].

Although ECAP proved to be quite efficient in enhancing hydrogen absorption and desorption ability of the alloy, the highest effect was achieved when it was combined with high-energy milling. The investigation of a commercial magnesium alloy AZ31 (96 wt.% Mg, 3 wt.% Al, 1 wt.% Zn) processed by ECAP between 423 K and 573 K [154] also revealed that the optimal hydrogen absorption and desorption parameters of AZ31 were obtained when three different mechanical processing techniques [ECAP, cold rolling, and high-energy ball milling] were combined. Thus, it seems safe to assume that the full advantage of ECAP can be taken if it is combined with other processing techniques, rather than when it is used alone.

Another method of interest to improve hydrogenation kinetics and microstructure of the materials is rapid solidification (RS) process. Rapid solidification permits to obtain several structural features favourable from the viewpoint of mechanical properties and thermal stability. These include, (i) finely dispersed microstructure, (ii) presence of metastable crystalline and/or quasi-crystalline intermetallic phases, (iii) high super-saturation of solid solutions, and; (iv) the presence of amorphous phases.

$LaMg_{12}$ prepared by RS at 2000 rpm was reported by Poletaev *et.al*.[149], the obtained materials showed slow hydrogenation rate that took 30 min to reach 90% and complete hydrogen release was complete after 3 hours. Introducing Ni to the alloy composition to reach a composition $LaMg_{11}Ni$, a positive influence in hydrogenation kinetics was noted but the overall hydrogen capacity decreased because of the replacement. From the

obtained results, $LaMg_{11}Ni$ alloy RS at 2000 rpm exhibited the fastest hydrogenation kinetics, reaching maximum hydrogenation capacity of 5.02 wt.%H in several minutes. Studies of the hydrogenated RS ribbons showed the formation of the nano-scale embryos of MgH_2, growing to form polyhedral grains of magnesium dihydride. Wu *et.al*. [150] also showed improved H-absorption/desorption kinetics for melt-spun ribbons of Mg–10Ni–2Mm by increasing the solidification rate of the alloy. The maximum hydrogen storage capacity of the melt-spun ribbons was found to be dependent on the contents of different hydride composition with the various solidification rate: 5.1, 4.6 and 4.2 wt.% H were obtained for the 300, 1000 and 2000 rpm samples, respectively. The improvement is assumed to be a result of grain refinement and the formation of nanocrystalline microstructures from amorphous phases and similar findings were reported by Poletaev *et.al*. [149].

2.4.3. High-energy Reactive Ball Milling

2.4.3.1. Nanostructuring during BM of Mg and MgH_2 as efficient way for the improvement of hydrogenation/dehydrogenation kinetics

Numerous studies have been addressed in an effort to enhance magnesium hydrogenation rate [151]. One of the most promising approaches was found to be mechanical milling (MM). This method was found to be among other methods used for the preparation of nanostructured materials characterized by improved kinetics of hydrogenation and dehydrogenation. The work of many researchers [6-8] has proved this as an efficient way to modify composition and structure of the parent material, thus improving its hydrogenation and dehydrogenation kinetics. During MM, powder particles are trapped between colliding balls or between balls and container wall. These high-energy impacts

induce fracturing and cold welding of particles and define the ultimate structure of the powder. The product often exhibits unusual physico-chemical properties and enhanced reactivity, in particular, with respect to hydrogen. The enhancements are especially pronounced for Mg-based materials where a combination of nanostructuring with surface modification results in a dramatic improvement of the hydrogenation kinetics [50].

The formation of defects on the material may aid in hydrogen sorption by providing many active sites with low activation energy. By reducing the particle size, the thermodynamic properties of the material may be changed to a point where surface free energy can govern the reaction [152]. Additional improvement of the hydrogenation performances of Mg was observed upon the introduction of catalytic additives like transition metals [50, 159-162], hydride-forming alloys and intermetallic compounds [157, 158], oxides of 3*d* metals [159-161], metal halides [162, 163], etc.

However, one should keep in mind that ball-milling process is dependent on many parameters, such as the nature of the milling vessel, milled material, weight of the balls, amount of milled material and many other factors [164]. Thus, for each system optimum conditions have to be determined. When the milling time is prolonged, the influence of milling is not always giving positive results. This is thought to result from change in surface area and inertial stress of the material during milling. The milled material particle size becomes smaller with large surface area and bringing out more dislocation and defects which explain why the milled sample has higher hydrogen storage capacity and is easily activated. When the sample is milled too long, the particle become smaller with the particles subjected to oxidation and inter-particle stress become larger resulting in reduce hydrogen storage capacity and hydrogen absorption rates [165-167].

Despite very intensive studies of MM and HRBM of the Mg-based hydrogen storage nanocomposites, certain lack of the information about hydrogenation behaviour of the material during HRBM takes place. Usually, the evolution of phase-structural changes in the materials during the milling is carried out by periodic sampling of the material from the milling vial followed by XRD and other analyses [168, 169], and only in few cases hydrogen absorption during HRBM is monitored directly by observing the pressure in the milling vial [170]. Getting such information for HRBM of Mg-based composites, together with the supplementing data about structure, morphology and dehydrogenation/re-hydrogenation properties would be of a high value for further understanding of mechanism of the improvement of hydrogen sorption performances and, further, would promote the development of highly-efficient light-weight hydrogen storage materials.

2.4.3.2. HRBM preparation of MgH_2 based hydrogen storage nanocomposites and their performances

2.4.3.2.1. MgH_2 – carbon nanocomposites

The use of different carbon types as additives/dopants to improve hydrogen storage performances of Mg/MgH_2 is well reported [171-175], but the role of these additives is not yet fully understood. Graphite when ball milled with Mg or MgH_2 has been shown to significantly enhance the hydrogen sorption rate, with the resultant hydrides sample exhibiting shorter activation time during hydrogen cycle studies [176]. Shang *et.al*. [177] investigated the order of addition during ball milling of MgH_2 and graphite, the obtained results showed that; addition of graphite before milling increase the absorption rate, preventing the formation of oxide layer on the magnesium surface but had little effect on

the desorption rate [171]. The advantage of using graphite is that it may prevent cold welding of particles by forming an inert layer in-between, by shearing on over the other layer may totally envelope the particles and thus prevent particle contact. The decomposition studies of MgH_2 prepared with different carbon materials that were subjected to mild oxidation treatment prior to their milling shows the resulted decomposition peak to be shifted slightly to higher temperatures compared with the same carbons that were not subjected to oxidation [171]. The shift in decomposition temperatures could result from the reduction in carbons activity due to an increase oxygen level in the carbon surface or the transfer of oxygen surface from the carbon to magnesium, forming the inhibitive MgO layer in the reaction.

Imamura *et.al*. [173, 174, 178] have shown that MM of Mg and graphite carbon with organic additives (benzene, cyclohexene, cyclohexane) results in the improvement of hydrogenation kinetics and decrease of dehydrogenation temperature. The MM (4 to 40 hours long) resulted in the generation of dangling carbon bonds in graphite promoting the formation of C–H bonds and thus forming new hydrogen-storing sites. Huot *et.al*. [179] have shown that graphite significantly accelerates reactive synthesis of MgH_2 during 1 hour long ball milling in H_2 (300°C, 4 bar) with the formed composites showing improved hydrogenation and dehydrogenation kinetics. The use of various carbon species (graphite, activated carbon, carbon black, carbon nanotubes, fullerenes, nano-diamonds and other forms of nanoscale carbon) ball milled with Mg or MgH_2 reduces hydrogen sorption temperature, improves kinetics and also prevents MgH_2 particles growth during hydrogenation/dehydrogenation cycling [177, 180-184].

2.4.3.2.2. Additives of transition metals, and/or hydride-forming metals, alloys and intermetallic compounds

To further improve the thermodynamic and kinetic limitations of Mg/or MgH_2, composite materials were prepared by ball milling of Mg with different transition metals either absorbing hydrogen (e.g, V, Nb, Pd, Pt) [191, 192] or not (e.g, Ni, Fe, Cu, Co) [187, 188]. V and Nb do not alloy with Mg and small hydrogenated TM particles in the composites are supposed to act as gateways for hydrogen to the magnesium matrix. The role of TM is not been settled yet, but the formation of hydride was observed in the case of TiH_x and VH_x which may act as hydrogen donors.

Detailed studies on the effects of ball milling on the H-sorption properties of Mg, both with and without the addition of a catalyst has been reported by Zaluski *et.al*. [4, 50, 68]. During ball milling, a reduction in grain size for the milled materials was observed with powders particle size of ~10 μm having significant improved hydrogenation kinetics. Addition of Pd catalyst showed improved hydrogenation kinetics due to its catalytic properties towards dissociation of H_2 molecules and recombination of H-atoms.

Metal oxides may have a strong catalytic effect even when small quantities are used, Oelerich *et.al*. [189] reported that Cr_2O_3 yields the fastest hydrogen absorption, whereas V_2O_5 and Fe_3O_4 showed most rapid desorption rate of hydrogen. Ikeda *et.al*.[190] disclosed a method for producing of hydrogen storage material on the basis of MgH_2 by mechanically pulverizing magnesium powder in a hydrogen atmosphere. The hydrogenation of Mg is facilitated by the addition of TiO_2 and/or Nb_2O_5. Song *et.al.* [161] studied HRBM of magnesium at the presence of some metal oxides. They showed that the addition of 10 wt.% of Al_2O_3 or Cr_2O_3 to magnesium significantly improves its

hydrogenation during HRBM allowing to achieve hydrogen sorption capacity of the material about 5.5 wt.% during ~ 1 hour long ball milling at initial room temperature and hydrogen pressure of 11 bar. The material is characterised by quite fast dehydrogenation and re-hydrogenation performances, especially for Cr_2O_3 additive allowing to desorb up to 4.5 wt.% H during one hour at the temperature of 310°C and H_2 pressure of 0.5 bar, and re-absorb up to 5 wt.% H at H_2 pressure of 11 bar and the same temperature.

Addition of oxides to improve HRBM process of MgH_2 preparation seems to be quite promising and in some cases, a cost saving option. At the same time, within the prior art, this route has some disadvantages hindering practical implementation of the method. Most of the oxides used as additives to Mg which show significant improvements of the hydrogenation during HRBM are very hard materials. For example, Al_2O_3 has a hardness from 8 (γ-modification) to 9 (α-modification) Mohs; and the hardness of Cr_2O_3 is about 8.5 Mohs. These values are higher than the hardness of not hardened (up to 5 Mohs) and hardened (up to 8 Mohs) steels used for the making of milling tools (vial and balls) so that their long-time operation will result in a premature wearing of this expensive hardware. Additionally, this introduces more hazards to quite unsafe HRBM process that requires filling of the milling vial with high pressure hydrogen. Nb_2O_5 exhibits good improvements of hydrogenation of magnesium during HRBM and the best (as compared to other oxide additives) dehydrogenation and re-hydrogenation performances of the final product (as shown by Barkhordarian *et.al*. [160]). The hardness of Nb_2O_5 (5 - 6 Mohs) seems to be acceptable for the application, but this material is quite expensive. For the alternative oxide additives, further improvements of the dehydrogenation and re-hydrogenation performances (first of all, reversible hydrogen storage capacity) of the final nanocomposites are necessary as well.

Furthermore, Mg-based compounds with a (xH_y) complex are of considerable interest for hydrogen storage applications, that is Mg_2Ni, Mg_2Co and Mg_2Fe. In contrast to MgH_2, the hydrogen in the Mg_2xH_y hydrides is located around the transition metal atom. Mg_2NiH_4 (3.6 wt.%), Mg_2CoH_5 (4.5 wt.%) and Mg_2FeH_6 (5.5 wt.%) are inexpensive, light weight and low-toxicity. When Mg_2Ni reacts with hydrogen it transforms into Mg_2NiH_4 complex hydride phase with dehydrogenation temperature of 250°C-300°C at 2.5 bar, which is much lower than for the pure Mg. However, their low storage capacity is a limitation for on-board storage [50]. It also turns out that the microstructure plays a dominant role on the hydrogenation properties of this type of metal hydrides [50, 191-193]. In Mg_2CoH_5 and Mg_2FeH_6, Mg and Co (or Fe) does not form a single alloy phase and thus material transport plays an important role.

Additionally, the use of easily hydrogenated alloys such as body centred cubic (BCC) alloys has been shown to improve the hydrogenation kinetics of MgH_2 which suggest that doping with a BCC alloy might be able to reduce the ball-milling time for the formation of MgH_2 [60]. The composites of Mg-TiVMn alloy milled for 40 hours under argon showed improved hydrogenation/dehydrogenation kinetics with 6.2 wt.% H absorbed within 2 minutes and desorbed the same amount in 7 minutes at 300°C. But further milling beyond 40 hours was found to lead to reduced storage capacity even though the desorption kinetics properties were observed to improved [194, 195]. The samples milled for 40 and 80 hours showed the onset of their dehydrogenation at 368.4C and 362.3°C in pressurized differential scanning calometry (PDSC) measurement. Much improved results were observed for dehydrogenation of MgH_2-$Ti_{0.4}Cr_{0.15}Mn_{0.15}V_{0.3}H_x$ alloy showing hydrogen release peak at 185°C when the heating rate is 2°C/min, and can desorbed ~6.2 wt% H [60]. Improved thermodesorption results were reported by Guo

et.al. [196] for MgH_2-$T_{0.4}Mn_{0.22}Cr_{0.1}V_{0.28}$ ball milled for 24 hours in argon and the obtained results showed the composites to have an T_{onset} at 280°C and having a T_{max} at 316°C. The kinetics studies showed the composite to absorb about 5.7 wt.% H in 195 seconds.

2.4.3.2.3. Mixed dopants additives

Another approach for improving hydrogen sorption rates and thermodynamics of Mg/MgH_2 is the use of mixed dopants such as carbonaceous materials with transition metal (TM), transition metal oxides or hydriding alloy with carbonaceous materials [197, 198]. Increase hydrogen dissociation and diffusion rate are obtained when mixed dopant are used as compared to hydrogenation kinetics promoted by mono-dopants (e.g., carbons, TM, oxides and carbon-oxides/TM) alone [153, 199]. The use of carbon supported nickel catalysts has shown superior performance than just using carbon and nickel physically mixed [200]. This indicates the synergistic interaction among the mixed dopants that may be an effective strategy to lower the operation temperature and to increase hydrogenation kinetics [198]. Fast hydrogen absorption kinetics (5 minutes) using ball-milled carbon nanotubes and V-Ti-Mg were observed with hydrogen storage capacity of 5.1 and 5.8 wt% at 150°C and 200°C. The increase hydrogenation capacity was believed to result from the synergistic effect of V-Ti-CNTs dramatically increasing the hydrogenation kinetics as well as its capacity, especially at the temperature as low as 150°C which is important for practical hydrogen storage [201].

The above investigations evidence the beneficial effect of mechanical milling simultaneously with the addition of metallic catalysts, hydrides or carbonaceous materials

as approaches to enhance hydrogen absorption and desorption kinetics in MgH_2. Mechanical milling improves hydrogen storage properties by microstructural refinement as well as by the production of nanocrystalline MgH_2, because grain boundaries are both active sites for the nucleation processes and preferential diffusion paths for hydrogen atoms. The hydriding/dehydriding behaviour of MgH_2 is strongly influenced by different factors such as the nature of the metal catalyst, its ability to form a hydride phase, its distribution and size in the MgH_2 matrix and also the simultaneous presence of carbonaceous additives [202]

2.5. Conclusion of the literature review

Energy systems of the future will have to be more reliable, flexible and cost-efficient and have higher availability to meet the increasing energy demand. There has been interest in the use of hydrogen as an energy carrier in the recent past due to its non-polluting effect, but storage issues have been a challenge. Hydrogen as an energy carrier requires adequate storage materials that can satisfy the demands of field applications such as high hydrogen content, reversibility of hydrogen uptake and release under moderate conditions. Hence, preparation and characterization of novel materials are receiving significant focus. Known hydrogen storage materials, such as metallic or complex hydrides were prepared by solvent-based synthesis methods or by direct solid-gas hydrogenation reactions. Amongst the various forms of hydrogen storage, solid-state metal hydrides are promising candidate for on-board vehicle applications. The method is of interest due to its high gravimetric and volumetric capacity, especially light weight metal like Mg.

Hydrogen storage in magnesium and magnesium-based alloys are very attractive, owing to their high gravimetric and volumetric capacities (7.6 wt.% and 110 kg H/m^3 respectively) combined with a low price and high availability. But, there remains a number of problems to be solved with these systems since Mg and Mg-based alloys have some shortcoming which include, (i) poor hydrogen absorption/desorption kinetics, (ii) too stable for most applications, (iii) difficult to be activated for hydrogen absorption. To solve these problems, there have been a number of research efforts on focusing on these subjects.

Therefore, the purpose of this research study was to prepare Mg-based hydrides by HRBM under hydrogen atmosphere with *in situ* pressure-temperature monitoring during the course of milling. Mg-base hydrides were prepared starting from elemental magnesium with different additives; this includes different carbon types and/or metal alloys, and oxide-based additives that have not previously been milled with Mg under hydride. The formed hydrides materials were characterized for their microstructure, phase structure and hydrogen sorption properties to gaining further insight into the reaction mechanisms.

CHAPTER 3: Methodology

In this chapter, the methodology and materials used to prepare the materials under study will be presented. The function of various characterization techniques employed for analysis of these materials are explained.

3.1. Materials and Chemicals:

The following nanocomposites were investigated in the course of this study:

- Magnesium + sp^2-hybridized carbon (1–10 wt.%), including*:*
    - graphite (G),
    - activated carbon (AC),
    - multi-wall carbon nanotubes (MWCNT),
    - expandable graphite (EG),
    - thermally-expanded graphite (TEG).
- Magnesium + carbon and/or hydride-forming metal alloy, including:
    - Pd-black (0.1–5.0 wt.%).
    - BCC-V alloy (10 wt.%),
    - ZrNi (10 wt.%),
- Magnesium + carbon and/or mixed titanium – iron oxide ($TiFeO_3$, 2–20 wt.%).

The materials used for the preparation, handling and hydrogenation of the composites included:

➢ Hydrogen gas (purity 99.999%) and argon (99.96%) were purchased from Afrox South Africa;

- Palladium dichloride hydrated ($PdCl_2.xH_2O$); purchased from Sigma Aldrich;
- Hydrazine ($N_2H_4.2H_2O$); purchased from Sigma-Aldrich;
- Sodium hypophosphite ($NaHPO_4$) purchased from Sigma-Aldrich;
- Deionized water (DI H_2O), was distilled by a Zeneer Power III (TOC) water purification system;
- Mg powder (-20 + 100 mesh, 99.8%; metal basis) and MgH_2 (98% purity, powder) were purchased from Alfar-Aersar;
- Multi-wall carbon nanotubes (diameter; 5-20 nm, length: 10 μm, aspect ratio > 500; bulk density: 0.04-0.06 g/cm^3, impurities: amorphous carbon, Fe (<10%)) was purchased from Carbon Nano-material Technology Co., Ltd. (Korea);
- Graphite (99+%; powder, length ≤ 20 μm, bulk density 1900 g/cm^3) from Fluka;
- Activated carbon (YP-50F, coconut based, diameter: 3-20 μm, surface area: 1600-1700 m^2/g) from Kuraray Chemical Co., Ltd.(Japan);
- Expandable graphite powder (GB 10698-1989), 50 mesh (>80%), 99.9+%, sulphur <100 ppm, chlorine <10 ppm, expansion rate 220, purchased from Yichang Xincheng Graphite Co.,Ltd. (China);
- Thermal expanded graphite was prepared by heating the expandable graphite to 900°C in an opened tube furnace, for 1 hour. XRD characterization of the light flake-like product showed that it contained single graphite-like phase with lattice periods *a*=2.470 Å, *c*=6.788 Å corresponding well to typical values (*a*=2.45–2.47 Å, *c*=6.83–6.90 Å) presented in the literature [203];

$FeTiO_3$ (50.78 wt.% Fe_2O_3, 44.48 wt.% TiO_2, 4.74 wt.% of: B, Mn, Al, Mg, Na, Ni, Ca and V) from Saldanha Steel, Western Cape Province, South Africa.

3.1.1. Alloys preparation

The $Zr_{50}Ni_{50}$ alloy was prepared by arc-melting of Zr and Ni under argon atmosphere inside a water cooler copper crucible in order to avoid contamination. The purities were 99.9% for Zr and Ni. A reduction of contamination from furnace atmosphere was obtained by melting a sacrificial button before Zr. The arc was established by torch with tungsten tip. The additive was remelted three times to ensure homogeneity. Subsequently, the prepared metal ingots were pulverized by ball-milling in hydrogen atmosphere for 20 min.

3.1.2. Palladium black preparation

All the glassware and Teflon-coated magnetic stirring bars were cleaned with *aqua regia,* followed by copious rinsing with distilled water before drying in the oven.

In a typical preparation: $PdCl_2$ .xH_20 (1.0 g, 5.64 mmol) was added to HCl (1.0 mL) to aid the salt dissolution in deionized water (100 mL). The formed solution was warm to ~70°C under vigorous stirring to give a clear colour solution followed by drop-wise addition of $N_2H_4.H_2O$ (3-4 mL) forming black precipitate material which hydrazine served as the stabilizer. The precipitate was left stirring for 30 minutes after the addition to complete the reduction reaction with the resulting material collected by gravity filtration and dried at 120°C for 12 hour. The resultant materials were characterized by SEM, TEM, XRD methods.

The preparation of $NaHPO_4$ stabilized Pd^{2+} particles followed similar procedure to the above and the obtained material obtained as black particles that were characterized by SEM, TEM and XRD.

3.2. Experimental procedure

3.2.1. High-energy Reactive Ball Milling (HRBM)

In recent years, there has been an increased interest in using ball milling method to improve the properties of Mg-based materials. These interests stem mainly from the fact that ball milling can produce dislocation and special defects, generate fresh and highly reactive surface during milling operation, which in turn increases the hydrogen absorption rate. The most typical processing techniques to produce the nanocrystalline hydrogen storage powder are mechanical alloying (MA) or mechanical ball milling (MM) [204]. Mechanical alloying (MA) describes the process when mixtures of powders (different metals or alloys/compounds) are milled together. During this process material transfer is involved to obtain a homogeneous alloy. On the other hand, the milling uniform (often stoichiometric) composition powders, such as pure metals, intermetallic, or pre-alloyed powders are used. No material transfer happens in the process of mechanical milling (MM) [205].

Among the different ball milling techniques, high-energy reactive ball milling technique has evolved a fundamental approach. High-energy reactive ball milling is a convenient method to prepare metal hydride with high surface area, creation of defects on the surface and interior of the material. The pulverization and deformation process occurring during high-energy ball milling play a major role in the hydriding reactions.

A

B

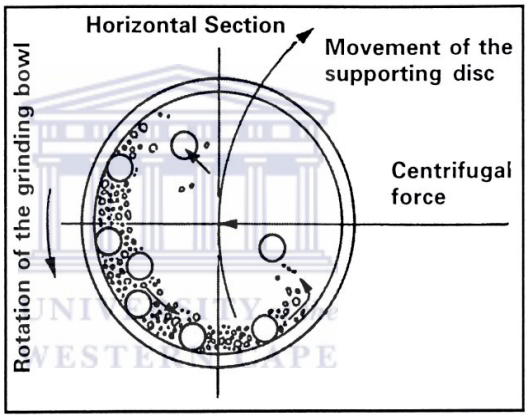

C

Figure 3-1: Planetary ball mills pictures; (A**) Fritsch P6, (**B**) Retsch PM 100, and (**C**) schematic drawing depicting the ball motion inside the ball mill vial [205]**

During the initial stage of high-energy reactive ball milling, a fraction of the powder is trapped between the colliding surfaces and therefore subjected to an impulsive mechanical load. The rotation movement of the jar and the one of the supporting plate are in opposite direction. These movements impress high centrifugal forces to balls and powder as shown in Figure 3.1(C). The surfaces undergo fracturing, cold welding, and mechanical deformation which results in the generation, migration and accumulation of

point and extended lattice defects and the contemporary formation of new surfaces [4, 215]. Once the minimum steady state grain size is reached, further refinement ceases. Initially the kinetic energy transfer leads to the production of an array of dislocations. This is accompanied by atomic level strains. At a certain strain level, these dislocations annihilate and recombine to form small angle grain boundaries separating the individual grains. Thus sub-grains are formed with reduced grain size. During further milling, this process extends throughout the entire sample. To maintain this reduction in size, the material must experience very high stresses. But extended milling could not able to maintain the high stresses and hence reduction of grain size is limited in extended milling. The two other parameters which also cause this limit to grain size reduction are the local temperature developed due to ball collisions and the overall temperature in the vial. Temperature upswing arises from balls to balls, balls to powder and balls to wall collisions.

Since the kinetic energy of the balls is a function of their mass and velocity which determine the kinetic energy transfer, dense materials like stainless steel or tungsten carbide are preferred. Other materials used as balls are agate, sintered corundum, zirconium dioxide, Teflon, chrome nickel, silicon nitride, etc. The impulsive load of grinding balls is given by the equation 3.1:

$$F = \frac{mv}{t} \qquad (\mathbf{3.1})$$

where 'm' is the ball mass, 'v' the ball velocity and 't' the ball-vial contact time.

In order to prevent excessive abrasion, the hardness of the grinding bowl used and of the grinding balls must be higher than that of the materials used. Normally grinding bowls and grinding balls of the same material should be chosen.

Atmospheric contamination can be minimized by sealing the vial with flexible 'O' ring after the powder has been loaded. A few parameters exists in high energy ball milling which on changing, can produce a wide range of fine particles with different sizes and consequently with different physical properties. These parameters are: (i) type of mill, (ii) milling atmosphere, (iii) milling media, (iv) intensity of milling, (v) ball to powder weight ratio (BPR), (vi) milling time and (vii) milling temperature.

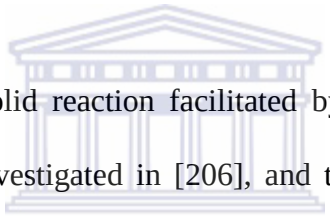

In earlier studies, gas-solid reaction facilitated by milling in hydrogen atmosphere to prepare hydrides was investigated in [206], and the extent of metal-hydrogen reaction was monitored by periodic sampling of the material from the milling vial followed by *ex situ* XRD and other analysis methods [168, 169]. The use of HRBM technique has been a "black box" that does not give information about hydrogenation behaviour of the material during milling only in few cases *in situ* hydrogen absorption during HRBM is monitored directly by monitoring the pressure and/or temperature change inside the milling vial [170, 208, 209]. In the current study, a High pressure ball milling vial equipped with pressure-temperature monitoring system (Evico Magnetics GmbH) shown in Figure 3.2 was employed.

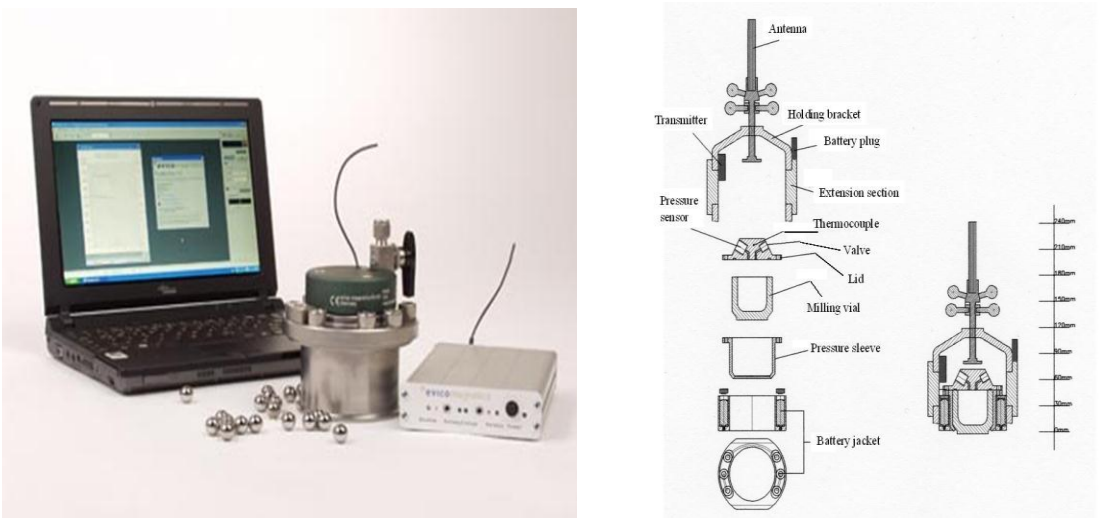

Figure 3-2: High pressure milling vial equipped with pressure-temperature monitoring system (Evico Magnetics GmbH) (A**), explosion drawing of the milling vial (**B**)**

3.2.2. Preparation of Mg and Magnesium-based hydride materials

The Mg-based composites were prepared by high-energy ball-milling (HRBM) of Mg powder (~8.0 g) taken alone, or mixed with the additives, under hydrogen atmosphere. First HRBM studies were carried out at the Institute for Energy Technology (IFE) using a custom-built 80 ml Duplex SS2377 (austenitic–ferritic steel) vial and Fritsch Pulverisette P6 planetary mill. The balls-to-powder weight ratio (BPR) was from 40:1 up to 80:1 (total sample weight about 3 g; 30 or 60 steel balls, 10 mm in diameter). The vial was initially evacuated and filled with 30 bar H_2. The milling was performed at 500 rpm. To monitor the hydrogenation process, the milling was paused (typically in 20–30 min intervals) and the vial, after cooling to room temperature, was connected to a Sieverts-type apparatus to monitor the amount of hydrogen absorbed. The vial was then refilled with hydrogen, and milling was continued.

In the further experiments, the materials were ball milled in hydrogen gas using Retsch PM 100 ball mill and 220 mL hardened steel vial with pressure–temperature monitoring system (Evico Magnetics GmbH). The vial allows to operate at pressures up to 150 bar and temperatures up to 70°C. The ball milling was performed with a ball-to-powder-ratio of 40:1 (82 steel balls, 10mm in diameter) at 500 rpm. Prior to the milling, the vial was evacuated followed by filling with H_2 gas (P~30 bar) supplied from metal hydride hydrogen storage and supply unit on the basis of AB_5-type alloy. The hydrogen pressure in the vial was kept above 20 bar by refilling each time (P~30 bar) when the pressure dropped below. When the vial temperature approached 70°C, the milling was stopped and resumed again after cooling the vial to the room temperature. The amount of hydrogen absorbed in the sample was calculated starting from actual pressure–temperature values (with the correction to hydrogen compression factor) and plotted versus milling time.

After each filling the vial was leak-tested using H2000 Plus hydrogen leak detector with AP-57 probe (Adixen). If a leak (≥0.2 ppm H_2) was observed, the corresponding dataset for the sample was rejected, and the milling experiment was re-done. Total milling time was 6 hours. After all milling experiments, the samples handling were carried out in a glove box filled with argon (contamination levels, $O_2 \leq 20$ ppm; $H_2O \leq 5$ ppm) to prevent any contact with air and moisture. This is particular important since the formed metal hydride are easily oxidized when in contact with small traces of oxygen and water because absorbed impurities can block adsorption sites in the materials or lead to erroneous results when hydrogen storage properties are being investigated. Hence, sample preparation and handling under inert conditions are indispensable.

The above procedure was applied for the composites containing 1 to 5 wt.% of carbon and/or hydrogenation catalyst: 10 wt.% of $V_{75}Ti_{10}Zr_{7.5}Cr_{7.5}$ (BCC) alloy or ZrNi alloy, taken either in hydrogenated or non-hydrogenated state; 2 to 20 wt.% $FeTiO_3$,. 0.1 to 5 wt.% of Pd black. In some experiments, the $V_{75}Ti_{10}Zr_{7.5}Cr_{7.5}$ alloy was surface-modified by fluorination and electroless deposition of Pd [210]. The powder samples were then used for hydrogen storage property tests and microstructure characterization.

In the case of a sigmoidal behaviour of $C/C_{max}(t)$, the data obtained on hydrogen absorption during HRBM and re-hydrogenation (the procedure will be described below) were processed by a formal kinetic analysis using a modified *Avraami-Erofeev* equation 3.2:

$$\frac{C}{C_{\max}} = \begin{cases} 0, & t \le t_0 \\ 1 - \exp\left\{-\left[\left(\frac{t - t_0}{t_R}\right)^n\right]\right\}, & t > t_0 \end{cases}; \qquad (\mathbf{3.2})$$

where C, $C_{\max}$ are the actual and maximum H concentration, respectively; t is time; t_0 is the incubation period; t_R is characteristic hydrogenation time (reciprocal rate constant); and n is an exponential factor indirectly related to the reaction mechanism.

3. 3. Samples Characterization

The phase composition/crystal structure, morphology and particle size are of important in Mg-based metal hydrides materials in studying their hydrogen sorption properties. Alteration in these factors may enhance or detoriate the performance of the metal hydride

materials. Therefore, an array of characterization methods used to analyze the above-mentioned factors on the properties of Mg-based hydrides is detailed.

3.3.1. Powder X-ray diffraction (XRD)

X-ray diffraction (XRD) is a versatile, non-destructive technique that reveals detailed information about the chemical composition and crystal structure of the materials, its features and working principle are represented schematically in Figure 3.3. XRD utilizes the diffraction of an incident beam of X-rays in order to examine the crystal structure of a material. The X-ray diffraction pattern of a pure substance is unique and thus a fingerprint of the substance. The wavelength range of X-rays is of the same order of magnitude as the distance separating ions or atoms in a crystal. The comparable size of the wavelength and inter-species spacing causes a crystal to diffract an X-ray beam passing through it. The crystal diffracts the beam at signature angles depending on the crystal orientation and structure, and x-ray wavelength [211]. X-ray beams are primarily diffracted by the electron density of a crystal, denoted by peak in the recorded XRD pattern. Analysis of the diffracted beams allows the creation of an electron density map of the crystal, from which information about the crystal structure of the material can be deduced.

A typical X-ray diffractometer utilizes an x-ray tube to generate X-rays by bombarding a metal target with high energy electrons, ca 10-100 keV, causing emission of core electrons. An electron from the outer shell then fills the vacant hole in the inner shell and emits an X-ray photon. Molybdenum and copper are common targets as they both produce strong X-ray emissions at 0.071 and 0.154 pm respectively [212]. The beam created by the X-ray generator strikes the sample and is diffracted and then detected by

either photographic film or a movable proportional counter (Figure 3.3(A)). Consider the two parallel planes of atoms A–A' and B–B' in Figure 3.3(B), which have the same *h*, *k*, and *l* Miller indices and are separated by the interplanar spacing d_{hkl}.

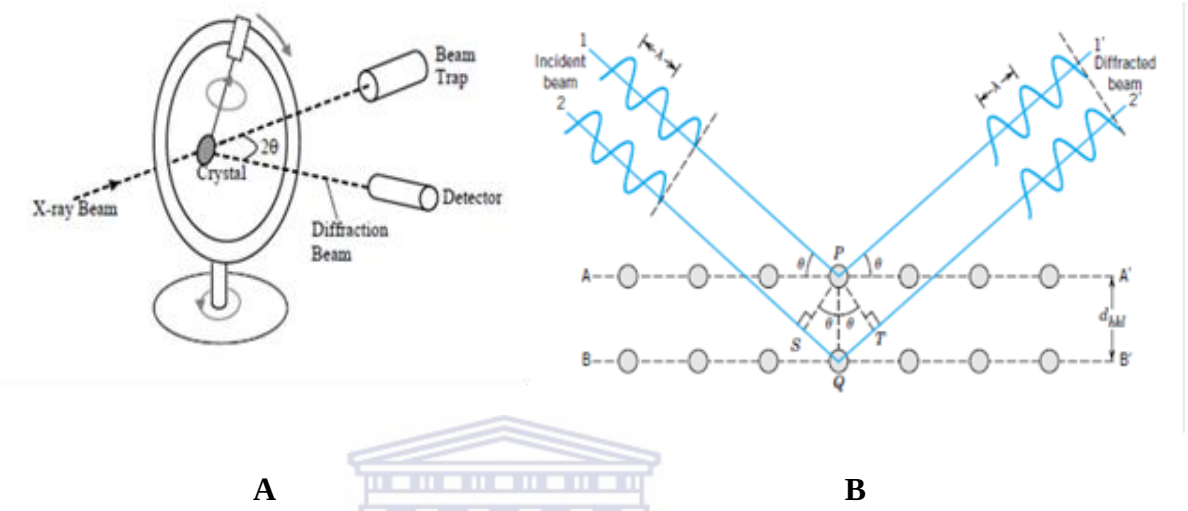

A **B**

Figure 3-3: (A) Schematic of an X-ray diffractometer and (B) Geometrical representation of Bragg's law [213]

Now assume that a parallel, monochromatic, and coherent (in-phase) beam of x-rays of wavelength λ is incident on these two planes at an angle θ. Two rays in this beam, labelled 1 and 2, are scattered by atoms P and Q. Constructive interference of the scattered rays 1' and 2' occurs also at an angle θ to the planes, if the path length difference between 1–P–1' and 2–Q–2' (i.e., SQ + QT) is equal to a whole number, n, of wavelengths. That is, the condition for diffraction is:

$$n\lambda = SQ + QT$$

or

$$n\lambda = d_{hkl}\sin\theta + d_{hkl}\sin\theta$$

$$= 2d_{hkl}\sin\theta \qquad (\mathbf{3.2})$$

Equation 3.2 is known as Bragg's law; also, n is the order of reflection, which may be any integer (1,2,3,….) consistent with sin θ not exceeding unity. Thus, we have a simple expression relation the x-ray wavelength and interatomic spacing to the angle of the diffracted beam. If Bragg's law is not satisfied, then the interference will be non-constructive in nature so as to yield a very low-intensity diffracted beam.

The magnitude of the distance between two adjacent and parallel planes of atoms (i.e., the interplanar spacing d_{hkl}) is a function of Miller indices (*h*, *k* and *l*) as well as the lattice parameter(s). For crystal structures that have cubic symmetry,

$$d_{hkl} = \frac{a}{\sqrt{h^2 + k^2 + l^2}} \qquad (\mathbf{3.3})$$

in which *a* is the lattice parameter (unit cell edge length).

The neutron and x-ray diffraction of powder samples results in a pattern characterised by reflections (peaks in intensity) at certain positions. The height, width and position of these reflections can be used to determine many aspects of the materials structure. The Rietveld method uses a least squares approach to refine a theoretical line profile until it matches the measured profile. The introduction of this technique was a significant step forward in the diffraction analysis of powder samples as, unlike other techniques at that time; it was able to deal reliably with strongly overlapping reflections.

The method was first reported for the diffraction of monochromatic neutrons where the reflection-position is reported in terms of the Bragg angle 2θ. This terminology will be used here although the technique is equally applicable to alternative scales such as x-ray

energy or neutron time-of-flight. The only wavelength and technique independent scale is in reciprocal space units or momentum transfer Q, which is historically rarely used in powder diffraction but very common in all other diffraction and optics techniques. The relation is:

$$Q = \frac{4\pi \sin(\Theta)}{\lambda} \qquad (\mathbf{3.4})$$

The shape of a powder diffraction reflection is influenced by the characteristics of the beam, the experimental arrangement, and the sample size and shape. In the case of monochromatic neutron sources the convolution of the various effects has been found to result in a reflex almost exactly Gaussian in shape. If this distribution is assumed then the contribution of a given reflection to the profile yi at position 2θi is:

$$y_i = I_k \exp\left[\frac{-4\ln(2)}{H_k^2}(2\Theta_i - 2\Theta_k)^2\right] \qquad (\mathbf{3.5})$$

where H_k is the full width at half peak height (full-width half-maximum), $2\theta_k$ is the centre of the reflex, and I_k is the calculated intensity of the reflex (determined from the structure factor, the Lorentz factor, and multiplicity of the reflection)

At very low diffraction angles the reflections may acquire an asymmetry due to the vertical divergence of the beam. Rietveld used a semi-empirical correction factor, as to account for this asymmetry

$$A_S = 1 - \left[\frac{sP(2\Theta_i - 2\Theta_k)^2}{\tan \Theta_k} \right] \qquad (\mathbf{3.6})$$

where P is the asymmetry factor and s is +1,0,-1 depending on the difference $2\theta_i$-$2\theta_k$ being positive, zero or negative respectively.

At a given position more than one diffraction peak may contribute to the profile. The intensity is simply the sum of all reflections contributing at the point $2\theta_i$.

The XRD studies were performed using Bruker AXS D8 Advance diffractometer with Cu-K_α (λ_1 = 1.5406 Å, λ_2 = 1.5444 Å, λ_2/λ_1 = 0.5) radiation from a conventional water-cooled X-ray tube. The Bragg angle range was 2θ = 10–90°, and scan rate was 1.2°/min with a step size of 0.02°. The nanograin (crystallite) size of phases residing in the milled powders was calculated from the broadening of their respective XRD peaks. Since the Bragg peak broadening in an XRD pattern is due to a combination of grain refinement (nanograin/crystallite) and lattice strains, it is customary to use computing techniques by means of which one can separate these two contributions.

The collected XRD data were refined by the Rietveld whole-profile refinement. Preliminary phase analysis was carried out using Powder Cell 2.4 software. Precise refinement of the XRD data was performed using GSAS software [216], where the peak shapes were described using the Thompson-Cox-Hastings pseudo-Voight-type function (CW profile function 2). A standard α-Al_2O_3 sample was used for the determination of the instrumental contribution into peak profile parameters. During refinement, Gaussian profile parameters (GU, GV and GW) were fixed (kept the same as for the Al_2O_3 standard), and only two Lorentzian profile parameters were refined, LX (size broadening) and LY (strain broadening).

The refinements yielded lattice periods of the constituent phases, as well as estimations of their abundances and crystalline sizes/strains. The sizes of the crystallites and strains in the materials were evaluated from the refinements of the Rietveld powder profile parameters using the following equations:

$$D_V = \frac{\lambda}{\beta_S \cos\theta}; \qquad (\mathbf{3.7})$$

$$e = \frac{\beta_D}{4 \tan\theta}; \qquad (\mathbf{3.8})$$

where D_V is a volume-weighted crystallite size, λ is a wavelength, β is an integral peak width, θ is a Bragg angle, and e is a microstrain.

For the GSAS refinements, according to [216], the equations (3.7) and (3.8) were respectively transformed as:

$$D_V = \frac{18000\, K\, \lambda}{\pi\, X}; \qquad (\mathbf{3.9})$$

$$e = \frac{\pi}{18000}\left(Y - Y_i\right)\cdot 100\%; \qquad (\mathbf{3.10})$$

where K is the Scherrer constant (assumed to be equal to 1), X and Y are Lorentzian profile parameters LX and LY, respectively, and Yi is a value of LY for the Al_2O_3 standard (associated with instrumental contribution into LY value). The formed magnesium hydrides diffraction pattern were refine using the following reference data:

Mg: Space group $P6_3/mmc$ (194); a= 3.2099 Å, c= 5.2108 Å [217].

α-MgH_2: Space group $P4_2/mnm$ (136); a= 4.519 Å, c= 3.020 Å [218].

γ-MgH_2: Space group $Pbcn$ (60); a= 4.5213 Å, b= 5.4382 Å, c= 4.9337 Å [219].

3.3.2. Transmission Electron Microscope (TEM)

TEM is a non-destructive electron microscopy technique, which is based on the imaging of a thin sample (<100 nm) by means of transmission of an electron beam. Collisions of the electrons with the sample can have different results: electrons can either change their initial flight direction by elastic scattering or loose energy by inelastic collisions (exciting or ionizing atoms in the sample) or they can lose their coherence. The result is a reduction of intensity of the transmitted electron beam with respect to the incident one. This attenuation is related both to the thickness of the sample and to the material which the electrons interact with (packing density, atomic weight, crystalline orientation, are all parameters affecting the transmitted beam). Collection of the transmitted electrons forms an image of the sample which is related to the sample morphology/microstructure. Another important consequence of the sample bombardment with electrons is the emission of X-ray radiation whose wavelength depends on the emitting atoms. The used instrument is also equipped with an EDS microprobe which allows a chemical qualitative and quantitative analyses, detecting x-rays emitted by the sample.

A basic schematic of a typical modern TEM can be seen in Figure 3.4. The electron gun produces a stream of monochromatic electrons. The condenser lenses focus the beam to a small, thin and coherent beam and the condenser aperture removes high angle electrons. The beam then strikes the sample. The electron beam is affected by the structure of the sample. This results in only part of the electron beam being transmitted through certain

parts of the sample. The objective aperture enhances the contrast of the image by blocking diffracted, high angle, electrons and the selected area aperture allows control of the area viewed. The intermediate and projector lenses act to enlarge the image. Finally, the beam hits the phosphor image screen generating light creating an image. The darker regions of the TEM image originate from areas where fewer electrons were transmitted and so represent the denser areas of the sample. Another useful function of TEM analysis is the ability to be able to focus on the diffraction pattern of the electron beam caused by selected areas of the material being studied.

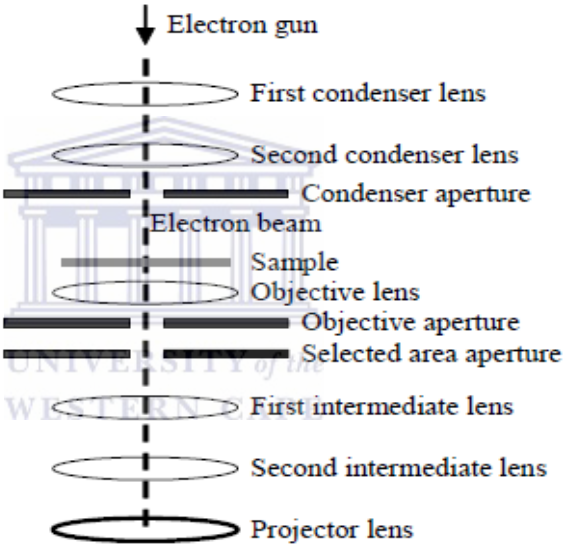

Figure 3-4: Basic schematic of typical TEM [220]

High Resolution Transmission Electron Microscope (HRTEM) FEI Tecnai 30 operating at 120 kV was used to analyze the as-prepared and re-hydrogenated Mg-based samples. The sample holder was cooled to liquid nitrogen temperature (~90 K) so as to increase the stability time of the hydride phase under the electron beam. It was possible to investigate the microstructure of the hydride with minimal indication of beam-induced decomposition. Conventional bright-field imaging was employed to analyze the samples.

3.3.3. Scanning Electron Microscope (SEM)

A typical SEM primarily yields information about a sample's topography and morphology, but with additional equipment can yield information about the composition of the sample in an area as small as 1 μm. The highest resolution achievable by a modern SEM is approximately a nanometer. The basic design of an SEM is illustrated in Figure 3.5. The scanning coils, the feature that SEM takes its name from, scan the beam in a grid-like fashion, dwelling on points for a period of time determined by the scan speed. The objective lens then focuses the scanning beam on the part of the sample to be studied. When the electron beam strikes the sample interactions occur, which are detected by various instruments, such as secondary and backscatter electron detectors. Before the beam moves to its next point, these instruments count the number of interactions and a pixel is displayed on a monitor whose intensity is proportional to the number of interactions counted. This process is repeated until the grid scan is complete, creating an SEM image.

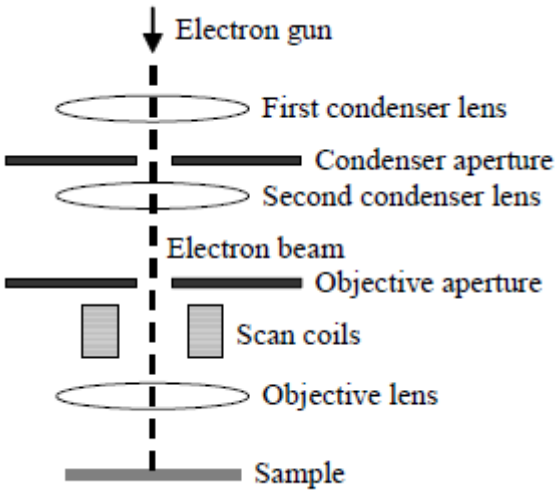

Figure 3-5: Schematic representation of SEM [220]

The High Resolution Scan Electron Microscope (HRSEM) Hitachi S-4800 (Norwegian University of Science and Technology); working distance 15 mm, accelerating voltage 20 kV, emission current 9800-11400 nA was used to determine morphology of the ball milled samples. Furthermore, SEM that of Hitachi X-650 EM; working distance = 15 mm; accelerating voltage = 25 kV; emission current = 75-80 μA (University of the Western Cape) was employed for samples analysis.

3.3.4. Particles sizer

The Malvern Zetasizer Nano ZS is a high performance two angle particle and molecular size analyzer for the enhanced detection of aggregates and measurement of small or dilute samples, and samples at very low or high concentration using dynamic light scattering with 'NIBS' optics. The ZS also incorporates a zeta potential analyzer that uses electrophoretic light scattering for particles, molecules and surfaces, and a molecular weight analyzer using static light scattering. Using Non-Invasive Backscatter optics (NIBS) it has significantly better performance than systems using 90 degree scattering optics, the instruments detect the scattering information at 173°. This is known as backscatter detection. In addition, the optics are not in contact with the sample and hence the detection optics are said to be non-invasive.

There are many advantages of using non-invasive backscatter detection, one of them is that sensitivity is improved. The sample volume probed by the optics is about 10 times higher than in conventional 90 degree 'bulk' optics. When combined with the data collection efficiency of the NIBS optics, the sensitivity is increased by two orders of magnitude, enabling the size measurement of dilute solutions of molecules and dispersions of sub-nanometre particles. A wider range of sample concentrations can be

measured. The laser does not have to travel through the entire sample. By measuring particles close to the cuvette wall, light passes through a shorter path length in the sample, eliminating or reducing an effect called multiple scattering, where light from one particle is itself scattered by other particles. This enables much higher concentrations of sample to be measured and sample preparation is simplified. The effects of dust are greatly reduced as contaminants such as dust scatter most light in the forward direction. Therefore, by using backscatter detection the effect of contaminating dust is minimised.

The measurement position within the cuvette of the Nano ZS is automatically set to accommodate the requirements of high sensitivity or high concentration. This position is changed by moving the focusing lens. Figure (3.6) shows the working principle of Malvern Zetasizer Nano ZS.

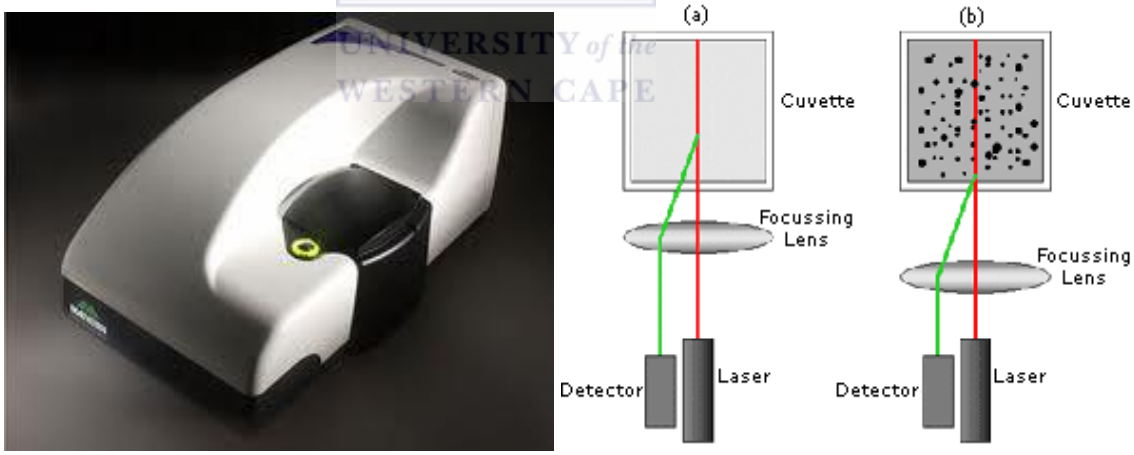

Figure 3-6: Schematic and working principle of Malvern Zetasizer Nano ZS

For small particles, or samples at low concentrations, it is beneficial to maximize the amount of scattering from the sample. As the laser passes through the wall of the cuvette, the difference in refractive index between the air and the material of the cuvette causes "flare". This flare may interfere with the signal from the scattering particles. Moving the

measurement position away from the cuvette wall towards the centre of the cuvette will remove this effect (Figure 3.6 (**A**)). Large particles or samples at high concentrations scatter much more light. Measuring closer to the cuvette wall reduces the effect of multiple scattering by minimizing the path length through which the scattered light has to pass (Figure 3.6 (**B**)).

In this work, Malvern Zetasizer Nano ZS series instrument (resolution range from 0.6nm - 6µm) was employed to obtain quantitative particle size distribution. Mg-based composites were suspended in anhydrous isopropanol medium by ultrasonicating for equal time prior to the measurements. Particle size measurements were performed at same stirring speed and obscuration level.

3.4. Analysis of hydrogen sorption properties

3.4.1. Thermal gravimetric analysis (TGA)

The gravimetric method is relatively simple in terms of the measurement principle; however, in this method the sample is fixed in a balance and the equilibrium status of the microbalance is influenced by the desorbed/adsorbed gas pressure in the system and the sorption temperature. In thermogravimetric analysis (TGA), the weight change of the sample is followed, while it is being subjected to temperature program. Buoyancy effects, caused by changes in the used of gas can be determined by running a correction run in an empty crucible. Schematic overview of (DSC/TGA, Pyris apparatus of Perkin Elmer Co, Perkin Elmer STA 6000) is shown in Figure 3.7 which was used for thermal analysis described in this work. The machine is also able to performed DSC analysis.

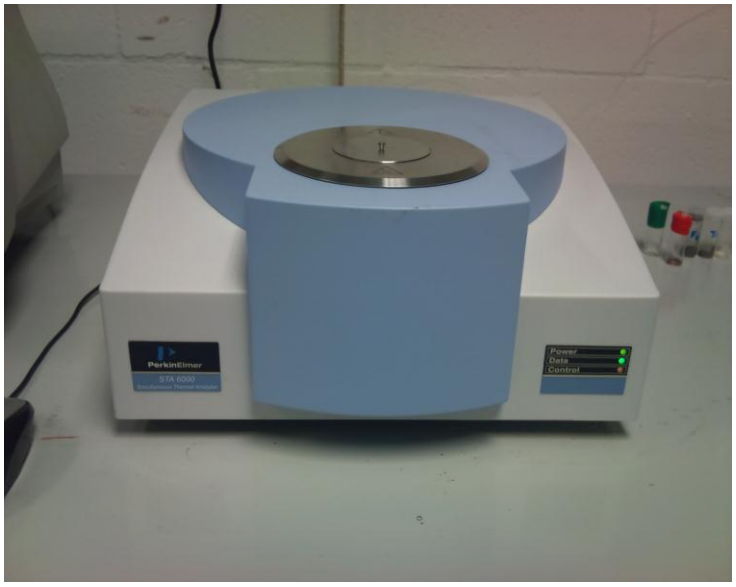

Figure 3-7: DSC/TGA, Pyris apparatus of Perkin Elmer Co, Perkin Elmer STA 6000 picture

3.4.2. Differential Scanning Calorimeter (DSC)

DSC measures the alteration in the enthalpy of a material due to changes in its physical and chemical properties such as melting, oxidation, hydrogen desorption and other heat-related changes as a function of temperature or time and provides quantitative and qualitative data during phase transitions. The apparatus used (DSC/TGA, Pyris apparatus of Perkin Elmer Co, Perkin Elmer STA 6000) are shown in Figure 3.7, with a temperature range from -70°C to 1200°C. Sample required weight of 5-60 mg in aluminium crucible and argon flow between 0 and 200 mL/min, with capacity to switch up to 4 gases such as: air, argon, nitrogen and oxygen.

Hydrogen desorption performance of the as-milled and re-hydrogenated samples were studied by simultaneous differential scanning calorimetry-thermogravimetric measurements (DSC/TGA, Pyris apparatus of Perkin Elmer Co, Perkin Elmer STA 6000). All the samples analysis (heating from 25-550°C at the heating rate, Φ = 5, 10, 15

and 20°C/min) were performed in a standard alumina crucibles which were moved to the instrument in sealed container, followed by quick loading into the sample holder of the instrument for measurements. The measurements were performed under purified argon flow (100 mL/min) as purge gas to prevent samples oxidation during measurement. The instrument was calibrated using the following standards: naphthalene (melting point 80°C, enthalpy of fusion 160 J/g), indium (157°C, 29 J/g) tin (232°C, 60 J/g), lead (328°C, 23 J/g), zinc (420°C, 109 J/g) and magnesium (650°C, 358 J/g). The heat effects of samples decomposition were calculated by the integration of time dependence of the specific heat flow in the decomposition temperature intervals. The samples dehydrogenation activation energy (E_A) was estimated by Kissinger method [215] using the DSC data at different heating rates (Φ = 5, 10, 15, 20°C/min) similarly to the procedure used by Danaie *et.al*. [220]. The DSC endothermic or exothermic peak positions are shifted slightly during experiments measurement at different heating rates (Φ), so Kissinger analysis uses this peak shift to obtain dehydrogenation activation energy (E_A) for the reactions represented by each individual peak. When overlapping between peaks is important, this method offers a suitable procedure to estimate the activation energies. The hydrogen desorption activation energy can be obtained from the following Kissinger equation:

$$d\ln(\Phi/T_{max}^2)/d(1/T_{max}) = E_A/R \qquad \textbf{(3.11)}$$

The Kissinger plots is constructed by plotting $\ln(\Phi/T_{max}^2)$ versus $1/T_{max}$ and the E_A determined from the slope of these plots, where T_{max} is the peak temperature maximum at different applied heating rates (Φ = 5, 10, 15, 20°C/min). For samples with multiple

peaks in the DSC curves, the most intense desorption peak was taken as the maximum peak temperature.

3.4.3. Volumetric hydrogen sorption (TDS/re-hydrogenation)

The dehydrogenation and re-hydrogenation performances of the prepared Mg-based materials after HRBM were studied using a Sieverts-type volumetric installation (South African Institute for Advanced Material Chemistry, SAIAMC) which performs quantitative analysis of the gas-solid reaction. The installation conducted accurate volumetric measurements of quantities of hydrogen absorbed or desorbed by hydrogen sorption materials. The procedure consists of determining the quantity of hydrogen absorbed or desorbed by the material at a certain pressure at a fixed temperature, and after thermal desorbed in vacuum. The installation consists of gas distribution, control, and measurement systems. The pressure within the system was monitored using 2.5, 16, and 160 bar absolute pressure transducers. A schematic diagram of the installation at SAIAMC is given in Figure 3.8.

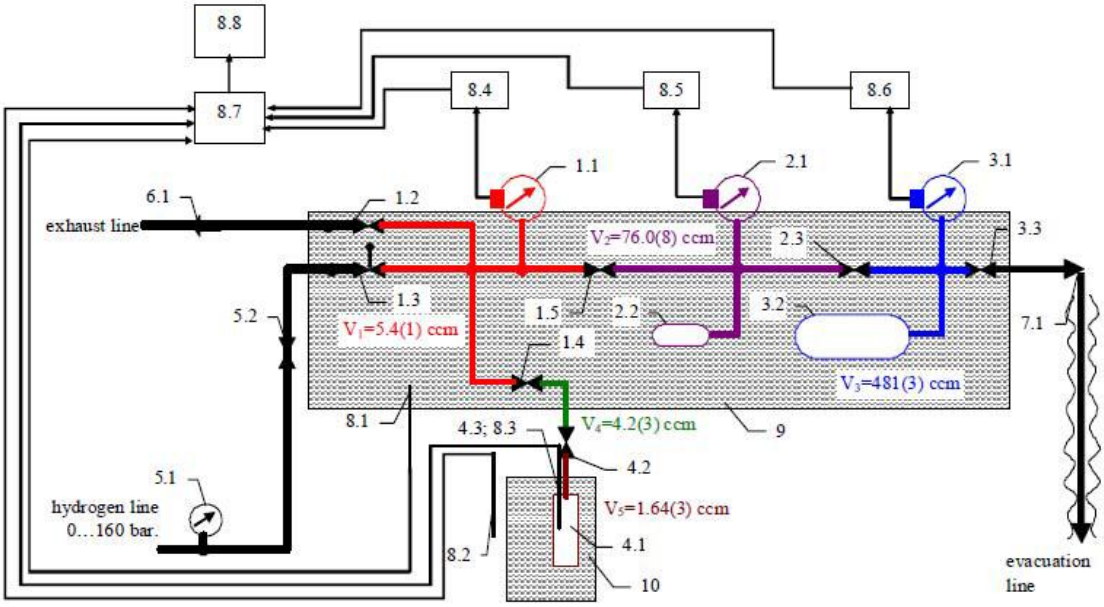

1. High-pressure collector:
   1.1. Pressure sensor 160 bar FS
   1.2. Exhaust valve
   1.3. H_2 input valve
   1.4. Reactor valve
   1.5. Medium-pressure connection valve
2. Medium-pressure collector:
   2.1. Pressure sensor 16 bar FS
   2.2. Buffer cylinder 75 cm^3
   2.3. Low-pressure connection valve
3. Low-pressure collector:
   3.1. Pressure sensor 2.5 bar FS
   3.2. Buffer cylinder 500 cm^3
   3.3. Evacuation valve
4. Reactor assembly
   4.1. Reactor body
   4.2. Gas connection line with locking valve
   4.3. Thermocouple
5. H_2 supply line:
   5.1. Manometer 160 bar FS
   5.2. H_2 supply valve
6. Exhaust line:
   6.1. Check valve
7. Evacuation line
   7.1. Vacuum valve
8. Data acquisition system
   8.1. Thermistor measuring bath temperature
   8.2. Thermistor measuring room temperature
   8.3. Thermocouple measuring sample temperature
   8.4. 160 bar pressure indicator / transmitter
   8.5. 16 bar pressure indicator / transmitter
   8.6. 2.5 bar pressure indicator / transmitter
   8.7. 34970A data acquisition / switch unit
   8.8. PC
9. Bath (filled with ethylene glycol)
10. Thermostat / furnace

Figure 3-8: Schematic diagram of Sieverts-type volumetric installation at SAIAMC

The sample powder (200 mg) was loaded into stainless steel reactor which, together with measurement system, was further evacuated to $<10^{-4}$ mbar. Thermal desorption measurements (TDS) were performed by heating the reactor at constant heating rate (5°C/min) from 25 to 400–470°C providing H_2 desorption during permanent evacuation. The vacuum sensor was calibrated on the flow rate of H_2 supplied into the measurement system. Further re-hydrogenation was carried out at ~15 bar H_2 and 250°C for ~4 hours followed by cooling down to room temperature and subsequent TDS measurements performed as described above. Two TDS/re-hydrogenation cycles were applied for each sample. Some samples were studied several times, at various maximum heating temperatures in the course of TDS. H_2 absorption capacity was determined by calculating total amount of gaseous H_2 in the internal volumes of the gas-distributing system and reactor, starting from the monitored H_2 pressures, P_i, therein; as well as the temperatures, T_i, of these volumes using the following equation:

$$n = \sum \frac{p_i V_i}{Z(p_i T_i) R T_i} \quad (\mathbf{3.12})$$

where n is the total number of moles of H_2 in the volumes V_i taken into account (maintained at the corresponding temperatures, T_i), R = 8.3143 J/(mole·K) is the gas constant, and Z is the compression factor of hydrogen gas at the specified pressure P_i and temperature T_i. Calculating starting (n_0) and actual (n_1) amounts of hydrogen gas in the system, the hydrogen absorption capacity (x) of the material will be expressed as:

$$x\left(\frac{cm^3}{g} STP\right) = \frac{22400(n_0 - n_1)}{m} \quad (\mathbf{3.13})$$

where m is sample weight; 22400 cm^3/mole is the molar volume of hydrogen at normal conditions (T= 0°C, P=1 bar).

The starting (n_0) and actual (n_1) number of moles of H_2 in the system were calculated as:

$$n_o = \frac{p_o v_j}{Z(p_o T_o) R T_o} \quad (\mathbf{3.14})$$

$$n_1 = p\left(\frac{v_s}{Z(p_i T_s) R T_s} + \frac{v_c}{Z(p_i T_R) R T_R} + \frac{v_j}{Z(p_i T_o) R T_o}\right) \quad (\mathbf{3.15})$$

where P_0 is equal to the pressure in the system before opening reactor valve; P is the actual hydrogen pressure; V_j and V_C are the volumes of thermostated (at T_0) measurement

system and connecting pipeline (at room temperature, T_R), respectively; V_S is the internal volume of reactor with the sample kept at temperature T_S. The amount of hydrogen desorbed by the material was calculated in a similar manner as hydrogen absorption capacity.

3.5. Conclusion of the Methodology

The present study detailed experimental studies on preparation of Mg-based composites by HRBM under hydrogen atmosphere with *in situ* pressure-temperature monitored as a function of time. The effects of HRBM of magnesium with different amounts of additives (graphite (G), activated carbon (AC), multi-wall carbon nanotubes (MWCNT), expandable (EG), thermally-expanded (TEG) graphite, BCC alloy, ZrNi alloy, $TiFeO_3$ and Pd^0) on hydrogen sorption performances, thermal decomposition, phase composition and microstructural evolution were investigated as well. Special attention was paid to the influence of sample pre-history and air exposure (associated with overheating or surface contamination) on dehydrogenation and re-hydrogenation performances.

The *in situ* HRBM information together with the supplementing data about structure, morphology and dehydrogenation/re-hydrogenation properties would be of a high value for further understanding of hydrogen sorption mechanism during hydrogen storage materials preparation.

The mechanism behind the improvement of the hydrogen absorption/desorption performance of the nanocomposites will be proposed and discussed in the chapters to follow.

The hydrides forming materials used as catalysts were prepared by various techniques; these include arc-melting and wet synthesis as described above.

The techniques used in the analysis of prepared materials are summarized as follows:

- Crystal structure and phase composition could qualitatively be studied using XRD;
- Surface morphology could qualitatively be studied by TEM and SEM:
- Particles size average distribution were obtained by Malvern Zetasizer Nano ZS series:
- Hydrogen volumetric capacity and sorption kinetics could be qualitative studied using Sievert's type apparatus and:
- Heat effect, activation energy and weight loss associated with hydride decomposition (H_2 desorption) could be studied using DSC-TGA apparatus.

CHAPTER 4: Results and Discussion

The following nomenclatures were adopted for the formed hydrides composite under study and are as follows:

- Magnesium alone, MgH_2; Magnesium with Graphite, Mg-*x*G; Magnesium with Multi-Wall Carbon Nanotubes, Mg-*x*MWCNT; Magnesium with Activated Carbon, Mg-*x*AC; Magnesium with Expandable Graphite, Mg-*x*EG; Magnesium with Thermally Expanded Graphite, Mg-*x*TEG, where x = 1, 2, 5, 10 wt.%.
- Magnesium with Palladium; Mg-*x*Pd (x=0.5;, 1, 2 and 5 wt.%).
- Magnesium with $V_{75}Ti_{10}Zr_{7.5}Cr_{7.5}$, Mg-BCC-V; Magnesium with Graphite and $V_{75}Ti_{10}Zr_{7.5}Cr_{7.5}$, Mg-G-BCC-V; Magnesium with Multi-Wall Carbon Nanotubes and $V_{75}Ti_{10}Zr_{7.5}Cr_{7.5}$, Mg-MWCNT-BCC-V; Magnesium with Activated Carbon and $V_{75}Ti_{10}Zr_{7.5}Cr_{7.5}$, Mg-AC-BCC-V; Magnesium with Expandable Graphite and $V_{75}Ti_{10}Zr_{7.5}Cr_{7.5}$, Mg-EG-BCC-V; Magnesium with Thermally Expanded Graphite and $V_{75}Ti_{10}Zr_{7.5}Cr_{7.5}$, Mg-TEG-BCC-V. Where BCC-V = $V_{75}Ti_{10}Zr_{7.5}Cr_{7.5}$ (10 wt.%); C = AC, MWCNT, G, EG, TEG; and x = 1, 2 and 5 wt.%.
- Magnesium with Zirconium-Nickel, Mg-ZrNi; Magnesium with Graphite and Zirconium-Nickel, Mg-*x*G-ZrNi; Magnesium with Multi-Wall Carbon Nanotubes and Zirconium-Nickel, Mg-*x*MWCNT-ZrNi; Magnesium with Activated Carbon and Zirconium-Nickel, Mg-*x*AC- ZrNi;10 wt.% ZrNi; C = AC, MWCNT, G, EG, TEG; and x = 1, 2 and 5 wt.%.
- Magnesium with Titanium-Iron Oxide, Mg-*y*$TiFeO_3$; Magnesium with Activated Carbon and Titanium-Iron Oxide, Mg-*x*AC-*y*$TiFeO_3$; Magnesium with Multi-Wall Carbon Nanotubes and Titanium-Iron Oxide, Mg-*x*MWCNT-*y*$TiFeO_3$; Magnesium with Graphite and Titanium-Iron Oxide, Mg-*x*G-*y*$TiFeO_3$; AC = Activated Carbon; MWCNT

= Multi-Wall Nanotubes; G = Graphite; where x = 1, 2 and 5 wt.%; y = 2, 5, 10, 15, 20 wt.%.

4.1. Magnesium-carbon hydrogen storage nanocomposites

In the following chapter, the investigation of *in situ* pressure-temperature monitoring during HRBM of magnesium metal with various carbon additives (≤5 wt.%), including graphite (G), activated carbon (AC), multi-wall carbon nanotubes (MWCNT), expandable (EG) and thermally-expanded (TEG) graphite is reported. The effects of HRBM of magnesium with different quantities of the carbon type on the hydrogenation rate, thermal decomposition and re-hydrogenation performances, phase composition and microstructural evolution were investigated as well. Special attention was paid to the influence of sample pre-history and air exposure (associated with overheating or surface contamination) on dehydrogenation and re-hydrogenation performances.

4.1.1. Hydrogenation behaviour during HRBM of Mg with different carbon additives

Figure 4.1 presents hydrogenation performances of Mg and Mg–xC materials (C = G, MWCNT; x = 2, 5 and 10 wt.%) during their preparation using Fritsch Pulverisette 6 planetary mill at BPR = 80:1 (Figure.4.1(A)) and 40:1 (Figure 4.1(B)). For pure Mg, a nearly complete Mg→MgH_2 transformation took place within 6 hours of milling. At BPR=80:1 (Figure 4.1(A)), graphite additives lead to the noticeable increase of the Mg→MgH_2 transformation rate. Addition of 2 wt.% graphite to Mg results in more than a two-fold increase of the hydrogenation rate. However, this effect gradually weakens following further increase of the quantity of graphite in the mixture. Moreover, graphite

addition leads to the appearance of the incubation period, especially pronounced at the lower BPR (Figure 4.1(B)). Duration of the incubation period increases with increase in the quantity of graphite. Incubation period is likely to be caused by 'absorption' of mechanical energy by graphite, resulting in its delamination.

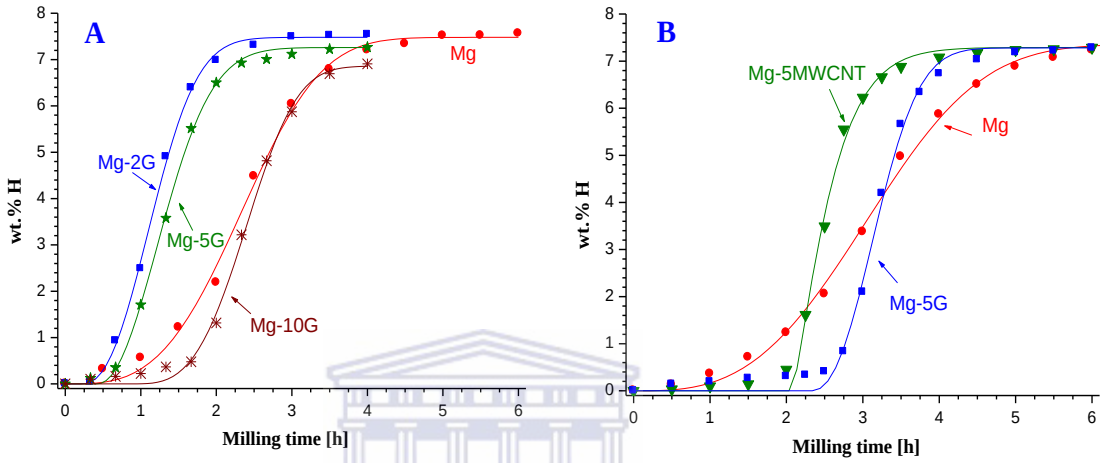

Figure 4-1: **Hydrogenation during HRBM (Fritch P6) at BPR=80:1 (**A**) and 40:1 (**B**) of magnesium and Mg–C materials containing 2 to 10 weight % of carbon additives: experimental data (symbols) and fitting results (lines)**

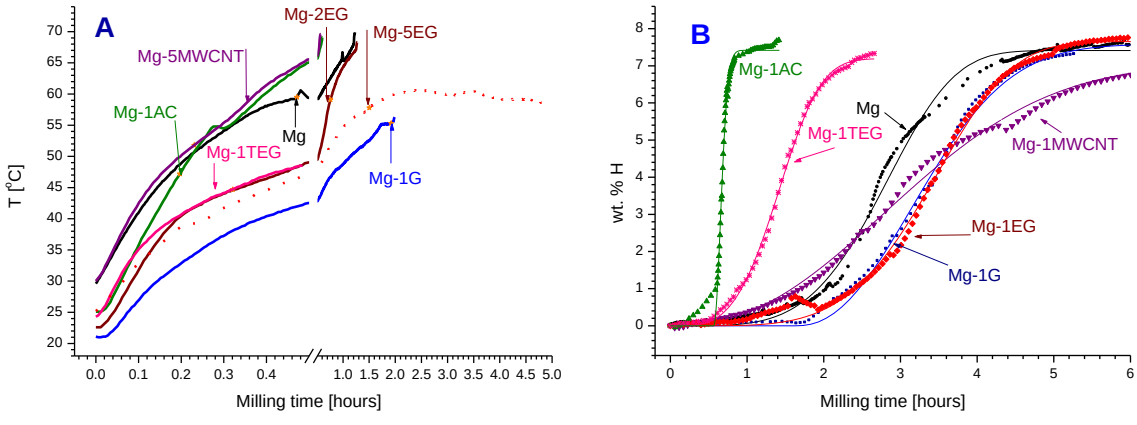

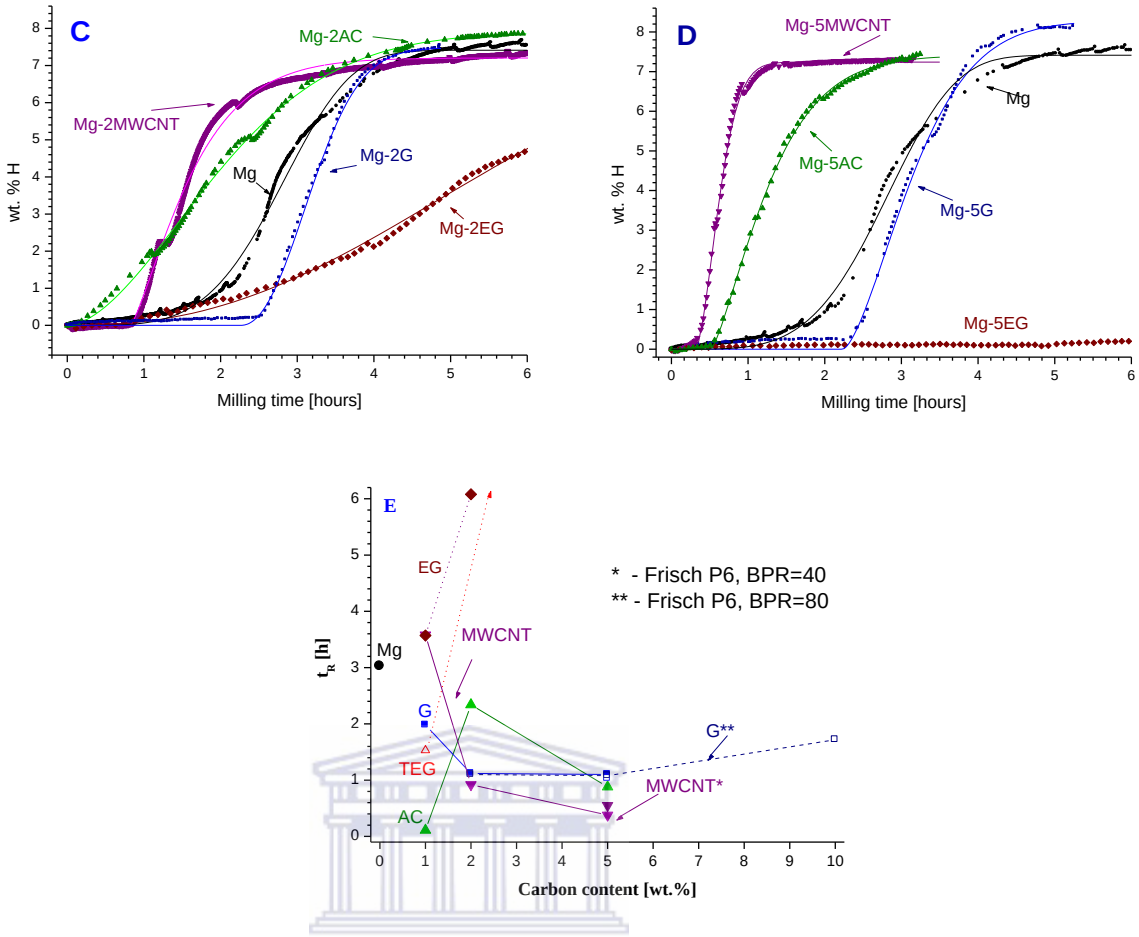

Figure 4-2: **HRBM behaviour of Mg and Mg–C materials: (**A**) time dependence of the vial temperature during HRBM, (**B–D**) hydrogenation during HRBM (Retsch PM100) of magnesium and magnesium-based materials containing 1 (**B**), 2 (**C**) and 5(**D**) weight % of carbon additives: experimental data (symbols) and fitting results (lines); (**E**) Effect of different carbon additives on the characteristic time of Mg→MgH_2 transformation during the HRBM**

Taking into account more profound hydrogenation behaviours observed for the various Mg-C materials synthesized at lower BPR (Figure 4.1(B)), further HRBM experiments were carried out at BPR = 40:1 using Retsch PM100 ball mill. Hydrogenation performances of Mg and Mg–C materials during HRBM in Retsch PM100 are presented in Figure 4.2 and Table 4.1. The hydrogenation curve of Mg presents a slow but

noticeable hydrogenation before absorption starts and the formed hydride reaches a constant hydrogen capacity in ~6 hours of HRBM. The experimentally measured maximum hydrogen absorption capacity is very close to the theoretical value for MgH_2 (7.66%).

Introduction of different carbon type's additives significantly changes the hydrogenation behaviour during HRBM and also affects the temperature changes during the milling. The changes are strongly dependent on both nature and amount of the carbon additive. The hydrogenation curves of HRBM Mg-C composites studied using Fritsch P6 (Figure4.1) and Retsch PM100 (Figure 4.2(B–D)) showed mutual agreement between the two experimental sets, with just one exception for Mg–5MWCNT. In the latter case, a well-defined incubation period before hydrogen absorption was noted during ball milling in Fritsch P6 was about 7 times longer than one observed during milling in Retsch PM100, and had approximately the same value as the incubation period for Mg–5G (~2 hours) observed for both types of planetary mills. Since the only difference in the ball milling conditions was in the vial dimensions (d=65 mm×h=28 mm and d=75 mm×h=50 mm for Fritch and Retch, respectively), one may assume them to affect the milling process and to be responsible for the differences in behaviour noticed for Mg–MWCNT during the HRBM. We believe that the bigger vial diameter in case of Retsch ball mill results in higher (~1.15x) linear speeds and centrifugal forces at the same rotation speed, and thus increases the mechanical energy supplied to the charge during the HRBM.

During HRBM, a gradual increase in vial temperature was noted due to collision between the steel balls and also the balls colliding with vial wall and additional contribution of the exothermic reaction, and the heat generated dissipate through the vial walls. The increase is less pronounced for materials containing TEG, EG and G and, has similar and higher

rates for Mg alone and for the materials containing AC and MWCNT. A typical time dependence of the vial temperature during HRBM is presented in Figure 4.2(A).

Table 4.1: Hydrogenation characteristics of Magnesium and Magnesium – Carbon materials during HRBM (for Fig. 4.1 and Fig 4.2)

Composite	Maximum H capacity [wt.% H]		Fitted kinetic parameters (eqn. 3.2)			
	Theoretical [a]	Experimental	t_0 [hours]	t_R [hours]	n	Pearson correlation coefficient, R^2
Mg[b] (80:1)	7.66	7.54	0	2.62 ± 0.003	3.2 ± 0.002	0.99686
Mg[b] (40:1)	7.66	7.36	0	3.47 ± 0.003	3.0 ± 0.001	0.99783
Mg	7.66	7.69	0	3.025 ± 0.005	4.27 ± 0.003	0.99706
Mg–1G	7.59	7.38	1.65 ± 0.005)	1.98 ± 0.001	2.20 ± 0.001	0.99715
Mg–2G[b] (80:1)	7.52	7.48	0.23 ± 0.003	1.10 ± 0.004	2.36 ± 0.009	0.99896
Mg–2G	7.52	7.54	2.25 ± 0.002	1.12 ± 0.002	2.18 ± 0.004	0.99866
Mg–5G[b] (80:1)	7.32	7.27	0.42 ± 0.003	1.08 ± 0.003	2.11 ± 0.007	0.99905
Mg–5G[b] (40:1)	7.32	7.28	2.32 ± 0.005	1.03 ± 0.006	2.33 ± 0.002	0.99582
Mg–5G	7.32	8.10	2.23 ± 0.002	1.10 ± 0.002	1.55 ± 0.004	0.9975
Mg–10G[b] (80:1)	7.01	6.86	0.86 ± 0.008	1.72 ± 0.009	3.3 ± 0.002	0.99704

Mg–1MWCNT	7.59	7.20	0	3.58 ± 0.001	2.31 ± 0.001	0.99746
Mg–2MWCNT	7.52	7.35	0.83 ± 0.001	0.92 ± 0.001	1.27 ± 0.002	0.99549
Mg–5MWCNT[b] (40:1)	7.32	7.29	2.08 ± 0.002	0.55 ± 0.003	1.24 ± 0.007	0.99714
Mg–5MWCNT	7.32	7.37	0.31 ± 0.001	0.38 ± 0.001	1.69 ± 0.004	0.99838
Mg–1AC	7.59	7.89	0.59 ± 0.001	0.11 ± 0.001	1.43 ± 0.004	0.99066
Mg–2AC	7.52	7.87	0	2.34 ± 0.001	1.76 ± 0.001	0.99846
Mg–5AC	7.32	7.40	0.515 ± 0.005	0.88 ± 0.001	1.33 ± 0.001	0.99912
Mg–1EG	7.59	7.75	0.12 ± 0.001	3.57 ± 0.001	4.42 ± 0.002	0.99665
Mg–2EG	7.52	4.69	0	6.08 ± 0.001	2.38 ± 0.001	0.99404
Mg–5EG	7.32	0.22	Not fitted			
Mg–1TEG	7.59	7.33	0.02 ± 0.003	1.53 ± 0.003	3.6 ± 0.001	0.99872
Mg–5TEG	7.32	0.24	Not fitted			

[a] – Assuming 100% formation of MgH_2 and no hydrogenation of carbon

[b] – The marked samples were studied in Fritsch P6 (BPR=80:1 and 40:1); otherwise the HRBM experiments were carried out in Retsch PM100 (BPR=40:1)

The incubation period is much shorter or absent for other forms of carbon additives in the experiments performed using Retsch PM100 mill (Figure 4.2). The material with 1 wt.% of MWCNT (Figure 4.2(B)) absorbed hydrogen without an incubation period, but slower hydrogenation kinetics than pure Mg. Thus, ball milling for 8 hours was necessary for the sample to reach saturation level with hydrogen. Further increase of the MWCNT content resulted in a significant improvement of the hydrogenation kinetics, which become superior as compared to pure Mg. For Mg–5MWCNTs composite, saturation level was achieved in less than 1.5 hours HRBM (Figure 4.2(D)). The Mg-AC composites (≥ 2 wt.%) also show improved hydrogenation kinetics but to a lesser extent than for Mg–MWCNT composites. However, reduction of AC content down to 1 wt.% (Figure.4.2(B)) showed an increase in hydrogenation rate with similar hydrogenation performance to Mg–5MWCNT. The hydrogenation of Mg-EG composites proceeds slower than pure Mg and the hydrogenation rates slow down with the increase of EG content. As an example, Mg–2EG sample absorbed less than 5 wt.% H during ~6 hours HRBM and the increase of EG contents to 5 wt.% results in almost complete suppression of H-absorption. Similar hydrogenation performance to the above was also observed for Mg-5TEG composite. The observed features may be a result of efficient damping of the collisions during ball milling at the presence of EG (which, most probably, exfoliates during the ball milling) or TEG where ball milling is known to result in the folding of the crinkled graphite sheets and in generating in-plane defects [230]. These processes consume mechanical energy that, in turn, reduces the amount of mechanical energy supplied to the particles of magnesium during HRBM. At the same time, the composites containing lowest quantity of EG (1 wt.%) has relative better hydrogenation performances which are very close to that observed for Mg–1G. Replacement of the EG with TEG (1 wt.%) results in a significant improvement of the hydrogenation

performances (Figure 4.2(B)). Ball milling of graphite (both natural and expanded) is reported to have a strong shearing effect that results in the delamination perpendicular to the *c*-direction [221, 222]. Most probably, at the beginning of the HRBM of the materials containing natural, expandable or expanded graphite, part of the mechanical energy is spent to destroy the original graphitic structure and to produce graphene nano-sheets.

It should be noted that for some carbon-containing materials, measured hydrogen storage capacities exceeded the values corresponding to the formation of a stoichiometric magnesium dihydride MgH_2. We believe this is caused by a combination of (i) hydrogen adsorption on and its dissociative interaction with nano-carbon; (ii) hydrogen trapping on the lattice defects and on the grain boundaries of MgH_2 produced in the course of HRBM. The observed results are in qualitative correspondence with the ones reported by Rud *et.al*. [182], where the best hydrogenation during HRBM was observed for the composites containing amorphous carbon (somewhat similar to activated carbon used in this work), and highly-dispersed graphite. However, in present, the hydrogenation is much faster (was completed within 1–5 versus in more than 20 hours observed in [182]), due to higher energy of milling, higher H_2 pressures and smaller quantities of carbon additives used.

During HRBM, the presence of an incubation period in some samples preparation is ascribed to critical concentration of defects that has to be reached before the dissociation of the hydrogen molecule and its subsequent diffusion into the bulk of magnesium could start [170]. During this time, the mechanical activation promotes several effects such as breakdown of surface oxide layers, introduction of structural defects and increase of specific surface area etc. Once the molecular hydrogen dissociates into atoms on the Mg

surface, hydrogen atoms diffuse into Mg to form MgH_2. The diffusivity of hydrogen atoms within MgH_2 and the formation rate of MgH_2 on the Mg surface and/or along the grain boundaries (if any) are the key factors for hydrogenation capacity and kinetics. This is because the diffusion coefficient in MgH_2 is much smaller than that in Mg [223]. During MgH_2 formation: the hydrogen atoms diffuse very fast in Mg, after which hydrogen diffusion becomes very slow and it becomes very difficult for hydrogen atoms to penetrate through the shell of MgH_2. Once the hydride layer has been formed, the hydrogenation rate of the remaining magnesium decrease with increased hydride layer thickness [218]. The hydrogenation of Mg is the controlling step before the shell is completely formed while the diffusion of hydrogen in MgH_2 becomes the controlling factor after the shell formation. The formation of MgH_2 is associated with nucleation and growth of MgH_2 nuclei and also the structure of MgH_2 and Mg.

To further investigate the sorption kinetics during HRBM of Mg and Mg-C samples, the obtained results were fitted by *Avraami* equation 3.2, and the obtained data summarized in Table 4.1. Though the fitted parameters do not allow reaching an unambiguous conclusion concerning the mechanism of the hydrogenation, the *n* value is considered as a footprint of the process [233]. The hydrogenation kinetics curves of Mg exhibit typical S-shaped curve, with *Avraami* exponent factor $n \approx 4$. However, approaching saturation level, the H_2 concentration is slower than it would be expected from the fitting. When $n \geq 3$ (Mg, Mg–10G, Mg–1EG, Mg–1TEG), the rate-limiting step of the reaction can only be the phase transformation, with either 3D ($n = 3^{(1)},4^{(2)}$) or 2D ($n = 3^{(2)}$) growth of MgH_2 nuclei. The lower *n* values were observed for the other materials and indicate that the rate-limiting step changes to a phase transformation ($n = 2$ for the $2D^{(1)}$ and $1D^{(2)}$ growth,

[1] At a constant number of nuclei.
[2] At a constant nucleation rate.

respectively) or to H diffusion (n = 1, 1.5, 2, and 2.5 for different nucleation mechanisms and growth dimensionalities).

All Mg–C hybrid materials, independent of type and amount of carbon additive, were found to be extremely pyrophoric, especially after completed hydrogen desorption.

4.1.2. Morphological and phase characterization of MgH_2 and Mg-C composites materials

4.1.2.1. XRD

The XRD patterns for as-milled magnesium and magnesium–carbon composites materials are summarized in Table 4.2. The samples exhibit broad peaks corresponding to two main constituent phases, a rutile-type α-MgH_2 and metastable orthorhombic γ-MgH_2, the latter phase is well reported in the course of HRBM of Mg [170] and Mg–C composites materials [225]. Recently, the formation γ-MgH_2 phase has been reported in [226] using High Pressure Torsion (HTP) process. The experimentally measured γ-MgH_2 phase content varies from 4–6 to 17–31%; the upper value is close to the value observed by Denys *et.al.* [236] in the course of SR XRD study of HRBM Mg (28.5%). The amount of γ-MgH_2 observed in the Mg–C hybrid materials has a trend of lowering, especially, for C = EG and TEG; the latter samples also showed reduced microstrains and the crystalline of α-MgH_2. The crystalline size of both composites phases were quite small, ~7 nm in average. The minimum values, below 6 nm, were observed for Mg–2AC and Mg–5MWCNT. The maximum crystalline size (9.5 nm, 36% higher than the average value) was observed for Mg–1TEG. The as-milled sample of Mg–2EG contained the lowest amount of γ-MgH_2 phase; its conversion to MgH_2 gave the poorest yield, so a significant

amount of unreacted Mg was observed. The lattice periods of Mg in as-milled Mg–2EG are somewhat higher than the values reported in the literature [229] and ones determined by the refinement of the patterns of the re-hydrogenated samples (Table 4.2).

Comparison of the SR XRD pasterns of Mg–5MWCNT before the end of the incubation period (Figure 4.3(C)) and after completion of HRBM (Figure 4.3(D)) shows interesting changes. In the former case, the pattern contain sharp peaks belonging to the major phase of the unreacted Mg and showing a pronounced texture along (100) direction, together with the peaks of the incipient α-MgH_2 phase whose crystalline size was found to be about 3 times higher than that for MgH_2 after the HRBM. No contribution from crystalline carbon-based phases was observed in the XRD pattern that testifies about (i) disappearance of the crystalline graphite-like phases (C = G, EG, TEG), and (ii) absence of chemical interaction between Mg and C yielding magnesium carbide. Moreover, absence of dissolution of carbon in Mg and MgH_2 during the HRBM can be confirmed by a very good agreement between the values of their unit cell parameters with the ones specific for as-milled Mg and reported in the reference data [229, 230]. Most of the C-containing materials also show the presence of MgO presumably formed due to a slight oxidation of Mg/MgH_2 during storage and preparation of the samples for the XRD analysis. In addition, the precise XRD pattern collected using synchrotron radiation also show the presence of trace amounts of α-Fe (<0.5 wt.% for BPR 40:1, and ~1 wt.% for BPR 80:1) contamination from the milling tools.

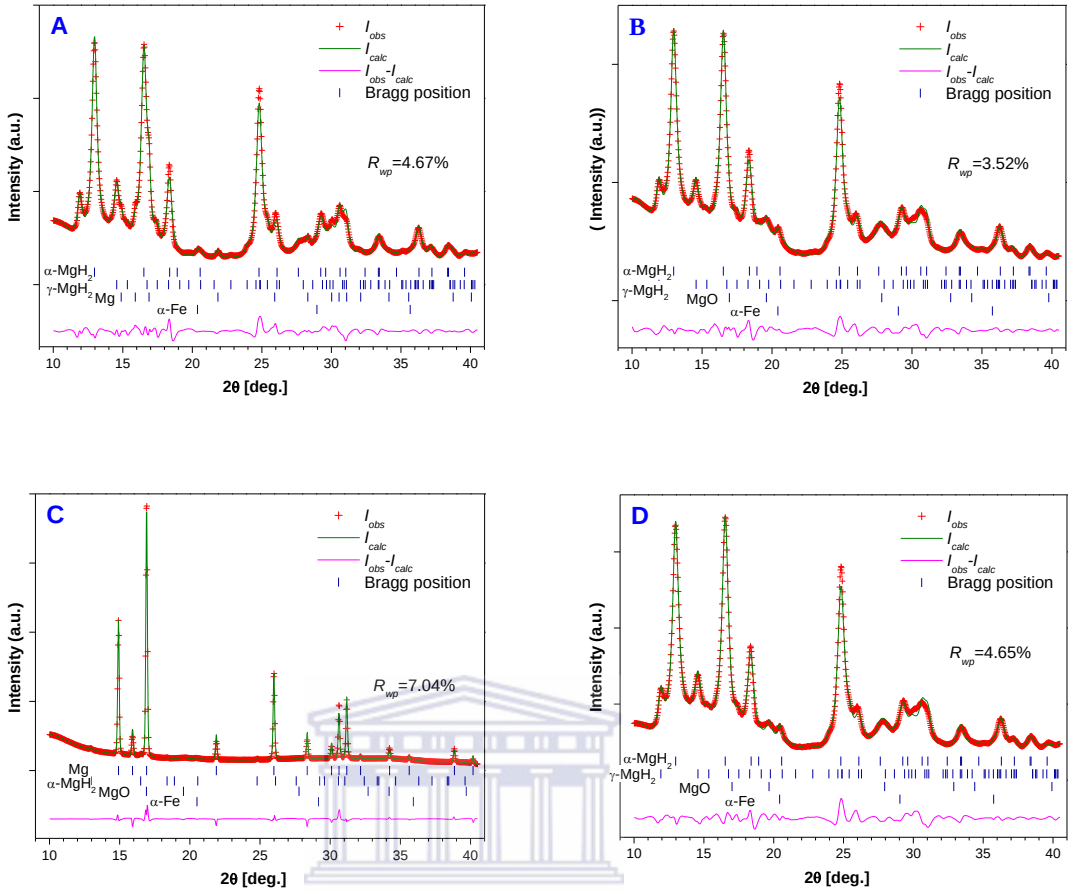

Figure 4-3: SR XRD patterns (SNBL, BM01A; λ = 0.72085 Å) for the as-milled samples of Mg (A**), Mg–5G (**B**) and Mg–5MWCNT collected before the end of the incubation period (**C**) and after completion of the HRBM (**D**)**

All the obtained diffraction patterns for the re-hydrogenated composites materials exhibit similar patterns. The patterns for the re-hydrogenated composites (Figure 4.4) exhibit sharp peaks that are ascribed to: (i) elimination of microstrain in the crystals and (ii) crystalline growth during hydrogen cycling [232]. The unit cell parameters of α-MgH_2 (Table 4.2) are similar for all studied samples and agree with the reference data [229]. The patterns also indicate a presence of minor amounts of unhydrogenated Mg (1–8%).

The α-MgH_2 phase abundance is high in re-hydrogenated samples than the as-milled composite materials with small traces of Mg. The Mg reflection is believed to result from unreacted Mg during hydrogen cycling and/or from the Mg which were present in as-milled composite materials. No trace peaks of metastable orthorhombic γ-MgH_2 phase were observed in re-hydrogenated samples. Thus, it is reasonable to say that γ-MgH_2 was eliminated during hydrogen cycling because the composites were heated to ~460°C. Re-hydrogenation resulted in a significant increase of crystalline size of α-MgH_2 due to re-crystallization in the course of TDS/re-hydrogenation cycling. However, carbon-containing composites show much smaller crystalline size for α-MgH_2, nearly 4 times lower than the value for the re-hydrogenated HRBM Mg (Table 4.2). This was evidenced by differences in the peak broadening of the XRD pattern shown in Figure 4.4 (see insert in Figure 4.4). The observed α-MgH_2 crystalline size in the Mg–C materials (5–7 for as-milled and 40–100 nm for the re-hydrogenated samples) agrees well with the values reported by Fuster *et.al.* [183], for Mg–G (5 nm for as-milled and 30–70 nm for the re-hydrogenated samples). The presence of carbon additives inhibit the re-crystallization processes thus resulting in an increase in the cycle life for the Mg-based hydrogen storage materials. This effect, however, is less pronounced for the re-hydrogenated samples containing small amounts (1 wt.%) of EG and TEG where the crystallite size was in the range 106 to 125 nm, against ~60 nm for Mg–MWCNT, 40–45 nm for Mg–AC, Mg–G and Mg–2EG, and ~180 nm for Mg without carbon additives.

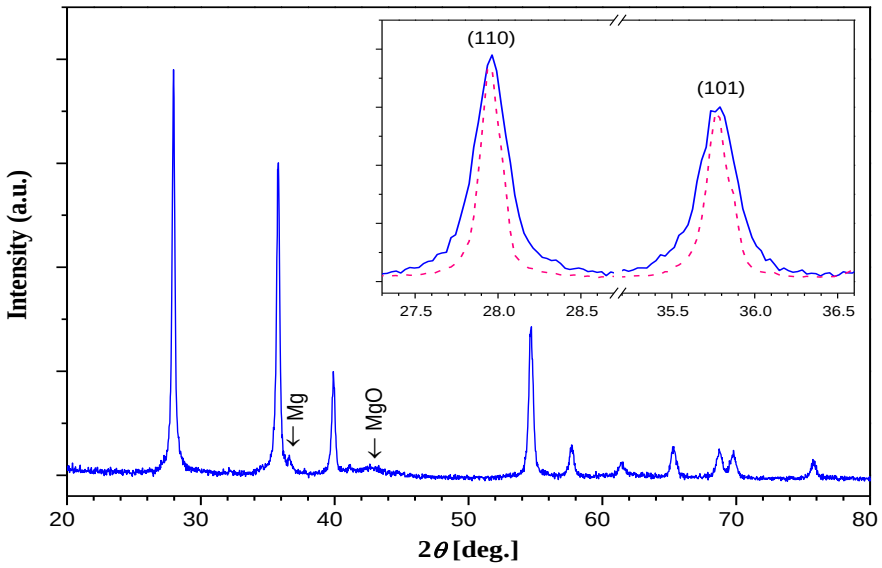

Figure 4-4: **XRD pattern of re-hydrogenated Mg–5G material (Cu-K_α). Inset shows comparison of peak broadening of α-MgH_2 in re-hydrogenated RBM Mg (dash line) and Mg–5G (solid line)**

Table 4.2: Characteristics crystallographic data of as-milled and re-hydrogenated Mg-*x* wt.% carbons composites constituent phases calculated by the refinement of the XRD data [(a)].

Sample	MgH_2 crystalline size [nm]	α--MgH_2			γ-MgH_2				Mg		
		Abundance [wt.%]	*a* [Å]	*c* [Å]	Abundance [wt.%]	*a* [Å]	*b* [Å]	*c* [Å]	Abundance [wt.%]	*a* [Å]	*c* [Å]
Mg (as milled)	6.5–7.5	69–82	4.518–4.523	3.021–3.022	18–24	4.521–4.536	5.410–5.438	4.934–4.953	0–7	3.215	5.215
Mg–1G (as milled)	7.4	94	4.523	3.027	6	4.521	5.438	4.934	0	–	–
Mg–2G (as milled)	6.2	83	4.520	3.020	15	4.521	5.438	4.934	2	3.21	5.21
Mg–5G (as milled)	6.1–6.5	76–89	4.517–4.521	3.021–3.022	11–19	4.521–4.540	5.406–5.438	4.934–4.948	0	–	–
Mg–2MWCNT (as milled)	6.5	78	4.520	3.020	17	4.521	5.438	4.934	0	–	–
Mg–5MWCNT (as milled)	5.4–6.1	74–89	4.519–4.521	3.021–3.022	10–22	4.521–4.543	5.404–5.438	4.934–4.95	0	–	–
Mg–5MWCNT (as	21	1.6	4.513	3.023	0	–	–	–	95.4 (textured)	3.205	5.204

milled; before the end of incubation period)											
Mg–1AC (as milled)	7.8	85	4.519	3.022	15	4.521	5.438	4.934	0	–	–
Mg–2AC (as milled)	5.5	81	4.519	3.019	17	4.521	5.438	4.934	2	3.21	5.21
Mg–5AC (as milled)	6.2	83	4.519	3.019	13	4.521	5.438	4.934	4	3.213	5.216
Mg–1EG (as milled)	6.7	90	4.519	3.023	10	4.521	5.438	4.934	0	–	–
Mg–2EG (as milled)	7.3	57	4.520	3.018	4	4.521	5.438	4.934	36	3.213	5.216
Mg–1TEG (as milled)	9.5	91	4.519	3.024	9	4.521	5.438	4.934	0	–	–
Mg (re-hydrogenated)	182	78.3	4.5178	3.0210	0	–	–	–	2.1	3.214	5.211
Mg–1AC (re-hydrogenated)	45	81.5	4.5177	3.0213	0	–	–	–	7.1	3.211	5.218
Mg–5G	43	86.2	4.5200	3.0223	0	–	–	–	1.1	3.214	5.211

(re-hydrogenated)											
Mg–5MWCNT (re-hydrogenated)	57	83.5	4.5193	3.0217	0	–	–	–	2.1	3.215	5.210
Mg–1EG (re-hydrogenated)	106	90.0	4.5164	3.0205	0	–	–	–	7.4	3.212	5.213
Mg–2EG (re-hydrogenated)	42	81.5	4.5176	3.0211	0	–	–	–	8.2	3.214	5.212
Mg–1TEG (re-hydrogenated)	125	94.1	4.5162	3.0201	0	–	–	–	4.9	3.212	5.215

[a] Errors of the lattice periods are approximately equal to one unit of last digit of the values presented in the table.

4.1.2.2. Morphology

The morphology of the as-milled and re-hydrogenated Mg-C composites materials were investigated by SEM and TEM analysis. Figure 4.5-4.7 shows the SEM micrographs of the as-milled and re–hydrogenated Mg-C samples. Figure 4.5 (A, B) show the micrographs of starting magnesium powder having particles of regular, close to spherical shape that are several hundred μm in size with smooth surface with few cracks. HRBM of Mg under hydrogen atmosphere for 6 hours results in the formation of porous agglomerates, from several to few tens μm in size, each agglomerate consist of submicron-size particles (Figure 4.5(C, D)). Sintering/agglomeration causes a loss in the total surface area for a given volume for the hydride (metal) and an increase in the diffusion distance for hydrogen atoms. The observed size increase agrees with the established explanation regarding the reason for the increase kinetics sluggishness of the metal hydride powders with prolonged high temperature sorption cycling.

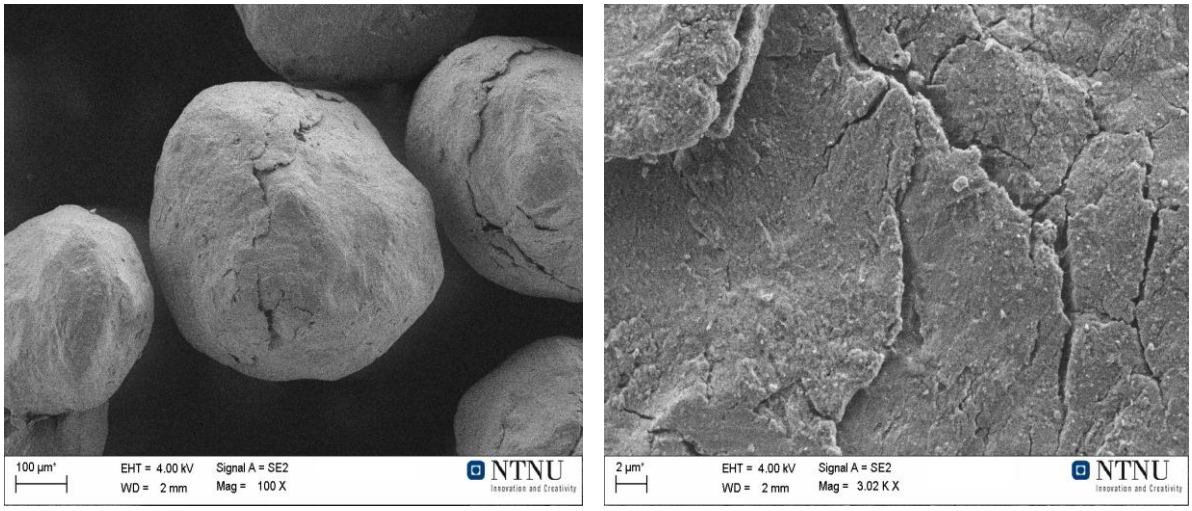

A **B**

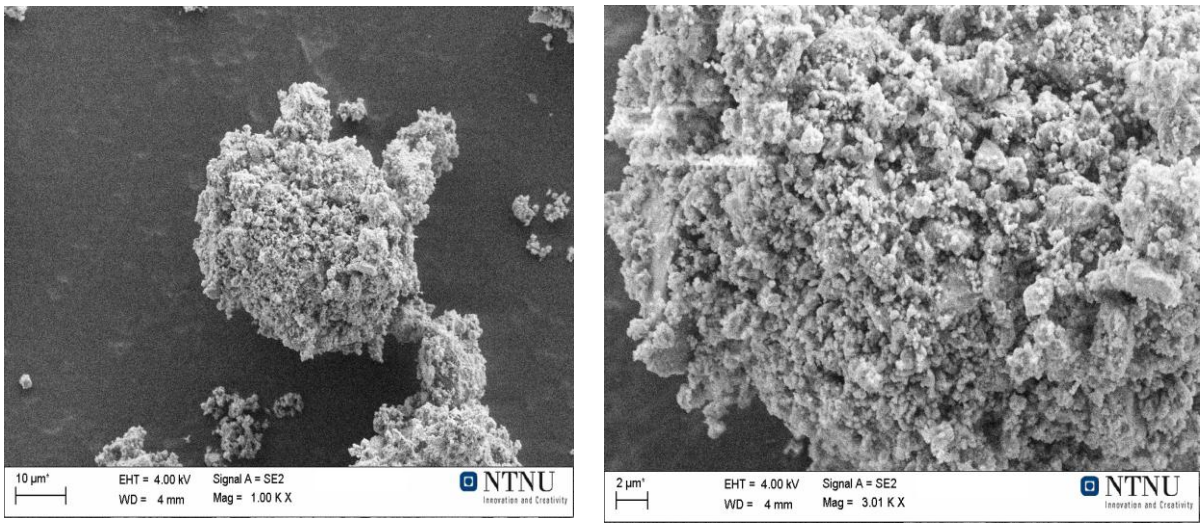

C **D**

Figure 4-5: **SEM micrographs of magnesium powder particles before HRBM (**A, B**) and MgH_2 after 6 hours-long HRBM of the magnesium (**C, D**). Scale bars correspond to 100 (**A**), 10 (**C**) and 2 (**B, D**) μm**

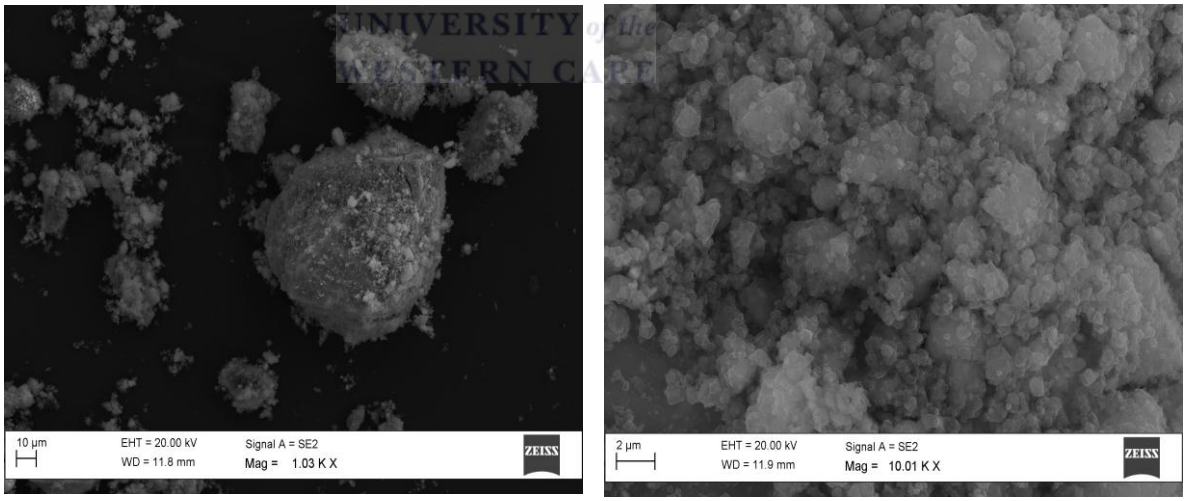

A **B**

Figure 4-6: **SEM micrographs of MgH_2 after TDS/re-hydrogenation cycle. Scale bars correspond to 10μm (**A**) and 2 μm (**B**)**

Carbon materials when added to Mg or MgH_2 during ball milling are reported to act as a lubricating agent, thus reducing the adhesion and agglomeration of its particles [231, 232]. Figure 4.7 shows the SEM micrographs of HRBM Mg-5MWCNT material. The observed micrograph before the beginning of intense hydrogen absorption consists of quite large (hundreds μm) plates formed by "forging" of the individual spherical particles of magnesium with carbon additives uniformly distributed on their surface (Figure 4.7 (A, B)). Further milling (Figure 4.7 (C, D)) resulted in the formation of porous agglomerates of MgH_2 similar to the ones observed after the HRBM of pure magnesium (Figure 4.5(C, D)). The presence of carbon material reduces sintering/agglomeration of MgH_2 particles in HRBM Mg–C as compared to samples prepared without carbon additives (Figure 4.6) and also contribute towards the reduction of crystalline size in the re-hydrogenated Mg-C samples as observed in XRD results.

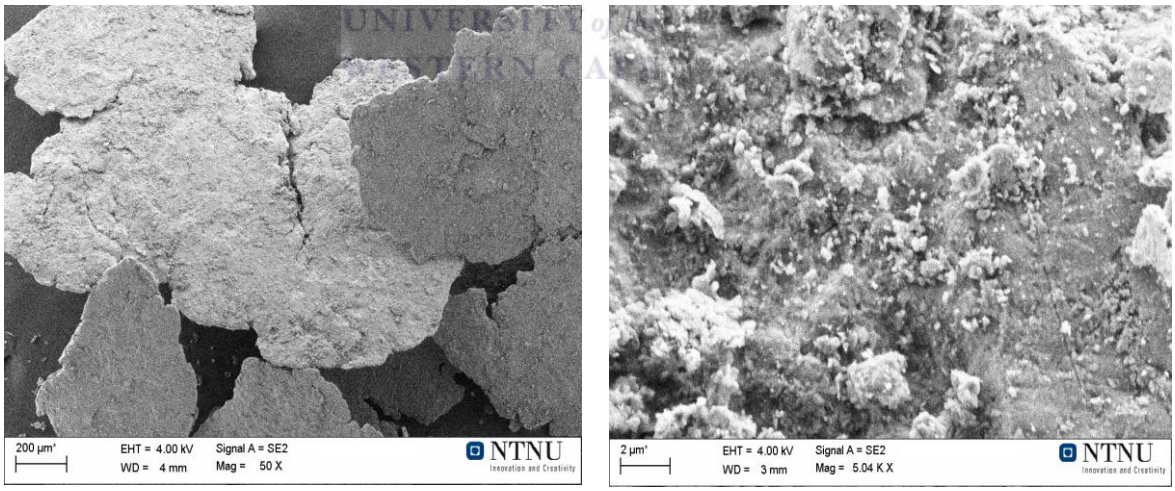

A **B**

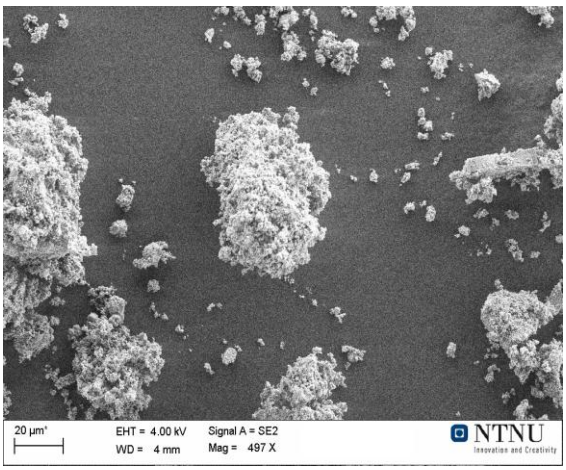

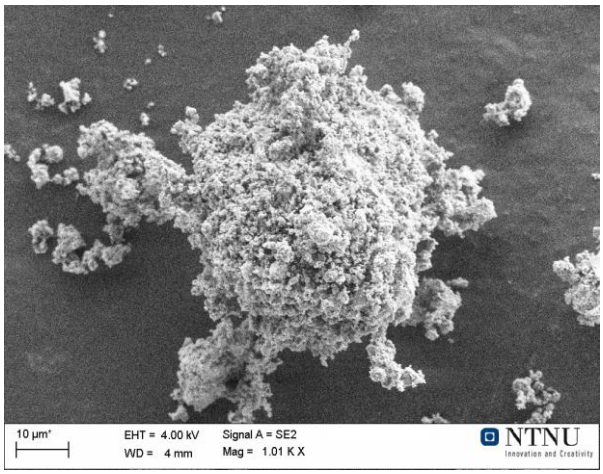

C **D**

Figure 4-7: SEM micrographs of as-milled Mg–5MWCNT material before the end of incubation period (A, B**) and after completion of hydrogenation (**C, D**). Scale bars correspond to 200 (**A**), 2 (**B**), 20 (**C**) and 10 (**D**) μm**

The HRTEM studies were limited to sub-μm particles since larger ones were not electron transparent. Typical TEM micrographs of Mg sample after HRBM are shown in Figure 4.8 (A). The obtained micrographs shows irregularly shaped grains of various sizes, with the larger grains exhibiting a nano-scale twining. The multiple twinning is shown in Figure 4.8 (B) and its selected area diffraction pattern (SAD) obtained from this grain shown in Figure 4.8 (C). Similar findings to the above were reported by Danaie *et.al*. [220]. The crystallite boundaries act as preferential sites for the heterogeneous nucleation of the twins and for the formation of solid solution by release of the lattice strain energy [232]. The SAD pattern shows a continued ring pattern representing a very fine grain size material and this was also reported in [198] for Mg-FeTi-CNT milled for 60 hours.

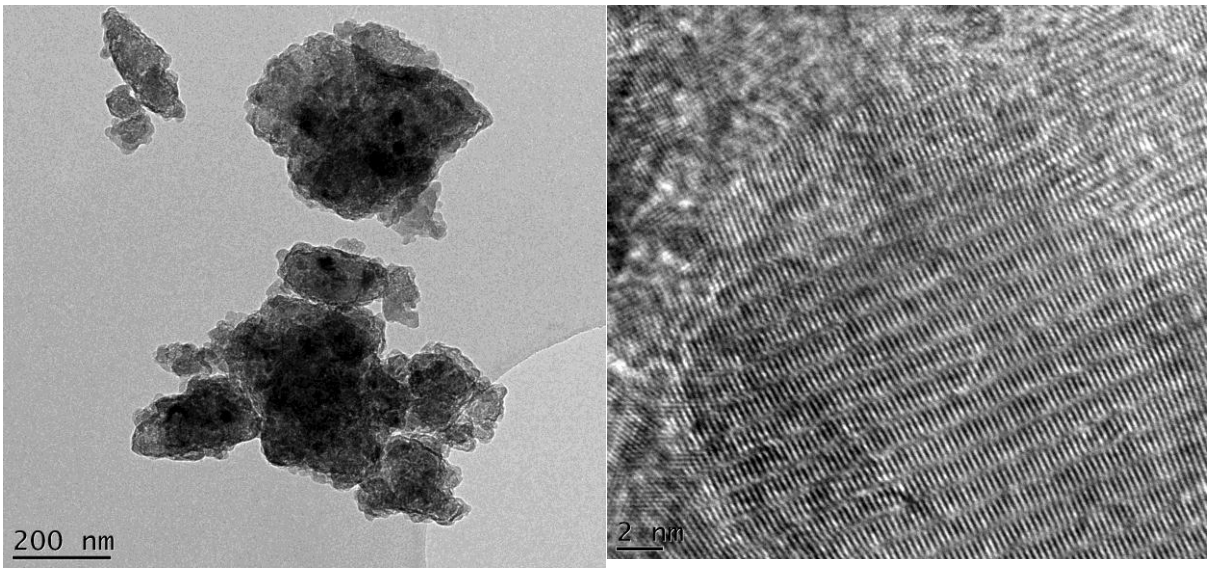

A **B**

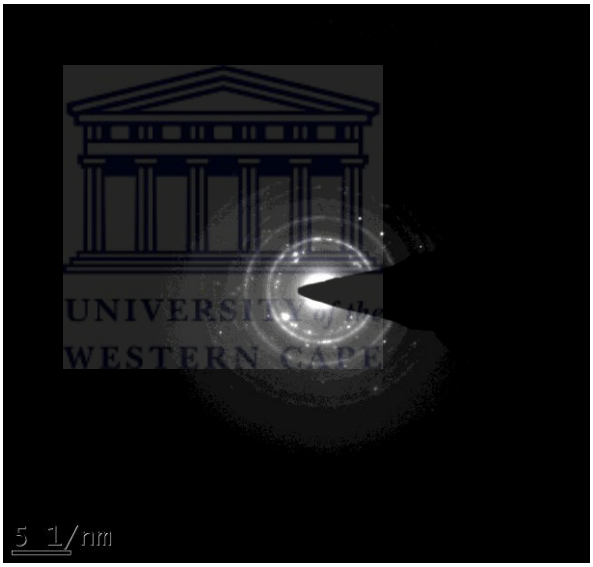

C

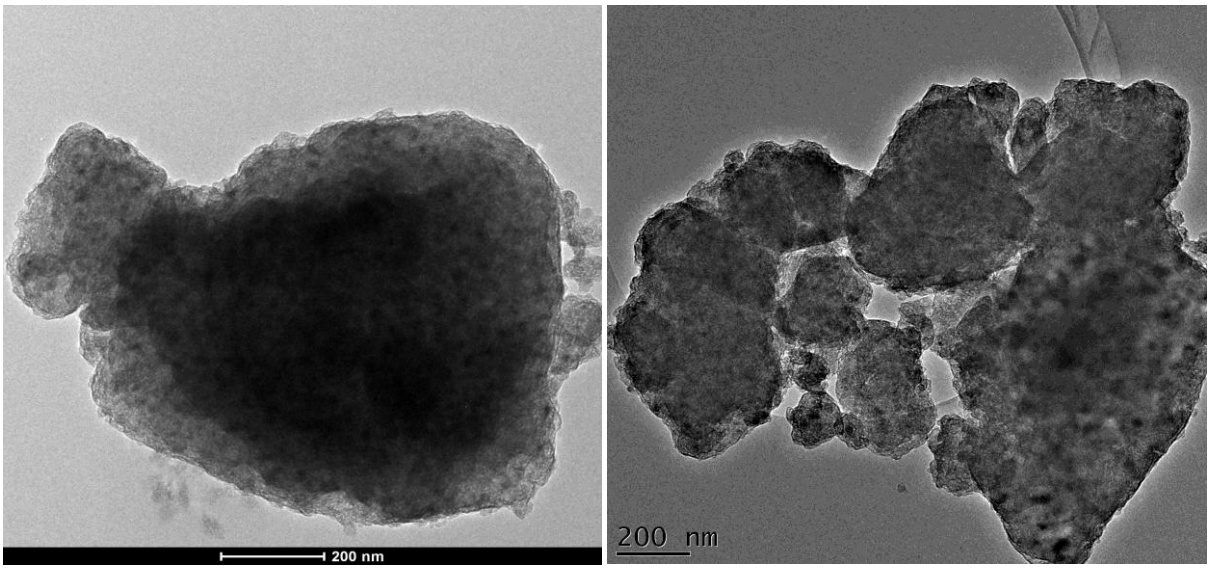

D **E**

Figure 4-8: TEM micrographs of HRBM samples: bright field micrograph of Mg (A**), Diffracting area** (B)**, SAD of pattern of Mg (**C**), bright field micrograph of Mg-5MWCNT (**D**) and bright field micrograph of Mg-5AC (**E**)**

TEM micrographs of HRBM Mg-5MWCNT and Mg-5AC are shown in Figure 4.8(D, E). From the obtained micrographs, it can be seen that Mg and carbon materials were fully mixed with nanometer size particles of carbon materials embedded in the MgH_2 aggregates validating the SEM results in Figure 4.7.

Re-hydrogenated micrographs of Mg and Mg-5C hybrid materials are shown in Figure 4.9. Figure 4.9 (A, B) show the TEM micrograph of re-hydrogenated MgH_2 sample showing an interface where it appears that, multiple initially separated hydrides particles have sintered/agglomerated together. However, in carbon-containing hybrid materials, a separation between nano-particles of the hydride (light streaks) is clearly seen both in the as-milled (Figure 4.8(D, E)) and re-hydrogenated (Figure 4.9) materials. This observation confirms that during HRBM of magnesium with carbon, the latter forms

nanoscale layers in-between MgH_2 particles thus suppressing their re-crystallization during consequent dehydrogenation/re-hydrogenation. Since the diffraction peaks specific for the graphite-type phases were not observed by XRD, we assume that in the Mg–C hybrid materials, carbon is present either in amorphous form or, most probably, as the stacked graphene layers. The thickness of these layers is small, not exceeding ten atomic layers in combination with a low content of carbon types in the materials and a low atomic scattering factor of X-rays for carbon. This results in absence of the corresponding carbon-related X-ray diffraction pattern.

Some of the hydride particles consisted of one or several large MgH_2 crystallites. While the crystallites did contain defects such as twins, overall, their number frequency was much lower than in HRBM Mg sample, implying that some of them were annealed out. Other hydrides particles consisted of numerous nanoscale hydride grains.

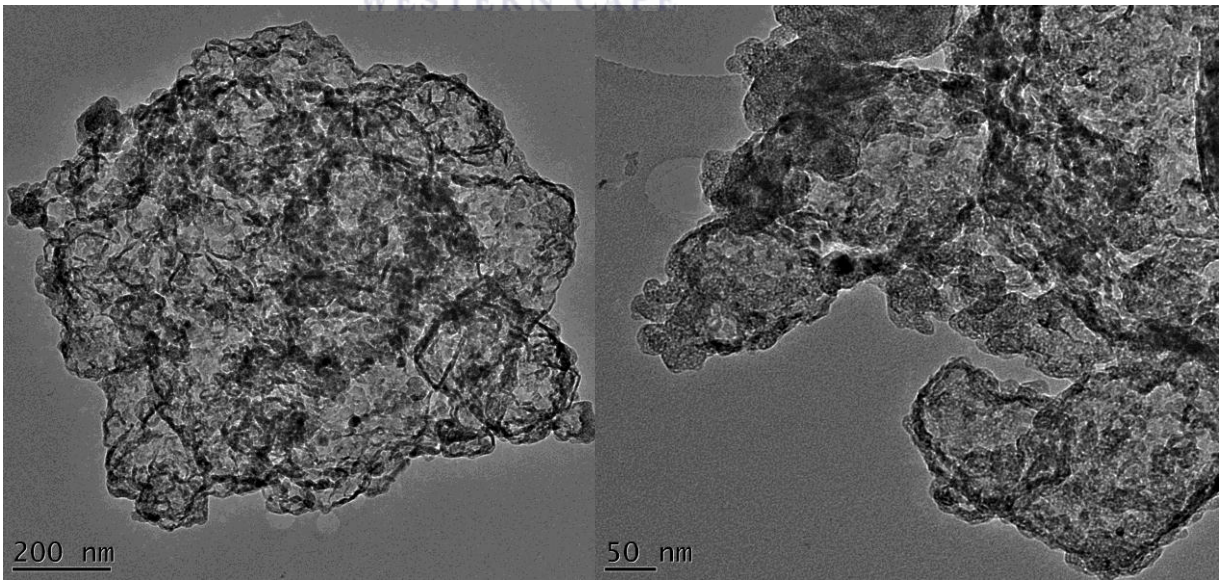

A **B**

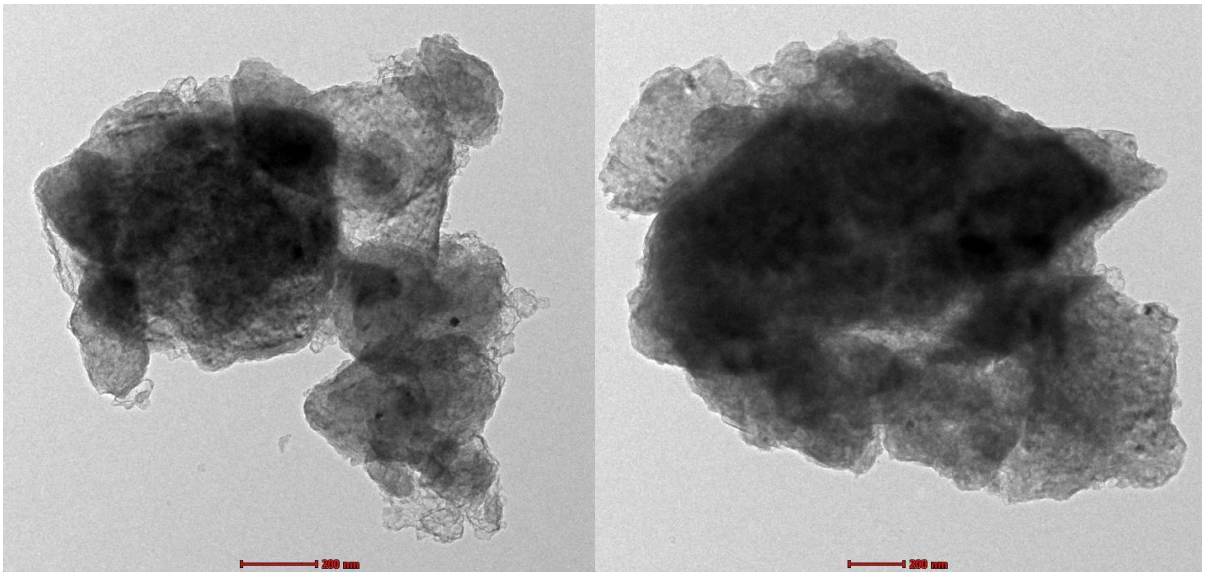

C **D**

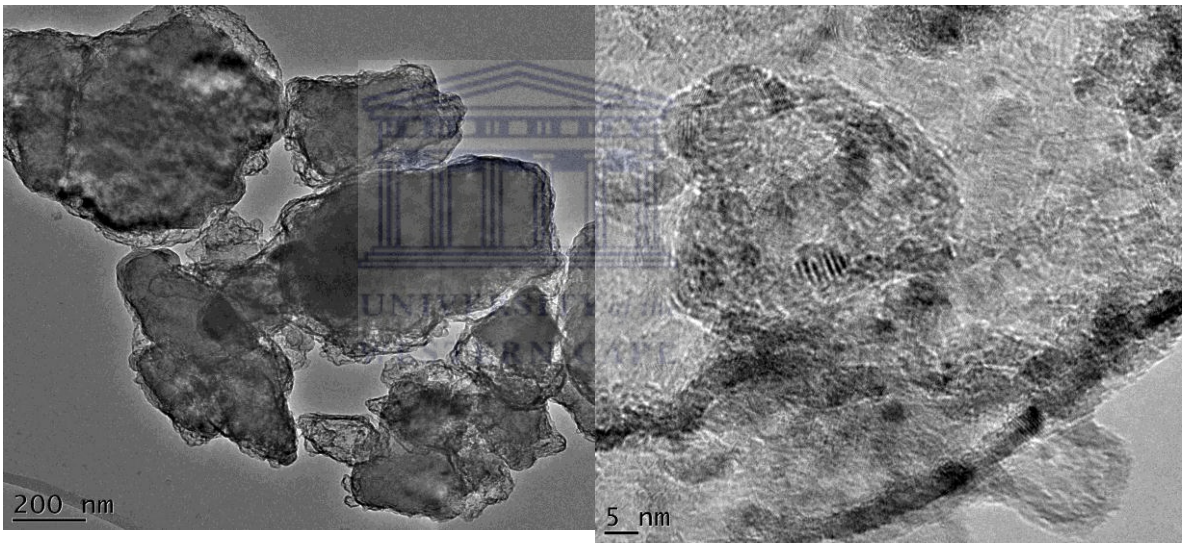

E **F**

Figure 4-9: TEM micrographs of re-hydrogenated materials; MgH_2 (A, B**), Mg-5MWCNT (**C**), Mg-5G (**D**) and Mg-5AC (**E, F**)**

Based on SEM and TEM in the above observation, it is possible to offer an explanation of differences in the hydrogenation behaviours during HRBM of magnesium with different carbon additives. Replacement of soft graphite (hardness 0.5–1 Mohs) with activated carbon which has hardness (≥3 Mohs) higher than magnesium (2.5 Mohs), enables

carbon species to be "indented" into magnesium during the ball milling, that promotes further grain refinement. In the case of MWCNT known to be very hard in axial direction and quite soft in radial one, the "indentation" effect becomes pronounced when a sufficient amount of axially-oriented MWCNT will appear, i.e. when the total amount of MWCNT increases. Further improvement of the hydrogenation during the HRBM, most probably, has its origin in the formation of graphene nano-sheets.

4.1.3.3. Mean particle size for as-milled and re-hydrogenated Mg-C hybrid materials

Table 4.3: **Average particle sizes HRBM and re-hydrogenated hybrid materials**

Sample	**Average particle size (nm)**	
	as-milled	**re-hydrogenated**
Commercial MgH_2	not measured	1459
MgH_2	853	983
Mg-1MWCNT	not measured	975
Mg-2MWCNT	1025	912
Mg-5MWCNT	843	537.
Mg-1G	not measured	2789
Mg-2G	1291	not measured
Mg-5G	843	557
Mg-1AC	1451	1327
Mg-2AC	not measured	2387
Mg-5AC	not measured	1104
Mg-1EG	1365	not measured
Mg-5EG	not measured	2198
Mg-1TEG	1638	1173

The average particle sizes for as-milled and re-hydrogenated hybrid materials were obtained by using Zeiter Sizer instrument and results summarized in Table 4.3. Since the observed particles sizes are not round (see Figure 4.5-4.7), so the value obtained accounts for the multi-dimension factors affecting the particle size. A typical particle generally contains thousands of grains. Measurements of the mean particle sizes of as-milled samples showed that for undoped magnesium is ~ 852.77 nm. A decrease in particle size was observed for all the re-hydrogenated hybrid materials, the materials containing G and MWCNT showed a two-fold reduction in particle size ($0.84 \pm 0.009 – 0.89 \pm 0.008$ μm). The presence of different carbon type in the hybrid materials during re-hydrogenation was observed not only to stabilize the nanoparticles formed, which is essential for maximizing the hydrogenation of Mg, but also acts as a grain growth inhibitor that prevents the coarsening of Mg/(MgH_2) particles during dehydrogenation/re-hydrogenation cycle [198]. These findings can also be confirmed in the SEM and TEM micrographs of the different Mg hybrid material after rehydrogenation cycling; with the Mg sample ball milled without carbon addition shows an agglomeration of particles. These indicate that the particles size (and the grain size) remains almost identical to those of as-milled hybrid materials.

4.1.3. Hydrogen sorption properties

4.1.3.1. TDS/ re-hydrogenation

The re-hydrogenation results for all the studied samples are summarized in Table 4.4 and their kinetics curves (H_2 wt.% vs time) at 250°C (~15 bar H_2) after *in situ* dehydrogenation in the course of TDS studies are shown in Figure 4.9. The as-milled magnesium and all Mg–C composite materials exhibited high re-hydrogenation rates,

which are superior to that for the de-hydrogenated commercial MgH_2 (Figure 4.9(A)). The amount of hydrogen re-absorbed in 2.5 hours (250°C/15 bar H_2) varies within 4–6 wt.%.

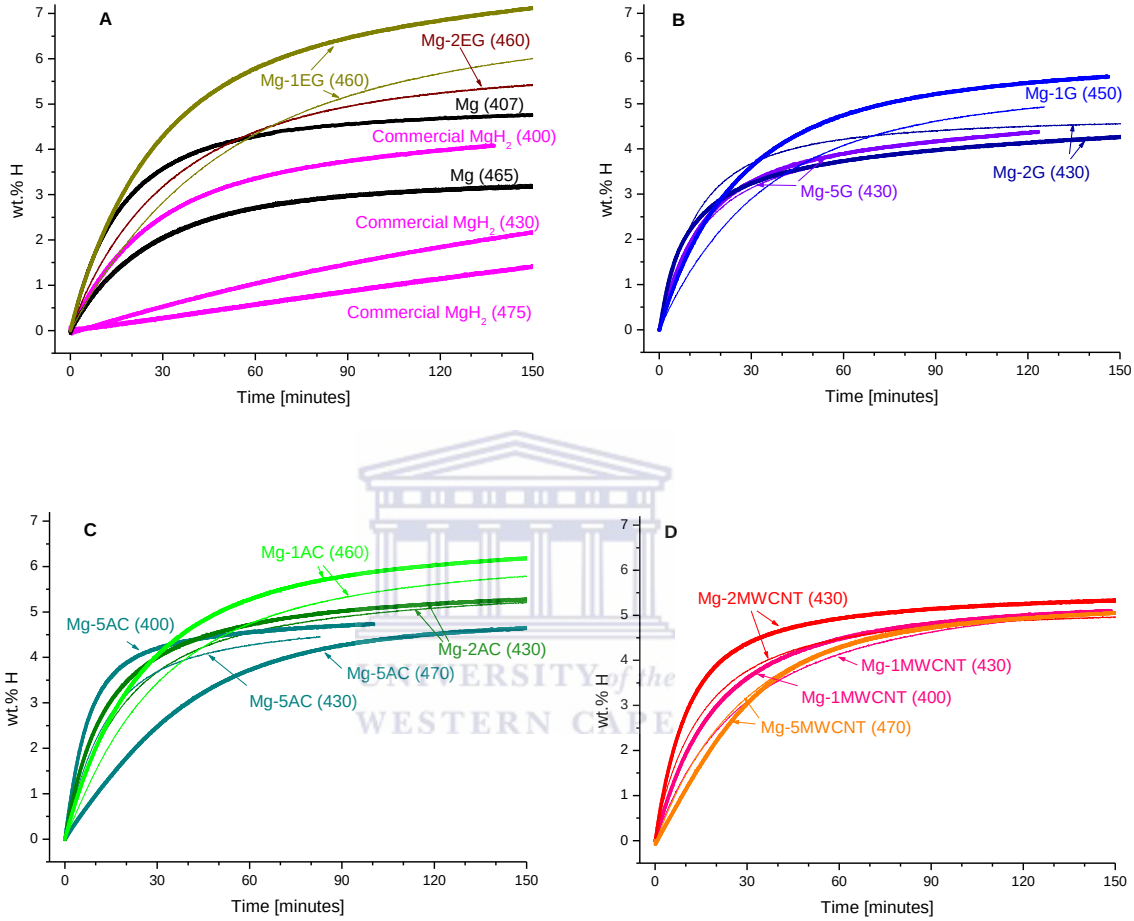

Figure 4-10: **Kinetics of re-hydrogenation at 250°C and 15 bar H_2 of the samples de-hydrogenated by vacuum heating (maximum temperature is specified in brackets): (A): commercial MgH_2, HRBM Mg and Mg–EG composites; (B): Mg–G; (C): Mg–AC; (D): Mg–MWCNT. Thick lines relate to the first and thin ones – to the second re-hydrogenation**

The kinetics of re-hydrogenation Mg–C composite materials were found to be very similar to those for the as-milled Mg indicating that the addition of carbon has minor (if any) catalytic effect. At the same time, the maximum amount of hydrogen reversibly absorbed and the re-hydrogenation rate were found to be quite sensitive to maximum hydrogen desorption temperature applied prior to re-hydrogenation. The decelerated re-hydrogenation rates were observed when increasing the temperature (as well as for the repeated TDS–rehydrogenation cycles). This is associated with re-crystallization of Mg resulting in increased grain size and the corresponding increase of the length of hydrogen diffusion pathways. This effect was found to be much less pronounced for re-hydrogenated Mg-C nanocomposites where, according to the XRD data (Table 4.2), the increase of MgH_2 crystalline size for the re-hydrogenated materials was 2-4 times lower than for the materials without carbon additives. The observed improvements appear even at low quantities (1 wt.%) of carbon additives, especially, AC, EG and TEG. In all re-hydrogenation kinetics curves, the plots shape presents a continuously decreasing rate of hydriding and almost constant hydrogen content reached. From the obtained kinetics curves, it can be appreciated that the presence of carbon materials substantially improves the re-hydrogenation kinetics of magnesium.

Table 4.4: Fitted re-hydrogenation characteristics of magnesium and magnesium-carbon composites

Sample	Conditions		Fitted kinetic parameters (eqn. 3.2)[(a)]			
	Preceding dehydrogenation temperature [^{o}C]	Cycle #	C_{max} [wt.% H]	t_R [minutes]	n	Pearson correlation coefficient, R^2
Commercial MgH_2	400	2	4.160 ± 0.003	33.70 ± 0.007	0.873 ± 0.001	0.99918
	430	2	4.981 ± 0.002	261 ± 0.001	1.003 ± 0.001	0.99964
	475	1	4.223 ± 0.001	324.2 ± 0.002	1.172 ± 0.001	0.99934
HRBM Mg	465	1	3.405 ± 0.001	35.05 ± 0.005	0.726 ± 0.001	0.99365
	407	2	4.976 ± 0.001	23.47 ± 0.005	0.731 ± 0.002	0.99323
Mg–1G	450	1	5.640 ± 0.002	29.86 ± 0.004	0.882 ± 0.001	0.9995
	450	2	5.101 ± 0.002	36.42 ± 0.003	0.952 ± 0.001	0.9999
Mg-2G	430	1	4.13 ± 0.006	17.71 ± 0.279	1 ± 0.019	0.92895
	430	2	4.769 ± 0.002	34.29 ± 0.403	1 ± 0.0132	0.78393
Mg–5G	460	1	6.067 ± 0.003	24.32 ± 0.002	1.047 ± 0.001	0.99988
	460	2	6.145 ± 0.006	24.66 ± 0.003	0.951 ± 0.001	0.99991

Mg–1MWCNT	400	1	5.092 ± 0.002	24.17 ± 0.004	0.843 ± 0.002	0.99885
	430	2	5.261 ± 0.002	35.78 ± 0.004	0.837 ± 0.001	0.9993
Mg–2MWCNT	430	1	5.585 ± 0.001	17.18 ± 0.005	0.569 ± 0.001	0.97882
	430	2	5.005 ± 0.001	20.01 ± 0.002	0.755 ± 0.001	0.99893
Mg–5MWCNT	470	1	5.375 ± 0.001	38.80 ± 0.007	0.855 ± 0.002	0.98711
	470	2	5.039 ± 0.002	30.11 ± 0.003	0.975 ± 0.001	0.99986
Mg–1AC	460	1	6.436 ± 0.003	31.60 ± 0.005	0.808 ± 0.002	0.99742
	470	2	5.360 ± 0.002	31.18 ± 0.002	0.977 ± 0.001	0.99986
Mg–2AC	430	1	5.402 ± 0.002	20.83 ± 0.003	0.679 ± 0.001	0.99615
	430	2	5.454 ± 0.001	27.96 ± 0.004	0.691 ± 0.001	0.99478
Mg–5AC	400	1	4.189 ± 0.004	8.16 ± 0.002	0.941 ± 0.002	0.99935
	430	2	3.878 ± 0.004	12.95 ± 0.002	0.973 ± 0.001	0.99995
	470	1	4.417 ± 0.005	37.01 ± 0.004	1.096 ± 0.001	0.99995
Mg–1EG	450	1	6.141 ± 0.002	27.43 ± 0.001	0.940 ± 0.001	0.99998
	465	2	5.679 ± 0.002	46.75 ± 0.003	0.982 ± 0.001	0.99996
Mg–2EG	460	1	5.009 ± 0.005	31.64 ± 0.004	0.934 ± 0.001	0.99996
Mg–1TEG	465	1	5.258 ± 0.003	25.23 ± 0.002	0.890 ± 0.001	0.99996

	470	2	4.973 ± 0.001	30.40 ± 0.001	0.932 ± 0.001	0.99996

(a) Assuming incubation period, $t_0 = 0$

Figure 4.11 illustrates the effect of carbon on the cycle stability of the as-milled Mg and Mg–C hybrid materials. A clear decrease of both hydrogenation rate and maximum hydrogen absorption capacity was observed for the as-milled Mg. At the same time, addition of carbon to the Mg–C hybrid materials improves their cycle stability. Indeed, the material containing 5 wt.% of graphite shows a stable reversible hydrogen capacity during ten H_2 desorption – absorption cycles, and high rates of the hydrogenation which increase during the first cycles.

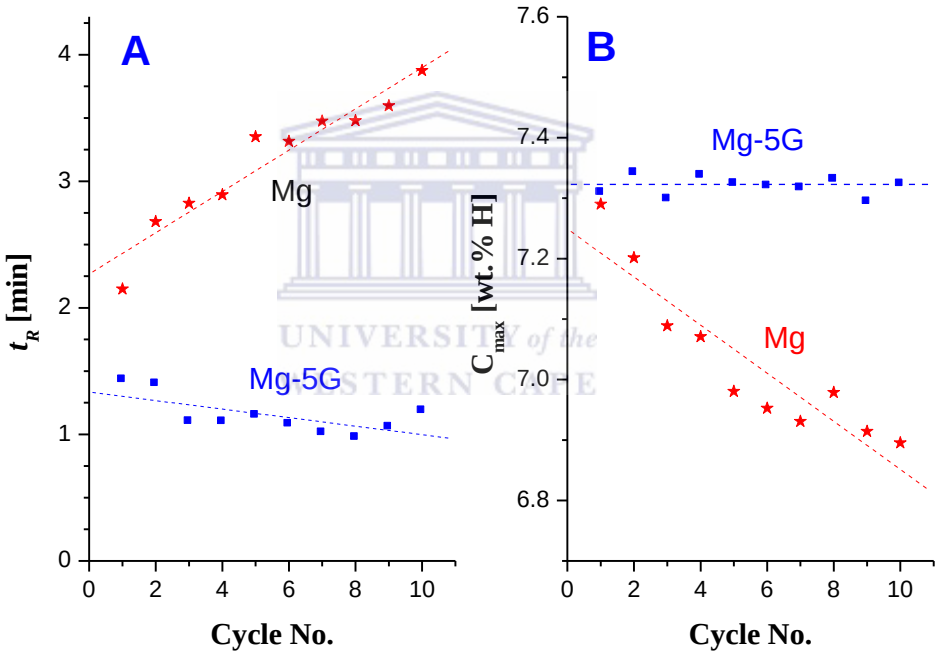

Figure 4-11: Dependencies of characteristic hydrogenation time (reciprocal to rate constant) (A**) and maximum hydrogen concentration (**B**) on a number of desorption-absorption cycles at 350°C for HRBM Mg and Mg–5G hybrid material**

4.1.3.2. De-hydrogenation performance of as-milled and re-hydrogenated samples

The hydrogen desorption properties of as-milled and re-hydrogenated Mg-C nanocomposites were studied by TDS and DSC/TGA measurements, and results obtained are summarized in Table 4.5. Selected DSC and TDS thermograms for as-milled and re-hydrogenated samples at 5°C/min heating rate are presented in Figure 4.12. The DSC decomposition of commercial MgH_2 show an onset decomposition temperature, T_{onset}, at 390°C with a very sharp endothermic peak temperature (T_{max} = 404°C) followed by a gradual decrease of the decomposition rate. The peak temperature for as-milled MgH_2 was lowered by ~ 49°C to that of commercial MgH_2, having an onset temperature and peak temperature at 320°C and 355°C, respectively.

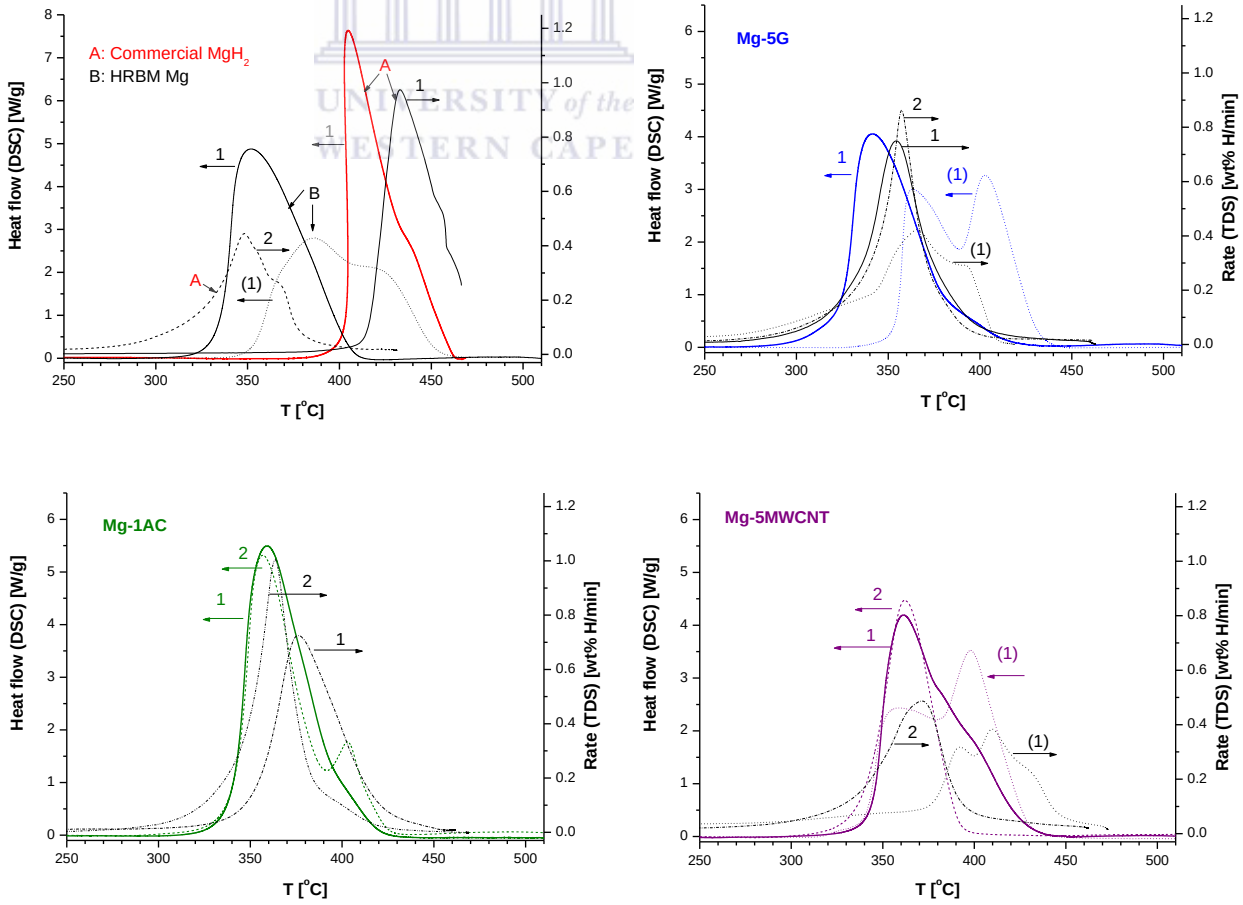

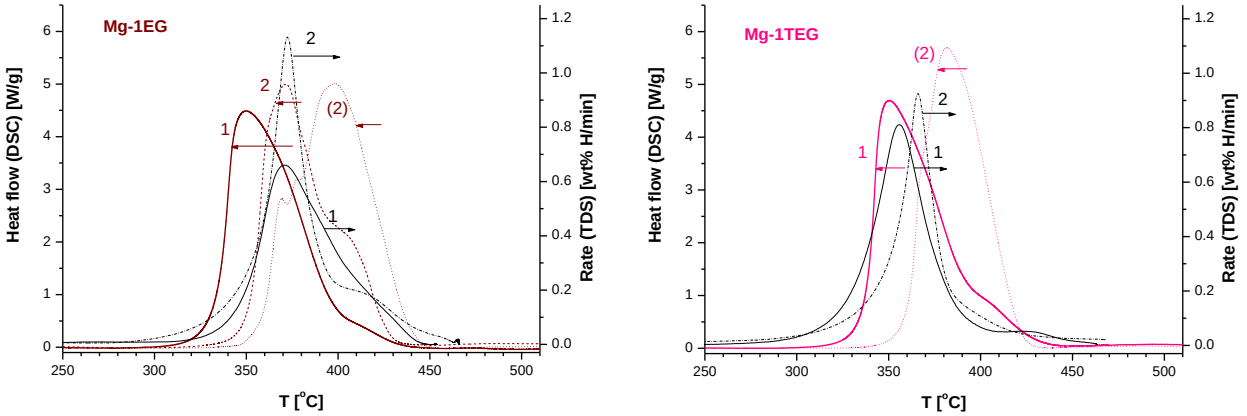

Figure 4-12: Selected DSC and TDS spectra (heating rate 5°C/min) for as milled/as delivered (1) and re-hydrogenated (2) samples. The spectra taken for "contaminated" samples are shown as dot lines, the curve captions are taken in brackets

Since the thermodynamic desorption process of MgH_2 is characterized by high operating temperature, in this regard, carbon additives addition to Mg could lead to considerable improvement on the hydrogen desorption temperature. So, the decomposition properties of as-milled and re-hydrogenated Mg-C composites were also studied similar to undoped Mg and the obtained results summarized in Table 4.5. Selected TDS and DSC thermograms for as-milled and re-hydrogenated samples are shown in Figure 4.12. From the obtained DSC results, it can be seen that the T_{onset} and T_{max} of as-milled Mg-C samples are shifted to lower temperatures with the incorporation of carbon additives than those of MgH_2, respectively. T_{onset} varies between 290-320°C and T_{max} 340-380°C, and completed in T = 415-450°C depending on the carbon types used. Re-hydrogenated Mg-C samples shows their decomposition peaks to be shifted slightly towards higher temperatures after hydrogen cycling but still lower than that of commercial MgH_2. The increase in decomposition temperature after cycling, also reported in [177, 243], seems to

be associated with its structural changes during cycling and recrystallization of the material.

TDS and DSC behaviours appear to be quite similar, with gas evolution peaks for TDS shifted towards higher temperatures to those of DSC. The main reason for the difference seems to be in poor heat transfer between the evacuated sample and the reactor body, where the temperature was monitored in the course of TDS studies. This resulted in a lag, in the increase of sample temperature during heating, such as difference further increased during endothermic decomposition of large quantities of hydride sample whose weight was ~4 times higher than for the samples used in DSC analysis.

Another important feature was the very high sensitivity of the DSC (for the as-milled samples) and TDS traces to the samples pre-history of storage. Samples stored more than one month in a glove box or several seconds air exposure during analysis show an increase onset temperature and peak temperature, as well as the appearance of several peaks in the decomposition traces (see corresponding plots in Figure 4.12 labelled as "contaminated", dotted lines). This shows high affinity of the as-milled Mg-C composite materials includes high pyrophoricity and easy oxidation leading to the observed MgO phase in the XRD study. Similar findings are reported in [177, 235, 236], with hydrogen kinetics deteriorating as an oxide layer is allowed to grow at the surface of MgH_2 particles. Although hydrogen could strongly absorb at defective oxide sites and dissociate, such a heterolytic dissociation would most likely result in the formation of surface hydroxyls that would be reduced or removed upon heating [237, 238].

So in the current studies, when "contaminated'' samples were subjected dehydrogenation (TDS) measurements, similar dehydrogenation and re-hydrogenation performance to

those of pure (freshly ball milled samples that were studies after preparation) samples were observed. The re-hydrogenated samples were found to be more sensitive to oxidation as compared to the as-milled materials, as observed in the XRD studies showing an increase in MgO phase abundance.

Table 4.5: Summary of DSC/TGA characteristics of commercial MgH_2, HRBM Mg, and as-milled Mg-C hybrid materials

Sample	Decomposition temperature range [°C]	T_{max} [°C]	Gravimetric capacity [%]	Dehydrogenation heat effect [kJ/mol H_2] ($\Delta_D H$)	Dehydrogenation activation energy [kJ/mol H_2] (E_A)
Commercial MgH_2	390–470	404	6.96	78.5	188
Mg (as milled)	320–415	355	7.15	71.6	105
Mg (re-hydrogenated)	332–458	365	5.54	76.6	133
Mg-1G (as-milled)	358-460	(384), 418	6.22	76.6	
Mg-2G (as-milled)	345-450	(385), 414	6.26	73.9	170
Mg–5G (as milled)	280–430	341	6.97	61.6	113
Mg–5G (re-hydrogenated)	283–400	347	6.51	73.9	115
Mg-1MWCNT (as-milled)	320-455	(383), 406	5.45	73.1	134
Mg-2MWCNT (as-milled)	320-454	384	6.34	80.1	Not measured
Mg–5MWCNT (as milled)	300–455	361	6.99	65.5	128
Mg–5MWCNT (re-hydrogenated)	290–422	348	4.90	74.1	128
Mg–1AC (as milled)	310–435	359	7.30	70.7	133
Mg–1AC (re-hydrogenated)	295–440	(357), 404	6.64	74.2	125
Mg-2AC (as-milled)	325-466	(388), 416	6.57	80.87	Not measured

Mg–5AC (as milled)	315–460	364	7.76	74.8	77
Mg–5AC (re-hydrogenated)	290–422	360	6.35	73.8	142
Mg–1EG (as milled)	302–450	351	7.06	70.0	94
Mg–1EG (re-hydrogenated)	320–455	371, (400)	6.27	81.7	147
Mg–2EG (as milled)	380-470	390	6.27	70.7	Not measured
Mg-2EG (re-hydrogenated)	380–470	390	4.66	70.7	Not measured
Mg–1TEG (as milled)	300–445	351	6.74	73.7	119
Mg–1TEG (re-hydrogenated)	331–445	382	6.64	79.0	124

The heat required for hydrogen desorption ($\Delta_D H$) from the formed composite samples was determined by the differential scan calometry (DSC). The heat effect of commercial MgH_2 (78.5 kJ/mol H_2) was observed to be close to enthalpy formation of MgH_2 (-74.7 kJ/mol H_2 [224]). The observed dehydrogenation heat effects of as-milled Mg-C composites samples are lower than that of commercial MgH_2 with the exception of Mg-2AC having higher dehydrogenation heat effect. The lowest dehydrogenation heat effect was observed for Mg-5G having 61.6 kJ/mol H_2. An average value of 70 ± 0.004 kJ/mol H_2 for as-milled Mg-C composites samples that is 7% lower than the reference value was obtained. Whilst the re-hydrogenated Mg-C composites samples show an increase in the observed dehydrogenation heat effect but still lower than the reference value. The dehydrogenation heat effects of as-milled and re-hydrogenated Mg-5AC composite were very similar. Higher values to that of reference value were observed for re-hydrogenated Mg-1EG and Mg-1TEG. An average value of dehydrogenation heat effects (77 ± 0.003 kJ/mol H_2) for re-hydrogenated samples was obtained compared to the corresponding reference data. The decrease of dehydrogenation heat effect in as-milled samples can be explained by the presence of less stable γ-MgH_2 during HRBM and smaller crystalline size. In the re-hydrogenated samples, the γ-MgH_2 phase was not observed and the samples showed an increase crystalline size.

4.1.2.3. Determination of activation energy of dehydrogenation (E_A)

In order to understand the H-sorption kinetics arising upon doping with different carbon types, quantitative estimation of kinetics barrier was carried out by the determination of the apparent activation energy (E_A) by the Kissinger method (equation 3.3). In all the obtained results, the endothermic peaks (T_{max}) corresponding to maximum rate of

dehydrogenation are shifted to higher temperatures as the heating rate (Φ) is increased. From the obtained T_{max} at different heating rate (Φ), the Kissinger plot, i.e. $\ln[\Phi/T_{max}^2]$ vs $(1/T_{max})$ was used to obtain the E_A for the different Mg-nanocomposites and results obtained summarized in Table 4.1.5 with selected plots shown in Fig.4.1.13. From the obtained results, all Mg-C composite show an increase dehydrogenation kinetics (reduced E_A), in the range of 95-140 (± 0.003-0.015) kJ/mole H_2 for both as-milled and re-hydrogenated Mg-C composites samples compared to commercial MgH_2 with E_A 188 ± 0.009 kJ/mol H_2 corresponding well to the data presented by Danaie *et.al*. [222]. The increase dehydrogenation kinetics for the as-milled composites is associated with a change in the rate-limiting step. The re-hydrogenated Mg-C composite samples show an reduced dehydrogenation kinetics (increase in E_A) approaching that of as-milled MgH_2, the increase E_A was ascribed to the catalytic effect of carbon additives that may be lost during repeated TDS/re/hydrogenation study.

Unfortunately, we don't have sufficient information regarding the absorption activation energy to make a significant comparison of hydrogenation versus dehydrogenation behavior.

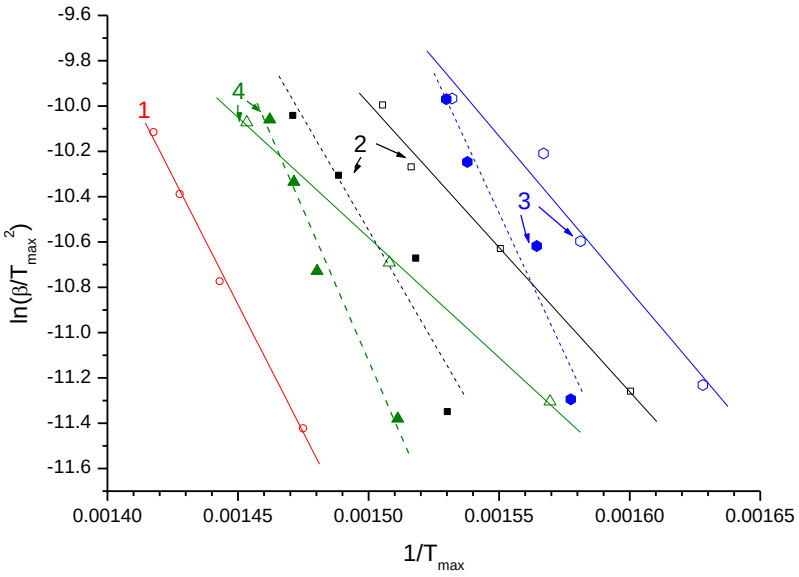

Figure 4-13: Kissinger plots for commercial MgH_2 (1) and as milled HRBM Mg (2), Mg–5G (3) and Mg–5AC (4). The data for "contaminated" samples are shown as filled symbols and dashed lines

The E_A values for "contaminated" samples were found to be overestimated approaching 180–220 kJ/mole H_2. However, for the composites containing MWCNT, this tendency was found to be less pronounced, especially when the amount of the carbon additive added was increased from 1 to 5 wt.%. In addition, the Mg–MWCNT composites showed noticeable weight increase (up to 0.6 wt.%) at T > 200°C in the course of TGA/DSC studies performed at lower flow rate of argon (20 mL/min). The observed results allows us to suppose that MWCNT acts as a "scavenger" of trace amounts of impurities (O_2 and H_2O) which presumably interact with more reactive carbon atoms forming the end caps. In turn, this protects the surface of MgH_2 from the interaction with the impurities. Such a protection also results in the smaller deviations of DSC curves taken for the "pure" and "contaminated" as milled samples (see section 4.1.3.2).

The gravimetric capacity of as-milled and re-hydrogenated samples were studied by TGA and obtained results summarized in Table 4.5. From the obtained results, all the as-milled samples desorbed around 6.2 wt.% H and the re-hydrogenated samples show lowering in the amount of hydrogen that is desorbed. The observed lowering in hydrogen desorbed amount is ascribed to microstructural change in the material when subjected to repeated TDS/re-hydrogenation measurement and this can be seen in the XRD and SEM/TEM results (see section 4.1.2.2)

4.1.4. DISCUSSION

This study clearly shows that HRBM is an efficient way to prepare Mg–C composite materials with significantly improved hydrogenation-dehydrogenation performance as compared to magnesium alone.

At the beginning of the ball milling, the soft Mg particles are subjected to a severe plastic deformation (see Figure 4.1.7A). It results in heating the material up and, finally, the local temperature becomes high enough for the beginning of the hydrogenation process. Because the hydrogenation of Mg is rate-limited by a slow H-diffusion in the formed MgH_2, this process is quite slow, limited by the removal of MgH_2 from the surface of the "forged" Mg particles during the ball milling leading to the formation of a "fresh" surface of the unreacted Mg. Introduction of graphite as a "soft" carbon material has a "lubricating" effect that results in (i) lowering of the heating rates and, (ii) covering of the Mg particles with carbon layers limiting or preventing H_2 supply to the surface of Mg. As a result, no hydrogenation is observed throughout incubation period. In contrast, "harder" carbon additives, like AC, cause "scratching" and milling of Mg particles

leading to their further disintegration during the HRBM that results in a significant shortening or disappearance of the incubation period.

At the same time, ball milling results in disintegration of the original structure of carbon additives to produce graphene type sheets containing sp^2 hybridized carbon atoms. Indeed, carbon materials studied in present work are built of graphene sheets, which either are rolled into co-axial nanometer-size cylinders (MWCNT), or stacked on the top of each other yielding graphite (G), or graphite-like (TEG, EG) structures. Similarly, AC is formed by curved layers containing pentagons and other non-hexagonal rings in addition to hexagons [232], which can be considered as related to the deformed graphene layers. Graphene layers easily form during the mechanical delamination of graphite [175] and during destruction of the mostly resistant to the milling tubular structures of the MWCNT requiring 2 hours of milling at 370–510 rpm [239] to start their fracturing. Delamination of expanded graphite containing graphene planes with much increased interlayer distances, is much easier. This takes place in case the side processes of folding and generation of defects do not dominate (as discussed in section 4.1 above, the latter process contributes at higher contents of EG and TEG).

Consequently, after the HRBM, all the Mg–C hybrid materials, where C = G, EG, TEG, MWCNT or AC, contain nanostructured magnesium/magnesium hydride with crystallite sizes of 7–10 nm and with hydride nanoparticles separated by the graphene layers. The graphene layers play a double role in influencing hydrogen absorption and desorption: (i) they prevent growth of the Mg particles during the high temperature cycling, thus assisting in improving cycle resistance of the materials; (ii) they provide an interface for the diffusion of the atomic hydrogen to reach Mg/MgH_2. Thus, when the initial carbon

structures disintegrate to produce graphene nano-sheets, the Mg–C hybrid materials prepared by HRBM start to show a superior hydrogenation performance even at a minor carbon content of 1 wt.%[3].

All the carbon species studied in this work are related to sp^2 hybridization of the carbon atoms and built of graphene sheets, either rolled into nanometer-size cylinders (MWCNT), or stacked into graphite-like structures (others). A feature of the graphene "blocks" is in the presence of 2D electron system (formed by π electrons) in the proximity to their "surface" [241]. Presence of the 2D-distributed negative charge creates favourable conditions for spill-over of monatomic hydrogen carrying an effective positive charge. Such observation has been earlier reported during the studies of the hydrogen spill-over effect [242]. A possibility for the improvements of hydrogen sorption performances of the Mg–C materials via an H spill-over mechanism was also pointed out by Wu *et.al*. [242].

Taking into account the easiness of the formation of few- and even mono-layer graphene which can occur even in the course of mechanical peeling off *c*-axis-oriented graphite [243], we can assume that similar processes take place during HRBM of Mg–C composites, where C = G, EG, TEG, or AC. As a result, the formed graphene-like flakes attach to the surface of magnesium and facilitate penetration of H atoms thereto. Presumably, the H atoms are formed by H_2 dissociation on the surface of iron nanoparticles produced during ball milling, and further transported via spill-over mechanism. Similar processes take place for MWCNT, but in this case the formation of

[3] The threshold of graphene concentration in polymer-based composite materials, where sharp changes in electric conductivity take place, is as low as 0.1 vol. %. [240]. Thus, even minor amount of graphene present in a composite or hybrid material may strongly modify electronic properties and affect the hydrogenation / dehydrogenation performances of Mg–C.

the graphene flakes is replaced by uniform distribution of the nanotubes along the surface of Mg/MgH_2 particles.

The presented hypothesis can explain the observed incubation period of the hydrogenation during HRBM for the composites containing graphite whose "peeling" is more difficult as compared to highly dispersed (AC), or exfoliated (TEG) graphite-like carbon species which show superior hydrogenation characteristics during HRBM even at minor, 1 wt.% concentrations. Similar hydrogenation performances were observed for the composites containing MWCNT but at the higher, 5 wt.%, concentrations. This can be explained by a lower contact area of the rolled graphene "surface" in the proximity to Mg/MgH_2 particles than for the planar one and, therefore, bigger amount of MWCNT is necessary to provide similar improvements of the hydrogenation.

By such a way, the surface of the MgH_2 particles is covered by the thin stacked graphene layer that prevents the particles from sintering and preserves fast re-hydrogenation kinetics even at rather high (up to 460°C) dehydrogenation temperatures. At the same time, the graphene flakes were shown to have very high affinity to oxygen-containing species like SiO_2 [253] or H_2O [240]. Thus formation during the milling of graphene-based layers makes the HRBM Mg–C hybrid materials quite sensitive to the surface oxidation, which results in; (i) their high pyrophoricity, (ii) formation of MgO, and (iii) significant variation of the hydrogen thermal desorption behaviour after exposure to the gases, containing even trace amounts of oxygen and water vapours. Less sensitivity of Mg–MWCNT composites (where the planar graphene flakes are presumably not formed) to the surface "contamination" additionally confirms our hypothesis.

4.2. Magnesium-based nanocomposites with the addition of PGM

Reported studies have illustrated the role of Pd catalyst in enhancing the hydrogenation kinetics of Mg in thin film. Palladium has high hydrogen diffusivity and solubility and for these reasons, it has been considered a promising catalyst in the magnesium based alloys. Reactive mechanical milling technique has been demonstrated to be an effective way to obtain nanostructured Mg-based alloys, and also to enhance the formation of hydrides.

However, to our knowledge there are no reports on the study of *in situ* pressure-temperature monitoring during HRBM of Mg with Pd under hydrogen atmosphere. The work carried out for this study aims to contribute to the study of HRBM Mg with reduced palladium metal that have not previously been milled with Mg, as well as characterizing these materials with the aim of gaining further insight into the materials.

4.2.1. Hydrogenation behaviour during HRBM of Mg with Palladium black

The hydrogenation performances of magnesium and palladium black (crystalline or amorphous phase) during HRBM under hydrogen atmosphere are summarized in Table 4.6. Figure 4.14 shows the hydrogen absorption curves for Mg with amorphous Pd and crystalline Pd catalysts. The hydrogenation kinetics curves of Mg with amorphous Pd (Figure 4.14(A)) show sluggish hydriding rate and took > 4 hour to reach a constant hydrogen capacity. Improved hydrogenation rate was observed when crystalline Pd was used. It is seen that Mg with crystalline Pd (Figure 4.14(B)) absorbed ≥ 6.42 wt.%H in ≤ 1 hour. The absorption rate of Mg-1Pd sample was observed to be much faster than all other prepared samples and reaches its maximum capacity in ~ 48 minutes. The samples

of Mg with crystalline Pd showed much improved hydrogenation rate than that of undoped Mg, which attained its maximum hydrogen capacity in >1 hour of HRBM. Significant enhancement of hydrogenation rate was observed upon addition of minor (1wt.%) amount of AC with 5wt.% crystalline Pd black. The observed improvement can be ascribed to the carbon material aggregating along the grain boundary of Mg decreasing the diffusion path length for hydride formation, in so doing, it leads to the observed fast hydrogenation rate. The co-presence of AC and crystalline Pd is postulated to have a synergistic effect on the hydrogen properties, e.g. increase the capacity of Mg-1AC-5Pd without reducing the hydrogenation rate.

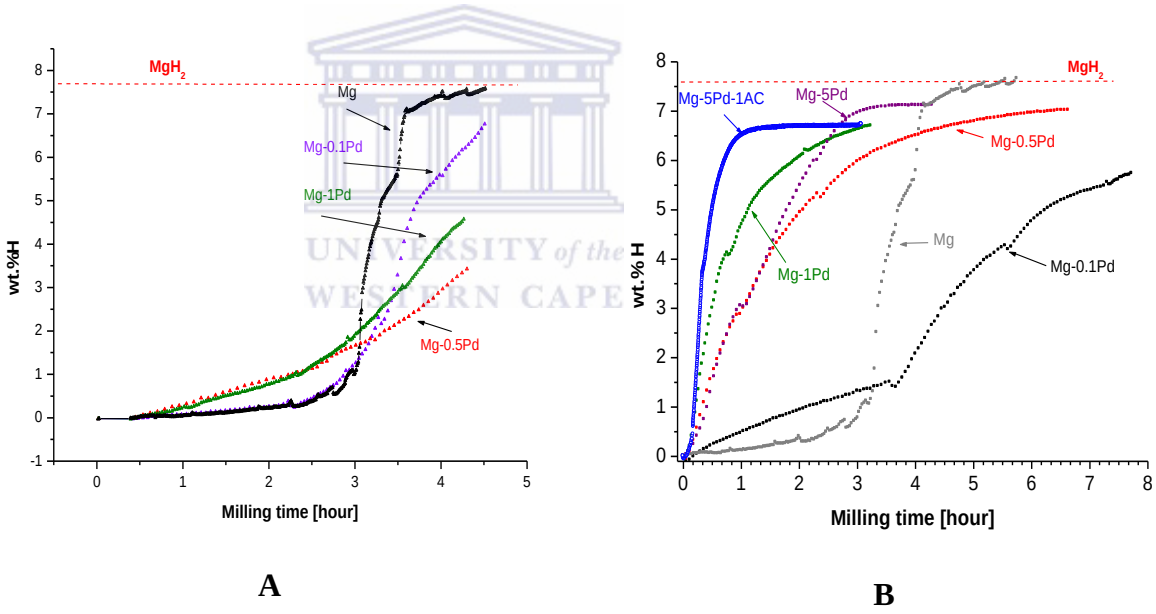

Figure 4-14: Hydrogen absorption during HRBM of magnesium and different quantities of Pd black under hydrogen atmosphere: (A**) amorphous Pd black, (**B**) crystalline Pd black**

Table 4.6: Hydrogenation characteristics of Magnesium and Magnesium–Palladium during HRBM (for Figure 4-14)

Sample	Maximum H capacity [wt.% H]	Fitted kinetic parameters (eq. 3.2)			
		t_O [h]	t_R [h]	n	Pearson correlation coefficient, R^2
Mg	7.69 ± 0.001	0.14 ± 0.112	2.89 ± 0.005	4	0.99706
Mg-0.1Pd[a]	6.42 ± 0.107	0.10 ± 0.158	5.36 ±0.121	2.38 ± 0.120	0.98229
Mg-0.5Pd[a]	7.10 ± 0.016	0.10 ± 0.139	1.07 ± 0.014	1.63 ± 0.030	0.99204
Mg–1Pd[a]	6.66 ± 0.025	0.10 ± 0.006	0.802 ± 0.008	1 ± 0.017	0.99332
Mg-5 Pd[a]	7.59 ± 0.041	0.10 ± 0.020	1.47 ± 0.018	1.47 ± 0.035	0.99216
Mg-0.5 Pd[b]	5.61 ± 0.659	0.10 ± 0.133	4.54 ± 0.294	2.14 ± 0.172	0.98192
Mg-1Pd[b]	7.18 ± 0.367	0.10 ± 0.135	4.20 ± 0.076	2.91 ± 0.179	0.9927
Mg-1AC-5Pd[a]	6.69 ± 0.002	0.16 ± 0.007	0.25 ± 0.009	1.02 ± 0.005	0.99899

[a]Palladium black (reduced with $N_2H_4.H_2O$).

[b]Palladium black (reduced with NaH_2PO_2).

4.2.2. Morphological and phase characterization of Mg-Pd composite materials

4.2.2.1. XRD

Noticeable changes of phase-structural characteristics of Mg-Pd nanocomposites were observed for the samples containing the maximum studied amount of the crystalline Pd black, 5 wt.%. The refined XRD patterns of the as-milled and re-hydrogenated Mg-5Pd are presented in Figure 4.15 (A, B), respectively. The refinement results are presented in Table 4.7.

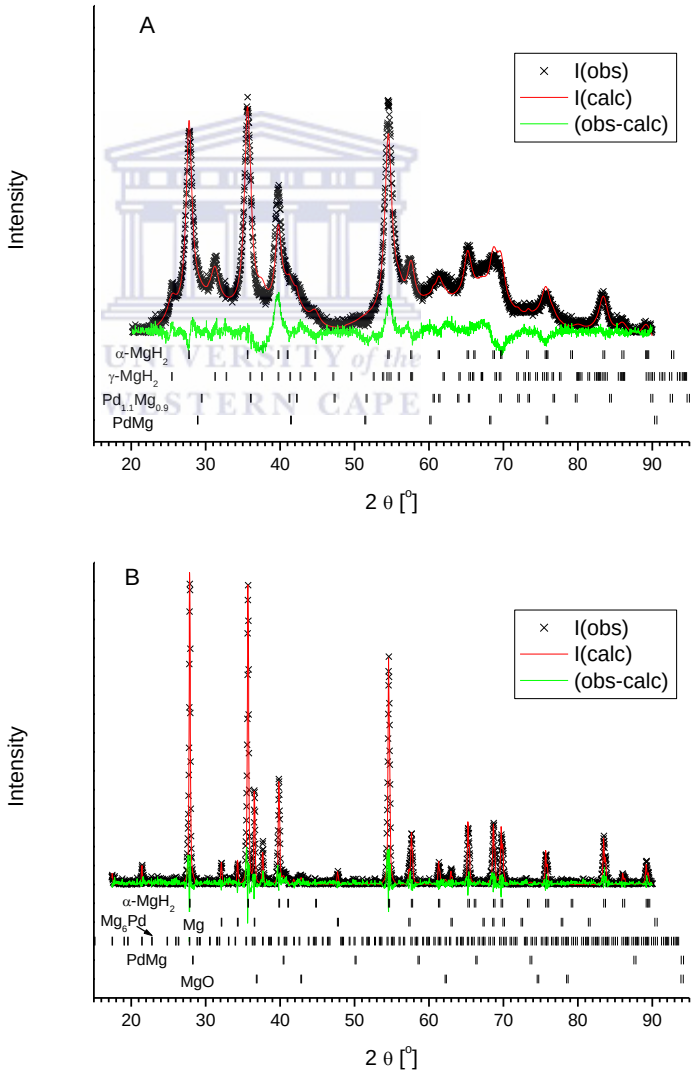

Figure 4-15: XRD patterns of as-milled (A) and re-hydrogenated (B) samples Mg – 5 wt.% of crystalline Pd black

Table 4.7: Phase-structural characteristics of the samples Mg – 5 wt.% of crystalline Pd black

Phase	Sample							
	As milled				Re-hydrogenated			
	Abundance [wt.%]	Unit cell parameters [Å]	Crystallite size, D_V [nm]	Microstrain, *e* [%]	Abundance [wt.%]	Unit cell parameters [Å]	Crystallite size, D_V [nm]	Microstrain, *e* [%]
α-MgH_2	69.7	*a*=4.514(1) *c*=3.0162(7)	11	0.3	76.5	*a*=4.5122(3) *c*=3.0177(3)	95	0
γ-MgH_2	23.4(5)	*a*=4.512(6) *b*=5.436(8) *c*=4.965(6)	7	0	–	–	–	–
Mg	–	–	–	–	16.6(5)	*a*=3.2078(5) *c*=5.213(1)	128	0
$Mg_{0.9}Pd_{0.1}$	0.27(5)	*a*=3.014(4) *c*=4.36(1)	84	0.5	–	–	–	–
MgPd	6.5(2)	*a*=3.068(2)	4	3.3	0.52(6)	*a*=3.146(2)	33	0.1

Mg_6Pd	–	–	–	–	4.3(2)	*a*=20.203(4)	172	0.1
MgO	–	–	–	–	2.0(2)	*a*=4.214(2)	38	0

Similarly to the individual Mg and Mg-C nanocomposites (Figure 4.15(A, B)), the pattern of the as-milled sample exhibits broad peaks of α- and γ-modifications of MgH_2 having phase abundances 69.7 and 23.4 wt.%, respectively, and crystallite size 7 to 11 nm. Palladium and palladium hydride were not observed in the pattern. Instead, a noticeable amount of MgPd intermetallide (CsCl-type, space group # 221) characterised by very small (4 nm) crystallite size and significant microstrain (~3%) was detected. The observed lattice period of this phase was about 1.6% lower than the value of *a*=3.12 Å reported in the literature [244]. In addition, there was detected trace amount of $Mg_{0.9}Pd_{1.1}$ intermetallide (AuCu-type, space group # 123) with quite large crystallites (84 nm). The observed lattice periods were in a satisfactory correspondence with the literature data [245]: *a*=3.03 Å, *c*=3.42 Å.

The re-hydrogenated sample contained a major phase of α-MgH_2, abundance 76.5 wt.% and crystallite size about 100 nm. A significant amount (16.6 wt.%) of non-hydrogenated Mg, crystallite size about 130 nm, was observed as well. The main impurity phase was Mg-rich Mg_6Pd intermetallide (space group # 216; lattice period reported in the literature [246] a=20.108 Å) with crystallite size about 170 nm. MgPd was also observed in the re-hydrogenated sample, but in the lower amount than in the as-milled one. This observed lattice period corresponded well to the literature data [244].

Finally, the XRD pattern of the re-hydrogenated sample exhibits a presence of MgO formed due to oxidation of the sample.

Our observations allow us to conclude that mechanical alloying of magnesium with palladium takes place already on the stage of HRBM. Most probably, this process starts

from the formation of $Mg_{0.9}Pd_{1.1}$, the most stable intermetallide in Mg–Pd system [247], on the surface of Pd particles. During the milling followed by dehydrogenation/re-hydrogenation, due to diffusion of Mg, this phase is enriched with Mg to form MgPd and, further, Mg_6Pd. Similar results were obtained by Pasquini *et al* [248] who observed the formation of MgPd, Mg_5Pd_2 and Mg_3Pd in the course of PVD of Pd onto Mg nanoparticles.

4.2.2.2. Morphology

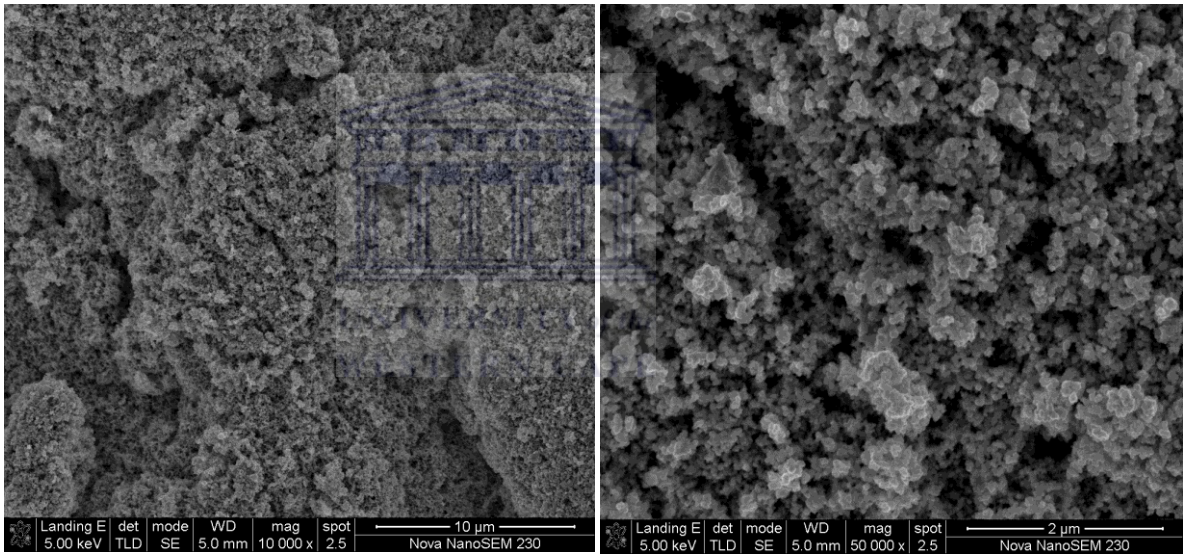

A

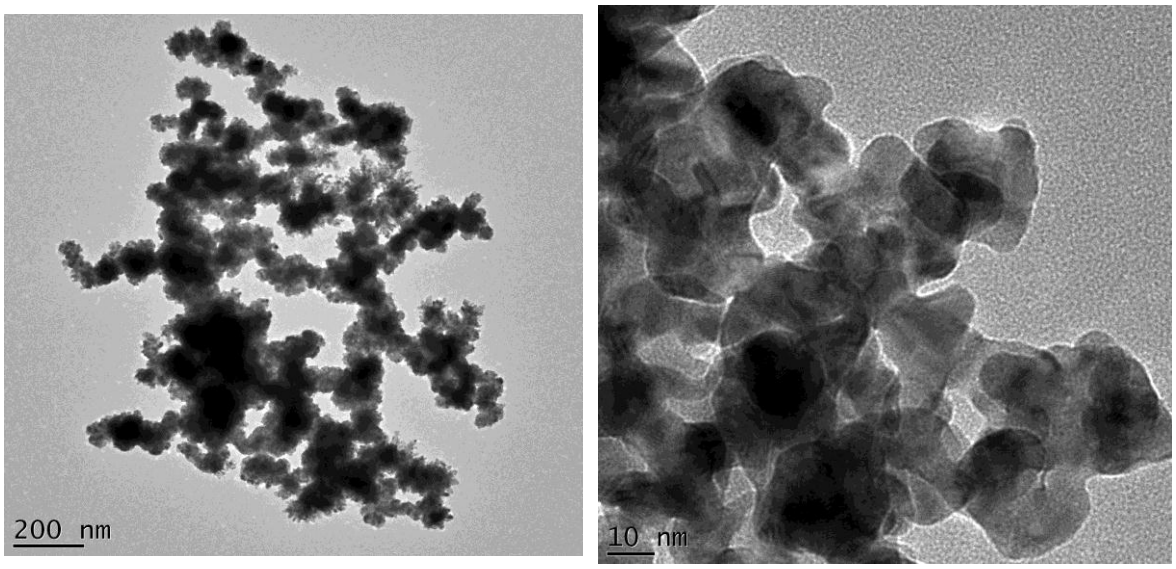

B **C**

Figure 4-16: Micrographs of crystalline Pd (reduced with $N_2H_4.H_2O$): (A**) SEM , (**B-C**) TEM**

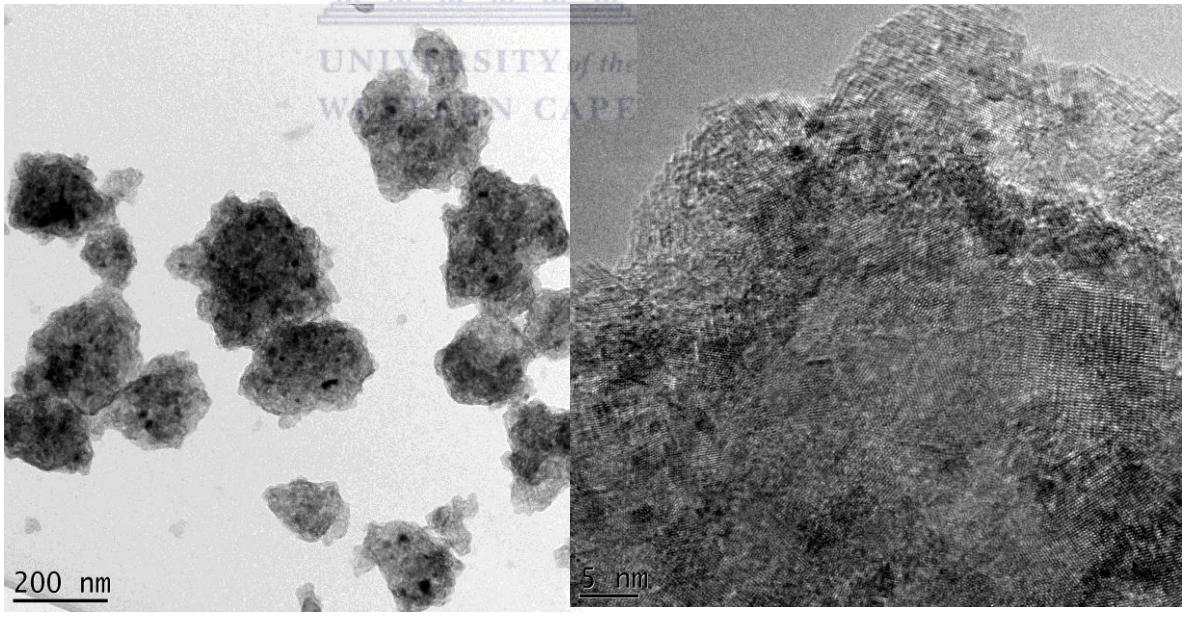

A **B**

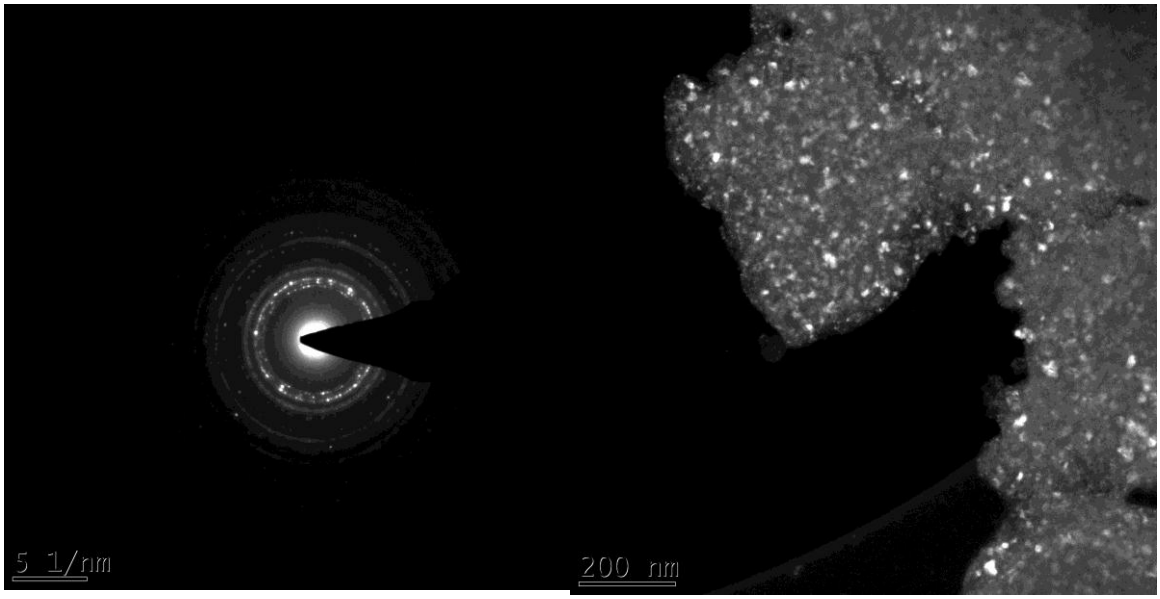

C **D**

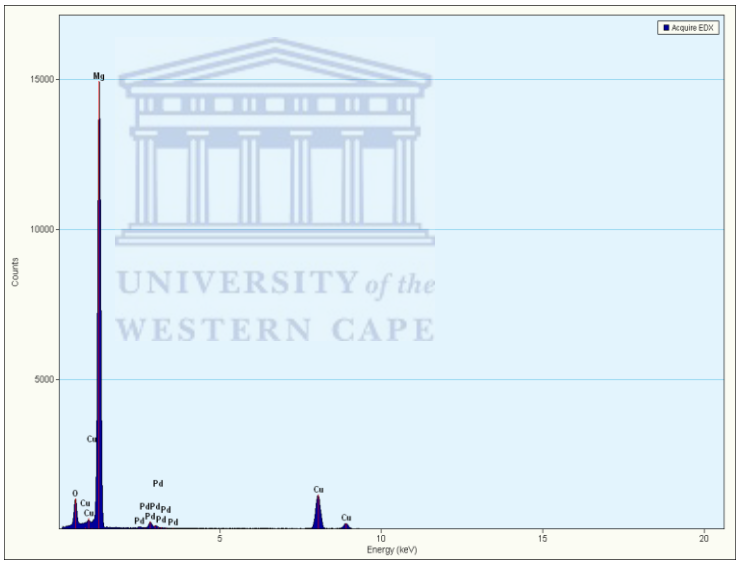

E

Figure 4-17: TEM micrographs of as-milled Mg with crystalline 5wt.% Pd: (A**) Bright-field, (**B**) High-magnification, (**C**) Selected area diffraction, (**D**) dark-field, (**E**) EDX**

The SEM and TEM micrographs of crystalline Pd obtained by reducing $PdCl_2.xH_2O$ with $N_2H_4.2H_2O$ are shown in Figure 4.16. From the obtained micrograph, small spherical

particles that are of nanometre in size were obtained. Average particle sizes of 331 nm were measured by Zeiter Sizer instrument. The obtained particles were HRBM with magnesium under hydrogen atmosphere and the materials obtained imaged as shown in Figure 4.17. The TEM bright-field micrograph shows cluster of clearly-like particle that have some black spot in the matrix. The agglomerates are made up of small particles that are of polycrystalline nano-size. Figure 4.17(B) shows the high magnification twinning area of the particle indicating that nanosize materials were formed by HRBM as was shown in XRD. The SAD shows a solid discontinuous ring pattern and the dark-field was performed to identify the crystallites. From the dark-field micrograph in Figure 4.17(D), it can be noted that nano-crystals were formed by HRBM and palladium-containing particles are homogeneously distributed over the Mg/MgH_2 particle surface. High-energy reactive ball milling leads to either a complete coating of the surface of individual particles, or homogeneous but discontinuous distribution on the surface which allows the additives to act as hydrogen dissociation catalysts. Additionally, the coating of Mg with Pd catalyst could protect the surface from oxidation which can be considered to be an advantage for practical applications. The composition of Mg-Pd was measured by TEM-EDX and the spectrum shown in Figure 4.17(E). From the EDX spectrum, three elements i.e., magnesium, palladium and oxygen were observed. The presence of oxygen indicates that traces amount of magnesium may have reacted to form magnesium oxide (also confirmed by XRD) during sample preparation.

4.2.3. Hydrogen sorption properties of Mg-based composites containing Pd black

4.2.3.1. Hydrogen absorption studies

The re-hydrogenation properties of Mg with crystalline Pd black samples after *in situ* dehydrogenation in the course of TDS studies are summarized in Table 4.8. Figure 4.18 shows the re-hydrogenation curves for Mg-Pd samples and as a reference, pure magnesium is also included. For pure magnesium show hydrogen re-absorption curve that reach constant hydrogen capacity in ~35 minutes. In the case of Mg-Pd composites, the maximum amount of hydrogen that was re-absorbed and the re-hydrogenation rates were very sensitive to the maximum desorption temperature applied prior to re-hydrogenation. An increase in re-hydrogenation rate was noted when desorption temperature was increased. In all the composites, the re-hydriding kinetics curves present a continuously decreasing rate of hydriding and almost constant hydrogen reached.

The composite of Mg-2Pd shows improved re-hydrogenation rates with higher hydrogen capacity than Mg. Adding less or more than 2wt.% Pd reduces the hydriding rates with the resultant composite showing lower hydrogen capacity than Mg. The current re-hydrogenation results are much improved that those observed in [249] for cold rolled and/or ball milled Mg with Palladium foil that reached their full capacity in 1500 minutes, the latter also presented an incubation period of more than 500 minutes. In another study, palladium deposited on magnesium surface by wet chemical process was able to absorbs 2.13 wt.%H in 45 minutes at 300°C [250].

From the obtained re-hydrogenation kinetics curves, the presence of crystalline Pd improves the hydrogenation kinetics. In all the obtained composites, > 4.15 wt.% H was re-absorbed. All the composites gave a similar sigmoidal absorption curves showing that nucleation and growth processes take place during re-absorption. The *Avraami* exponent

(*n*) obtained by fitting the hydrogen absorption kinetics curves for the HRBM composites are summarized in Table 4.8 and they are in the range n = 1-2.9

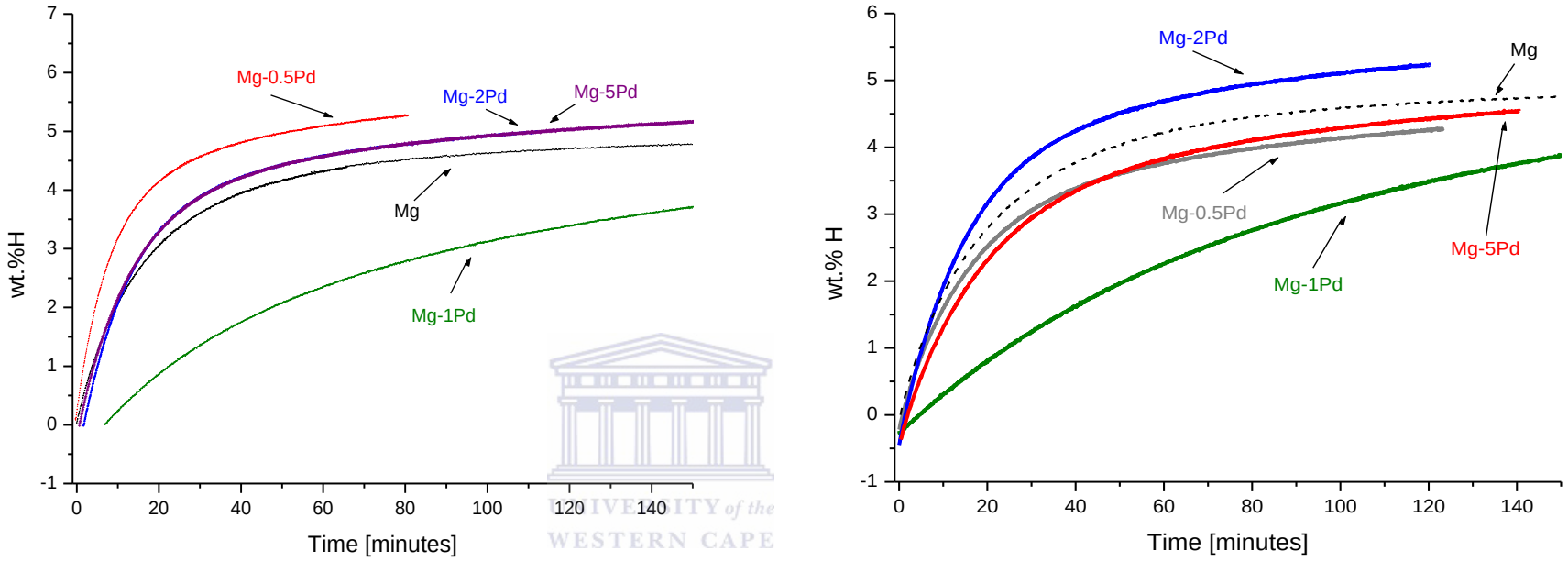

A **B**

Figure 4-18: Re-hydrogenation curves of Mg with crystalline Palladium black at 250°C under ~15 bar H_2 atmosphere; (A) first re-hydrogenation measurement, (B) second re-hydrogenation measurement

Table 4.8: Fitted re-hydrogenation characteristics of the Mg-*x*Pd black composites

Sample	Conditions		Fitted kinetic parameters (eqn. 3.2)			
	Preceding dehydrogenation temperature [^{o}C]	Cycle #	C_{max} [wt.% H]	t_R [minutes]	n	Pearson correlation coefficient, R^2
HRBM Mg	407	2	4.97 ± 0.001	23.47 ± 0.005	0.731 ± 0.002	0.99323
	465	1	3.41 ± 0.001	35.05 ± 0.005	0.726 ± 0.001	0.99365
Mg-0.5Pd[a]	470	1	5.13 ± 0.009	11.23 ± 0.138	1 ± 0.016	0.98119
	463	2	4.15 ± 0.005	22.58 ± 0.123	1 ± 0.008	0.99403
Mg-1Pd[a]	410	1	5.24 ± 0.002	112.53 ± 0.528	1 ± 0.006	0.96865
	410	2	5.56 ± 0.002	113.49 ± 0.466	1 ± 0.005	0.97534
Mg-2Pd[a]	452	1	4.88 ± 0.006	16.63 ± 0.139	1 ± 0.106	0.99055
	474	2	5.11 ± 0.053	21.11 ± 0.109	1 ± 0.007	0.99516
Mg-5Pd[a]	468	1	5.56 ± 0.005	22.58 ± 0.395	1 ± 0.020	0.85469
	467	2	4.45 ± 0.005	27.74 ± 0.134	1 ± 0.007	0.99491

[a]Palladium black (reduced with $N_2H_4.H_2O$).

4.2.3.2. Thermal hydrogen desorption behaviour of as-milled and re-hydrogenated Mg-Pd composites

Hydrogen thermal desorption properties of the prepared Mg-Pd composites under study are summarized in Table 4.9 and representative thermogram shown in Figure 4.19. Shift in the peak maximum to lower temperatures was noted upon repeated TDS/re-hydrogenation cycling measurement. The presence of Pd catalyst on the surface of formed hydride may help in the recombination process of H-atoms into hydrogen molecules leading to lower desorption peak temperature than that of undoped Mg. Factors that contribute to lowering in desorption peak temperature, such as crystalline size, microstrain and the presence of Pd catalyst were considered in [251, 252].

In the present study, the catalytic effect of Pd was retained in all cycling studies as was observed by Tang *et.al*. [253] for Mg nanoblades coated with Pd. Also, Pd and Mg can form alloys in the interface region at a temperature as low as 50°C [254, 255]. This conclusion corresponds well to our XRD observations (Table 4.7) according to which the formation of Mg–Pd intermetallides was observed already during HRBM. Once the Pd has been fully alloyed, it could eliminate or minimize its catalytic effect resulting in the increase of the dehydrogenation temperature. According to our results, the catalytic effect, though quite modest, still remains, as the composites presented a single desorption peak at lower temperature than the peak for HRBM Mg (Figure 4.19).

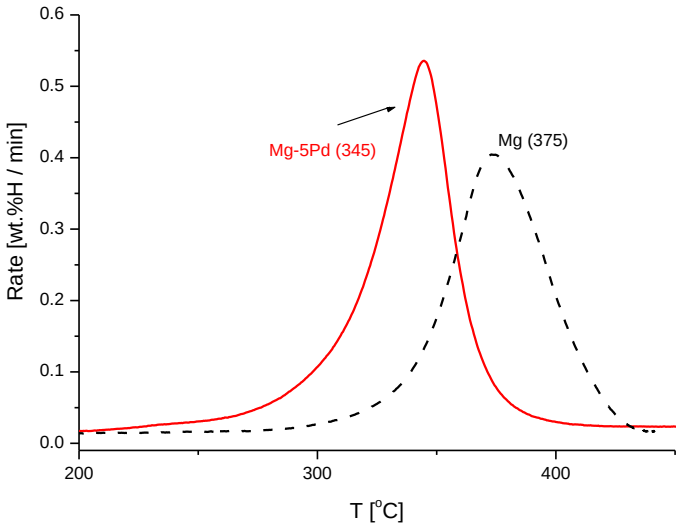

Figure 4-19: Selected TDS spectra (heating rate of 5°C/min under vacuum) for re-hydrogenated Mg and Mg-5Pd

Table 4.9: **Hydrogen thermodesorption properties of Mg-*x*Pd measured in a Sievert–type apparatus heated from RT to ~ 460°C at 5°C/min under vacuum.(#1 for as-milled, #2 re-hydrogenated)**

Composites	Cycle #	Decomposition temperature range [°C]	Peak desorption Temperature [T_{max}]
Mg	1	340-380	364
	2	325-402	375
Mg-0.5Pd	1	320-418	363
	2	260-402	350
Mg-1Pd	1	366-405	384
	2	320-406	377
Mg-2Pd	1	328-443	370
	2	260-392	341
Mg-5Pd	1	304-407	356
	2	248-396	345

4.2.4. DISCUSSION

According to the results of this study, the addition of Pd black to Mg improved its hydrogenation performances during HRBM only for crystalline Pd obtained using N_2H_4 as a reduced agent. The improvements are much more pronounced when adding activated carbon together with Pd (section 4.2.1). The obtained nanocomposites are characterised by a modest improvement of their dehydrogenation and re-hydrogenation as compared to HRBM Mg. The reason for that seems to be in quite high "metallurgical affinity" of Mg and Pd forming a wide spectrum of intermetallic compounds. Hydrogenation of Mg–Pd intermetallides is quite difficult, so far it was reported only about formation of α-solid solution $Pd_3MgH_{0.7}$ [256] and ternary hydride $PdMg_2H$ [257]. It is logical to suppose that the formation of Mg–Pd intermetallides observed in the course of the XRD studies (section 4.2.1) results in the lowering of the catalytic activity of initial Pd particles thus exhibiting the minor effect (if any) for the improvement of hydrogen sorption performances of the Mg-based nanocomposites.

4.3. Magnesium-based nanocomposites containing BCC-V and ZrNi

4.3.1. Mg–C–BCC-V

In the present chapter, BCC alloy of the type $V_{75}Ti_{10}Zr_{7.5}Cr_{7.5}$ was chosen because of its good hydrogen sorption kinetics and hydrogen storage capacity [258]. The body centred cubic (BCC) alloy structure has a non-closest packed lattice. Its packing efficiency is low compared with face centred cubic (FCC) and hexagonal close packing (*hcp*) lattice and the octahedral sites and tetrahedral sites per atom in BCC lattice are much more than those in FCC and *hcp* lattice, which means more interstitial sites for hydrogen occupancy are available for hydrogen storage in BCC structure materials. Yu *et.al*. [259] reported use of hydrogenated BCC-V alloy milled with MgH_2, obtained results show that: hydrogenated BCC-V alloy lowers the thermodesorption peak of the composite in TGA.

Also, BCC-V alloy and different carbon types materials (AC, G, MWCNT, EG) were HRBM with elemental Mg powder under hydrogen atmosphere in order to improve its H-sorption behaviour and microstructure. During ball milling, the catalytic phases, i.e. BCC-V alloy ($V_{75}Ti_{10}Zr_{7.5}Cr_{7.5}$), can be distributed uniformly on the surface of Mg particles due to cold welding and shearing. By providing the diffusion passageway for hydrogen atoms and degrading the dissociation energy of hydrogen molecules breaking into atoms, $V_{75}Ti_{10}Zr_{7.5}Cr_{7.5}$ can accelerate the hydriding process of magnesium particles. In addition, ball milling is a non-equilibrium process that can create a specific state on the surface of the materials. A large surface-to-volume ratio and a significant amount of defects and imperfections can enhance the accessibility of a material for hydrogen penetration. As a result, the addition of BCC-V alloy and the mechanical force upgrade the diffusion capacity of hydrogen atoms which is regarded as the key step for the

hydriding process of milled Mg. The co-presence of carbon materials with BCC-V alloy can improve the H-sorption properties of MgH_2 with the carbon materials aggregating along the grain boundaries of Mg making easy access of hydrogen diffusion to the interstitials that would not be accessible by the BCC-V alloy alone.

4.3.1.1. Hydrogenation behaviour during HRBM of Mg with carbon and BCC-V alloy additives

Figure 4.20 shows the hydriding curves for Mg with carbon types and BCC-V alloys additives during HRBM under hydrogen atmosphere and the results summarized in Table 4.10. From the obtained hydrogenation curves, the transformation of Mg → MgH_2 is significantly enhanced with the formed hydrides reaching a constant hydrogen capacity in <1.5 hour. This facilitation has been achieved as a result of small particle/grain size formed during HRBM, thus decreasing a diffusion path length for hydrogen in the material and achieving a synergy in hydrogenation of BCC-V alloy and Mg. The hydrogen uptake by BCC-V alloy is characterized by fast rate of transformation to BCC-V_{1-x} at mild pressure-temperature conditions, thus promoting fast hydrogen exchange between H_2 molecules in the gaseous phase and H-atoms accommodated by solid. In turn, this results in the formation of non-equilibrium, excited species [260], thus explaining the catalytic effect of BCC-V alloy on the hydrogenation of Mg. In addition, fast hydrogenation of the catalytic BCC-V alloy additive is accompanied by a significant heat release which heats Mg/Mg alloy to reach the temperature when the hydrogenation rate becomes high enough [157] compared to undoped Mg.

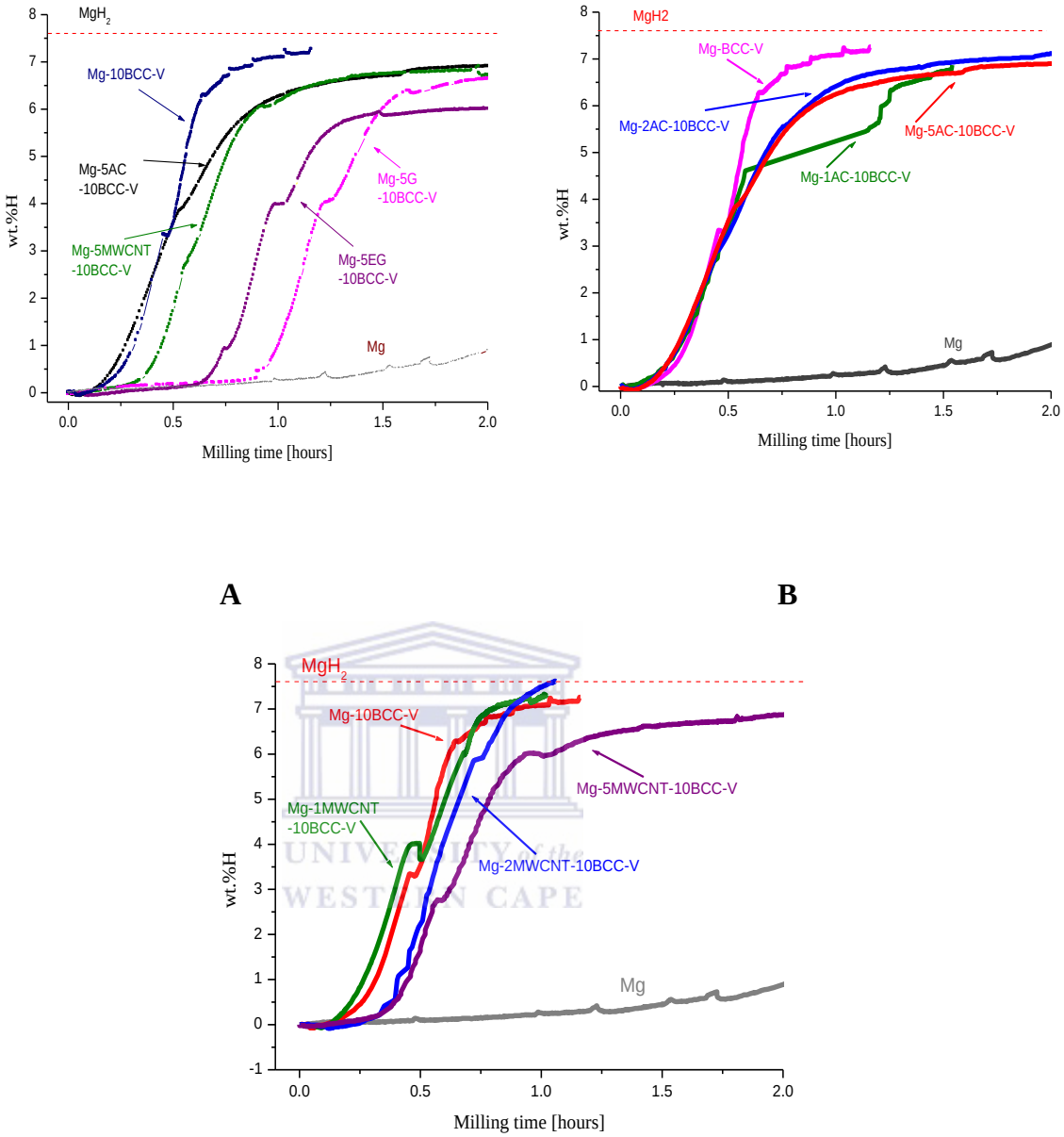

Figure 4-20: HRBM behaviour of Mg and Mg–C-BCC materials: (A**) hydrogenation during HRBM of magnesium-based materials containing 5 wt % of carbon additives and 10 wt.% BCC-V alloy, (**B**) HRBM of magnesium-based materials containing 1, 2, 5 wt.% activated carbon and 10 wt.% BCC-V alloy and (**C**) HRBM of magnesium-based materials containing 1, 2, 5 wt.% MWCNT and 10 wt.% BCC-V alloy**

Introduction of carbon results in the appearance of incubation period followed by a continuous increasing rate of hydriding until a constant hydrogen capacity is reached. The appearance of incubation period was also dependent on the kind of the carbon additive (AC < MWCNT < EG < G). Slight deterioration of hydrogenation kinetics with increase quantity of carbon was noted, except for the AC containing composites that presented much faster hydrogenation rates with all the quantities of AC introduced. In all the obtained hydrogenation curves, it is quite clear that transformation of $Mg \rightarrow MgH_2$ during ball milling is effective and this is evidence in their XRD results. The improved hydrogenation properties of Mg-C-BCC-V composites are ascribed to the presence of micro/nano-size BCC-V particles on the surface layers of the composites. These micro/nano-sized BCC-V particles not only result in greatly enhanced hydrogen atomic diffusivities in the nano-crystals relative to their conventional coarse grain counterparts, but also promotes the dissociation and recombination of hydrogen which may improve the kinetics properties of MgH_2 [259]. Therefore, the main catalytic effect of BCC-V alloy could be dissociation of hydrogen molecules at lower temperature and improve the first step of the hydrogenation mechanism. Furthermore, the co-presences of carbon material during ball milling enhanced the hydrogen storage capacity by aggregating along the grain boundaries of Mg particles and making it easy for hydrogen atoms diffusion to the centres of grain that may not be reachable for hydrogen atoms. Trial run experiments for composites having BCC alloy that was surface modified did not result in improved hydrogenation rates, with the observed results showing an increased incubation period. The presence of an incubation period, most probably at the beginning of HRBM part of the mechanical energy, is spent to destroy the original graphitic structure and to produce

graphene nano-sheets. These processes consume mechanical energy that in turn, reduces the amount of mechanical energy supplied to the particles of magnesium during HRBM. In all the obtained composites, hydrogen capacity of ≥ 6.02 wt.%H were achieved.

Table 4.10: Hydrogenation characteristics of Magnesium and Magnesium–Carbon-BCC-V materials during HRBM

Sample	Maximum H capacity [wt.% H]		Fitted kinetic parameters (eq. 3.2)			
	Theoretical	Experimental	t_O [h]	t_R [h]	n	Pearson correlation coefficient, R^2
Mg	7.66	7.69 ± 0.001	0.14 ± 0.112	2.89 ± 0.005	4.28 ± 0.003	0.99706
Mg–10BCC-V	7.27	7.07 ± 0.018	0.16 ± 0.020	0.36 ± 0.021	2.67 ± 0.003	0.99551
Mg-1MWCNT-10BCC-V	7.21	7.26 ± 0.023	0.15 ± 0.015	0.391 ± 0.016	2.18 ± 0.110	0.98650
Mg-2MWCNT-10BCC-V	7.15	7.89 ± 0.032	0.303 ± 0.006	0.363 ± 0.006	1.67 ± 0.042	0.99961
Mg–5MWCNT–10BCC-V	6.98	7.12 ± 0.001	0.355 ± 0.006	0.394 ±0.004	3.45 ± 0.003	0.99247
Mg-1AC-10BCC-V	7.20	6.87	Not fitted			
Mg-2AC-10BCC-V	7.15	7.07 ± 0.007	0.143 ± 0.005	0.476 ± 0.005	1.48 ± 0.021	0.99891
Mg-5AC–10BCC-V	6.98	6.84 ± 0.006	0.158 ± 0.0033	0.442 ± 0.004	1.37 ± 0.015	0.9992
Mg-5EG-10BCC-V	6.98	6.08 ± 0.006	0.633 ± 0.006	0.369 ± 0.007	1.62 ± 0.037	0.99824
Mg–5G–10BCC-V	6.97	6.81 ± 0.006	0.356 ± 0.006	0.917 ± 0.005	1.30 ± 0.003	0.99808
Mg–5G–10BCC-SM	6.98	6.82 ± 0.005	0.418 ± 0.012	0.925 ± 0.011	2.16 ± 0.072	0.99853

** – BCC-V: $V_{75}Ti_{10}Zr_{7.5}Cr_{7.5}$

*** – BCC-SM: $V_{75}Ti_{10}Zr_{7.5}Cr_{7.5}$ surface modified (F – APTES – Pd).

4.3.1.2. Morphological and phase characterization of MgH_2 and Mg-C-BCC-V composite materials

4.3.1.2.1. XRD

Phase structures for the as-milled and re-hydrogenated composites were established with XRD measurements and their data summarized in Table 4.11, and selected diffractograms are shown in Figure 4.21 and Figure 4.22. Figure 4.21(A) shows as-milled diffraction pattern of Mg-BCC-V sample. The obtained pattern presents broad peaks due to refinement of grains (crystalline) size, increase defects and/or accumulation of lattice strains that are introduced by HRBM. The sample contains α-MgH_2 as the main phase and also shows the presence of peaks belonging to γ-MgH_2 and VH_2. The metastable γ-MgH_2 phases is due to alteration of microstructure by HRBM and it is well reported in ball milled Mg-based samples [261] and in high pressure experiments of MgH_2 [226]. The traces of the hydrogenated BCC-V alloy (VH_2) were also reported in [196]. In the course of HRBM, the hydrogenated BCC-V retained its phase stability, and its catalytic role in the hydrogenation course of Mg was proved by the absence of phase formation between Mg and BCC-V. A contributions of MgO by air contamination during material handling or X-ray measurements cannot be ruled out even if all manual operations are done in noble gas such as helium or argon, the formation of MgO was still observed [262]. The observed MgO peaks results from the high reactivity of small traces of unreacted Mg when exposed to air or moisture. The presence of MgO was especially pronounced in re-hydrogenated samples.

The patterns for as-milled Mg-5G-10BCC-V composite is shown on Figure 4.21(B). The pattern is similar to one for the Mg-10BCC-V (Figure 4.21(A)).

The peaks for re-hydrogenated samples (Figure 4.22) are more intense and sharper than those of as-milled samples. The observed peaks change is attributed to elimination of microstress and grain growth as a result of dehydrogenation-rehydrogenation cycling at high temperature. The metastable γ-MgH_2 phase relaxes completely to α-phase upon dehydrogenation-rehydrogenation cycling at high temperature in agreement with the studies in [266]. Trace amounts of Mg peaks show that not all Mg was hydrided and this was also observed in the re-hydrogenation studies with the samples showing lowering in the amount of hydrogen re-absorbed upon repeated cycling. The amount of poorly-crystalline MgO is quite significant showing that the Mg-BCC-V-(C) composites are very sensitive to the oxidation. This explains their low reversible hydrogen storage capacity observed in the course of dehydrogenation / re-hydrogenation experiments (Section 4.3.1.3)

The estimated crystalline sizes for as-milled and re-hydrogenated Mg composites are shown in Table 4.11. The crystalline size for magnesium hydrides in as-millled composites is 9 to 14 nm corresponding well to the results reported in [267]. Re-hydrogenated Mg-BCC-V composites exhibits increase of the crystalline size of MgH_2 to ~60 nm. Smaller crystalline growth was observed for all the Mg-C-BCC composites (size about 40 nm).

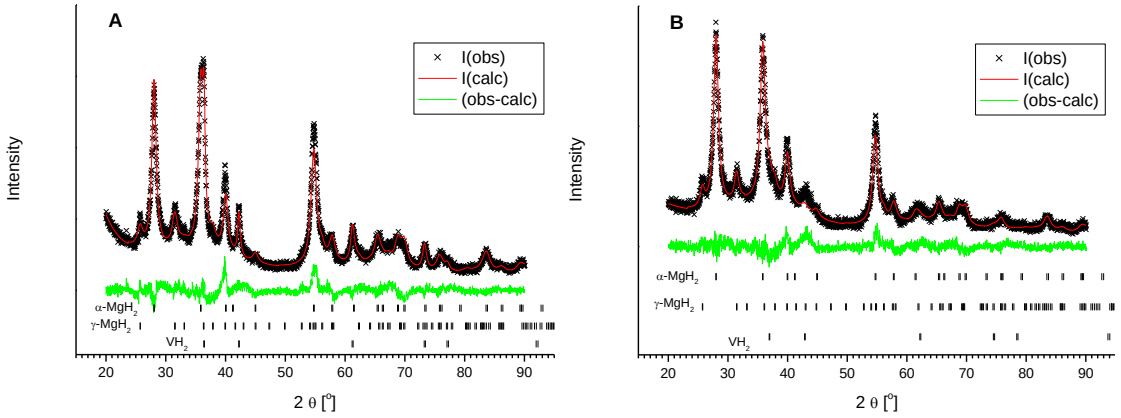

Figure 4-21. XRD pattern for as-milled composites: Mg-10BCC-V (A), Mg-5G-10BCC-V (B).

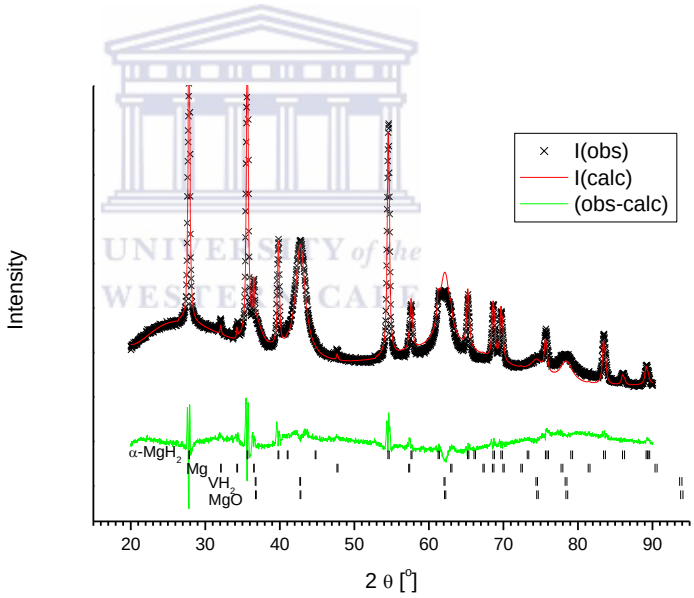

Figure 4-22. XRD pattern for re-hydrogenated Mg-5G-10BCC-V.

Table 4.11:Crystallographic data for the as-milled Mg-BCC-V and Mg-C-BCC-V composite samples.

Sample	Phase	Abundance wt.%	Lattice periods [Å]			Estimated crystalline size [nm]
			a	***b***	***c***	
Mg-BCC-V (as-milled)	α-MgH_2	67.6(-)	4.516(1)	–	3.0222(7)	14
	γ-MgH_2	19.9(4)	4.527(5)	5.432(7)	4.958(6)	9
	(VH_2)	8.5(1)	4.2883(8)	–	–	28
Mg-BCC-V(re-hydrogenated)	α-MgH_2	28.7(-)	4.5132(3)	–	3.0172(2)	60
	Mg	22.8(2)	3.2094(2)	–	5.2103(5)	59
	(VH_2)	1.5(2)	4.384(7)	–	–	13
	(V_2H)	4.1(2)	6.12(2)	–	6.41(3)	7
	MgO	42.9(4)	4.232(1)	–	–	6
Mg-5G-10BCC-V (as-milled)	α-MgH_2	78.8(-)	4.521(1)	–	3.0226(9)	10
	γ-MgH_2	15.2(4)	4.530(7)	5.419(9)	4.992(8)	11
	(VH_2)	6.1(3)	4.226(4)	–	–	6
Mg-5G-10BCC-V (re-hydrogenated)	α-MgH_2	41.2(-)	4.5120(4)	–	3.0179(3)	41
	Mg	2.0(1)	3.207(1)	–	5.212(4)	101
	(VH_2)	6.0(3)	4.22(-)	–	–	4
	MgO	50.8(3)	4.215(1)	–	–	7

BCC-V: $V_{75}Ti_{10}Zr_{7.5}Cr_{7.5}$

4.3.1.2.2. Morphology

The selected SEM micrographs of as-milled and re-hydrogenated samples are shown in Figure 4.23. The as-milled micrographs of the Mg-C-BCC-V samples show several small particles lying on larger particles (squared flat formation) that have cluster/agglomerated from smaller particles. The reduction in particle size is obvious for as-milled samples in comparison to re-hydrogenated samples. HRBM of elemental magnesium with additives, BCC and carbon type creates active nucleation sites and small particles size materials that shorten the diffusion path length for hydrogen atoms and formation of clean surfaces. This was observed during HRBM studies showing fast hydrogenation rate and the presence of BCC and carbon species acting as active nucleation sites.

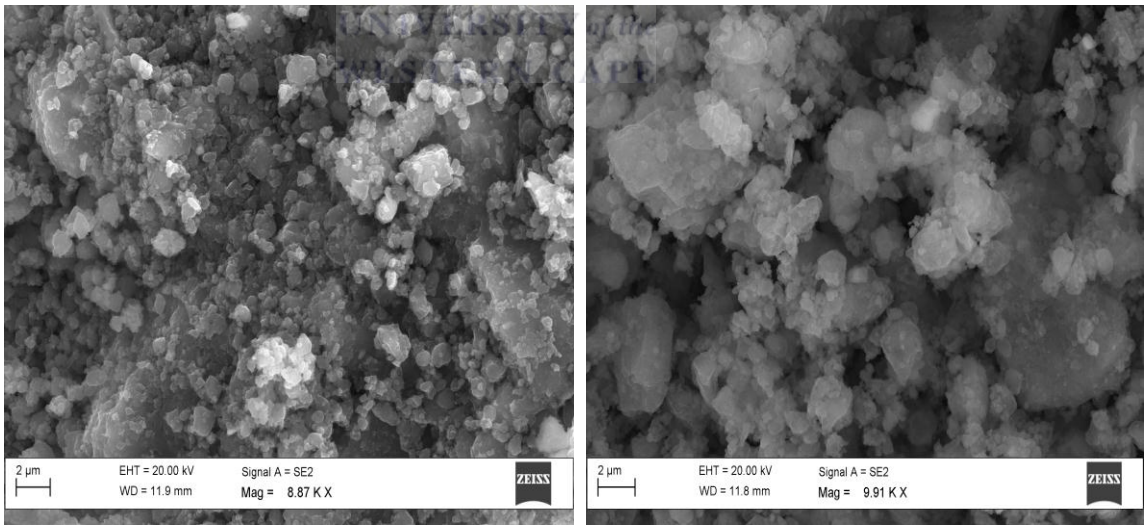

A **B**

Figure 4-23: SEM micrographs of Mg-5MWCNT-10BCC-V: (A**) as-milled and (**B**) re-hydrogenated**

An increase in particles size upon dehydrogenation-rehydrogenation cycling was noted. The size changes are due to the consequence of two opposite processes: fracture due to volume changes induced by hydriding and sintering. When the materials are in the dehydrogenated state, the particles agglomerate due to sintering processes. During dehydrogenation-rehydrogenation cycling, the aggregates fracture due to volume changes. However, this fracturing process seems to be more efficient in small agglomerates than in medium or large ones so as to reach equilibrium in the amount of small-size aggregates after cycling. The morphology of the agglomerates could favour this as it seems more difficult to split large aggregates into few medium ones than to separate several small agglomerates from each other. The increase in the particles size was less pronounced for Mg-C-BCC-V composite samples. This is attributed to the presence of carbon materials that inhibit crystalline growth, thus having an influence on their size because it anchors grain boundaries where it allocates as confirmed by TEM results below and in agreement with [171, 232, 268, 269]. The above findings were also confirmed by the XRD results, with the samples subjected to dehydrogenation-rehydrogenation cycling showing an increase in their crystalline size (Table 4.11). From the obtained micrographs it is evident that the alloy was homogenously distributed in the MgH_2/Mg matrix.

The above SEM findings were complimented by TEM studies as detailed below.

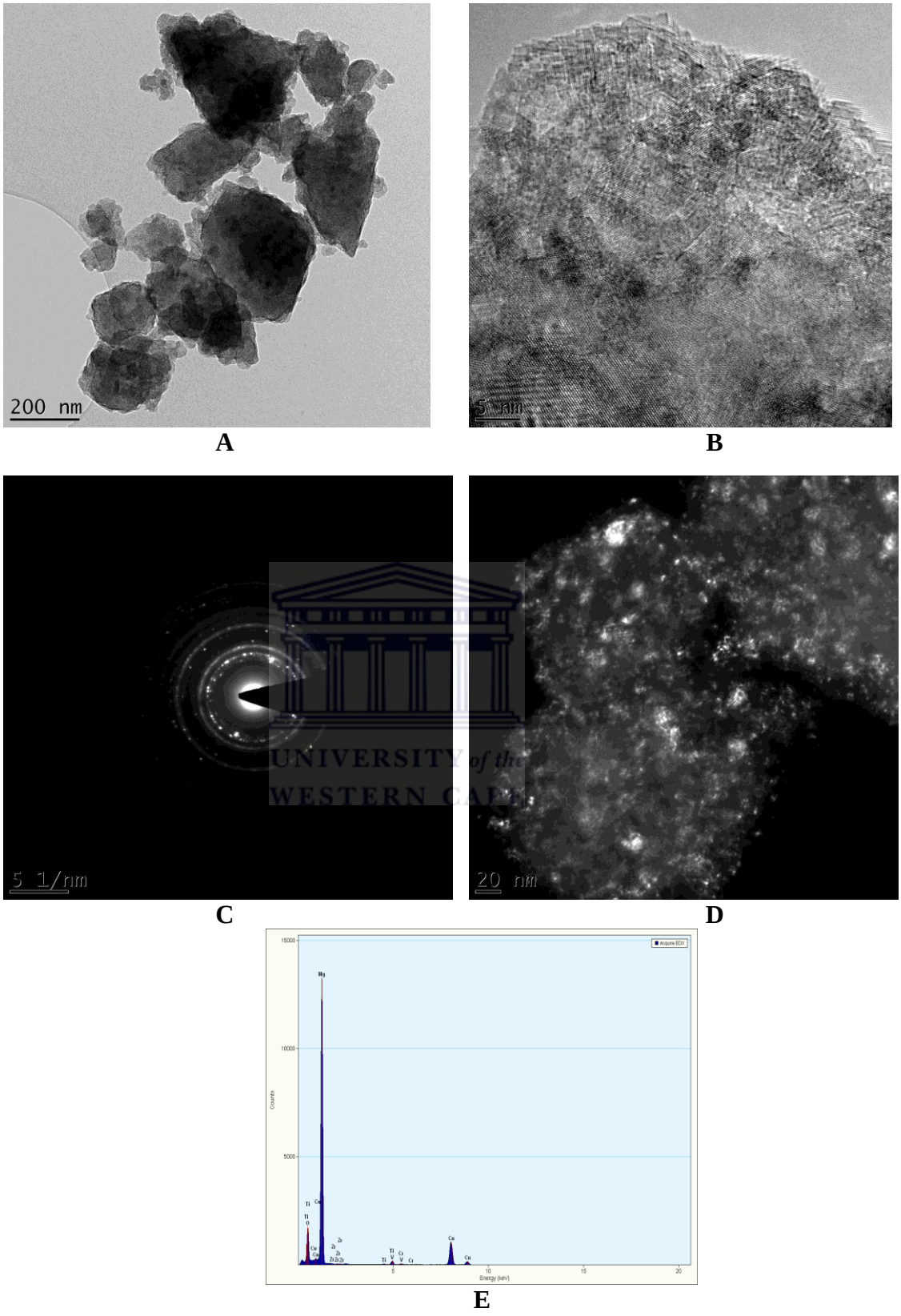

Figure 4-24: TEM micrograph of as-milled Mg-BCC-V: (A**) Bright-field micrograph of Mg-BCC-V, (**B**) High-magnification showing lattice fringes of Mg-BCC-V (**C**)**

selected area diffraction of Mg-10BCC-V, (D**) Dark-field micrograph HRBM of Mg-BCC-V (**E**) EDX of (D)**

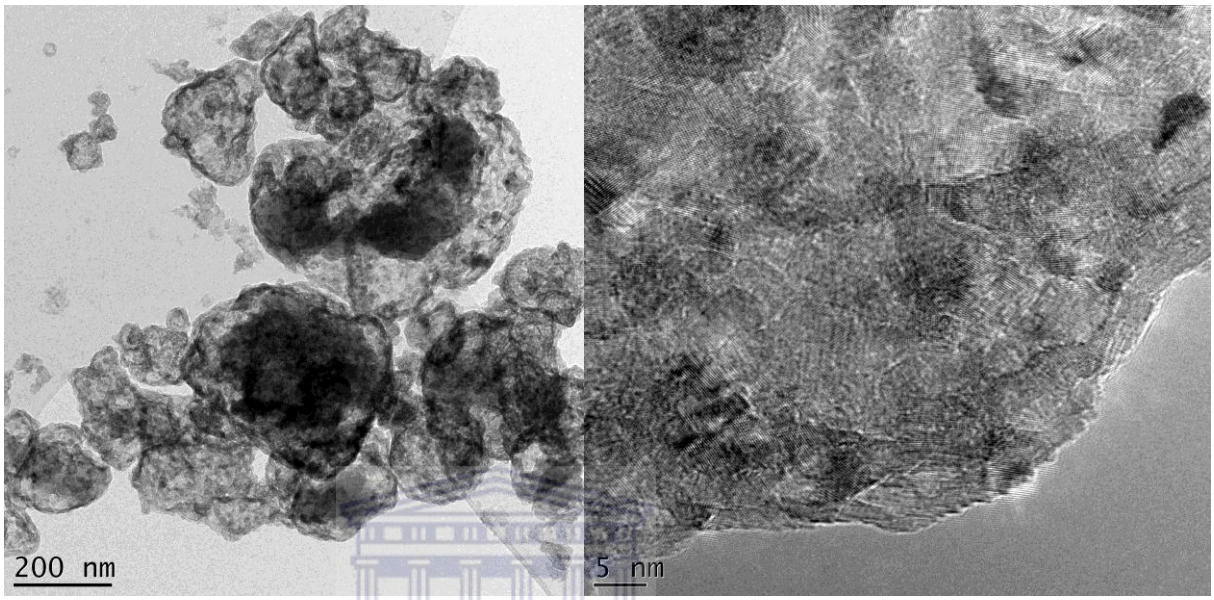

A **B**

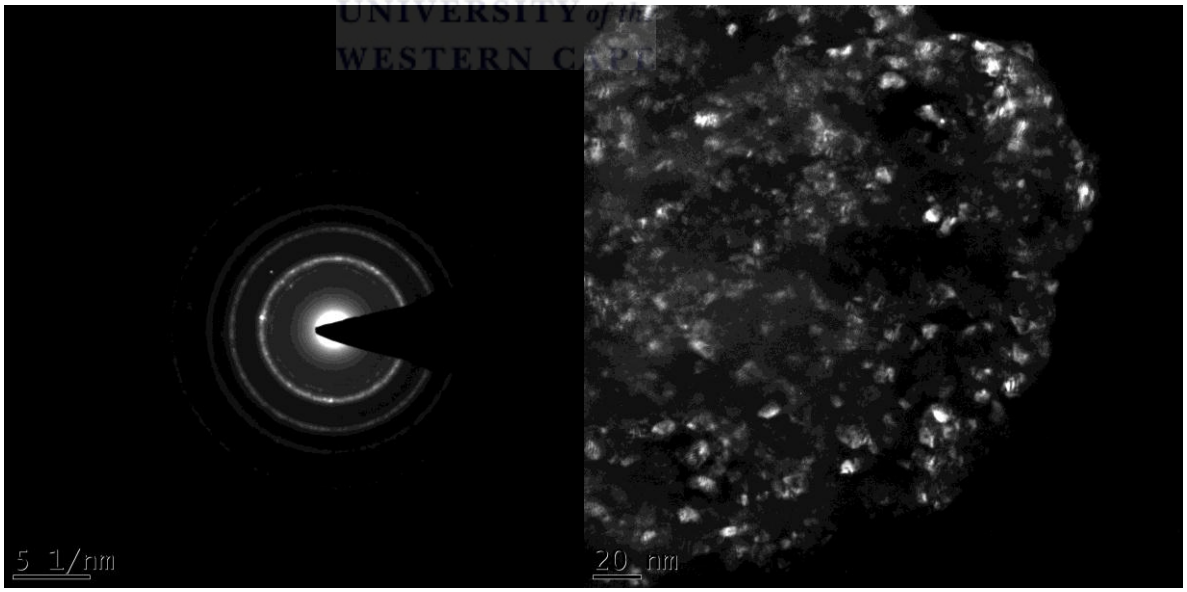

C **D**

Figure 4-25: TEM micrograph of re-hydrogenated Mg-BCC-V: (A**) Bright-field micrograph of Mg-BCC-V, (**B**) High-magnification showing lattice fringes of Mg-**

BCC-V (C) selected area diffraction of Mg-10BCC-V and (D) Dark-field from diffracting area

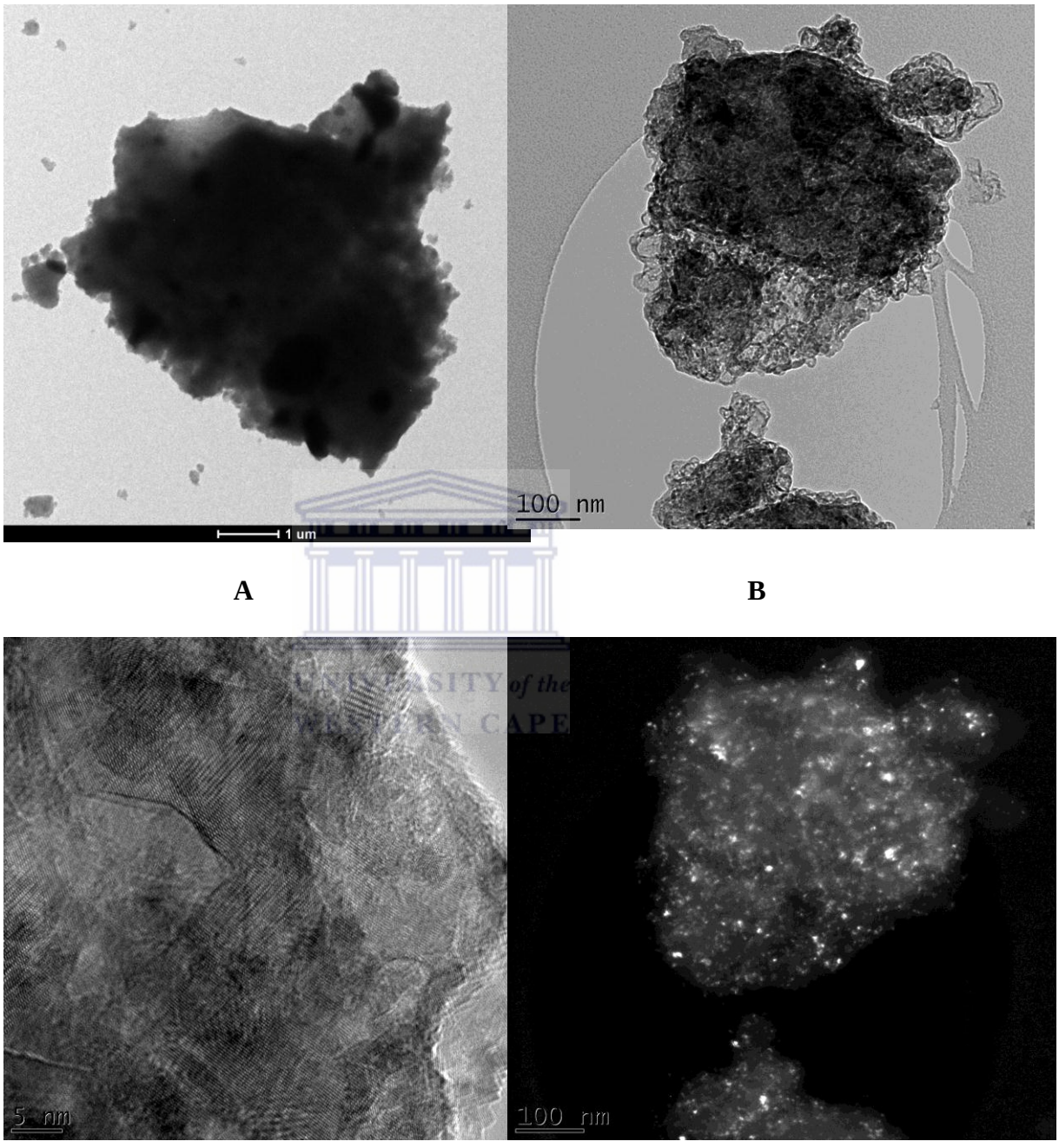

Figure 4-26: TEM micrographs of: (A) as-milled bright-field of Mg-5G-10BCC-V, (B) re-hydrogenated Mg-5G-10BCC-V, (C) High-magnification of B and (D) re-hydrogenated dark-field of Mg-5G-10BCC-V

Figure 4.24 - 4.26 show selected TEM micrographs of Mg-BCC-V and Mg-C-BCC-V samples. Figure 4.24 shows micrographs for the as-milled Mg-BCC-V. The bright-field micrograph (Figure 4.24(A)) consist cluster of small particles with some darker spots on the surface and some that may be embedded in the Mg/MgH_2 matrix. High-magnification of these particles show lattice fringes as presented in Figure 4.24(B). The presence of twinning in the material was introduced by HRBM. Selected area electron diffraction (SAD) pattern obtained from this lattice fringe is shown in Figure 4.24 (C) showing continuous ring pattern. EDX analysis for the obtained twining area confirmed the presence of Mg, BCC-V alloy phase. Mg nanoparticles are slightly oxidized during the preparation of TEM specimen and this was also observed in the XRD results. The peak of C and Cu are from the Cu-grid supporting a holey carbon for analysis in TEM. The obtained results are consistent to those of XRD.

TEM micrographs for the as-milled and re-hydrogenated Mg-5MWCNT-10BCC-V are shown in Figure 4.26. The bright-field micrograph for as-milled sample present flake-like material covered with some small crystalline black spot embedded in the carbon matrix. The flake-like materials are ascribed to that of carbon material covering the formed MgH_2 and the black spots to that of BCC-V alloy. No BCC-V additive nanoparticles were found outside the MgH_2 surface, which suggest that they may be trapped inside MgH_2 during the milling treatment. An increase in flake-like material was observed in the re-hydrogenated bright-field micrograph. High-magnification of the cluster shows coarse twinning area and this phenomenon is likely to influence hydrogen absorption/desorption properties [270].

4.3.1.3. Hydrogen sorption properties of Mg-C-BCC-V composites

4.3.1.3.1. Hydrogen absorption studies

The hydrogen sorption properties of as-milled and re-hydrogenated composite samples were investigated by TDS/re-hydrogenation measurements and the obtained results summarized in Table 4.12. The hydrogen absorption capacity for the formed hydrides of Mg-BCC-V and Mg-C-BCC-V were measured in relation to as-milled MgH_2. Typical hydrogen sorption kinetics curves (wt.% H vs time) after *in situ* dehydrogenation in the course of TDS process are shown in Figure 4.27. From the obtained results, Mg-BCC-V composite sample shows lower amount of hydrogen re-absorbed after completion of the TDS process. The lowering in hydrogen capacity for Mg-10BBC-V composite may occur due to overheating of the Mg particles contacting with BCC-V alloy during the re-hydrogenation cycles resulting in sintered/re-crystallized of sample particles. Also, very fast hydride formation in the course of combustion-type hydrogenation resulting in lower maximum hydrogen sorption capacity of the composite inhibiting H-atoms diffusion to un-reacted Mg core [157]. Subsequent re-hydrogenation of the sample did not show any hydrogen absorption even when the experiment was conducted over a long time.

Therefore, based on the morphology results in section 4.3.1.2, the sorption properties of Mg-C-BCC-V samples are predicted to be much improved to that of Mg-BCC-V due to reduced particle size growth and homogenously catalysts dispersion among Mg/MgH_2 studied under the same conditions. Figure 4.27 shows the hydrogen sorption kinetics curves of Mg-C-BCC-V samples and their results summarized in Table 4.12. From the obtained hydrogen curves, it can be seen that hydrogenation begins as soon as the powders are put in contact with H_2 gas and the kinetics are fast until the process gradually

slows down and almost constant hydrogen content is reached. The composites reached a constant hydrogen content in ~5.0 minutes and the amount of hydrogen re-absorbed varies between 3.36-4.85 wt.%H, with Mg-5AC-10BCC-V composite presenting the highest storage capacity of all the studies composites.

Introducing carbon show much improved re-hydrogenation rates with increased hydrogen storage capacity than those of Mg-BCC and Mg. This transformation at low amount of carbon type added greatly enhances hydride formation, but the quantity of carbon that can be introduced has a limit as >5wt.% leads to lower hydrogen storage capacity and also too little (1wt.%) of the carbon type leads to lowering in hydrogen storage capacity. The fast dissociation of the hydrogen molecules on the surface of the active phase and the subsequent quicker absorption can be ascribed to the co-presence of BCC-V alloy and carbon type materials combined with HRBM under hydrogen atmosphere forming small crystalline size composites materials as was reported in the morphology and phase structural studies. These disperse nanosized particles results in greatly enhanced reduction in hydrogen diffusion path lengths and increased coverage of the formed MgH_2 relative to their conventional coarse-grain of as-milled MgH_2. BCC-V alloy is known to dissociate hydrogen molecules into hydrogen atoms and transfers them to the Mg-BCC-V interface which acts as active nucleation sites for Mg hydride resulting in a decrease of nucleation barrier. The presence of carbon materials in the composites aggregating along the grain boundaries of bulk Mg acts as diffusion channel [60]. Dehouche *et.al*.[271] suggested that this may be due to the formation of nano-channels that facilitate the hydrogen access to the particle bulk.

When the samples were subjected to repeated re-hydrogenation cycles, lowering in hydrogen storage capacity was noted in all the samples except for Mg-AC-BCC samples which showed an increase in hydrogen storage capacity upon cycling. The lowering in hydrogen capacity was ascribed to quick formation of dense hydride layer of MgH_2 during re-hydrogenation measurements covering the unreacted Mg particles and acting as hydrogen atoms diffusion barrier. The partial agglomeration of particles (increase crystallize size) as seen in the morphology and phase structural studies results may contribute to the observed lowering in hydrogen storage capacity.

The kinetics curves were fitted by *Avrami* equation (eq.3.2) to obtain kinetic data for the catalyzed absorption process and their results summarized in Table 4.3.3. The *Avrami* exponent, *n*, evaluated by fitting the plots was approximately 1.0 ± (0.025-0.191) for all the composites. From the obtained *n* value, it shows that the rate-limiting step does not change within the pressure and temperature range of the experiment. The obtained *n* value corresponds to one- to two dimension grain growth with decreasing nucleation rate. As the absorption progress, the amount of unreacted Mg decreases which would decelerate further nucleation. The smaller *n* values obtained suggest that the nucleation and growth of hydride is inhibited even at an early stage of the reaction because of the rapid increase of the fraction of hydride.

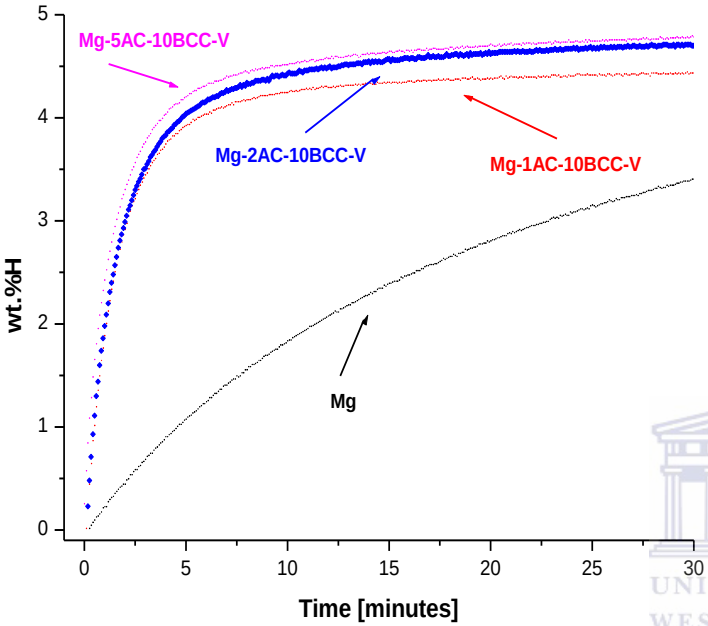

A

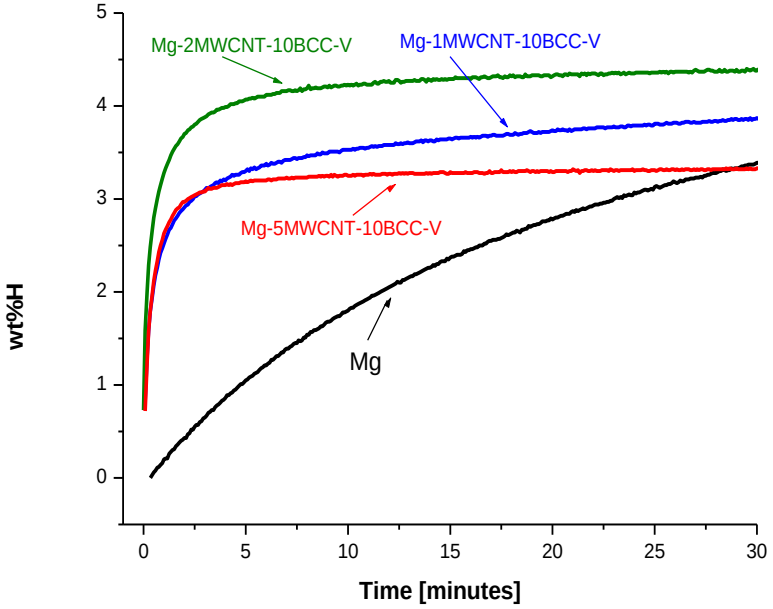

B

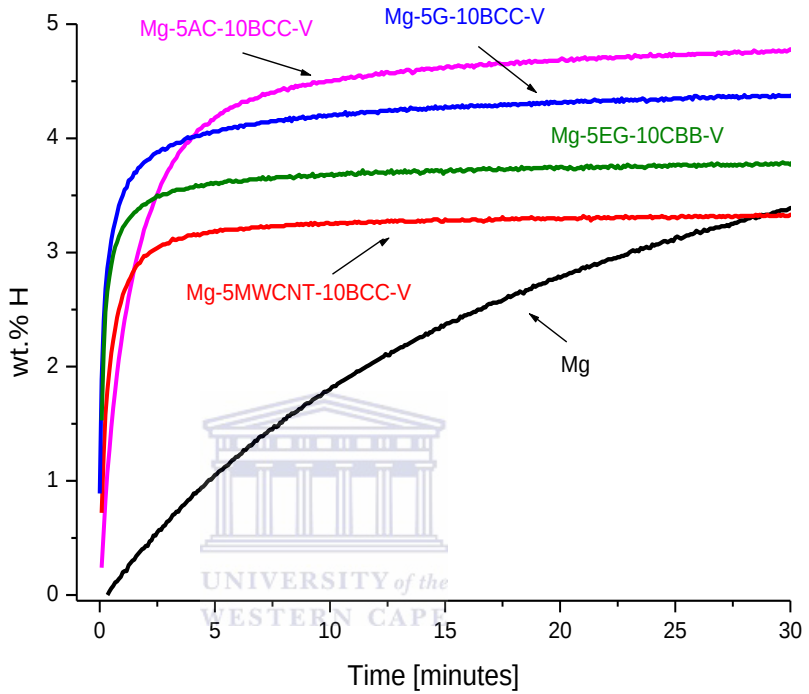

C

Figure 4-27: Typical hydrogen absorption behaviour of Mg-C-BCC-V (dehydrogenated first from RT to ~ 470°C under vacuum) at 250°C and 15 bar H_2

Table 4.12: Fitted re-hydrogenation characteristics of the studies composites

Sample	Conditions		Fitted kinetic parameters (eqn. 3.2)			
	Preceding dehydrogenation temperature [^{o}C]	Cycle #	C_{max} [wt.% H]	t_R [minutes]	n	Pearson correlation coefficient, R^2
HRBM Mg	407	2	4.97 ± 0.001	23.47 ± 0.005	0.731 ± 0.002	0.99323
	465	1	3.41 ± 0.001	35.05 ± 0.005	0.726 ± 0.001	0.99365
Mg–10BCC-V	462	1	1.53 ± 0.004	4.58 ± 0.263	1 ± 0.065	0.44013
	470	2	Not fitted (material sintered/re-crystallized)			
Mg–1MWCNT-10BCC-V	450	1	4.12 ± 0.013	1.500 ± 0.141	1 ± 0.104	0.54129
	456	2	3.92 ± 0.009	1.444 ± 0.125	1 ± 0.095	0.55774
Mg–2MWCNT-10BCC-V	456	1	4.66 ± 0.003	0.95 ± 0.056	1 ± 0.063	0.5636
	460	2	4.53 ± 0.004	0.76 ± 0.041	1 ± 0.081	0.46895
Mg–5MWCNT-10BCC-V	451	1	3.71 ± 0.002	1.086 ± 0.055	1 ± 0.049	0.87705
	462	2	3.36 ± 0.002	0.535 ± 0.036	1 ± 0.069	0.6995
Mg–1AC-10BCC-V	463	1	2.33 ± 0.003	2.731 ± 0.121	1 ± 0.042	0.96692
	470	2	4.53 ± 0.002	1.829 ± 0.049	1 ± 0.029	0.90392

Mg–2AC-10BCC-V	470	1	5.07 ± 0.004	2.44 ± 0.056	1 ± 0.026	0.9556
	466	2	4.77 ± 0.005	1.95 ± 0.065	1 ± 0.037	0.9076
Mg–5AC-10BCC-V	465	1	4.82 ± 0.003	2.45 ± 0.056	1 ± 0.025	0.9322
	462	2	4.85 ± 0.004	1.98 ± 0.062	1 ± 0.034	0.8847
Mg–5G-10BCC-V	461	1	4.24 ± 0.005	0.264 ± 0.052	1 ± 0.191	0.21905
	462	2	4.29 ± 0.009	0.326 ± 0.057	1 ± 0.174	0.53223
Mg-5EG-10BCC-V	473	1	3.89 ± 0.004	0.388 ± 0.038	1 ± 0.102	0.7417
	459	2	3.82 ± 0.004	0.249 ± 0.042	1 ± 0.161	0.3591

4.3.1.3.1. Thermal hydrogen desorption behaviour of as-milled and re-hydrogenated Mg-C-BCC-V composites

The hydrogen thermal desorption properties of as-milled and re-hydrogenated Mg-BCC-V and Mg-C-BCC-V nanocomposites were studied by thermal desorption spectroscopy (TDS) measurements and data summarized in Table 4.13. Figure 4.28 shows selected TDS spectra for the composites under study. From the obtained TDS results (Table 4.13), the as-milled and re-hydrogenated Mg-BCC-V presented a much broader desorption range and their peak maximum temperature shifted to higher temperature than those of Mg. Mg-BCC-V has T_{max} at 390°C and 385°C for as-milled and re-hydrogenated samples. Introduction of carbon lowers the onset and peak temperature, with the T_{onset} in the temperature range of ~190-275°C and T_{max} ≈ 285-351°C which is much lower than as-milled Mg having T_{onset} ≈ 340-380°C and T_{max} ≈ 364-375°C, respectively.

Re-hydrogenated samples show their T_{onset} and T_{max} to be shifts further to lower temperature range than those observed in as-milled ones. The T_{onset} and T_{max} were shifted to a temperatures range of ~190-225°C and 274-313°C, respectively. Lowering in T_{max} was noted when the quantity of carbon material was increased and this was much pronounced for MWCNT containing composites. A similar decrease in T_{max} for re-hydrogenated samples was reported in [171, 234] and it was suggested to be associated with structural change of the material during cycling.

From the obtained dehydrogenation results, the use of low quantity (1 and 2 wt.%) of carbon shifted the T_{onset} and T_{max} to lower temperature range comparable/or even better than 5wt.% quantities, with Mg-1AC-10BCC-V and Mg-2MWCNT-10BCC-V composites having the lowest peak decomposition temperature. Additionally, the co-doping of carbon types with BCC-V alloy during hydride formation results in materials with lower thermodesorption

properties than that of MgH_2. This can be ascribed to the synergistic effect of carbon additive and metal alloys along with ball milling process that improves hydrogen desorption properties of the formed magnesium hydride by reducing the barrier for nucleation, making hydrogen desorption happen at very low driving forces, and also the grain growth inhibiting factor of carbon played an important role for the above observed results.

In general, all re-hydrogenated Mg-C-BCC-V composites show significant lowering in their hydrogen desorption temperature as a consequence of cycling. The observed reduction in decomposition temperature indicated the thermodynamic destabilization of the formed hydrides.

Table 4.13: **Hydrogen thermodesorption properties of Mg-10BCC-V, and Mg-*x*C-10BCC-V measured in a Sievert–type apparatus heated from RT to ~ 460°C at 5°C/min under vacuum.(#1 for as-milled, #2 re-hydrogenated, C= G, MWCNT, AC and *x* = 1, 2, 5.wt.%)**

Composites	Cycle #	Decomposition temperature range [°C]	Peak desorption Temperature [T_{max}]
Mg	1	340-380	364
	2	325-402	375
Mg-10BCC-V	1	340-443	390
	2	331-443	385
Mg-1MWCNT-10BCC-V	1	275-430	342
	2	215-360	287
Mg-2MWCNT-10BCC-V	1	210-365	328
	2	190-342	278
Mg-5MWCNT-10BCC-V	1	276-438	351
	2	190-342	280

Mg-1AC-10BCC-V	1	205-370	302
	2	210-330	295
Mg-2AC-10BCC-V	1	210-380	303
	2	225-350	313
Mg-5AC-10BCC-V	1	195-360	285
	2	210-345	300
Mg-5G-10BCC-V	1	260-405	330
	2	190-331	274
Mg-5EG-10BCC-V	1	260-413	335
	2	185-335	270

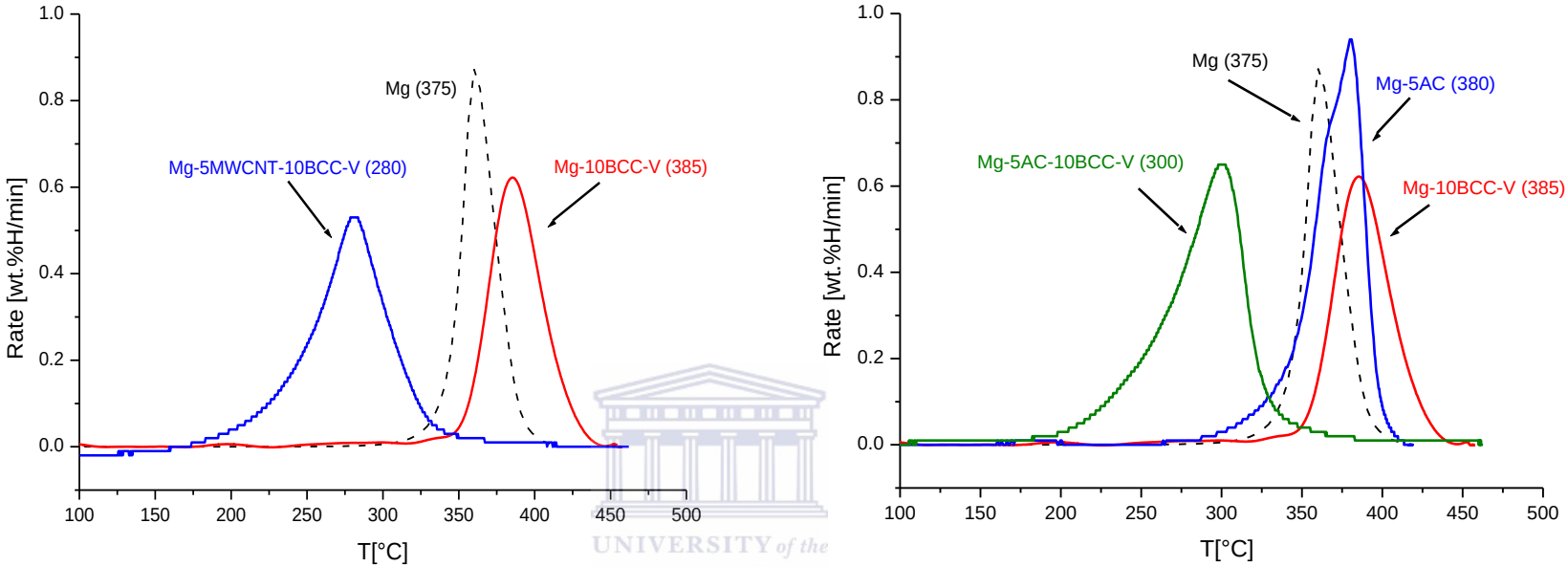

A **B**

Figure 4-28: Selected TDS spectra (heating rate of 5°C/min heating) for re-hydrogenated Mg-C-BCC-V composite samples

4.3.1.4. DISCUSSION

The present study clearly shows that HRBM of magnesium in the presence of BCC-V alloy and carbon species under hydrogen atmosphere afford the nanostructure composite samples with high hydrogen capacity. The *in situ* hydrogen measurement shows that the hydride formation rate is significantly faster than for HRBM Mg and Mg-C for all the Mg-C-BCC samples prepared reaching constant hydrogen content in less 1.5 hour of HRBM. The carbon materials aggregating along the grain boundaries of Mg acting as diffusion channel for H-atoms formed at the surface of V/VH_2 catalyst. It makes it easy for parts of the materials that were previously not accessible for hydrogenation, in so doing leading to enhanced hydrogen capacity as observed in all the HRBM samples. The introduction of carbon presented an incubation period that was dependent on the carbon type and quantity added to the composite with the proposed hypothesis for the observed incubation period explained in section 4.1.4. The co-presence of BCC-V alloy that dissociates the hydrogen molecules into atoms and transfer them to Mg, hydrogenation of BCC-V alloy is accompanied by heat release that drives the hydrogenation of Mg until the temperature of hydrogenation is high enough. This removes the obstacle often encountered during hydrogenation of Mg [210]. BCC-V alloy lowers the energy barrier for H_2 dissociation, and also it has an enthalpy of hydrogenation (to yield vanadium monohydride) of ~70 kJ/mol H_2, close to the enthalpy corresponding value of MgH_2 [272].

The synergistic effect of carbon and BCC showed fast hydrogenation rate and increased hydrogen capacity during dehydrogenation –rehydrogenation cycling compared to Mg-BCC-V and Mg, and this contributed to the observed lowering in the desorption peak temperature. The carbon aggregating along the grain boundaries of Mg serving as

hydrogen atoms diffusion channel and BCC-V recombining the desorbed H-atoms play and important role for the observed lowering desorption temperatures.

4.3.2. Mg–C–ZrNi

The aim of this chapter was to study catalytic effect of ZrNi alloy with or without carbon types (C = AC, MWCNT, G) during HRBM of magnesium metal under hydrogen atmosphere. The ZrNi alloy was chosen because of its good hydrogenation dynamic performances. It was also chosen because the co-presence of carbon type materials with ZrNi alloy during HRBM can improve the hydrogen sorption properties and also inhibit grain growth during dehydrogenation-re-hydrogenation cycling. Therefore, *in situ* pressure changes of hydrogen absorption by hydride forming materials during HRBM could be monitored and the resultant materials studied for hydrogen sorption properties, as well as its morphology and phase structure.

4.3.2.1. Hydrogenation behaviour during HRBM of Mg with carbon and ZrNi alloy additives

Figure 4.29 shows the hydrogenation curve of Mg-ZrNi and Mg-5C-10ZrNi during HRBM under hydrogen atmosphere and the data obtained summarized in Table 4.14. From the obtained results, the transformation of Mg → MgH_2 in the presence of ZrNi is significantly improved to that of undoped Mg milled under the same conditions with the former reaching constant hydrogen capacity in ~1 hour of HRBM. Comparable results for enhanced transformation of Mg → MgH_2 are reported in [151, 273, 274]. The hydrogenation curve of Mg-5AC-ZrNi presents similar hydrogenation kinetics to that for Mg-10ZrNi, with the former presenting higher hydrogen content. Introducing MWCNT and graphite presented an incubation period that was dependent on the carbon type, followed by hydrogenation curves that rose immediately as the materials were hydriding and gradually decelarating when the formed hydrides material reached a constant

hydrogen capacity with the latter taking ~3 hour for noticeable hydrogenation. The presence of an incubation period most probably arises at the beginning of HRBM with part of the mechanical energy spent to destroy the original graphitic structure and to produce graphene nano-sheets. These processes consume mechanical energy that in turn, reduces the amount of mechanical energy supplied to the particles of magnesium during HRBM leading to the observed incubation period. Of the carbon type employed, the use of graphite shows to absorb more of the mechanical energy (lowering the heating rate), with the observed incubation period even longer than that of undoped Mg. In all the obtained composites, hydrogen capacities of ≥ 6.58 wt.%H were obtained.

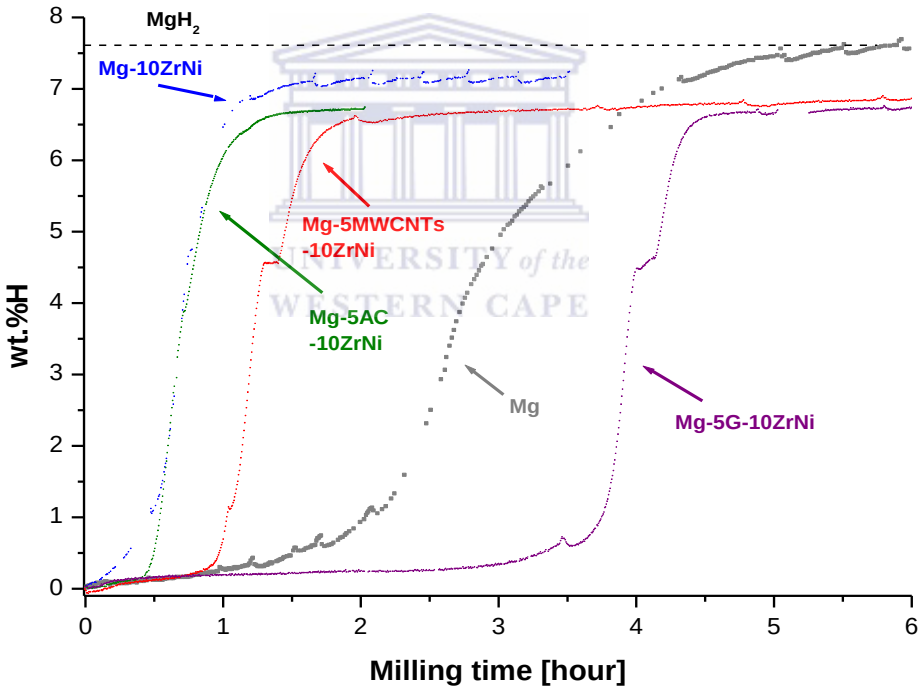

Figure 4-29: Hydrogenation curve during HRBM of Mg-10ZrNi and Mg-5C-10ZrNi composite materials

Table 4.14: Hydrogenation characteristics of Magnesium, Mg-10ZrNi and Mg-5C-10ZrNi samples during HRBM, (C = AC, MWCNT, G)

Sample	Maximum H capacity [wt.% H]		Fitted kinetic parameters (eq. 3.2)			
	Theoretical	Experimental	t_O [h]	t_R [h]	*n*	Pearson correlation coefficient, R^2
Mg	7.66	7.69 ± 0.001	0.14 ± 0.112	2.89 ± 0.005	4	0.99706
Mg-10ZrNi	7.26	7.07 ± 0.082	0.15 ± 0.088	0.61 ± 0.089	4	0.99644
Mg-5AC-10ZrNi	6.96	6.58 ± 0.010	0.16 ± 0.056	0.62 ± 0.057	4	0.99541
Mg–5MWCNTs–10ZrNi	6.97	6.67 ± 0.008	0.53 ± 0.067	0.82 ± 0.068	4	0.99479
Mg-5G-10ZrNi	6.96	6.74 ± 0.012	3.25 ± 0.579	0.82 ± 0.598	3.16 ± 0.247	0.99463

4.3.2.2. Morphological and phase characterization of MgH_2 and Mg-C-ZrNi materials

4.3.2.2.1. XRD

Phase structures for the as-milled and re-hydrogenated composites were established with XRD measurements and their data summarized in Table 4.15. Figure 4.30 shows the XRD patterns of the as-milled Mg-10ZrNi composite sample. The observed diffraction pattern shows peaks corresponding to α-MgH_2, γ-MgH_2 and $ZrNiH_3$ phases and their patterns exhibit significant line broadening associated with fine crystalline size of the constituent phases and introduction of micro-strain during HRBM. The γ-MgH_2 phase was observed in all the as-milled samples and its well reported for in ball milled Mg-based samples [129, 130, 170], and recently it has been observed in High Pressure Torsion (HTP) process [226].

Introduction of carbon materials results in 2-fold decrease in the abundance of $ZrNiH_3$ phase (probably due to its disproportionation during HRBM at the presence of carbon) having crystalline size of ~ 10 nm. Slight increase in the phase abundance and disappearance of strain in γ-MgH_2 was noted for all diffraction patterns. The diffraction patterns for the as-milled Mg-5C-10ZrNi samples were similar to the ones for Mg-10ZrNiH composite.

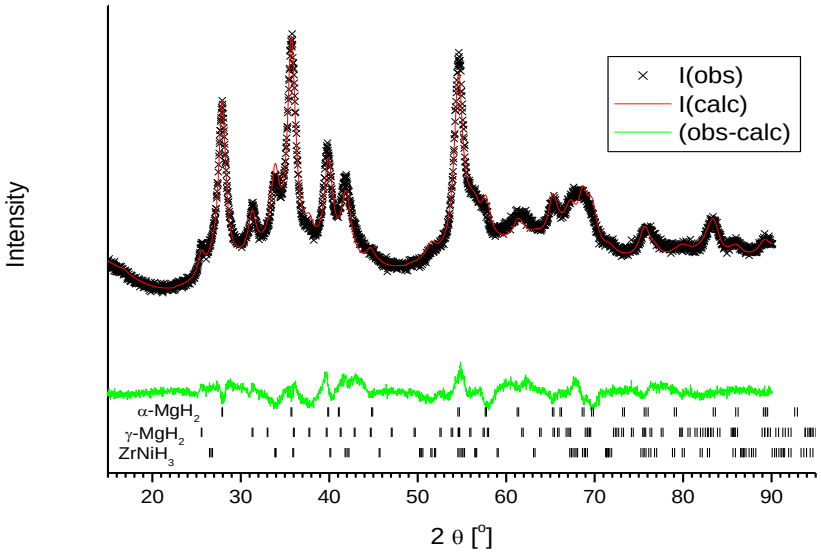

Figure 4-30: XRD pattern of the as-milled Mg-10ZrNi composite

The patterns for the re-hydrogenated composites (Fig.4.31) exhibit sharp peaks that are ascribed to: (i) elimination of microstrain in the crystals and (ii) crystalline growth during hydrogen cycling. The Major phase (~77 wt%) is α-MgH_2; the samples also contain non-hydrogenated Mg (up to 8 wt.%); the amount of the non-hydrogenated Mg decreases in ~2 times upon the introduction of carbon. The $ZrNiH_3$ phase observed in the as-milled samples disappeared in re-hydrogenated samples, instead, the Ni-enriched phase, monoclinic Zr_8Ni_{21}, was identified. Most probably, $ZrNiH_3$ disproportionates during TDS/re-hydrogenation to yield amorphous ZrH_2 (crystalline ZrH_2 was not found) and the Zr_8Ni_{21}.

All the as-milled composite samples show crystalline size about 10 nm. The observed crystalline sizes were comparable with those obtained in [267] for Mg+50 wt.% Ni mixture that was milled for 30 hours having a crystalline size of ~13 nm.

The re-hydrogenated Mg-ZrNi exhibits crystalline size about ~60 nm that is ~3 times lower than that of the Mg without additives. Further reduction of the crystalline size down to ~40 nm was achieved upon the introduction of carbon.

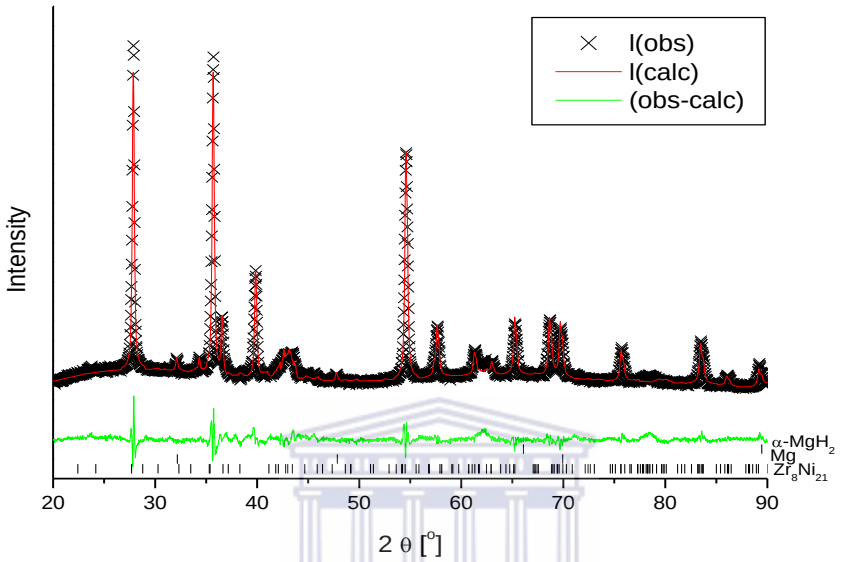

Figure 4-31: Diffraction pattern of re-hydrogenated Mg-10ZrNi

Table 4.15: Crystallographic data for the as-milled Mg-10ZrNi and Mg-5C-10ZrNi composite samples

Sample	Phase	Abundance	Lattice periods [Å]			Estimated grain size [nm]
		wt.%	*a*	*b*	*c*	
Mg-10ZrNi (as-milled)	α-MgH_2	69.19	4.517 (1)	–	3.023 (0.7)	10
	γ-MgH_2	16.02	4.547 (5)	5.515 (6)	4.979 (5)	16
	$ZrNiH_3$	14.8	3.439 (2)	10.680 (8)	4.339 (3)	8
Mg-5MWCNT-10ZrNi (as-milled)	α-MgH_2	70.89	4.518 (1)	–	3.023 (0.7)	10
	γ-MgH_2	21.85	4.542 (6)	5.415 (8)	4.960 (7)	7
	$ZrNiH_3$	7.30	3.529 (3)	10.690 (12)	4.260 (4)	10
Mg-5G-10ZrNi (as-milled)	α-MgH_2	69.57	4.58 (1)	–	3.023 (0.7)	10
	γ-MgH_2	24.13	4.478 (8)	5.613 (10)	5.093 (9)	5
	$ZrNiH_3$	6.30	3.568 (3)	10.531 (11)	4.278 (4)	10
Mg-10ZrNi (re-hydrogenated)	α-MgH_2	76.99	4.513 (0.1)	–	3.018 (0.1)	58
	Mg	8.30	3.208 (0.4)	–	5.209 (1)	71
	Zr_8Ni_{21}	14.7	6.568(0.4) α=72.96(7)°	7.845 (0.5) β= 67.50(5)°	8.770 (0.5) γ= 75.11(6)°	17
Mg-5MWCNT-10ZrNi (re-hydrogenated)	α-MgH_2	77.20	4.519 (0.2)	–	3.018 (0.1)	41
	Mg	4.60	3.207 (0.8)	–	5.213 (2)	76
	Zr_8Ni_{21}	18.10	6.574 (8) α=72.9 (1)°	7.984 (7) β= 67.5(1)°	8.806 (10) γ= 74.1(1)°	11

4.3.2.2.2. Morphology

The SEM micrographs for the as-milled and re-hydrogenated Mg-10ZrNi and Mg-C-ZrNi composite materials are shown in Figure 4.32 (A to F). In Figure 4.32 (A, B) , the SEM micrographs of as-milled Mg-ZrNi composite are shown. In this figure, the micrographs show several particles of micrometres that agglomerate due to high impact action of HRBM. The presence of smaller particle size with less agglomeration is well reported to enhance hydrogen storage properties by decreasing the diffusion path length of hydrogen atoms [13] and this was observed in the as-milled and re-hydrogenation samples. From the obtained micrographs, ZrNi particles are distributed on the Mg/MgH_2 matrix (Figure 4.32(B)) suggesting a close combination in atomic scale of Mg phase with ZrNi phase by this figure. The micrographs of as-milled Mg-C-ZrNi samples showed similar pattern to the above and representative micrographs are shown in Figure 4.32 (C, D).

The re-hydrogenated samples shows more uniformly dispersed particles with increased particle size (Figure 4.32 (E, F)). It can be deduced that during high temperature hydrogen cycling the agglomerates cracks and the individual particles grows. The observed growth of particles size agrees with established explanation regarding the reason for increased kinetic sluggishness of the metal hydride powder with prolong high temperature sorption cycling.

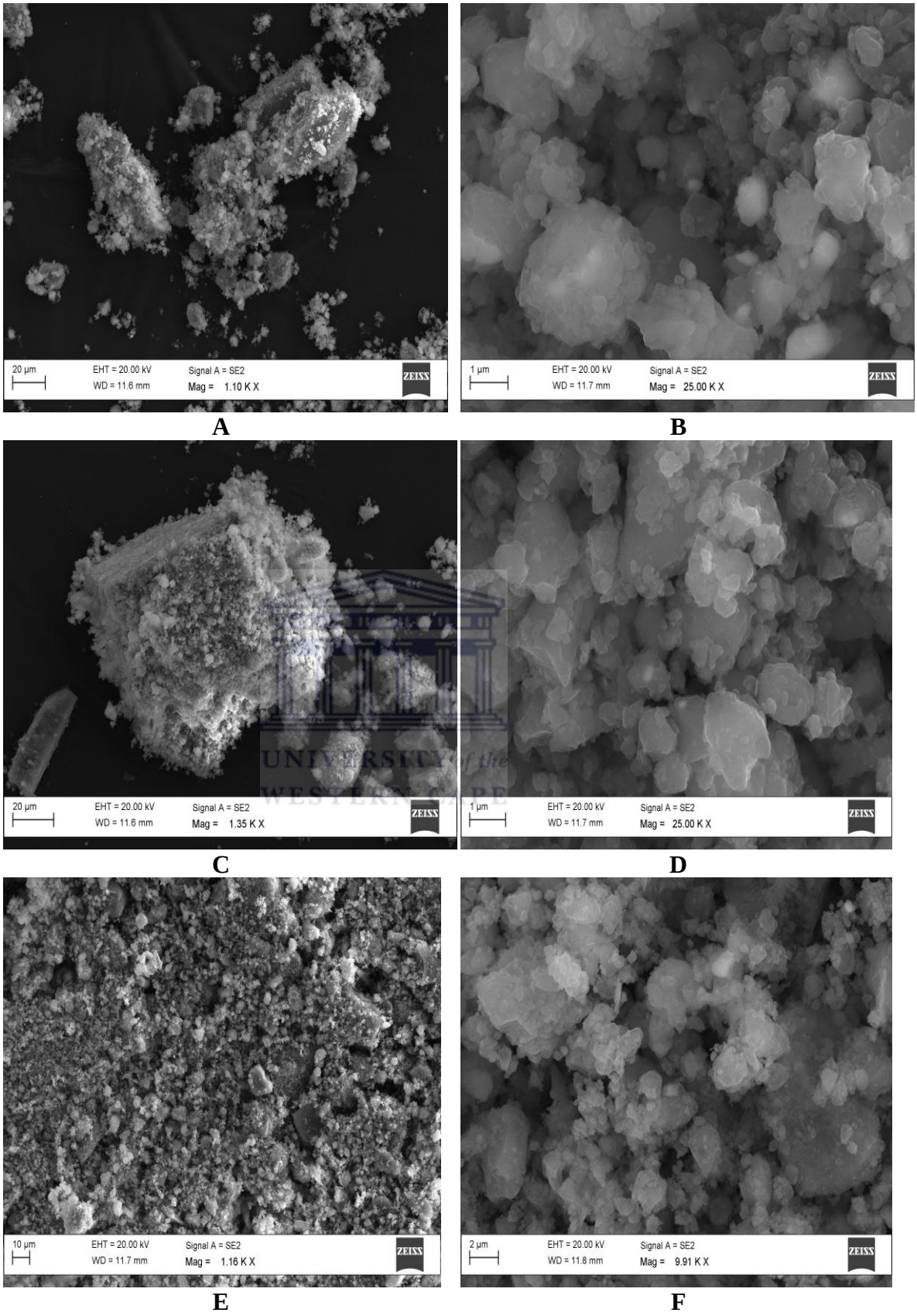

Figure 4-32: **SEM micrograph of: (**A, B**) as-milled Mg-10ZrNi, (**C, D**) as-milled Mg-5G-10ZrNi, and (**E, F**) re-hydrogenated MgH_2-5G-10ZrNi**

Additionally, the samples were analyzed by resolution transition electron microscopy (HRTEM). Figure 4.33 (A) shows the bright-field micrographs of Mg-10ZrNi sample that consist of clusters of small particles, some of which are darker. The dark spots are ascribed to ZrNi alloy phase distributed on the Mg/MgH_2 matrix and some of the alloy phase may be encapsulated within the lighter area, as was seen also in the SEM results. It can be seen that the clusters are made up of nano-particles size. High-magnification of the particle in Figure 4.33 (B) shows that each particle has a polycrystalline size structure with lattice fringe of different orientations. The observed twinning mode indicates that HRBM resulted in the formation of nanosized materials, twinning mode for ball milled Mg-based was also reported in [198, 202, 220]. The electron diffraction pattern of a particle gives a discontinued ring pattern, implying that the grain size has been significantly reduced during milling consistent with the XRD results having crystalline size of ~11 nm. The dark-field was performed to identify the crystallites. The dark-field micrograph is shown in Figure 4.33 (D). The micrograph shows that nano-crystals were formed during the course of HRBM. The bright-field micrograph for re-hydrogenated Mg-10ZrNi in Figure 4.34 (A) shows big clear particles that have clustered having black spot in the matrix. High magnification of the particle shows the presence of polycrystalline structure having coarser twins than those of as-milled Mg-ZrNi. The significant differences observed in the electron diffraction pattern of the re-hydrogenated Mg-10ZrNi from that of the as-milled powder is that, the electron diffraction pattern of a typical particle shows a continued ring pattern, representing very fine grain size.

The bright-field micrograph of Mg-5G-10ZrNi in Figure 4.35 presents clear particles that have some black spots similar to those observed in Mg-10ZrNi. The obtained SAD ring pattern consists of a mixture of bright spots with a continuous ring. Dark-field confirms

that the particles are nano-size with ZrNi homogeneously distributed on Mg/MgH_2 matrix that was confirmed by EDX. The above findings are parallel to those of SEM findings.

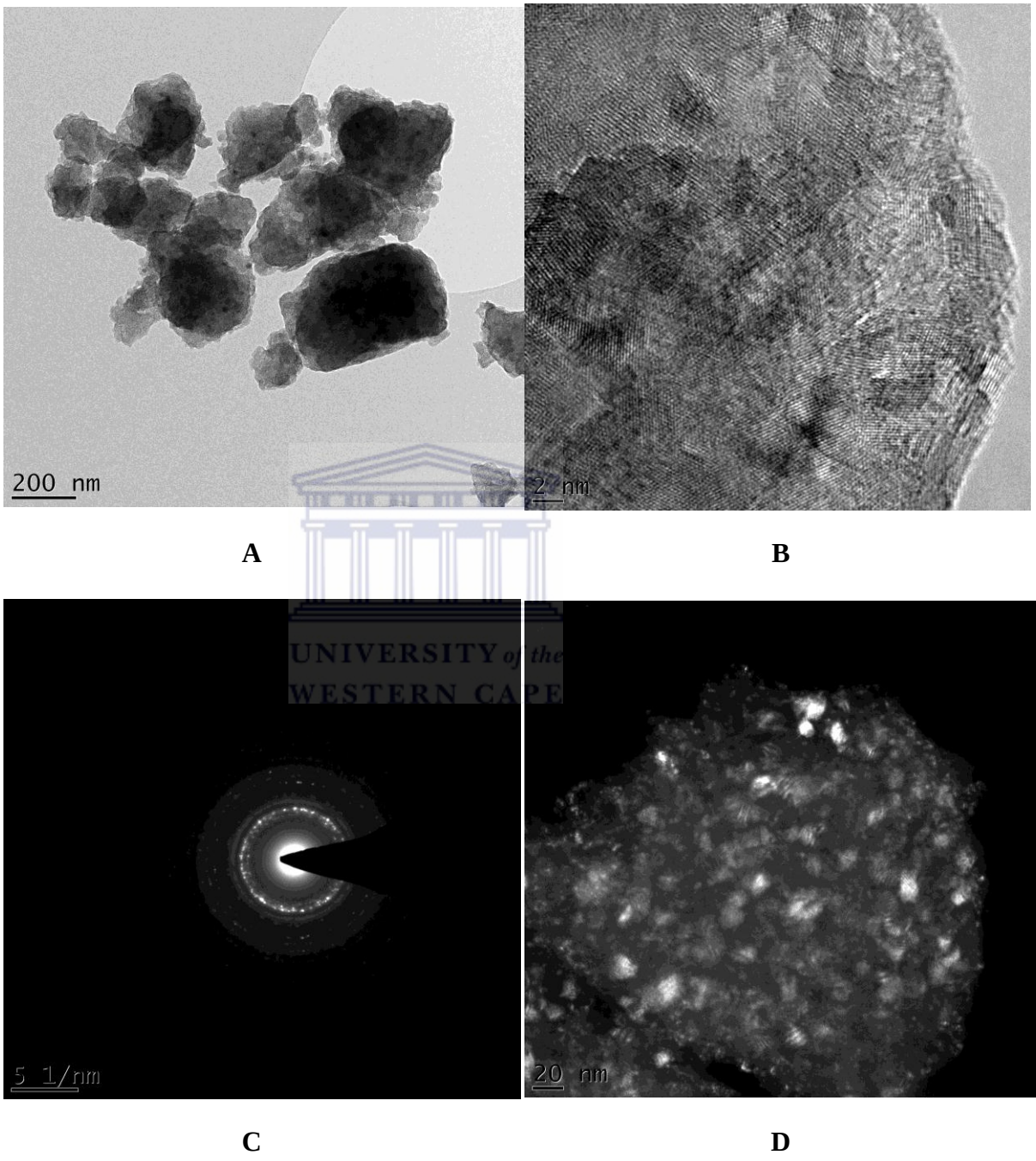

Figure 4-33: TEM micrographs of as-milled Mg-10ZrNi.:(A) bright-field, (B) high-magnification, (C) SAD, (D) dark-field

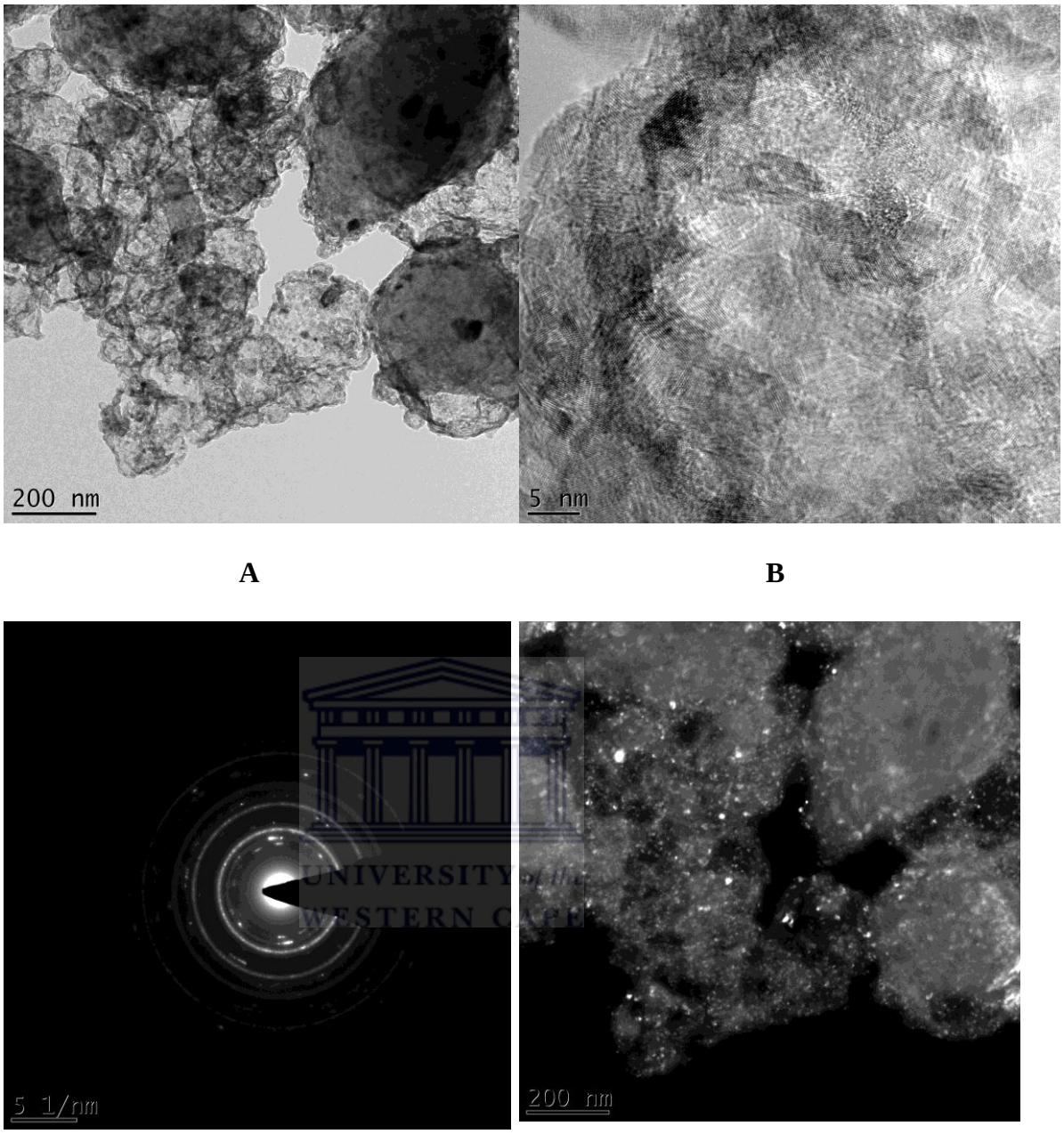

Figure 4-34: TEM micrograph of re-hydrogenated Mg-10ZrNi: (A**) bright-field, (**B**) high-magnification, (**C**) SAD, (**D**) dark-filed**

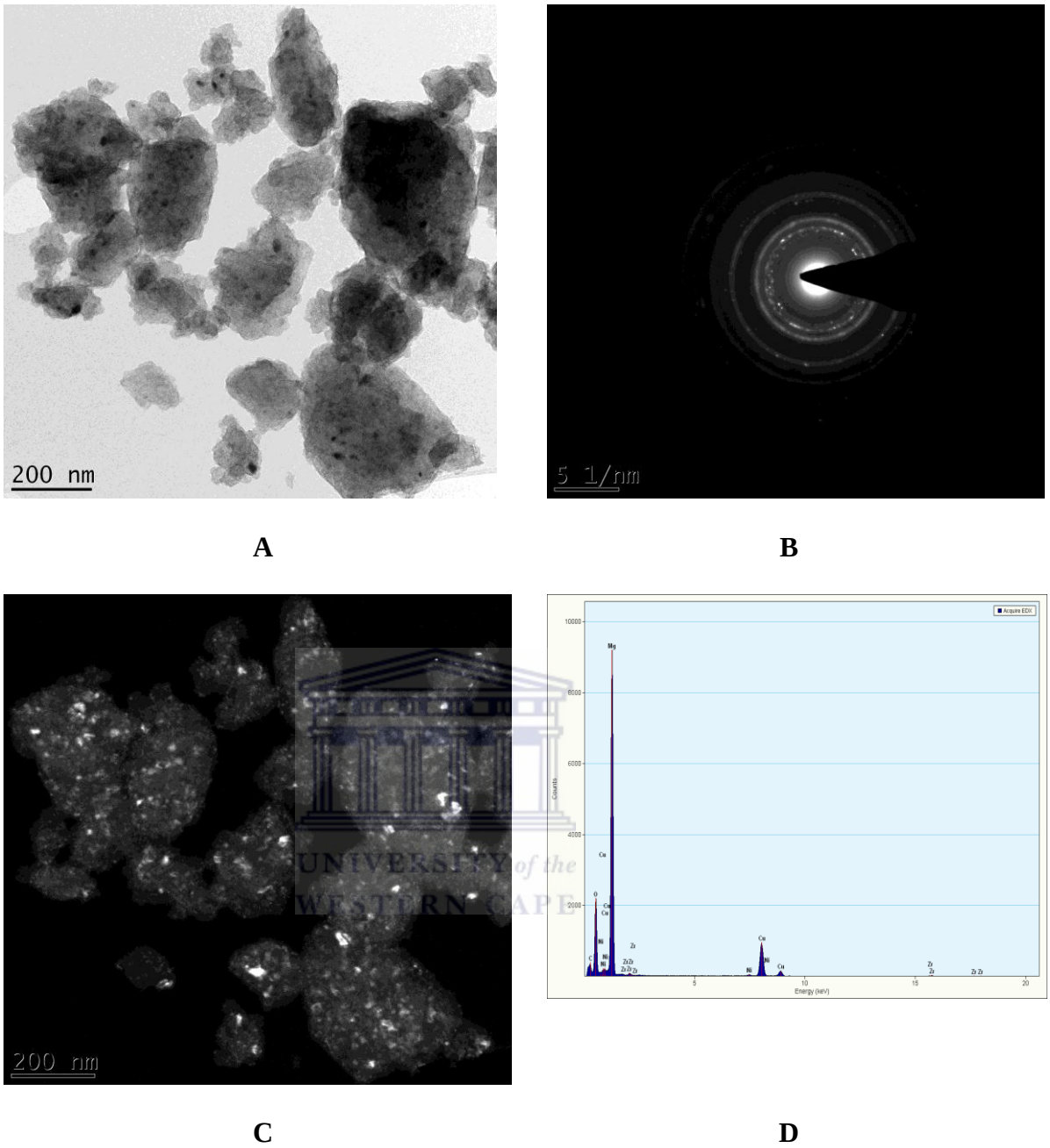

Figure 4-35: TEM micrographs of as-milled Mg-5G-10ZrNi: (A**) bright-filed, (**B**) SAD, (**C**) dark-field, (**D**) EDX**

4.3.2.3. Hydrogen sorption studies

4.3.2.3.1. Hydrogen absorption studies

Figure 4.36 shows the effect of hydrogen cycling on the kinetics of absorption for Mg-10ZrNi composite studied at 250°C under ~15 bar H_2 for a number of hydriding cycles (#). From the obtained hydrogen kinetics curves, all the hydriding cycles showed fast hydrogenation rates that are similar, whilst the fourth re-hydrogenation cycle showed total hydrogen capacity to be slightly reduced indicating agglomeration of the particles resulting in a reduced surface area and thus reducing H_2 penetration into the material which results in reduced uptake within a certain time period. Another reason that gives rise to the low hydrogen capacity is the limitation of the rate at which Mg metal decomposes hydrogen molecules into hydrogen atoms [50]. The re-absorbed hydrogen capacity were ~ 3.3-3.8 wt.%H.

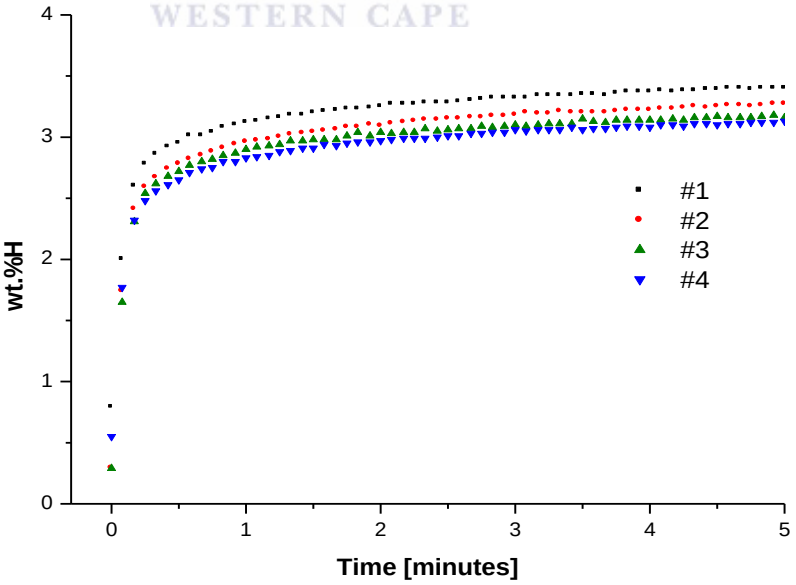

Figure 4-36: Hydrogen absorption curves of Mg-10ZrNi composite at 250°C under ~15 bar H_2 with the number of hydriding cycles (#)

Consequently, modification of the microstructure by using different additives to accelerate the dynamics of hydrogen absorption–desorption has been reported in [50, 275, 276]. The synergetic interactions between magnesium and carbon material as a result of mechanical grinding plays an important role in hydrogen uptake and release [173].

To further investigate the sorption kinetics characteristics of Mg-ZrNi sample, the re-hydrogenation measurements were carried out at three different temperatures (270°C, 300°C, 350°C) under ~ 15 bar H_2. The kinetics parameters were obtained by fitting the absorption files with *Avraami* equation 3.2 and data obtained summarized in Table 4.16. The trend in the kinetic constants confirms those obtained for sorption rates. From the observed re-hydrogenation curves shown in Figure 4.37, improved hydrogen storage capacity was noted as the re-hydrogenation temperature was increased, except at 350°C that show slower hydriding rate than at 250-300°C and this phenomenon is well reported for Mg-based composites [116]. The improved storage capacity at high temperature could be ascribed to the higher hydrogenation rates and larger number of available adsorption sites on the sample surface where hydrogen dissociative chemisorption proceeds. The number of these sites is different at the different temperatures and is associated with the formation of different numbers of MgH_2 nuclei. The composite behaviour during hydriding seems to be logical if one assumes that at the higher temperature the number of adsorption sites is smaller. In this case, a smaller number of nuclei are formed. They grow gradually and when their overlapping begins, the reaction stops, a rather high absorption capacity being attained. The large number of absorption sites (i.e. nuclei) at lower temperature accelerates the hydriding and leads to a faster overlapping of the hydride nuclei and as a result, the reaction stops earlier [116]. So, the kinetic measurement at 250°C show a better representation of the influence of the ZrNi

catalyst, since hydrogen diffusivity in the sorption material increases with temperature. It is therefore by far less important at 250°C than at higher temperatures. This is possibly caused by the high hydrogen absorption activity of magnesium at high temperature and less contribution of catalyst which is not needed to assist the hydrogen absorption at high temperatures.

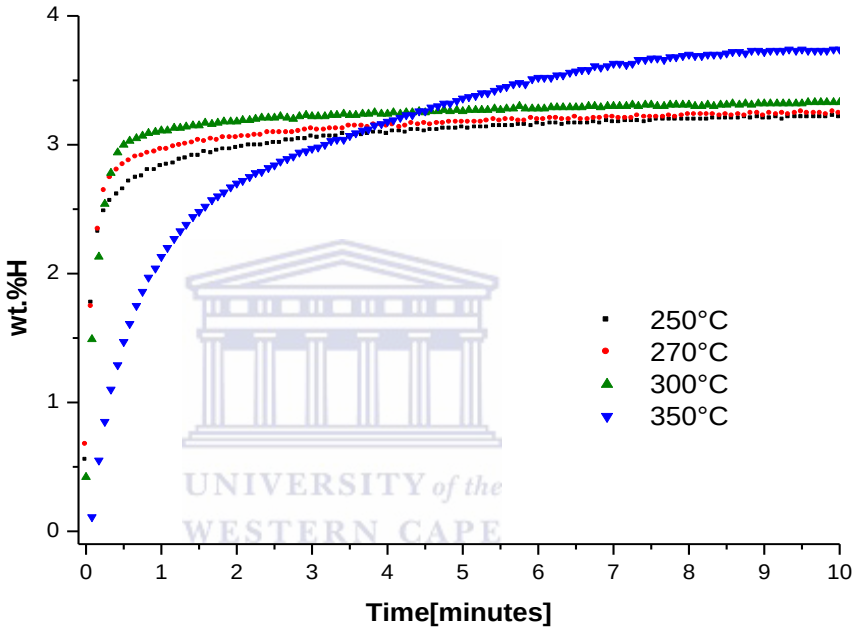

Figure 4-37: Hydrogenation curves at different temperatures for Mg-10ZrNi composite under~15 bar hydrogen pressure

Following the above results for the HRBM of Mg-ZrNi, modification of magnesium microstructure by introducing different carbon type additives with ZrNi with the intention to accelerate the dynamics of hydrogen absorption–desorption was undertaken and the obtained results compared with those of Mg-10ZrNi. The composites studied were those of Mg-5C-10ZrNi (C = MWCNT, Graphite) and data obtained summarized in Table 4.16.

Figure 4.38 shows the re-hydrogenation curves for Mg-5C-10ZrNi composites under study. From the observed re-hydrogenation curves, all the composites present fast hydrogen rates. The introduction of carbon materials slow down the re-hydrogenation kinetics. The composite of Mg-5G-10ZrNi present hydrogen storage capacity of ~2.8 wt.%H but still better than of Mg that could re-absorb < 2 wt.%H in the same time frame. Improved hydrogen storage capacity was obtained for Mg-5MWCNT-10ZrNi composite that could re-absorb ~4.3 wt.% H in ~ 10 minutes.

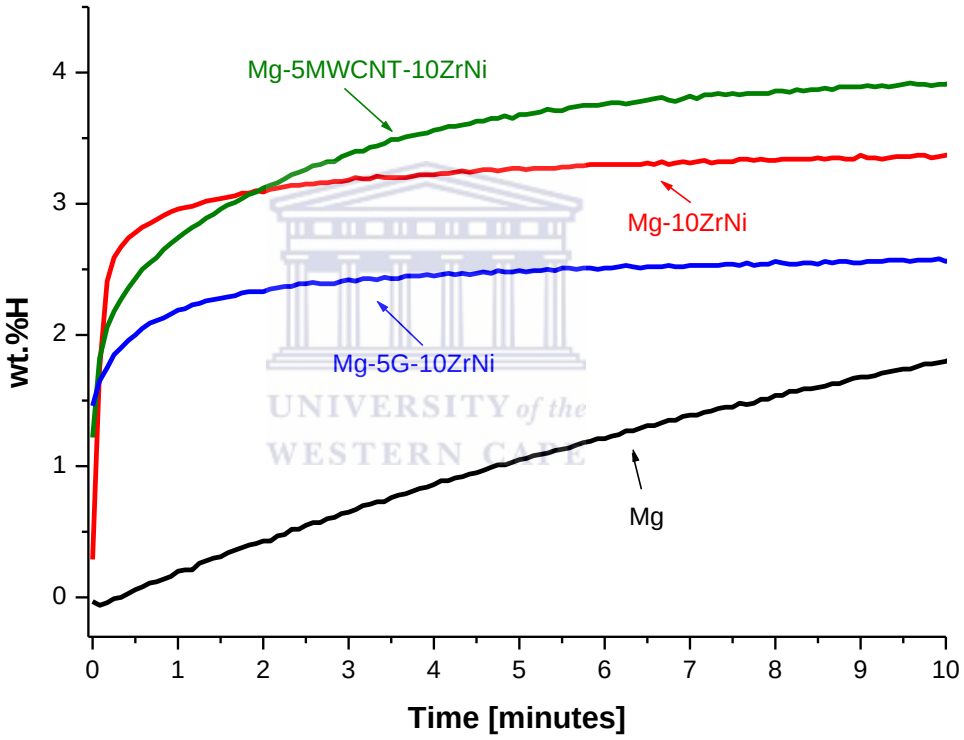

Figure 4-38: Time-dependence of the weight% of hydrogen absorbed at 250°C and ~15 bar H_2 for re-hydrogenated Mg-5C-10ZrNi composites

The re-hydrogenation kinetics curves were fitted by *Avraami* equation 3.2 and data summarized in Table 4.16. The *n* value in all cases was ~ 1; except for Mg-10ZrNi composite at 250°C that shows *n* in the range 2.7 to 4 for first and second re-

hydrogenation properties. Thus lowering the temperature during re-hydrogenation of Mg-10ZrNi results in change of the limiting step; from H-diffusion to phase transformation (detailed discussion is presented in section 4.1.1).

Table 4.16: Fitted re-hydrogenation characteristics (*P*=15 bar) for Mg, Mg-10ZrNi, and Mg-5C-10ZrNi samples

Sample	Conditions		Fitted kinetic parameters (eqn. 3.2)			
	Preceding dehydrogenation temperature [^{o}C]	Cycle #	C_{max} [wt.% H]	t_R [minutes]	n	Pearson correlation coefficient, R^2
HRBM Mg (T=250°C)	465	1	3.405 ± 0.001	35.05 ± 0.005	0.726 ± 0.001	0.99365
	407	2	4.976 ± 0.001	23.47 ± 0.005	0.731 ± 0.002	0.99323
Mg-10ZrNi (T=250°C)	466	1	3.73 ± 0.007	0.52 ± 0.250	2.69 ± 1.505	0.91467
	460	2	3.35 ± 0.008	0.23 ± 0.334	4	0.08143
Mg-10ZrNi (T=270°C)	460	1	3.38 ± 0.005	0.14 ± 0.070	1 ± 0.410	0.29112
Mg-10ZrNi (T=300°C)	460	1	3.43 ± 0.004	0.09 ± 0.096	1 ± 0.727	0.26645
Mg-10ZrNi (T=350°C)	475	1	3.47 ± 0.004	0.11 ± 0.639	1 ± 0.428	0.46960
Mg-5G-10ZrNi (T=250°C)	462	1	3.56 ± 0.006	0.72 ±0.073	1 ± 0.108	0.52575
	458	2	2.75 ± 0.005	0.32 ±0.068	1 ± 0.213	0.05520
Mg–5MWCNT-10ZrNi (T=250°C)	464	1	4.32 ± 0.051	1.66 ± 0.093	1 ± 0.062	0.64633
	460	2	4.28 ± 0.006	1.55 ± 0.096	1 ± 0.068	0.48199

4.3.2.3.2. Thermal hydrogen desorption behaviour of as-milled and re-hydrogenated Mg-ZrNi and Mg-C-ZrNi composites

The hydrogen thermodesorption properties of the Mg-10ZrNi and Mg-5C-10ZrNi composites are summarized in Table 4.17 and selected TDS curves are shown in Figure 4.39.

Table 4.17: Hydrogen thermodesorption properties of Mg, Mg-10ZrNi, Mg-5C-10 ZrNi composites measured in a Sievert–type apparatus heated from RT ~ 460°C at 5°C/min under vacuum.(#1 for as-milled, #2 re-hydrogenated; C = G, MWCNT, AC)

Sample	Cycle #	Decomposition range [°C]	Peak desorption Temperature [T_{max}]
Mg	1	340-380	364
	2	325-402	375
Mg-10ZrNi	1	184-350	277
	2	200-325	275
Mg-5MWCNT-10ZrNi	1	270-420	340
	2	220-340	285
Mg-5G-10ZrNi	1	245-400	313
	2	225-335	290

All the composites show their onset temperature and peak maximum temperature to be shifted to lower temperature range than those of Mg. The as-milled Mg-10ZrNi desorbs H_2 in the temperature range of 184-350°C with peak maximum at ~275°C and repeated TDS/re-hydrogenation shifts the desorption temperature range to 200-325°C with the same peak maximum. The obtained thermogram of Mg-ZrNi shows a single desorption peak even when its XRD pattern shows the presence of α-MgH_2 and $ZrNiH_3$. Such

behaviour suggests that MgH_2 coexisting with $ZrNiH_3$ has almost identical thermodesorption range, i.e. their thermodesorption peaks fully overlap. In the case of as-milled Mg-5C-ZrNi composites, the desorption temperature range is shifted to high values than those of Mg-10ZrNi but still lower than for Mg. Lowering in the desorption peak temperature was observed for re-hydrogenated Mg-5C-10ZrNi composites with Mg-10ZrNi and Mg-10ZrNi desorbing in the temperature of 225-335°C and 220-340°C with their peak maxima at 290°C and 285°C, respectively.

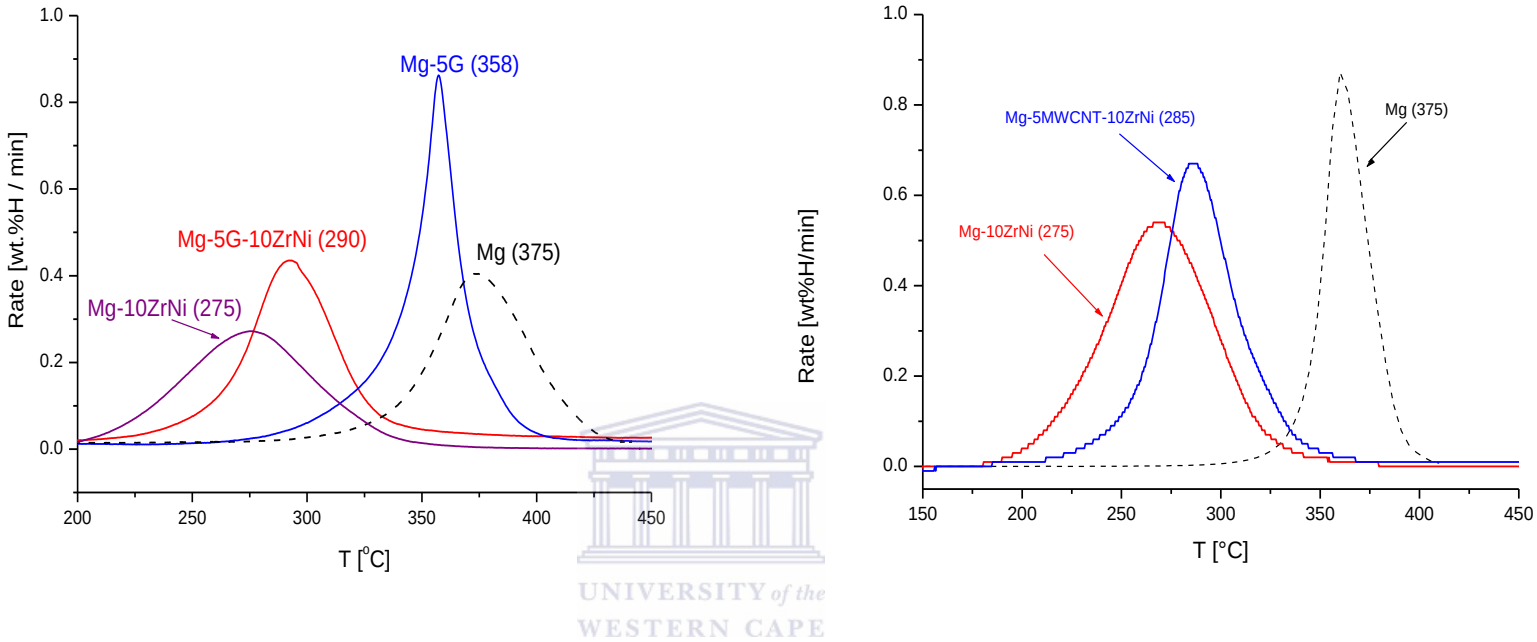

A **B**

Figure 4-39: Thermodesorption spectra of Mg-10ZrNi and Mg-5C-10ZrNi samples under vacuum

4.3.2.4. DISCUSSION

The effects of catalytic metal additive and different carbon types on the hydrogen sorption properties of magnesium formed by HRBM have been studied. The obtained results clearly demonstrate that HRBM of Mg with ZrNi alloy significantly improves the hydriding kinetics and maximum hydrogen storage capacity as compared to undoped Mg. The improved hydriding kinetics are due to high heating effect of ZrNi that drive the hydrogenation process over-coming the slow hydrogen atom diffusion into MgH_2. Introducing carbon type additives results in the appearance of an incubation period that was dependent on the carbon type. The composite having activated carbon did not present noticeable incubation period due to their "harder" character than Mg that leads to better particle refining and shortening the diffusion path length and its hydriding rate comparable to Mg-10ZrNi. Lower hydriding rate was obtained for Mg-5MWCNT-10ZrNi composite and much of the mechanical energy was used to disintegrate the carbon material and in so doing less energy was used to enhance hydrogen atoms diffusion into Mg grain. Mg-5G-10ZrNi presented sluggish hydriding rate that took ~4 hour before noticeable hydrogenation was observed, this was even longer than that of Mg. The better heat absorbing effect by graphite may be the reason for the observed long incubation period. Additionally, similar hydrogenation performances were observed for Mg-G composites as noted in section 4.1.

XRD patterns of the formed composites revealed the formation of nanocrystalline size α- and γ-MgH_2 (~10 nm) interdispersed with the nanocrystalline metal additives within the powder particles with reduced particles size. The re-hydrogenated composites showed crystalline

size growth, but it was much lower in the carbon containing samples. Fast re-hydrogenation rates were obtained in all the composites that reached maximum hydrogen capacity in less than 10 minutes. Lower hydrogen capacity for graphite containing composites than those of MWCNT containing was also noted. A shift of H_2 thermodesorption peak,s was observed with the carbon containing composites shifting their peak maximum to high temperature than that of Mg-10ZrNi (as discussed in section 4.1.4). The Mg-10ZrNi composite presented much improved thermodesorption properties than all the studied composites. This confirms the fact that the ZrNi alloy catalyze the hydrogen atom recombination and lowers the activation for hydrogen diffusion.

4.4. Magnesium-based nanocomposites containing carbon and $TiFeO_3$

To our knowledge, the use of $TiFeO_3$ (ilmenite) with or without carbon materials as catalytic additive for magnesium-hydride preparation has not been reported yet. In the following chapter, we report our investigation on the influence of $TiFeO_3$ with or without carbon materials during HRBM with elemental magnesium under hydrogen atmosphere. It is postulated that the use of mixed oxide ($TiFeO_3$) will present improved hydrogen sorption performances of MgH_2. Furthermore, the doping may reduce the time needed to prepare the hydride materials. We selected $TiFeO_3$ due to its lower cost as compared to individual metals such as Fe and Ti, or their alloys. The presence of Fe and Ti in the $FeTiO_3$ is expected to play a similar role to that of FeTi with the O sites supposed to be beneficial for hydrogenation of Mg and dehydrogenation of MgH_2.

The different carbon materials were selected as co-additives that could improve hydrogen storage capacity due to their beneficial effects on H sorption performances as discussed in section 4.1. Moreover, due to their reducing/deoxidizing character, they may facilitate activation process of the Mg-based system inhibiting the formation of new oxide layer on the powder surface after their exposure to hydrogen.

4.4.1. Hydrogenation behaviour during HRBM of Mg with $TiFeO_3$ and Mg with carbon and $TiFeO_3$ additives

Figure 4.40 shows hydrogenation kinetics of Mg, Mg-*x*$TiFeO_3$ and Mg-5C-10$TiFeO_3$ materials during HRBM under hydrogen atmosphere and the data obtained summarized in Table 4.18. From the observed hydrogenation curves, hydrogenation of Mg is very slow and requires more than 5 hours of milling to become saturated near the theoretical

capacity (7.66%). Improved hydrogenation kinetics was observed for samples containing $TiFeO_3$ with the time taken to reach a constant hydrogen capacity varying from one to two hours. All the hydrogenation curves of Mg-*x*$TiFeO_3$ composites gradually increase with the increased content of $TiFeO_3$ in the composite, and at the content of $TiFeO_3 \geq 5$ wt%, 5.8 to 6.7 wt.% hydrogen was absorbed during 1 hour of HRBM.

Following the fast hydrogenation rates observed for Mg-*x*$TiFeO_3$ composite samples during HRBM, Mg-5C-10$TiFeO_3$ composite samples were prepared similar to the aforementioned samples. The hydrogenation rates during HRBM were observed to proceeds slower than for the sample Mg–10$TiFeO_3$ and were characterized by an incubation period whose duration depends on the carbon type. The composites of Mg-5MWCNT-10$FeTiO_3$ and Mg-5AC-10$TiFeO_3$ took ~ 1 hour to reach a maximum hydrogen capacity. The graphite containing composite presented an incubation period of ~1 hour followed by the acceleration of the hydrogenation, when the saturation was reached in ~ 1 hour. Note that HRBM of magnesium with 5 wt.% graphite was characterized by two times longer incubation period (as was also reported in chapter 4.1). Nevertheless, the composite of Mg-5AC-10$TiFeO_3$ and Mg-5MWCNT-10$TiFeO_3$ absorbed about 7 wt.% of hydrogen during 1 hour HRBM and Mg-5G-10$TiFeO_3$ absorbed the same amount during 2 hours.

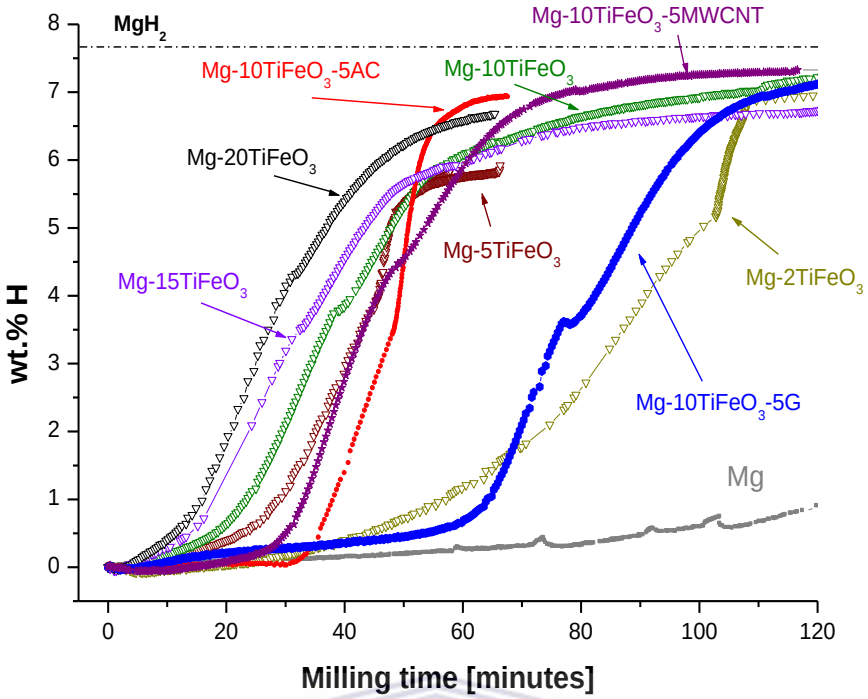

Figure 4-40: Hydrogenation curves of Mg-*x*TiFeO$_3$ and Mg-5C-10TiFeO$_3$ composite samples during HRBM under H$_2$ atmosphere

Table 4.18: Hydrogenation characteristics of magnesium, magnesium–*x*$TiFeO_3$ and Mg-5C-10$TiFeO_3$ samples during HRBM

Composite	Maximum H-capacity [wt.% H]		Fitted kinetic parameters (eq. 3.2)			
	Theoretical [(a)]	Experimental [(b)]	t_0 [hours]	t_R [hours]	n	Pearson correlation coefficient, R^2
Mg	7.66	7.69 ± 0.001	0.14 ± 0.112	2.89 ± 0.005	4.28 ± 0.003	0.99706
Mg-2$TiFeO_3$	7.51	7.35 ± 0.018	1.20 ± 8.338	91.85 ± 8.529	4	0.99451
Mg-5$TiFeO_3$	7.28	5.94 ± 0.022	1.74 ± 3.217	40.90 ± 3.267	4	0.99491
Mg-10$TiFeO_3$	6.89	7.62 ± 0.017	19.29 ± 0.280	28.63 ± 0.386	1 ± 0.018	0.99466
Mg-15$TiFeO_3$	6.51	7.05 ± 0.011	14.40 ± 0.517	24.62 ± 0.586	1 ± 0.026	0.99099
Mg-20$TiFeO_3$	6.13	6.70 ± 0.018	3.56 ± 0.396	28.20 ± 0.393	1.97 ± 0.042	0.99930
Mg-5AC-10$TiFeO_3$	6.51	6.94 ± 0.02	22.50 ± 2.456	27.01 ± 2.481	4	0.99580
Mg-5G-10$TiFeO_3$	6.51	7.21 ± 0.019	18.95 ± 4.035	66.58 ± 4.075	4	0.99673
Mg-5MWCNT-10$TiFeO_3$	6.51	7.37 ± 0.006	26.84 ± 0.181	23.34 ± 0.212	1.36 ± .0159	0.99931

[(a)] – Assuming 100% formation of MgH_2 and no hydrogenation of carbon and $TiFeO_3$.

[(b)] - HRBM under hydrogen pressure (~30 bar).

4.4.2. Phase structural and morphological characterization of as-milled and re-hydrogenated Mg-$TiFeO_3$ and Mg-C-$TiFeO_3$ nanocomposites

4.4.2.1. XRD

The diffraction patterns of the as-milled and re-hydrogenated Mg-*x*$TiFeO_3$ and Mg-5C-10$TiFeO_3$ composites are summarized in Table 4.19 and selected diffractograms shown in Figure 4.41. Figure 4.41(A) shows the XRD pattern of the as-milled Mg-10 $TiFeO_3$ sample, with the other as-milled Mg-$TiFeO_3$ samples resembling the similar diffraction pattern as the former. The obtained diffraction patterns of the as-milled Mg-10$TiFeO_3$ sample present broad peaks, typical for ball milled Mg-based materials and is attributed to the formation of small crystalline size materials as well as the increase in defects and mechanical strain created within the lattice by ball milling [261]. All the diffraction patterns of Mg-*x*$TiFeO_3$ composites show the presence of tetragonal α-MgH_2 as the main phase with trace amounts of orthorhombic γ-modification of MgH_2 and impurity phase of trigonal $TiFeO_3$ phase whose phase abundances in different samples were found to be quite close to the amounts of the $TiFeO_3$ introduced during their preparation. The presence of high-pressure metastable γ-MgH_2 is a result of alteration in the microstructure because of ball milling [261]. Also the formation of γ-MgH_2 is reported to have a positive effect on hydrogen sorption as a result of rearrangement in the cation and anion substructures which destabilizes the α-MgH_2 phase reducing the desorption temperature [166, 230]. Based on the extent of peaks broadening, the observed crystalline size of α-MgH_2 and γ-MgH_2 are in the range of 11-13 nm and 8-13 nm, respectively.

Table 4.19 also summarizes the XRD pattern for re-hydrogenated Mg-*x*$TiFeO_3$ composites, and selected diffraction pattern is shown in Figure 4.41(B). The obtained

diffraction patterns present intense, sharp peaks indicating a well crystallized sample with a relatively large particle size. All the samples show the presence of α-MgH_2 main phase, Mg, and trace amounts of, MgO and Fe. The crystalline sizes of α-MgH_2 and Mg estimated from line broadening are 30 and 40 nm, respectively. Lowering of $TiFeO_3$ quantity in the initial load results in a significant increase of the α-MgH_2 crystalline sizes: about 50 nm for re-hydrogenated Mg–2$TiFeO_3$ (both phases) and ~180 nm for re-hydrogenated HRBM Mg without additives (α -MgH_2). All the diffraction patterns of the re-hydrogenated samples do not contain the peaks of starting ilmenite, but a significant amount of poorly-crystallized MgO (estimated crystallite size below 10 nm). In addition, the pattern of the re-hydrogenated Mg–10$TiFeO_3$ clearly shows the presence of α-Fe, and the better refinement was obtained assuming the presence of trace amounts of TiFe and for both phases the estimated crystalline size was also below 10 nm. These findings allow us to assume that during dehydrogenation and re-hydrogenation $TiFeO_3$ reacts with magnesium (or magnesium hydride) according to the following reactions:

$$\mathbf{TiFeO_3 + 3\ Mg(H_2) \rightarrow TiFe + 3\ MgO\ (+ 3\ H_2)} \qquad (\mathbf{4.4.1})$$

$$\mathbf{TiFeO_3 + Mg(H_2) \rightarrow Fe + MgO + TiO_2\ (+ 3\ H_2)} \qquad (\mathbf{4.4.2})$$

Since neither TiO_2, nor possible product of its interaction with MgO (Mg_2TiO_4), were detected by XRD, we assume that these products of reaction (**4.4.2**) are amorphous. Nevertheless, both reactions result in:

i. generation of metallic nanoparticles which (especially, TiFe) are known to catalyse hydrogen dissociation and thus improve re-hydrogenation kinetics, at least, at the beginning of the process;

ii. consumption of magnesium to form MgO.

Most probably, reactions (**4.4.1**) and (**4.4.2**) take place at the end of the dehydrogenation process, and the formed MgO covers the Mg particles as a dense film inhibiting their re-hydrogenation, especially, when the formed layer of MgH_2 creates additional diffusion barrier for hydrogen atoms. Another reason for the lowering hydrogen storage capacity (see section 4.4.3) of the re-hydrogenated Mg–*x*$TiFeO_3$, whose XRD patterns exhibit quite high, up to 30 wt.%, phase abundances of MgO, may be in the reaction with trace amounts of O_2 and H_2O during storage of the samples in an argon glove box.

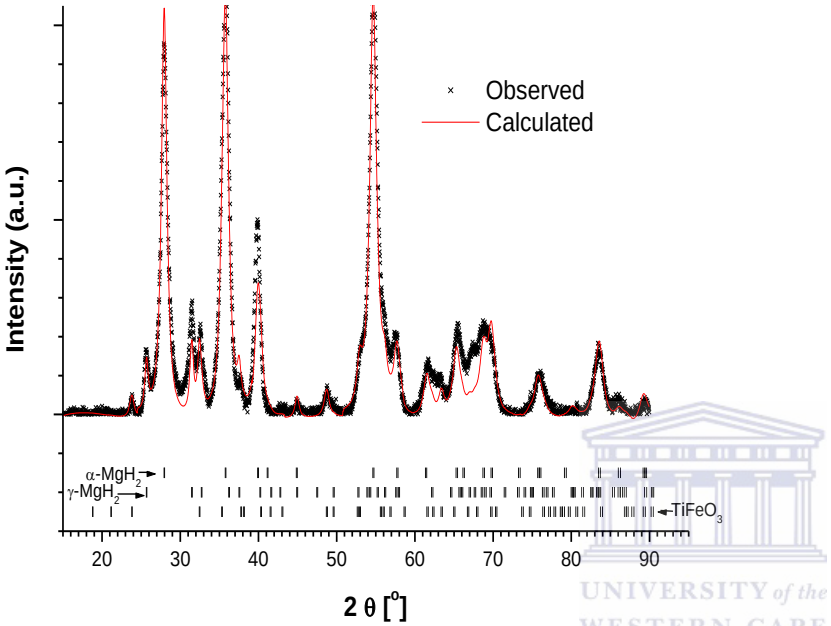

A

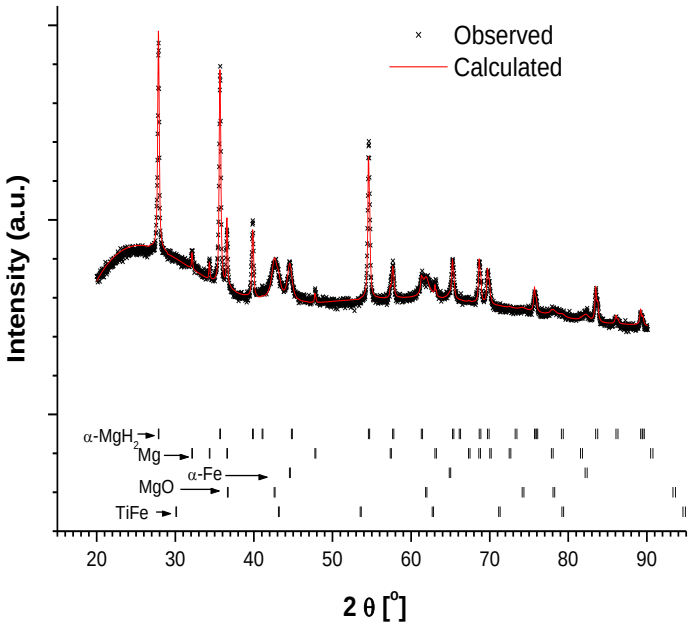

B

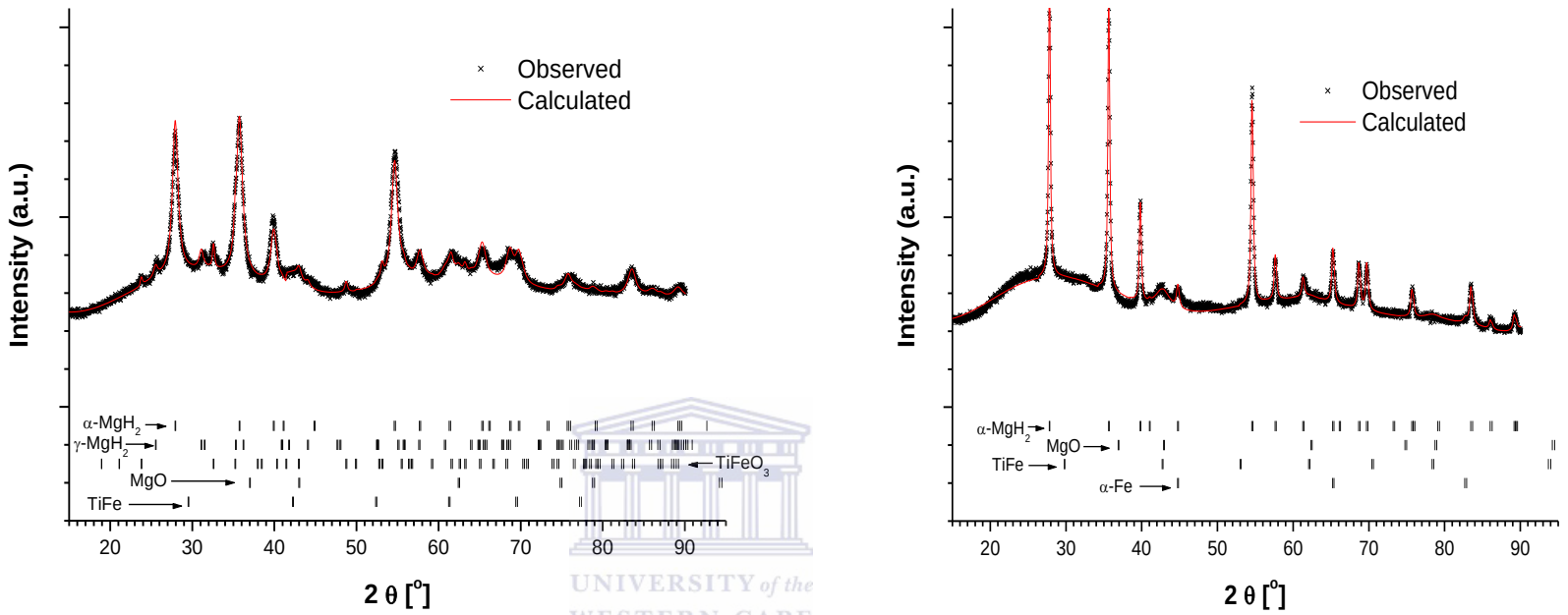

Figure 4-41: XRD patterns of: as-milled Mg-10 $TiFeO_3$ (A), re-hydrogenated Mg-10$TiFeO_3$ (B), as-milled Mg-5MWCNT-10$TiFeO_3$ (C), and re-hydrogenated Mg-5MWCNT-10$TiFeO_3$ (D)

Figure 4.41(C) shows the XRD patterns of the as-milled Mg-5MWCNT-10$TiFeO_3$ composite sample. The obtained diffractogram presents broad peaks due to refinement of grain size (crystalline), increased defects and/or accumulation of lattice strains that are introduced by HRBM. The major phases are α- and γ-modifications of MgH_2 with phase abundances and crystallite sizes similar to ones observed in Mg-10$TiFeO_3$. At the same time, the phase abundance of $TiFeO_3$ is approximately two times lower than in the case of Mg–10$TiFeO_3$, and the patterns exhibit appearance of poorly crystallized MgO and TiFe with estimated crystalline size between 8 and 13 nm. In so doing, reaction (**4.4.1**) takes place during HRBM of the materials containing $TiFeO_3$ together with the carbon species.

Representative XRD pattern for the re-hydrogenated Mg-5C-10$TiFeO_3$ composites is shown in (Figure 4.41(D)). The composites patterns contain only α-MgH_2 as a major phase and small amounts of TiFe, MgO and α-Fe were observed. The amount of MgO is much lower in the re-hydrogenated Mg-5MWCNT-10$TiFeO_3$. The phase abundance of TiFe is ~3.5 times higher and the phase abundance of α-Fe is ~4 times lower than the ones for the re-hydrogenated Mg–10$TiFeO_3$. Thus, the addition of carbon to Mg–*x*$TiFeO_3$ inhibits reaction (**4.4.2**) and promotes reaction (**4.4.1**) to yield nanocrystalline TiFe known to be a very efficient catalyst of hydrogen dissociation and recombination. Since all the samples were stored under the same conditions, the lower amounts of MgO in the re-hydrogenated Mg–C-$TiFeO_3$ samples are, most probably, originated from lower sensitivity of the carbon-containing composites towards oxidation. The resultant Mg-C-$TiFeO_3$ samples show good re-hydrogenation kinetics and high hydrogen capacity properties. The presence of (graphene materials in the ball milled samples) carbon is known to give origin to carbon based radicals that react with oxygen containing species during milling, thus, preserving magnesium from oxidation [280].

Table 4.19: Characteristic crystallographic data of as-milled and re-hydrogenated Mg-10$TiFeO_3$ samples phases calculated by the refinement of the XRD data[(a)]

Sample	Phase	Abundance [wt.%]	Lattice periods [Å]			Estimated grain size [nm]
			a	*b*	*c*	
Mg-2$TiFeO_3$ (as-milled)	α-MgH_2	72.92	4.5221	-	3.0287	10.7
	γ-MgH_2	24.09	4.5719	5.4944	4.9385	9
	$TiFeO_3$	2.99	5.142	-	13.7539	19.5
Mg-5$TiFeO_3$ (as-milled)	α-MgH_2	68.21	4.5241	-	3.0242	13.1
	γ-MgH_2	22.759	4.5576	5.4686	4.9372	12.4
	$TiFeO_3$	9.03	5.1249	-	14	12
Mg-10$TiFeO_3$ (as-milled)	α-MgH_2	65.68	4.524	-	3.0261	12.8
	γ-MgH_2	24.15	4.5616	5.4662	4.9498	12.1
	$TiFeO_3$	10.17	5.117	-	13.9703	13.2
Mg-15$TiFeO_3$ (as-milled)	α-MgH_2	67.50	4.5229	-	3.0266	11.1
	γ-MgH_2	21.59	4.5666	5.4612	4.9495	11.2
	$TiFeO_3$	13.33	5.1091	-	13.9792	12.7
Mg-20$TiFeO_3$ (as-milled)	α-MgH_2	67.50	4.5247	-	3.0284	11.1
	γ-MgH_2	16.97	4.5552	5.5561	5.0039	8.4
	$TiFeO_3$	15.53	5.1072	-	13.98	12.7
Mg-2$TiFeO_3$	α-MgH_2	69.57	4.5152	-	3.0192	49

(re-hydrogenated)	Mg	15.65	3.2112	-	5.2136	48
	MgO	14.79	4.209	-	-	12
Mg-10$TiFeO_3$ (re-hydrogenated)	α-MgH_2	56.48	4.5194	-	3.0201	26.7
	γ-MgH_2	5.87	3.2103	-	5.2118	42.8
	MgO	31.367	4.232	-	-	9
	Fe	6.297	2.8715	-	-	9
Mg-5AC-10 $TiFeO_3$ (as-milled)	α-MgH_2	68.84	4.5198	-	3.0284	11.5
	γ-MgH_2	8.97	4.5295	5.5471	4.9505	15.4
	MgO	22.20	4.2715	-	-	13.8
Mg-5G-10 $TiFeO_3$ (as-milled)	α-MgH_2	68.77	4.5204	-	3.0268	11.3
	γ-MgH_2	15.74	4.5355	5.5477	5.0118	8.4
	$TiFeO_3$	4.65	-	5.1139	-	67
	MgO	10.84	4.2551	-	-	8
Mg-5MWCNT-10 $TiFeO_3$ (re-hydrogenated)	α-MgH_2	81.60	4.5165	-	3.02	28
	MgO	14.05	4.2416	-	-	9
	α-Fe	4.36	2.8537	-	-	8

(**a**) Errors of the lattice periods are approximately equal to one unit of last digit of the values presented in the table

4.4.2.2. Morphology

The morphology and microstructure of the as-milled and re-hydrogenated Mg-$TiFeO_3$ composite samples were investigated by transmission electron microscope (TEM), with the representative micrographs shown in Figure 4.42-4.44. TEM micrographs of as-milled Mg-10$TiFeO_3$ are shown in Figure 4.42. The powder morphologies for as-milled Mg-10$TiFeO_3$ show irregular and smaller particles distributed on the surface of the flat formation composite matrix and the smaller particles that have agglomerated or clustered to relatively bigger particles. Similar micrographs were observed for the other as-milled Mg-*x*$TiFeO_3$ composite samples. From the observed micrographs, it shows that the $TiFeO_3$ particles are homogenously distributed throughout the Mg/MgH_2 matrix. TEM micrographs for re-hydrogenated Mg-10$TiFeO_3$ sample are shown in Figure 4.43. Furthermore, from the observed micrographs, the morphology of the sample drastically changes upon repeated high temperature cycling. The structure exhibits well-arranged, connected cubic nanosheets as observed in high-magnification in Figure 4.43(A) and its low magnification shows the nanosheets to consist of particles that have twins (Figure 4.43(B). The twinning showing nanocrystalline formation was also confirmed by its selected area diffraction (Figure 4.43(C)) and the total contribution of the twinning is shown by its conical dynamic circle in Figure 4.43(D).

Re-hydrogenated Mg-5AC-10$TiFeO_3$ TEM micrograph shows agglomerates that formed flake-like structure with some black spots (Figure 4.44(A)) and its dark-field micrograph show that nano-crystallites are formed (Figure 4.44(B)). Figure 4.44(C) is the low magnification showing the agglomerates consisting of nano-particles that are twinning

with its SAD shown in (Figure 4.44(D)) with discontinued ring pattern particles having some small bright spots.

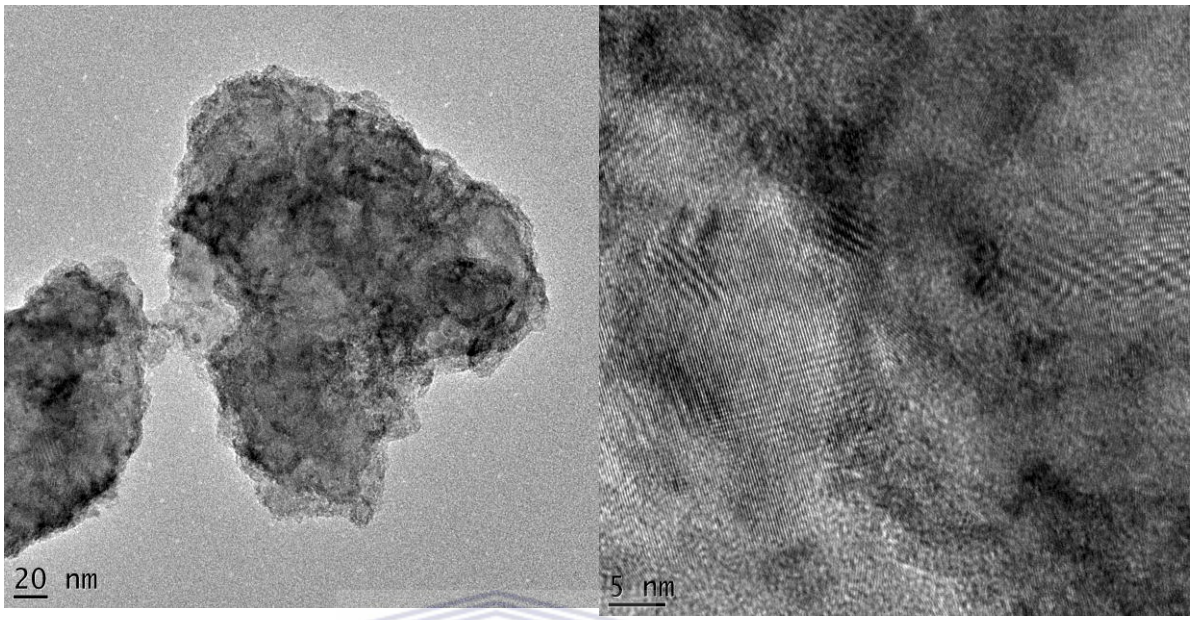

A **B**

Figure 4-42: TEM micrographs of as-milled Mg-10 $TiFeO_3$: (A) bright-field, (B) high-magnification

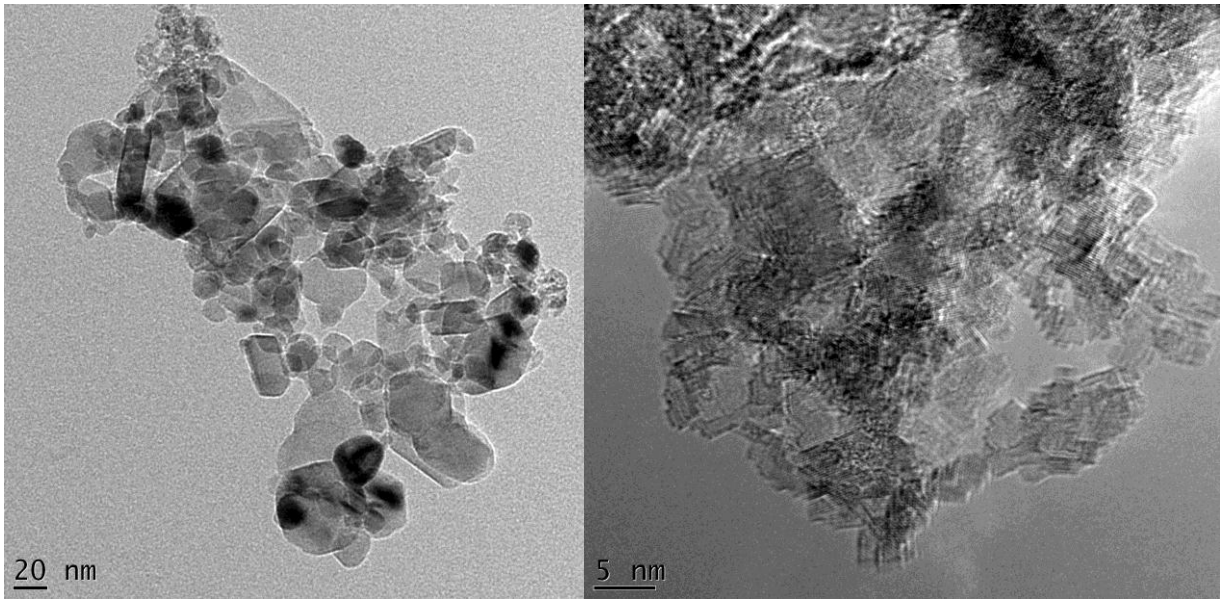

A **B**

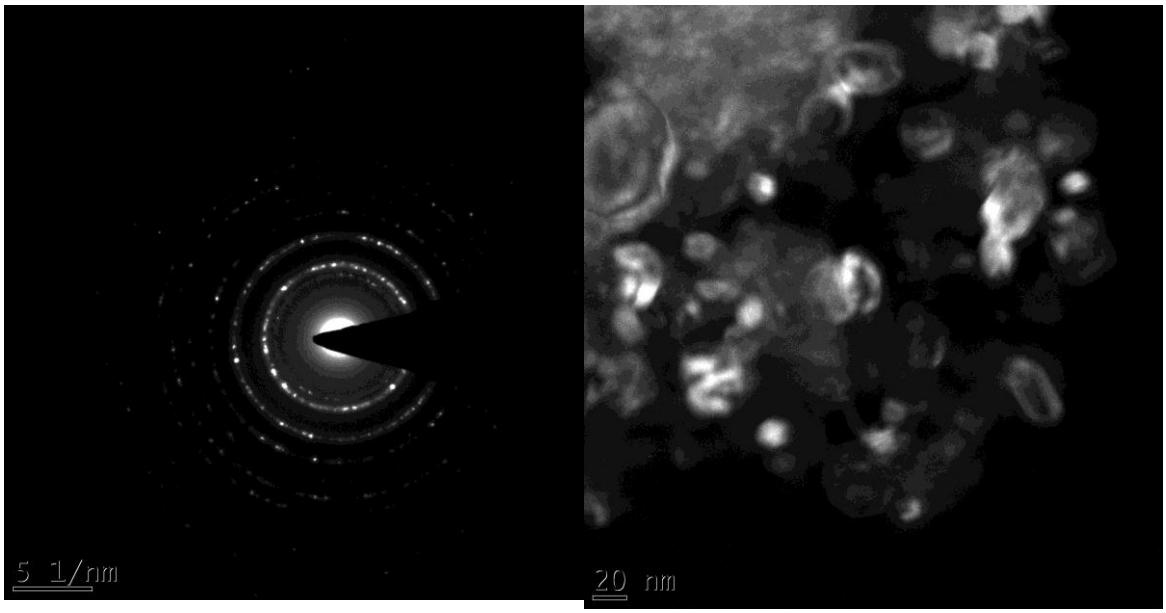

C **D**

Figure 4-43: **TEM micrographs of re-hydrogenated Mg-10TiFeO$_3$: (**A**) bright-field, (**B**) high-magnification, (**C**) selected area diffraction and (**D**) conical dynamic circle**

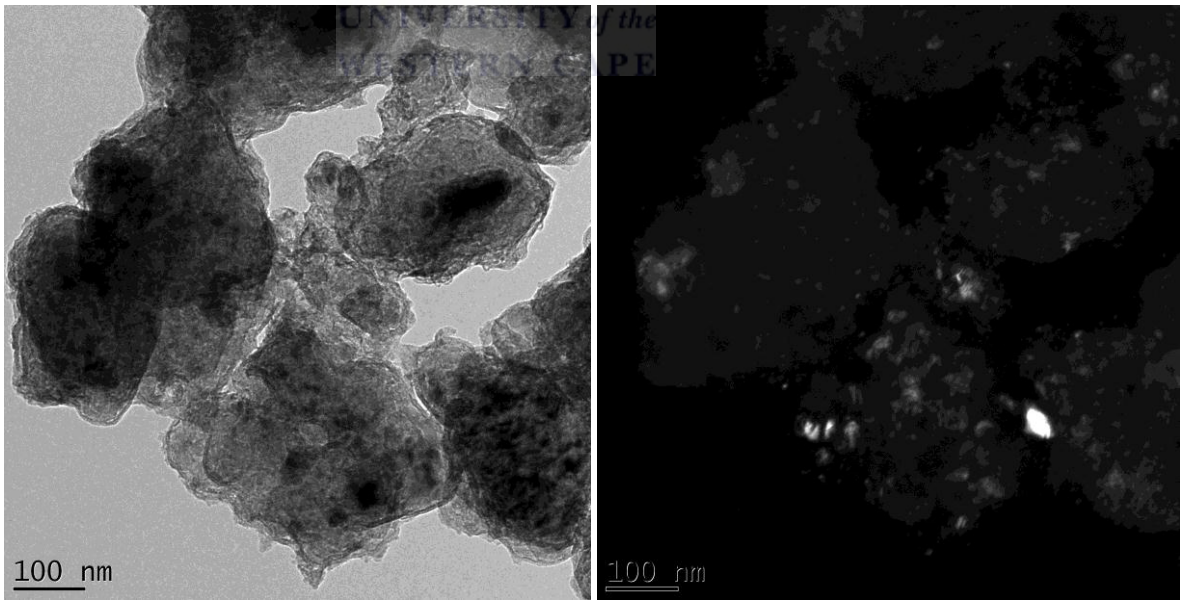

A **B**

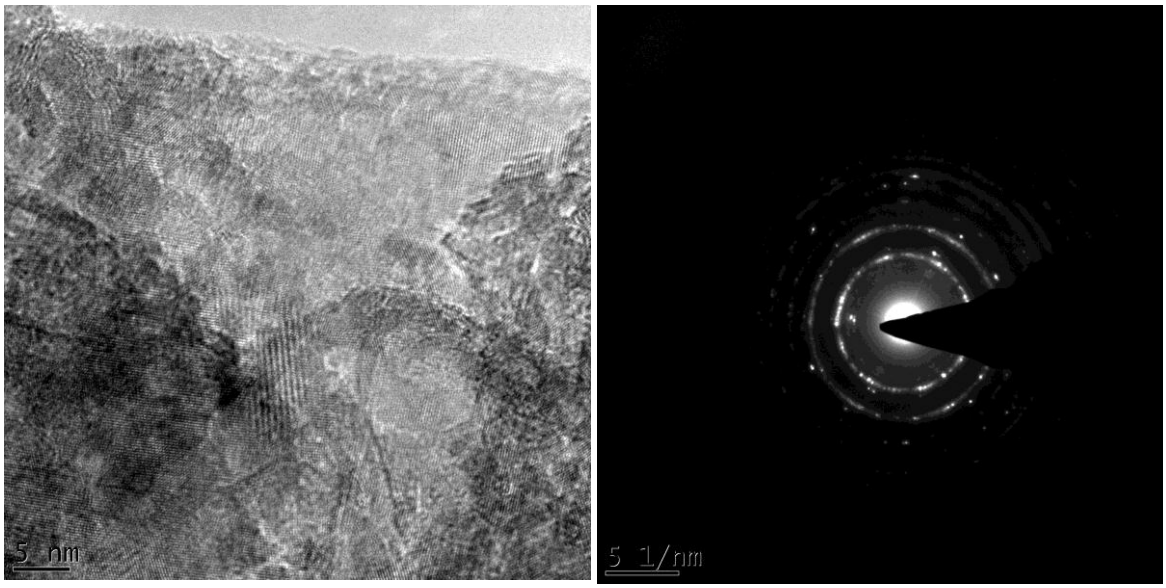

C **D**

Figure 4-44: **TEM micrographs of re-hydrogenated Mg-5AC-10FeTiO$_3$: (**A**) bright-field, (**B**) dark-field, (**C**) high-magnification, (**D**) selected area diffraction**

4.4.3. Hydrogen sorption properties

4.4.3.1. Hydrogen absorption studies

The kinetics data of the re-hydrogenation of Mg-*x*TiFeO$_3$ and Mg-5C-10TiFeO$_3$ composite samples at 250°C under ~15 bar H_2 are summarized in Table 4.20 and selected re-hydrogenation curves shown in Figure 4.45. The hydrogenation curves of Mg-*x*TFeO$_3$ samples during the first 5–7 minutes of re-hydrogenation process exhibit rates which are superior to undoped Mg. However, the maximum hydrogen capacity are as low as 3–4 wt.% H against ~5% achieved for Mg alone in ~5 hours. From the obtained results, it can be seen that the hydrogen storage capacity is also dependent on the additive quantity as a high storage capacity was achieved for Mg-2TiFeO$_3$ composite sample. The observed lowering in hydrogen storage capacity is in line with the observed XRD results showing

an increase in the quantity of $TiFeO_3$ results in an increased MgO phase abundance and reaction mechanism proposed therein. The presence of MgO phase is well reported to inhibit H-atom diffusion to the grains of Mg [237, 238].

Following the above re-hydrogenation studies for Mg-*x*$TiFeO_3$ samples, Mg-5C-$TiFeO_3$ composite samples were studied similarly and the obtained results summarized in Table 4.20. The composites of Mg-5C-$TiFeO_3$ showed much improved re-hydrogenation kinetics and hydrogen storage capacity than those of Mg-10$TiFeO_3$ and undoped Mg. The improved Mg-5C-$TiFeO_3$ hydrogenation rates is ascribe to co-presence of carbon materials aggregating along the grain boundaries of magnesium particles and also the lowering of MgO phase abundance as was observed in the XRD results. The presence of carbon materials is known to give origin to carbon based radicals that react with oxygen containing species during milling, thus, preserving magnesium from oxidation [280]. In so doing, this facilitates easy access of H-atoms to the magnesium grain that increases both the absorption kinetics and hydrogen storage capacity [196, 281]. The hydriding kinetics was also observed to be dependent on the carbon type, in the other composites their grains are not easily accessible for further hydrogenation with the grain boundaries become saturated in hydride-like structure and this can be seen by absorption curves plateau short of the theoretical capacity. In all the studied composites, the amount of hydrogen that can be re-absorbed in 10–30 minutes is up to 5 wt.% H.

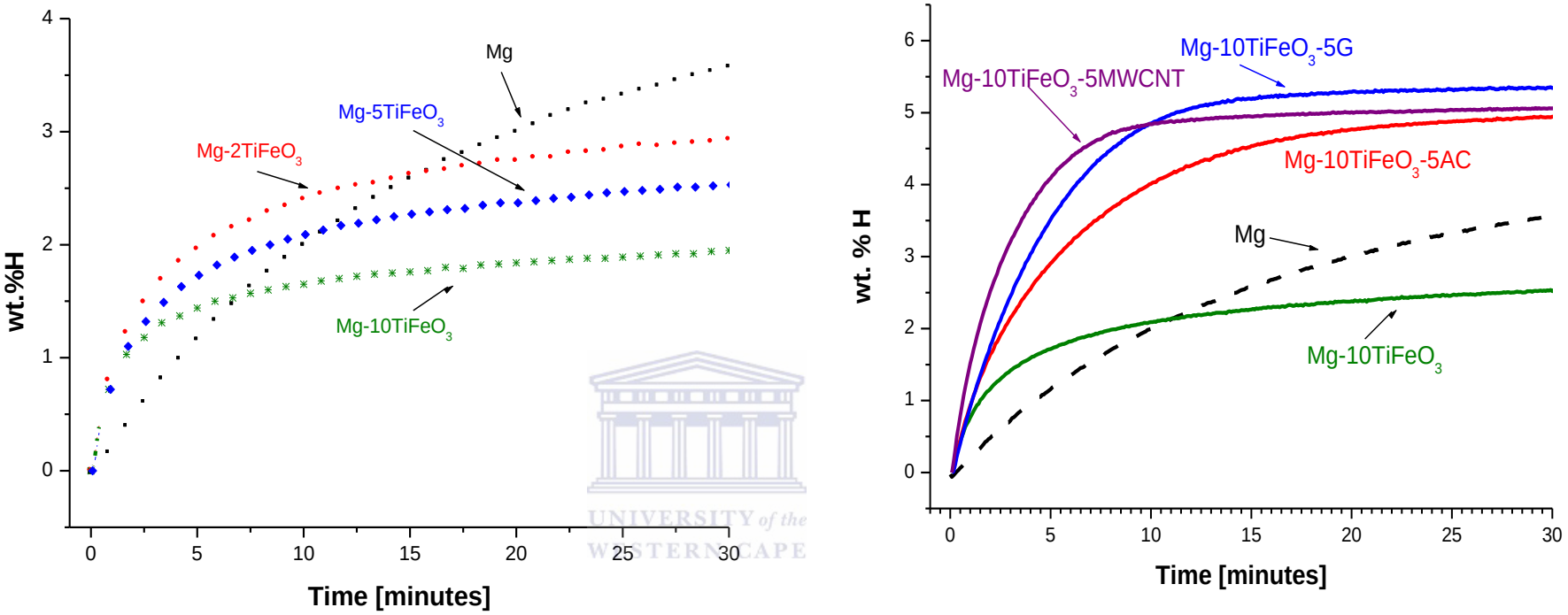

A **B**

Figure 4-45: TDS/re-hydrogenation curves at 250°C and ~15 bar H_2: (A) Mg-*x*$TiFeO_3$ and (B) Mg-5C-10 $TiFeO_3$ composite samples

Table 4.20: Fitted re-hydrogenation characteristics of Mg-*x*$TiFeO_3$ and Mg-5C-10$TiFeO_3$ composite samples

Sample	Conditions		Fitted kinetic parameters (eqn. 3.2)			
	Preceding dehydrogenation temperature [˚C]	Cycle #	C_{max} [wt.% H]	t_R [minutes]	*n*	Pearson correlation coefficient, R^2
HRBM Mg	465	1	3.405 ± 0.001	35.05 ± 0.005	0.726 ± 0.001	0.99365
	407	2	4.976 ± 0.001	23.47 ± 0.005	0.731 ± 0.002	0.99323
Mg-2$TiFeO_3$	470	1	3.608 ± 0.006	10.92 ± 0.288	1 ± 0.031	0.8315
	467	2	3.259 ± 0.005	7.64 ± 0.233	1 ± 0.035	0.8335
Mg-5$TiFeO_3$	453	1	2.304 ± 0.004	4.54 ± 0.216	1 ± 0.053	0.66282
	430	2	2.165 ± 0.005	6.32 ± 0.269	1 ± 0.048	0.7062
Mg-10$TiFeO_3$	465	1	2.981 ± 0.008	15.05 ± 0.468	1 ± 0.037	0.76307
	450	2	2.619 ± 0.007	5.41 ± 0.183	1 ± 0.040	089574
Mg-5AC-10$TiFeO_3$	470	1	5.298 ± 0.001	16.00 ± 0.038	1 ± 0.003	0.99907
	430	2	5.137 ± 0.003	6.43 ± 0.075	1 ± 0.013	098028
Mg–5MWCNT-10$TiFeO_3$	464	1	5.290 ± 0.002	4.15 ± 0.046	1 ± 0.013	0.98372
	457	2	5.179 ± 0.001	3.11 ± 0.049	1 ± 0.017	096947
Mg-5G-10$TiFeO_3$	470	1	5.44 ± 0.002	4.62 ± 0.031	1 ± 007	0.99459
	467	2	5.28 ± 0.002	5.43 ± 0.043	1 ± 0.009	0.99402

4.4.3.2. Thermal hydrogen desorption behaviour of as-milled and re-hydrogenated Mg-$TiFeO_3$ and Mg-C-$TiFeO_3$ composites

Table 4.21 summarizes the hydrogen thermodesorption properties of the as-milled and re-hydrogenated samples of the Mg-*x*$TiFeO_3$ and Mg-5C-$TiFeO_3$. Selected hydrogen thermodesorption traces from the re-hydrogenated hydride-forming materials are shown in Figure 4.46. From the obtained results in Table 4.21, the addition of $TiFeO_3$ to Mg during HRBM shifts the onset desorption peak temperature and peak maximum temperature lower by ~100°C and ~ 60°C to that of re-hydrogenated HRBM Mg having dehydrogenation temperature range and peak maximum temperature at 325-402°C and 362°C, respectively. The lowering of the H_2 evolution peak confirms improved dehydrogenation kinetics for the material prepared using $TiFeO_3$ additive to Mg. Dehydrogenation performances of the carbon-containing materials (Figure 4.46) were found to be shifted to lower temperature range than that of re-hydrogenated Mg. For the additives of graphite and activated carbon, the improvements, however, are less pronounced than for that for Mg–10$TiFeO_3$ and as for MWCNT, they are similar to the latter. The dehydrogenation temperature range and peak maximum were obtained at ~228-350°C and ~316°C for re-hydrogenated Mg-5MWCNT-10$TiFeO_3$.

Lowering in desorption rate was noted for the re-hydrogenated Mg-*x*$TiFeO_3$ composites samples as compared to their as-milled counterpart. This can be ascribed to the presence of MgO phase that makes it difficult for the hydrogen to diffuse through as observed in the XRD results. Introducing the carbon type significantly improved the

desorption rate, with the re-hydrogenation rates close to undoped Mg. This indicates that $TiFeO_3$ catalytic activity is more effective when the additive is dispersed within the powder than on the particle surface as observed in the TEM results. In all the Mg-5C-10$TiFeO_3$ composites, the area under the curve remains constant, that is to say, there is no loss of storage capacity during repeated re-hydrogenation measurements.

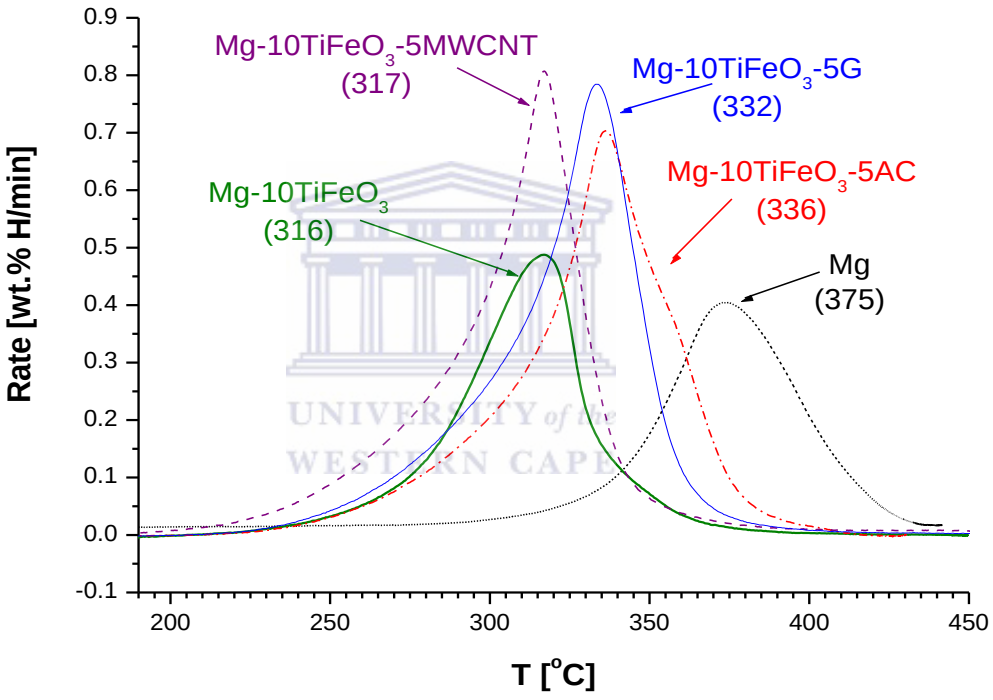

Figure 4-46: Thermodesorption spectra (heating rate of 5°C/min) of hydrogen from MgH_2 hydride of the as-milled Mg-*x* $TiFeO_3$ composite samples

Table 4.21: Hydrogen thermodesorption properties of Mg-*x*$TiFeO_3$ and Mg-5C-10$TiFeO_3$ measured in a Sievert–type apparatus heated from RT ~ 460°C at 5°C/min under vacuum.(#1 for as-milled, #2 re-hydrogenated; C= G, MWCNT, AC and x = 2, 5, 10 wt.%)

Sample	Cycle #	Decomposition range [°C]	Peak desorption Temperature [T_{max}]
Mg	1	340-380	364
	2	325-402	375
Mg-2$TiFeO_3$	1	281-413	347
	2	229-385	338
Mg-5$TiFeO_3$	1	263-386	328
	2	202-359	(300) 321
Mg-10$TiFeO_3$	1	258-377	293
	2	242-359	316
Mg-5AC-10$FeTiO_3$	1	223-367	317
	2	242-388	336
Mg-5G-10 $TiFeO_3$	1	227-372	319
	2	242-374	331
Mg-5MWCNT-10 $TiFeO_3$	1	218-373	320
	2	228-350	316

4.4.4. DISCUSSION

In this chapter, the use of $TiFeO_3$ with or without carbon materials as catalytic additive to promote hydrogenation of Mg by HRBM under hydrogen atmosphere was studied. From the obtained results, the addition of $TiFeO_3$ significantly enhanced sorption properties in comparison with undoped Mg. The addition of $TiFeO_3$ works very well both as dispersing agent, preventing the agglomeration and cold-welding of MgH_2 and

facilitates the refinement of the hydride particles during milling. And as a catalyst, it enhances the hydrogen diffusion throughout the Mg/MgH_2 matrix. The obtained materials exhibited high hydrogen capacity as well as an attainment of a constant hydrogen capacity in ~ 1 hour of HRBM and yielded nanostructured materials (crystalline size of ~10 nm). The hydrogenation rate were found to be dependent on the initial $TiFeO_3$ quantity milled with Mg with fast hydrogenation rate observed with higher quantity of $TiFeO_3$. The amount of $TiFeO_3$ added to magnesium should be from 2 to 20 wt.% as respect to the amount of the latter. The lower limit is a threshold when the improvements of the hydrogenation/dehydrogenation performances of the material appear. Phase structural studies show that reduction of $TiFeO_3$ during HRBM results in the formation of TiFe that is catalytic towards hydrogenation of Mg and reaction mechanism for this *in situ* reduction proposed in section 4.4.2.1. Re-hydrogenation properties showed improvement of dehydrogenation and re-hydrogenation kinetics, but reduces the reversible hydrogen storage capacity of the material when higher quantity of $TiFeO_3$ was used, and this is ascribed to the increased MgO phase abundance when high quantity of $TiFeO_3$ is used. The reversible hydrogen capacity can, however, be increased by the usage of carbon co-additives.

Moreover, the use of $TiFeO_3$ in the form of natural ilmenite has added advantages as is cheap and easily available material than their corresponding transition metal alone. The usage of ilmenite compared to known similar solutions of hydrogenation of magnesium at the presence of oxides, has the following advantages:

- Low cost (e.g., as compared to niobium oxide);

- Acceptable hardness (5–6 Mohs) that is high enough to facilitate nanostructuring of the softer magnesium (hardness 2.5 Mohs) and at the same time, low enough to avoid the damage of the grinding tools which can be made even by low-grade steels; and
- Significant improvements of hydrogenation, dehydrogenation and re-hydrogenation performances similar to ones achieved within the prior art with the usage of expensive metallic catalysts.

Co-doping of $FeTiO_3$ with carbon materials showed the presence of an incubation period that was dependent on the carbon type, followed by a hydriding curve that rose immediately until a constant hydrogen capacity. The incubation period is likely to be caused by the carbon materials absorbing some of the mechanical hydriding energy that is generated during HRBM. This was also explained in section 4.1 for Mg-C hybrid materials. Re-hydrogenated Mg-5C-10$TiFeO_3$ composites showed improved hydrogenation kinetics and storage capacity compared to Mg-$FeTiO_3$ composites without any carbon material, and their phase structural analysis show lowering in the MgO layer formation. The presence of carbon materials is known to give origin to carbon based radicals that react with oxygen containing species during milling, thus, preserving magnesium from oxidation [280]. In so doing, this facilitates easy access of H-atoms to the magnesium grain, which increases both the absorption kinetics and hydrogen storage capacity [196, 281]. The highest hydrogen capacity was observed for the composite of Mg-5MWCNT-10$FeTiO_3$.

CHAPTER 5:Conclusions and Recommendations

This chapter presents the conclusions and recommendations of the study. The main objective of the present study was to improve hydrogen sorption properties of MgH_2. The challenges with the use of MgH_2 as hydrogen storage material are: (i) poor hydrogen absorption/desorption kinetics, (ii) too stable for most applications, (iii) difficult to be activated for hydrogen absorption. In the current research study, the preparation of MgH_2 by HRBM of elemental magnesium with or without additives under hydrogen atmosphere was undertaken. Based on the results obtained in the current work, the results are summarized below as follows:

5.1. Summary: Mg – C nanocomposites

High energy reactive ball milling (HRBM) of magnesium under hydrogen atmosphere at the presence of (≥ 1 wt.%) of different carbon materials, including graphite, activated carbon, multi-wall carbon nanotubes, expandable, and thermally-expanded graphite, was studied and related to the type and amount of carbon. Structure, morphology, hydrogen absorption and desorption performances of the obtained composite materials were characterized using a number of complementary techniques including XRD and synchrotron XRD, particle size measurements, high resolution SEM and TEM, TGA/DSC, TDS, and volumetric measurements of the re-hydrogenation kinetics. Hydrogen absorption data was processed using formal kinetic analysis and yielded kinetic parameters of the (re)hydrogenation processes.

The HRBM of magnesium with the carbon materials results in the formation of the Mg–C composite materials exhibiting the following properties:

- Complete hydrogenation of magnesium to yield MgH_2 takes place and is accompanied by the formation of materials where carbon is uniformly distributed in between the nano-scale MgH_2 particles.
- Mg-C hybrid materials possess improved hydrogenation kinetics during HRBM compared to pure Mg. The additives of activated carbon and thermally-expanded graphite induce significant effect on the hydrogenation process already at their low content if 1 wt.%. For the anisotropically "hard" carbon materials like MWCNT, a larger amount of additive, 5 wt.%, is required to achieve the same increase in the hydrogenation rates.
- Appearance of an incubation period of hydrogenation of magnesium with additive of graphite is observed, which is required to delaminate the graphene layers from the bulk graphite. Similarly, the incubation period also appears for the MWCNT to start their fracturing. The duration of the incubation period is quite sensitive to the ball milling conditions and can be controlled by the optimization of the vial size and the rotation speed.
- Reduction of MgH_2 particle size for the as-milled and lower crystalline size for the re-hydrogenated samples, as compared to HRBM Mg.
- Improved hydrogen absorption-desorption cycle life and temperature stability of the composite materials tolerating cycling at a high temperature as 460°C.
- The destruction of the carbon species during the HRBM, to form stacked graphene layers, plays vital role in causing favourable changes and in facilitating the hydrogenation kinetics because of the formation of hydrogen-transferring interfaces on the phase boundaries between the carbon and the formed MgH_2.
- The composites of Mg-C showed minor (similar) improvements of the re-hydrogenation kinetics. Analysis of the corresponding experimental data shows absence

of the direct catalytic effect of carbon on hydrogenation – dehydrogenation of Mg and suggests that carbon plays a role of a carrier of the "activated" hydrogen by spill-over mechanism.

- Dehydrogenation performances of the magnesium–carbon nanocomposites were found to be very sensitive to exposure to the gases containing even trace amounts of oxygen and water vapours. The "contaminated" samples are characterized by higher dehydrogenation temperatures and appearance of multi-peaks on DSC or TDS curves. The "contamination" effect is less pronounced for the composites containing multi wall carbon nanotubes.

5.2. Summary: Mg-M-(C) (M=Pd, BCC-V, ZrNi) and Mg-$TiFeO_3$-(C) nanocomposites

The transformation of Mg→ MgH_2 during HRBM of Mg with Pd black, BCC-V, ZrNi, and $TiFeO_3$) in H_2 atmosphere was accomplished in < 1.5 hour with the formed hydride having high hydrogen capacity (Figure 5.1).

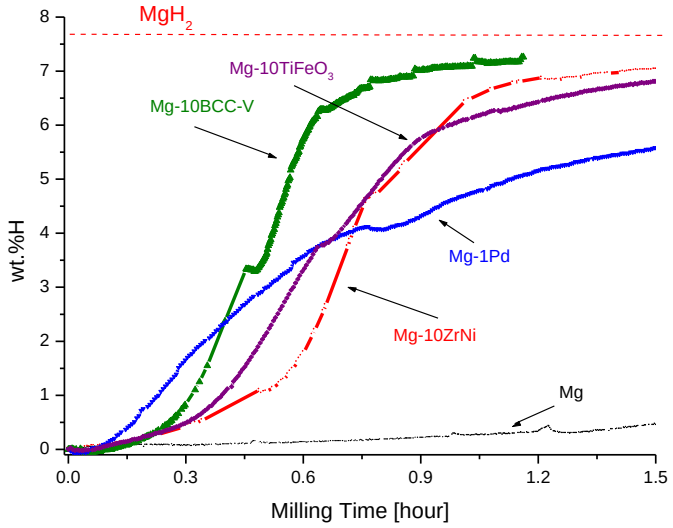

Figure 5-1: Hydrogenation kinetics curve of Mg with different additives HRBM under hydrogen atmosphere

The fast hydrogenation rate can be ascribed to the catalytic effect of metallic particles present in the composite (Pd, BCC-V, ZrNi), or formed due to reduction of the oxide additive ($TiFeO_3$) to dissociate hydrogen molecule at low temperature and release the H-atoms at the interface of Mg/M particle, in so doing it acts as H-atoms pump to improve the hydrogenation process. Once the hydrogenation has started, the outer region and the grain boundaries becomes saturated leading to lower hydrogenation kinetics and capacity as the centre of the grain becomes inaccessible for further hydrogenation. Fast hydrogenation kinetics rates were observed during TDS/re-hydrogenation measurements. However, the saturation of the hydrogenation curves at lower hydrogen capacity than their theoretical capacity took place. This was ascribed to crystallization/sintering of the material upon repeated cycling, with composites crystallite size showing increase in size compared to the as-milled composite, and their morphology show much bigger particles that agglomerates. Introducing carbon materials that would aggregate along the grain boundaries of Mg particles serving as hydrogen diffusion channel and inhibit particles/crystalline growth, in so doing both the absorption kinetics and hydrogen capacity can be increased [201]. However, HRBM of Mg-C-M presented an incubation period that was dependent on the carbon type. The presence of carbon materials during HRBM reduces the mechanical driving energy for H-atoms to be absorbed by Mg as was shown in chapter 4.1.

The best hydrogenation kinetics during HRBM for the Mg-C-M composites are shown in Figure 5.2. The hardness (3 Mohs) of AC compared to that of Mg metal (2.5 Mohs), played an important role during hydriding of magnesium as their continually break-off the formed MgH_2 layer formed on the Mg surface, resulting into smaller particle sizes and minimize agglomeration during ball milling. Smaller particles size and less agglomeration decrease the diffusion path length of H-atoms during absorption and

desorption. The composites of Mg-G-M presented much longer incubation period. This was ascribed to the consumption of mechanical energy during HRBM necessary for the delamination of graphite.

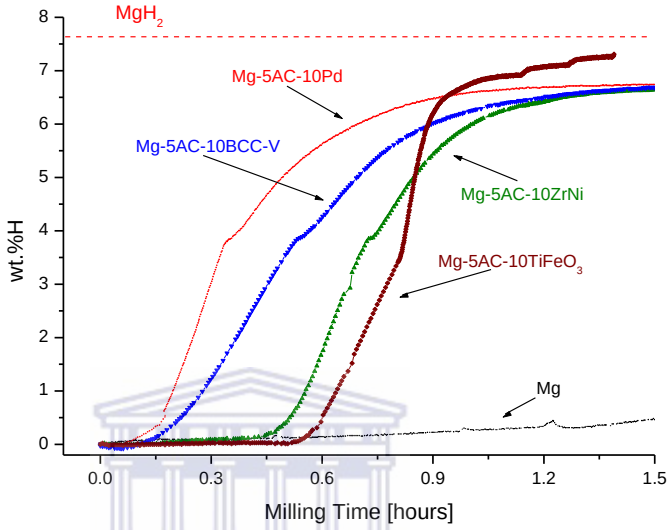

Figure 5-2: Hydrogenation kinetic curves of Mg with 5wt.% AC and different additives

Figure 5.3 show the thermodesorption properties of Mg-M composites after TDS/re-hydrogenation measurement. The composites presents much lower desorption peak temperatures, except for the composite of Mg-BCC. The lowering in desorption peak temperature shows that the metal particles on the surface of Mg/MgH_2 facilitate the recombination of H-atoms.

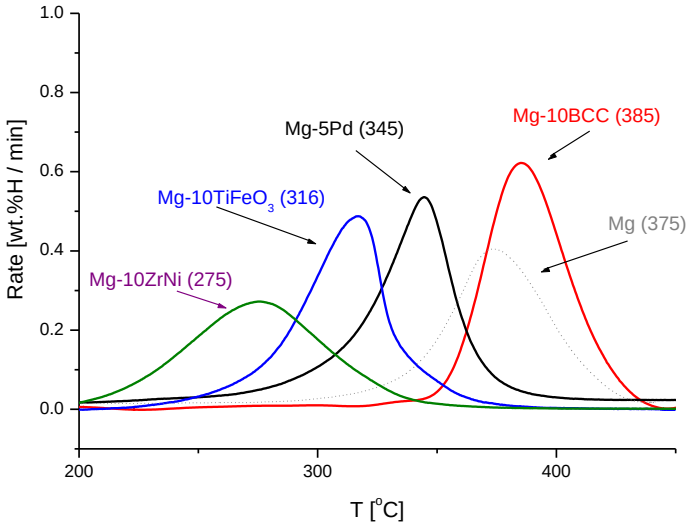

Figure 5-3: Thermodesorption properties of Mg-M composites

5.3. Conclusions

The following conclusions were drawn from this part of the research:

- Addition of Pd, BCC-V, ZrNi and $TiFeO_3$ to Mg significantly improves hydrogenation kinetics during HRBM.

- The re-hydrogenation performances of HRBM Mg alone and with non-carbon additives are very sensitive to the maximum heating temperature prior to the re-hydrogenation. Upon addition of carbon, this effect, however, is less pronounced, and the reaction rate and H-sorption capacities do not deteriorate after the heating to T_{max} = 460-470°C.

- The Mg-Pd composites did not present much improvement of the dehydrogenation and re-hydrogenation performances. This was associated with interaction of Mg with Pd to result in the disappearance of the catalytically active Pd particles and formation of Mg–Pd intermetallides.

- The improvements of the dehydrogenation and re-hydrogenation performances are much more pronounced for the additives of alloys (BCC-V, ZrNi) which do not interact with Mg during HRBM and dehydrogenation / re-hydrogenation and at the same time, are characterized by fast kinetics of the interaction with H_2 gas. The improvements were associated with catalytic effect of the additives towards dissociation of H_2 molecules (hydrogenation) and recombination of H atoms (dehydrogenation).

- The composites Mg-$TiFeO_3$ also exhibit improved dehydrogenation and re-hydrogenation kinetics due to catalytic effect of metallic nanoparticles formed by the reduction of $TiFeO_3$ during HRBM and subsequent dehydrogenation / re-hydrogenation.

- At the same time, the HRBM Mg-$TiFeO_3$ composites are characterised by low reversible hydrogen storage capacity because of formation of MgO which covers the Mg particles as a dense film inhibiting their re-hydrogenation. This effect, however, becomes much less pronounced upon addition of carbon resulting in the reduction of the amount of formed MgO.

- The effect of carbon addition to Mg + $TiFeO_3$ is also associated with the facilitation of reduction of $TiFeO_3$ in the composite to yield TiFe which plays role of hydrogenation/dehydrogenation catalyst.

5.4. Impact and Recommendations

This work was carried out within the South African Hydrogen and Fuel Cell Technologies Research, Development, and Innovation strategy (HySA) under the auspice of the Department of Science and Technology (DST) of South Africa; project KP3-S04 – On-Board Hydrogen Storage.

The knowledge emanating from this research project is expected to contribute to the development of hydrogen and fuel cell technology development in South Africa through the identification of promising compositions and preparation routes for weight-efficient magnesium-based nanostructured hydride materials utilising South African feedstock. These materials can be used in various stationary and mobile applications for hydrogen storage and related technologies (including heat management), and thus reduce the dependence of energy supply from fossil fuels.

Based on the analyses and conclusions of this study, the following recommendations regarding future R&D activities were made:

1. Magnesium-based nanocomposites can be used for weight-efficient hydrogen storage in a number of mobile and stationary applications where moderately high temperatures (~300°C) to provide hydrogen release from the materials available.
2. Taking into account high hydrogenation and dehydrogenation rates and good cycle stability of the studied nanocomposites at the temperatures up to ~450°C, as well as high heat effects of their hydrogenation and dehydrogenation, it seems to be very promising in addition to hydrogen storage, to use these materials in various heat management applications including heat transformation and heat upgrade in the temperature range 300–450°C.
3. Further optimisation of the hydrogen storage nanocomposite materials to be prepared by HRBM of Mg with additives should be based on the usage of abundant and cheap $TiFeO_3$ as a main (catalytic) additive and sp^2-hybridized carbon (activated carbon, MWCNT, graphite, etc.) as a co-additive.
4. The optimisation studies should be focused on (i) further improvement of dehydrogenation and re-hydrogenation performances, (ii) upscale the preparation

procedures, and (iii) integration of the materials in hydrogen storage and delivery systems.

5.5. Research outputs

Research outputs from this PhD project include:

1. Patent application "Method of preparation of hydride-forming material on the basis of nanostructured magnesium hydride" by M.W.Davids, M.Lototskyy, J.M.Sibanyoni, M.Williams, B.G. Pollet, V.Linkov (ZA2012/08851, 22.11.2012).
2. Research articles in peer-reviewed journals:
   2.1. "Magnesium-Carbon Hydrogen Storage Hybrid Materials Produced by Reactive Ball Milling in Hydrogen" by M.Lototskyy, J.M.Sibanyoni, R.V.Denys, M.Williams, B.G.Pollet, V.A.Yartys (Carbon; doi: 10.1016/j.carbon.2013.01.058, 19.01.2013).
   2.2. "Hydrogen Absorption Study of High-Energy Reactive Ball Milled Mg Composites with Palladium Additives", by M. Williams, J. M Sibanyoni, M. Lototsky, B.G. Pollet (Journal of Alloys and Compounds; doi:10.1016/j.allcom.2013.01.086, 18.01.2013).
   2.3. Upon finalising the filling procedure for the patent application (1), a research paper on magnesium-based HRBM composites containing additive of $TiFeO_3$ will be submitted to International Journal of Hydrogen Energy.
3. Presentations at international conferences:
   3.1. "Hydride-Forming Additives and Carbon for Hydrogen Storage", by M.Lototskyy, M.Williams, J.Sibanyoni, J.K.Solberg, V.A.Yartys, R.Denys; International Conference in Hydrogen Storage Systems, Norway, June 2010 (poster presentation).

3.2. "Nanostructured Composites of Magnesium, Hydride-Forming Additives and Carbon for Hydrogen Storage", by M.Lototskyy, M.Williams, J. M.Sibanyoni, J.K.Solberg, V.A.Yartys, R.Denys; International Symposium on Metal-Hydrogen Systems, Fundamentals and Applications (MH-2010), Moscow, Russia, July 19-23, 2010 (poster presentation; the abstract was published in the Book of Abstracts, part I, p.373).

3.3. "Hydrogen Absorption Study of High-Energy Reactive Ball Milled Mg Composites with Catalytic PGM-based Additives", by M.Williams, J.M.Sibanyoni, M.Lototskyy, B.Pollet; International Symposium on Metal-Hydrogen Systems, Fundamentals and Applications (MH-2012), Kyoto, Japan, October 21-26, 2012 (poster presentation; the abstract was published in the Program and Abstracts Book, p.238).

4. Presentations at local conferences:

4.1. "Hydrogen Storage in Magnesium", by J.M.Sibanyoni, M. Lototskyy; Hydrogen storage of South Africa: March, 2009, University of Stellenbosch Business School; Bellvista, South Africa.

4.2. "Hydrogen Storage in Mg prepared by high-energy reactive ball milling", by J.M.Sibanyoni, M.Lototskyy; Africa Energy Week Summit, July 2009; Cape International Convention Centre, South Africa.

4.3. "Microstructural Study of High Energy Ball milled Mg composites with Carbon additives", by J.M.Sibanyoni, M.Williams, M.Lototskyy; 49th Microscopy of the Southern African conference, CSIR conference centre, 05-09 December 2011, Pretoria. South Africa.

4.4. "In situ Pressure Monitoring of Nanostructured Solid Magnesium Hydride Preparation by Ball Milling Mg with Carbon allotropes/or with Metal alloy under

H_2 Atmosphere", by J.M.Sibanyoni, M.Williams, M.Lototskyy, SANHARP 2nd ANNUAL POSTGRADUATE CONFERENCE.,12-14 OCTOBER 2011, iTHEMBA LABS, CAPE TOWN

CHAPTER 6: References

1. J. Yang, A. Sudik, C. Wolverton, D. J. Siegelw; *Chem. Soc. Rev*., 39 (2010) 656-675.
2. G. Principi, F. Agresti, A. Maddalena, S. Lo Russo; *Energy*., 34 (2009) 2087-2091.
3. L. Schlapbach, A. Zuttel; *Nature*., 414 (2001) 353-358.
4. L. Zaluski, A. Zaluska, J. O. Ström-Olsen; *J Alloys Compds*., 253 (1997) 70-79.
5. J. Huot, G. Liang, R. Schulz; *Appl Phys.A*.,72 (2001) 187-195.
6. T. Vegge, L. S. Hedegaard-Jensen, J. Bonde, T. R. Munter, J. K. Norskov; *J Alloy Compds*., 386 (2005) 1-7.
7. M. Au; *J Alloys Compds*., 117 (2005) 37-44.
8. www.eskom.co.za.
9. http://ec.europa.eu/energy/publications/doc/2012_energy_roadmap_2050_en.pdf].
10. http://www.agenergy.org.
11. http://www.essortment.com.
12. W. Grochaia, P. P. Edwards; *Chem Rev*., 104 (2004) 1283-1315.
13. G. Liang; *J Alloys Compds*., 370 (2004) 123-128.
14. http://www.eere.energy.gov.afdc/fuels/hydrogen_alternative.html.
15. www.hydrogen.org.za.
16. F. Schuth, B. Bogdanović, M. Felderhoff; *Chem Comm*., 20 (2004) 2249-2258.

17. Satyapal *et.al*. 2006, U. S. Department of Energy, Energy Efficiency and Renewable Energy, Targets for on-board hydrogen storage systems (2008).

18. B. Gupta; Hydrogen Fuel; Production, Transport and Storage CRC Press, Taylor& Francis Group, Boca Raton London New York, 2009.

19. U. Bossel, B. Eliasson, G. Taylor; The future of the hydrogen economy: Bright or Break?, *Preceedings of the European Fuel cell Forum 2003 Fuel Cell Seminar*. European Fuel Cell Forum., (2003).

20. G. Sandí; *The Electrochemical Society Interface*., 13 (2004) 40–44.

21. R. von Helmont, U. Eberle;. *J. Power Sources*, 165 (2007) 833–843.

22. L. Zhou; *Renewable and Sustainable Energy Reviews*., 9 (2005) 395-408.

23. M. Rogers, S. Barcelo, X. Chen, T. J. Richardson, V. Berube, G. Chen, M. S. Dresselhaus, C. P. Grigoropoulos, S. S. Mao; *Appl Phys* A., 96 (2009) 349-352.

24. V. B. Kazansky, V. Y. Borovkov, A. Serich, H. G. Karge; *Microporous and Mesoporous Materials*., 22 (1998) 251-259.

25. H. W. Langmi, A. Walton, M. M. Al-Mamouri, S. R. Johnson, D. Book, J. D. Speight; *J. Alloys Compds*., 356–357 (2003) 710-715.

26. D. Fraenkel; *J Chem Soc, Faraday Trans*., 177 (1981) 2041.

27. G. T. Palomino, M. R. L. Carayol, C. O. Areán, *J Mater Chem*., 16 (2006) 2884.

28. P. Benard, R. Chahine; Scr Mater., 56 (2007) 803-808.

29. D. J. Collins, H. C. Zhou; *J Mater Chem*., 17 (2007) 3154-3160.

30. J. L. C. Rowsell, O. M. Yaghi; *Angew. Chem. Int. Ed*., 44 (2005) 4670–4679.

31. S. -Y. Lee, S. -J. Park; *Int. J. Hydrogen Energy*., 36 (2011) 8381-8387.

32. K. -S. Lin, A.K. Adhikari, K. -C. Chang, M. -T. Tu, W. Lu; *Cat. Today*., 164 (2011) 23-27.

33. E. G. Skolnik.; *Proceedings of the 2000 Hydrogen Program Review*, NREL/CP-570-28890.

34. J. L. C. Rowsell, O.M. Yaghi; *Mater*., 73 (2004) 3-14.

35. D. Saha, S. Deng; *Carbon*., 48 (2010) 3471-3476.

36. L. -P. Ma, Z. S. Wu, J. Li, E. -D. Wu, W. -C. Ren, H. -M. Cheng; *Int J Hydrogen Energy*., 34 (2009) 2329-2332.

37. Y. Yürüm, A. Taralp, T. N. Veziroglu, *Int J Hydrogen Energy*., 34 (9) (2009) 3784-3798.

38. X. R. Zhang, D. P. Cao, J. F. Chen; *J Phys Chem*. B., 107 (2003) 4942.

39. T. F. Baumann, M. A. Worsley, T. Y. -J. Han, J. H. Satcher Jr; *J Non-Crystalline Solids*., 354 (29) (2008) 3513.

40. F. H. Stephens, V. Pons and R. T. Baker; *Dalton Trans*., 2007, 2613

41. S. C. Amendola, M. Binder, S. L. Sharp-Goldman, M. T. Kelly, P. J. Petillo; *US Pat*., 6,534,033 B1, 2003.

42. Q. Zhang, G. M. Smith , Y. Wu; *Int. J. Hydrogen Energy*., 32 (2007) 4731-4735.

43. G. P. Pez, A. R. Scott, A. C. Cooper, H. S. Cheng; *US Pat*., 7, 429,372 B2, 2004.

44. R. P. Shrestha, H. V. K. Diyabalanage, T. A. Semelsberger, K. C. Ott, A. K. Burrell; *Int. J. Hydrogen Energy*., 34 (2009) 2616-2621.

45. C. W. Yoon, P. J. Carroll, L. G. Sneddon; *J. Am. Chem. Soc*., 131 (2009) 855-864.

46. C. W. Hamilton, R. T. Baker, A. Staubitz, I. Manners; *Chem. Soc. Rev*., 38 (2009) 279-293.

47. T. B. Marder; *Angew. Chem., Int. Ed*., 46 (2007) 8116-8118.

48. L-B-Systemtechnik GmbH, www. H2cars.de.2007.

49. B. Sakintuna, F. Lamari-Darkrim, M. Hirscher; *Int J Hydrogen Energy*., 32 (2007) 1121-1140.

50. A. Zaluska, L Zaluski, J. O. Ström-Olsen; *J Alloys Compds*., 288 (1999) 217-225.

51. F. D. Manchester, D. Khatamian; *Mater Sci Forum*., 31 (1988) 261-296.

52. C. P. Chen, B. H. Liu, Z. P. Li, J. Wu. Q. D. Wang; *Phys Chem*., 181 (1993) 259-267.

53. G. Liang, E. Wang, S. Fang; *J Alloys Compds*., 223 (1995) 111-114.

54. L. Schlapbach; *In Surface and Dynamic Properties , Applications*. Berlin; Springer., (1992) 328.

55. J. K. Nørskov, A. Houmøller, P. K. Johansson, B. I. Lundqvist; *Phys Rev Lett*., 46 (1981) 257-260.

56. N. Gerard, S. Ono; Hydride formation and decomposition kinetics.– In: L. Schlapbach (Ed.), Hydrogen in Intermetallic Compounds, Springer-Verlag, 1992, vol.2, p.165–195.

57. P. -A. Huhn, M. Dornheim, G. Barkhordarian, T. Klassen, R. Bormann. Thermal stability of catalyzed nanocrystalline MgH2 for hydrogen storage.– International

Symposium on Metal-Hydrogen Systems – MH2004, Kraków, Poland, 5-10 September 2004.

58. G. Sandrock, K. J. Gross, G. Thomas; *J Alloys Compds*., 339 (2002) 299-308.

59. K. S. Jeong, B. S. Oh; *J Power Sources*., 105, 1 (2002) 58-65.

60. X. B. Yu, Y. H. Guo, H. Yang, Z. Wu, D. M. Grant, G. S. Walker; *J. Phys. Chem.* C., 113 (2009) 5324-5328.

61. S. G. Chalk; J. F. Miller; *J Power Sources.*, 159 (2006) 73-80.

62. M. U. Niemann, S. S. Sriniavsan. A. R. Phani, A. Kumar, D. Yogi Goswami,, E. K. Stefanakos;. *J Nanomaterials*., vol 2008 (2008).

63. E. Fontes, E. Nilsson; *The Industrial Physicist*., August/September (2001) 14-17.

64. E. Martin, S. A. Shaheen, T. E. Lipman, J. R. Lidicker; *Int J. Hydrogen Energy*., 34 (2009) 8670-8680.

65. J. Hout, I. P. Swainson, R. Schulz; *J Alloys Compds*., 292 (1999) 292.

66. X. L. Wang, S. Suda; *J Alloys Compds*., 231 (1995) 380-386,

67. Z. P. Li, B. H. Liu, K. Hitaka, S. Suda; *J Alloys Compds*., 330 (2002) 776-781.

68. L. Zaluski, A. Zaluska, P. Tessier, J.O. Ström-Olsen, R. Schulz; *J Alloys Compds*., 227 (1995) 53-57.

69. M. Bououdina, D. Grant, G. Walker; *Int J Hydrogen Energy*., 31 (2006) 177-182.

70. J. H.N van. Vucht, F. A. Kuijpers, H.C.A.M. Bruning; *Phillips Res Rep*., 25 (1970) 133.

71. H. Aoyagi, K. Aoki, T. Masumoto; *J Alloys Compds*., 231 (1995) 804-809.

72. A. Demircan, M. Demiralp, Y. Kaplan, M. D. Mat, T.N. Veziroglu; *Int J Hydrogen Energy*., 30 (2005) 1437-1446.

73. B. Tanguy, J. –L. Soubeyroux, M. Pezat, J. Portier, P. Hagenmuller; *Mater. Res. Bull*., 11 (1976) 1441-1447.

74. B. Bogdanovic, M. Schwickardi; *J Alloys Compds*., 253 (1997) 1-9.

75. P. Chen, Z. Xiong, J. Luo, J. Lin, K. L. Tan; *Nature*.,420 (2002) 302-304.

76. D. Wenger. W. Polifke, E. Schmidt-Ihn, T. Abdel-Baset, S. Maus; *Int J Hydrogen Energy*., 34 (2009) 6265-6270.

77. H. Smithson, C. A. Marianetti, D. Morgan, A. Van der Ven, A. Predith, G. Ceder; *Phys. Rev*. B., 66 (2002) 144107-14416.

78. R. Yu, P. K. Lam; *Phys. Rev*. B., 37 (1988) 8730.

79. T. Norikate, M. Aoki, S. Towata, Y. Seno, Y. Hirose, E. Nishibori, M. Takata, M. Sakata; *Appl. Phys. Lett*., 81 (2002) 2008.

80. A. Zuttel, S. Rentsch, P. Wenger, P. Sudan, Ph. Mauron, Ch. Emmenegger; *J. Alloy Compds*., 356 (2003) 515-520.

81. A. Zuttel, P. Wenger, S. Rentsch, P. Sudan, P. Mauron, C. Emmenegger; *J. Power Sources*., 118 (2003).1-7.

82. J. Rijssenbeek, Y. Gao, J. Hanson, Q. Huang, C. Jones, B. Toby; *J Alloys Compds*., 454 (2008) 233-244.

83. H. Chu, Z. Xiong, G. Wu, T. He, C. Wu, P. Chen; *Int J Hydrogen Energy*., 35 (15) (2010) 8317-8321.

84. M. H. Sørby, Y. Nakamura, H. W. Brinks, T. Ichikawa, S. Hino, H. Fujii, B. Hauback,; *J Alloy Compds*.,428 (2007) 297-301.

85. S. Orimo, Y. Nakamori, J. R. Eliseo, C. M. Jensen; *Chem Rev*., 107 (2007) 4111-4132.

86. Y. Nakamori, K. Miwa, A. Ninomiya, H. Li, N. Ohba, S. Towata, A. Züttel, S. Orimo; *Phys. Rev*. B., 74 (2006) 045126-045134

87. T. Matsunaga, F. Buchter, P. Mauron, M. Bielman, Y. Nakamori, S. Orimo; *J Alloys Compds*., 459 (2008) 583–8,

88. K. Chlopek, C. Frommen, A. Leon, O. Zabara, M. Fichtner.; *J Mater Chem*., 33 (2007) 3496–3503.

89. V. N. Konoplev, V. M. Bakulina; *Russian Chemical Bulletin*., 20 (1971) 136–8.

90. H. W. Li, K. Kikuchi, Y. Nakamori, K. Miwa, S. Towata, S. Orimo; Scripta Materialia., 57 (2007) 679–82.

91. V. N. Konoplev, Russ. *J. Inorg. Chem*., 25 (1980) 964-966.

92. H. -W. Li, K. Kikuchi, Y. Nakamori, N. Ohba, K. Miwa, S. Towata, S. Orimo; *Acta Mater*., 56 (2008) 1342–1347.

93. G. L. Soloveichik, Y. Gao, J. Rijssenbeek, M. Andrus, S. Kniajanski, R. C. Bowman Jr., S. –J. Hwang, J. –C. Zhao; *Int. J. Hydrogen Energy*., 34 (2009) 916–928.

94. R. B. Biniwale, S. Rayalu, S. Devotta, M. Ichikawa; *Int J Hydrogen Energy*., 33 (2007)360-365.

95. S. Hodoshima, H Arai, S. Takaiwa, Y. Saito; *Int J Hydrogen Energy*., 28 (2003) 1255-1262.

96. P. Taube, M. A. Taube; *Adv Hydrogen Energy*., 2 (1981) 1077-1082.

97. J. K. Ali, J. Newson, D. W. T. Rippin; *Chem Eng Sci*., 13 (1994) 2129-2134.

98. N. Kariya, A. Fukuoka, M. Ichikawa; *Appl Catal A Gen*., 233 (2002) 91-102.

99. S. Hodoshima, H. Arai, Y. Saito; *Int. J Hydrogen Energy*., 28 (2003) 197-204.

100. F. Alhumaidan, D. Cresswell, A. Garforth; *Energy Fuels*., 25 (10) (2011) 4217-4234.

101. J. Huot, G. Liang, R. Schulz; J Alloys Compds., 353 (2003) L12-L15.

102. H. I. Schlesinger, H. C. Brown, A. B. Finholt, J. R. Gilbreath, H. R. Hockstra, E. K. Hydo; *J. Am. Chem. Soc*., 75 (1953) 215.

103. R. Aicllo, J. H. Sharp, M. A. Matthews; *Int. J. Hydrogen Energy.*, 24 (1999) 1123-1130.

104. J. H. Kim, H. Lee, S. C. Han, H. S. Kim, M. S. Song, J. Y. Lee; *Int. J. Hydrogen Energy*., 29 (2004) 263-267.

105. J. Widegren, R. G. Finke, *J. Mol. Catal. A: Chem*., 198 (2003) 317-341.

106. C. Song; *Catal. Today.*, 77 (2002) 17-49.

107. H. -Y. Tang, P. Erickson, H. C. Yoon, C-H. Liao; *Int J Hydrogen Energy*., 34 (2009) 7656-7665.

108. H. C. Yoon, P. A. Erickson. H-M. Kim; *Int J Hydrogen Energy*., 33 (2008) 6619-6626.

109. T. V. Choudhary, D.W. Goodman; *Catalysis Today*., 77 (2002) 65-78.

110. A. Wojcik, H. Middleton, I. Damopoulos, J. Van Herle; *J Power Sources*., 118 (2003) 342-348.

111. R. W. Wagemans, J. H. van Lenthe, P. E. de Jongh, A. J. van Dillen, K. P. de Jong; *J. Am. Chem. Soc*., 127 (2005) 16675-16680.

112. B. Bogdanovic; *J Alloys Compds*., 282 (1999) 84-92.

113. C. M. Arajuo; *J Appl Phys*., 98 (2005) 09610-09619.

114. A. M. Seayad, D. M. Antonelli; *Adv. Mater*., 16 (2004) 765-777.

115. G. Liang, J. Huot, S. Boily, R. Schulz; *J Alloys Compds*., 305 (2000) 239-245.

116. M. Martin, C. Commel, C. Borkhart, E. Fromm; *J Alloys Compds*., 238 (1996) 193-201.

117. K. Bukka. J. D. Miller, J. Shabtai; *Clays Clay Miner*., 40 (1992) 92-102.

118. Y. S. Lee. Y. Filinchuk, H. S. Lee, J. Y. Suh, J. W. Kim, J. S. Yu. Y. W. Cho; J Phys. Chem.C., 115 (2011) 10298-10304.

119. M. H. Mintz, Y. Zeeri; *J. Alloys Compds*., 216 (1994) 159-175.

120. G. Barkhordarian, T. Klassen, R. Bormann; *J. Alloys. Compds*., 407 (2006) 249-255.

121. M. P. Jollibois; Comptes rendus hebdomadaires des séances de l'Académie des Sciences., 155 (5) (1912) 353-355.

122. E. Wiberg, H. Goelttzer, R. Bauer; *Zeitschrift für Naturforschung. B.*, 6 (7) (1951) 394-395.

123. T. N. Dymova, Z. K. Sterlyadkina, N. G. Eliseeva: *Russ. J. Inorg. Chem.*, 6 (4) (1961) 768–773.

124. B. Bogdanovic, S. Liac, P. Sikorsky: *Angew. Chem.*, 92 (10) (1980) 845 – 846.

125. B. Vigeholm, J. Kjoller, B. Larsen; *J. Less-Common Met.*, 74 (1980) 341 –350.

126. F. J. Ellinger, C. E. Holley, B. B. Meinter; *J. Am. Chem. Soc.*, 77 (9) (1955) 2647-2648.

127. K. M. Mackay; *Hydrogen Compounds of the Metallic Elements*, E. & F.N. Spon, Ltd., London, 1966.

128. M. M. Antonova, R. A. Morozova. *Preparation Chemistry of Hydrides*; Kiev: "Naukova Dumka", 1976.

129. J. -P. Bastide, B. Bonnetot, J.-M. Létoffé, P. Claudy; *Mater Res Bull.*, 15 (9) (1980) 1215-1224.

130. J. -P. Bastide, B. Bonnetot, J.-M. Létoffé, P. Claudy; *Mater Res Bull.*, 15 (12) (1980) 1779-1787.

131. N. Gerard, S. Ono. Hydride formation and decomposition kinetics.– In: L.Schlapbach (Ed.), Hydrogen in Intermetallic Compounds, Springer-Verlag, 1992, vol.2, p.165–195.

132. T. N. Dymova e.a. Synthesis of magnesium hydride from non-activated metal; *Russ. J. Inorg. Chem.*, 6 (1963) 763–767.

133. C. M. Stander. Kinetics of formation of magnesium hydride from magnesium and hydrogen. *Z. Phys. Chem.*, 104 (1977) 229–238.

134. B. Vigeholm *et.al*. Hydrogen sorption performance of pure magnesium during continued cycling.– *Int. J. Hydrogen Energy*, 8 (10) (1983) 809-817;

135. M. H. Mintz, Z. Gavra, Z. Hadari. Kinetic study of the reaction between hydrogen and magnesium catalysed by addition of indium.– *J. Inorg. Nucl. Chem.*, 40 (1978) 765–768.

136. V. I. Mikheeva *et.al*. Hydrogen absorption by cerium alloys with magnesium.– *Russ. J. Inorg. Chem*., 8 (6) (1963) 1314–1319.

137. J. J. Reilly, R. H. Wiswall; *Inorg. Chem.*, 6 (12) (1967) 2220–2223.

138. J. J. Reilly, R. H. Wiswall; *Inorg. Chem.*, 7(11) (1968) 2254–2256.

139. B. R. Pauw, W. P. Kalisvaart, S. X. Tao, M. T. M. Koper, A. P. J. Jansen, P. H. L. Notten; *Acta Materialia*., 56 (2008) 2948-2954.

140. T. Kelkar, S. Pal, D. G. Kanhere; *Chem Phys Chem*., 9 (2008) 928-934.

141. M. Bououdina, Z. X. Guo; *J Alloy Compds*., 336 (2002) 222-231.

142. S. Bouaricha, J. P. Dodelet, D. Guay, J. Huot, S. Boily. R. Schulz; *J Alloy Compds*., 297 (2000) 282-293.

143. B. Darriet, M. Pezat, A. Hbika, P. Hagenmuller; *Int. J. Hydrogen Energy*., 5 (1980) 173–178.

144. B. P. Tarasov. Development of new hydrogen sorbing materials and rechargeable accumulators for hydrogen storage.– 2004 NORSTORE conference/workshop, Stavern, Norway, 3-5 June 2004.

145. Q. Li, Q. Lin, L. Jiang, K. –C. Chou; *J. Alloys Compds*., 368 (2004) 101–105.

146. R. Z. Valiev, R. K. Islamgaliev. L. V. Alexandrov; *Porg Mater Sci*., 45 (2000) 103-189.

147. T. G. Langdon,. *Rev. Adv. Mater. Sci*., 13 (2006) 15-26.

148. D. R. Leiva, D. Fruchart, M. Bacia, G. Girard, N. Skryabina, A. C. S. Villela, S. Miraglia, D. S. Santos, W. Botta,. *J. Int. J. Mater. Res*., 100 (2009) 1739-1747.

149. A. A. Poletaev, R.V. Denys, J. P Maehlen, J. K. Solberg, B. P. Tarasov, V. A. Yartys; *Int J Hydrogen Energy*., 37 (2012) 3548-3557.

150. Y. Wu, M. V. Lototsky, J. K. Solberg, V. A. Yartys, W. Hana, S. X. Zhou*; J Alloys Compds*., 477 (2012) 262-266.

151. I. P. Jain, C. Lal, A. Jain; *Int. J. Hydrogen Energy*., 35 (2010) 5133-5144.

152. H. Yuan, Y. A. G. Xu, C, Chen; *Material Chemistry and Physics*., 83 (2004) 340-344.

153. G. Liang, J. Huot, S. Boily, A. van Neste, R. Schulz; *J Alloys Compds*., 292 (1999) 247-252.

154. J. Charbonnier, P. de Rando, D. Fruchart, S. Miraglia, L. Pontonnier, S. Rivoirard, N. Skryabina, P. Vulliet; *J Alloys Compds*., 383 (2004) 205-208.

155. M. Y. Song, S. N. Kwon, H. R. Park, J. L. Bobet; *Int J Hydrogen Energy*., 36 (2011) 12932-12938.

156. J. L. Bobet, B. Chevalier, M. Y. Song, B. Darriet, J. Etourneau; *J Alloys Compds*., 336 (2002) 292-296.

157. M. V. Lototsky, R. V. Denys, V. A. Yartys*; Int J Energy Res*., 33 (2009) 1114-1125.

158. Y. B. Pan, Y. F. Wu, Q. Li; *Int J Hydrogen Energy*., 36 (2011) 12892-12901.

159. D. L. Croston, D. M. Grant, G. S. Walker; *J Alloys Compds*., 492 (2010) 251-258.

160. G. Barkhordarian, T. Klassen, R. Bormann; *Scr Mater*., 49 (2003) 213-217.

161. M. Y. Song, J. L. Bobet, B. Darriet; *J Alloys Compds*., 340 (2002) 256-262.

162. E. Ivanov, I. Konstanchuk, B. Bokhonov, V. Boldyrev; *J Alloys Compds*., 360 (2003) 256-265.

163. Y. Luo, P. Wang, L. P. Ma, H. M. Cheng; *J Alloys Compds*., 453 (2008) 138-142.

164. J. Huot, G. Liang, R. Schulz; *Appl. Phys*. A., 72 (2001) 187-195.

165. H. Yuan, Y. A. G. Xu, C, Chen; *Material Chemistry and Physics*., 83 (2004) 340.

166. J. Huot, G. Liang, S. Boily, A. van Neste, R. Schulz; *J Alloys Compds*., 293-295 (1999) 495-500.

167. F.C. Gennari, F.J. Castro, G. Urretavizcaya; *J. Alloys Compds*., 321 (2001) 46–53.

168. F. C. Gennari, G. Urretavizcaya, G. O. Meyer; *J Alloys Compds*., 356-357 (2003) 588-592.

169. S. Doppiu, P. Solsona, T. Spassov, G. Barkhordarian, M. Dornheim, T. Klassen, S. Surinach, M. D. Baró; *J Alloys Compds*., 404-406 (2005) 27-30.

170. S. Doppiu, L. Schultz, O. Gutfleisch; *J Alloys Compds*., 427 (2007) 204-208.

171. M. A. Lillo-Ródenas, Z. X. Guo, K. F. Aguey-Zinsou, D. Cazorla-Amorós, A. Linares-Solano; *Carbon*., 46 (2008) 126-137.

172. H. Imamura, S. Tabata, Y. Takesue, Y. Sakata, S. Kamazaki; *Int. J. Hydrogen Energy*., 25 (2000) 837-843.

173. H. Imamura. S. Tabata, N. Shigetomi, Y. Takasue, Y. Sakata; *J. Alloy Compds*., 330-332 (2002) 579-583.

174. H. Imamura, M. Kusuhara, S. Minami, M. Matsumoto, K. Masanari, Y. Sakata; *Acta Mater*., 51 (2003) 6407-6414.

175. A. D. Rud, A. M. Lakhnik, V. G. Ivanchenko, V. N. Urarw, A. A. Shkola, V. A. Dekhtyarenko, L. I. Kuskova; *Int J Hydrogen Energy*., 32 (2008) 1310.

176. M. Güvendiren, E. Baybörü, T. Öztürk; *Int. J. Hydrogen Energy.*, 29 (2004) 491-496.

177. G. X. Shang, Z. X. Guo; *J Power Sources*., 129 (2004) 73-80.

178. H. Imamura, Y. Takesue, T. Akimoto, S. Tabata; J Alloys Compds., 293-295 (1999) 564-568.

179. J. Huot, M. L. Tremblay, R. Schulz; *J Alloys Compds*., 356-357 (2003) 603-607.

180. D. Chen, L. Chen, S. Liu, C. X. Ma, D. M. Chen, L. B. Wang; *J Alloys Compds*., 372 (2004) 231-237.

181. C. Z. Wu, P. Wang, X. Yao, C. Liu, D. M. Chen, G. Q. Lu, H. M. Cheng; *J Alloys Compds*., 414 (2006) 259-264.

182. A. D. Rud, A. M. Lakhnik; *Int J Hydrogen Energy*., 37 (2012) 4179-4187.

183. V. Fuster, F. J. Castro, H. Troiani, G. Urretavizcaya; *Int J Hydrogen Energy*., 36 (2011) 9051-9061.

184. T. Spassov, Z. Zlatanova, M. Spassova, S. Todorova; *Int J Hydrogen Energy*., 35 (2010) 10396-10403.

185. G. Liang, J. Huot, S. Boily, A. Van Neste, R. Schulz; *J Alloys Compds*., 291 (1999) 295-299.

186. O. Gutfleisch, N. Schlorke-de Boer, N. Ismail; *J Alloys Compds*., 356–357 (2003) 598-602

187. J. -L. Bobet, S. Pechev, B. Chevalier, B. Darriet; *J. Mater. Chem*., 9 (1999) 315-321.

188. K. Zeng, T. Klassen, W. Oelerich, R. Bormann; *J Alloys Compds*., 283 (1999) 213-224.

189. W. Oelerich, T. Klassen, R. Bormann; *J. Alloys Compds.*, 315 (2001) 237-242.

190. T. Ikeda, H. Hashimoto, Y. Mori; Method for producing hydrogen storage material and hydrogen generation method. Patent JP2009132553 (2009).

191. M. Abdellaoui,S. Mokbli, F. Cuevas, M. Latroche, A. P. Guegan, H. Zarrouk; *Int J Hydrogen Energy*., 31 (2006) 247-250.

192. L. Aymard, M. Ichitsubo, K. Uchida, E. Sekreta, F. Ikazaki; *J Alloys Compds*., 259 (1997) L5-L8.

193. U. Haussermann, H. Blomqvist, D. Noreus; Inorg Chem., 41 (2002) 3684-3692.

194. H. Gu, Y. Zhu, L. Li; *J Alloys Compds*., 424 (2006) 382-387.

195. A. L. Yonkeu, I. P. Swainson, J. D. Dufour, J. Huot; *J Alloys Compds*., 460 (2008) 559-564

196. A. Ranjbar, M Ismail, Z. P. Guo, X. B. Yu, H. K. Liu; *Int J Hydrogen Energy*., 35 (2010) 7821-7826.

197. C. Z. Wu, P. Wang. X. Yao, C. Liu, D. M. Chen, G. Q. Lu; *J Alloy Compds*., 414 (2006) 259-264.

198. X. Yao, C. Wu, A. Du, G.Q. Lu, H. Cheng. S. C. Smith; *J Phys Chem*. B., 110 (2006) 11697-11703.

199. N. Bazzanella, R. Checchetto, A. Miotello, C. Sada, P. Mazzoldi, P. Mengucci; *Appl. Phys let*., 89 (2006) 014101-1 - 014101-3.

200. M. A. Lillo-Ródenas, K. F. Aguey-Zinsou, D. Cazorla-Amorós, A. Linares-Solano, Z. X. Guo,; *J Phys Chem*. C., 112 (2008) 5984-5992.

201. X. Yao, C. W, A. Du, J. Zou, Z. Zhu, P. Wang, H. Cheng, S. Smith, G. Lu; *J. Am. Chem. Soc.*, 129 (2007) 15650.

202. M. G. Veron, H. Troiani, F. C. Gennari; *Carbon*., 49 (2011) 2413-2423.

203. A. E. Teplykh, S. G. Bogdanov, Y. A. Dorofeev, A. N. Pirogov, Y. N. Skryabin, V. G. Makotchenko, A. S. Nazarov, V. E. Fedorov; *Crystallography Reports*., 51 (Suppl.1) (2006) S62.

204. R. A. Varin, T. Czujko; *Mater and Manufacturing Processes*., 17 (2002) 129-156.

205. C. Suryanarayana; *Progress in Materials Science*., 46 (2001) 1-184.

206. K. Aoki, A. Memezawa, T. Masumoto; J. Mater Res., 8 (1993) 307-313.

207. J. M. Bellosta von Colbe, M. Felderhoff, B. Bogdanović, F. Schuth, C. Weidernthaler; *Chem Comm*., (2005) 4732-4734.

208. J. X. Zhang, F. Cuevas, W. Zaidi, J. P. Bobet, L. Aymard, J. L. Bobet; *J Phys Chem. C*., 115 (2011) 4971-4979.

209. http://www.evico-magnetics.de

210. M. Williams, M. V. Lototskyy, V. M. Linkov, A. N. Nechaev, J. K. Solberg, V. A. Yartys; *Int. J. Energy Res.*, 33 (2009): 1171-1179.

211. I. A. S. Edward; Structure in Carbons and Carbon Forms. *In* H. Marsh (Ed), *Introduction to Carbon Science*, London, Butterwoths., 1989.

212. B. D. Cullity, S. R. Stock; *Elements of X-ray Diffraction*, Upper saddle River, NJ, Prentice Hall., 2001.

213. D. F. Shriver, P. W. Atkins; *Inorganic Chemistry*, New York, W. H. Freeman and Co., 1999

214. P. W. Atkins; *Physical Chemistry*, New York, Freeman., 1998.

215. H. E. Kissinger; *Anal Chem*., 29 (1957) 1702-1706.

216. A. C. Larson, R. B. Von Dreele; General Structure Analysis System (GSAS), Los Alamos National Laboratory Report LAUR 86-748 (2004).

217. D. S. Sholl; *J Alloys Compds*., 446 (2007) 462-468.

218. L. E. A. Berlouis, E. Carbrera, E. Hall-Barientos; *Mater Trans*.,16 (2001) 45-57.

219. J. F. Stampfer, C. E. Holley, J. F. Suttle; *J. Am. Chem. Soc*., 82 (14) (1960) 3504.

220. M. Danaie, S. X. Tao, P. Kalisvaart, D. Mitlin; *Acta Mater*., 58 (2010) 3162-3172.

221. X. Yue, H. Wang, S. Wang, F. Zhang, R. Zhang; *J Alloys Compds*., 505 (2010) 286-290.

222. W. Duan; *Appl Mech Mater*., 80-81 (2011) 229-232.

223. D. S. Sholl; *J Alloys Compds*., 446 (2007) 462-468.

224. A. Karty, J. Grunzweig-Genossar, P. S. Rudman; *J Appl Phys*., 50 (1979) 7200-7209.

225. V. Fuster, G. Urretavizcaya, F. J. Castro; *J Alloys Compds*., 481 (2009) 673-680.

226. D. R. Leiva, A. M. Jorge, T. T. Ishikawa, J. Hout, D. Fruchart, S. Miraglia, C. S. Kiminami,. W. Botta;. *J. Adv. Eng. Mater.*, 12 (2010) 786-792.

227. R. V. Denys, A. B. Riabov, J. P. Maehlen, M. V. Lototsky, J. K. Solberg, V. A. Yartys; *Acta Mater*., 57 (2009) 3989-4000.

228. D. Hardie, R. N Parkins; *Phil Mag*., 4 (1959) 815.

229. J. M. Haschke, M. R. Clark; *High Temp Sci*., 7 (1975) 152.

230. M. Bortz, B. Bertheville, G. Böttger, K. Yvon; *J Alloys Compds*., 287 (1999) L4-L6.

231. Z. G. Huang, Z. P. Guo, A. Calka, D. Wexler, H. K. Liu; *J Alloys Compds*., 427 (2007) 94-100.

232. S. Aminorroaya, H. K. Liu, Y. Cho, A. Dahle; *Int J Hydrogen Energy*., 35 (2010) 4144-4153.

233. K. Maweja, M. Phasha, N. van der Berg; *Powder Technol*., 199 (2010) 256–63.

234. R. A. Varin, T. Czujko, Z. Wroski; *Nanotechnology*., 17 (2006) 3856-3865.

235. O. Friedrichs, J.C. Sanchez-Lopez, C. Lopez-Cartes, T. Klassen, R. Bormann, A. Fernandez; .*J. Phys. Chem*., 110 (2006) 7845-7850.

236. Z. Dehouche, J. Goyette, T. K. Bose, J. Huot, R. Schulz; *Nano Lett*., 1 (2001) 175-178.

237. M. C. Paganini, M. Chiesa, E. Giamello, S. Coluccia, G. Martra, D. M. Murphy, G. Pacchioni; *Surf. Sci.*, 421 (1999) 246-262.

238. M. Sterrer, T. Berger,O. Diwald, E. Knozinger,P. V. Sushko, A.L. Shluger; *J. Chem. Phys*., 123 (2005) 064714:1-064714:7.

239. A. D. Rud, A. M. Lakhnik; *Int J Hydrogen Energy*., 37 (2012) 4179-4187.

240. S. Stankovich, D. A. Dikin, G. H. B. Dommett, K. M. Kohlhaas, E. J. Zimmey, E. A. Stach, R. D. Piner, S. T. Nguyen, R. S. Ruoff; *Nature*., 442 (2006) 282-286.

241. P. Avouris, C. Dimitrakopoulos; *Materials Today*., 15 (2012) 86-97.

242. C. Wu, H. M. Cheng; *J Mater Chem*., 20 (2010) 5390-5400.

243. K. S. Novoselov, A. K. Geim, S. V. Morozov, D. Jiang, Y. Zhang, S. V. Dubonos, I. V. Grigorieva, A. A. Firsov; *Science*., 306 (2004) 666-669.

244. H. H. Stadelmaier., W. K. Hardy; Ternäre Kohlenstofflegierungen von Palladium und Platin mit Magnesium, Aluminium, Zink, Gallium, Germanium, Kadmium, Indium, Zinn, Quecksilber, Thallium und Blei, Zeitschrift für Metallkunde., 52 (1961) 391-396.

245. P. I. Kripyakevich., E. I. Gladyshevskii; Soviet Physics Crystallography, translated from Kristallografiya., 5 (1960) 552-554.

246. S. Samson; Acta Crystallographica, Section B: Structural Crystallography and Crystal Chemistry., 28 (1972) 936-945.

247. A. A. Nayeb Hashemi, J. B. Clark; Mg-Pd (Magnesium-Palladium), in: Binary Alloy Phase Diagrams, Second Edition, Ed. T. B. Massalski, ASM International, Materials Park, Ohio., 3(1990) 2535-2536.

248. L. Pasquini, E. Callini, M. Brighi, F. Boscherini, A. Montone, T. R. Jensen, C. Maurizio, M. V. Antisari, E. Bonetti; *J. Nanopart Res*., 13 (2011) 5727–5737.

249. J. Dufour, J. Huot; *J Alloys Compds*., 439 (2007) L5-L7.

250. X. Xu, C. Song; *Prepr. Pap. Am. Chem. Soc. ,Div. Fuel Chem*., 48 (2003) 941-942.

251. R. Checchetto, N. Bazzanella, A. Miotello, R. S. Brusa, A. Zecca, A. Mengucci; *J. Appl. Phys*., 95 (2004) 1989-1995.

252. K. Higuchi, H. Kajioka, K. Toiyama, H. Fujii, S. Orimo, Y. Kikuchi; *J. Alloys Compounds.*, 293–295 (1999) 484-489.

253. F. Tang, T. Parker, H. -F. Li, G. -C. Wang T. –M. Lu; *Nanotechnology*., 19 (2008) 465706-465711.

254. A. Krozer, A. Fischer, L. Schlapbach; *Phys. Rev.* B., 53 (1996) 13808-13816.

255. J. L. Slack, J. C. W. Locke, S. –W. Song, J. Ona, T. J. Richardson; *Sol. Energy Mater. Sol. Cells.*, 90 (2006) 485-490.

256. H. Kohlmann, G. Renaudin, K. Yvon, C. Wannek, B. Harbrecht; *J. Solid State Chem*., 178 (2005) 1292-1300.

257. Y. Goto, H. Kakuta, A. Kamegawa, H. Takamura, M. Okada; *J. Alloys Compds*., 404-406 (2005) 448–452.

258. M. V. Lototsky, V. A. Yartys, IYu. Zavaliy; *J Alloys Compds*., 404-406 (2005) 421-426.

259. X. B. Yu, Z. X. Yang, H. K. Liu, D. M. Grant, G. S. Walker; *Int J Hydrogen Energy*., 35 (2010) 6338-6344.

260. Yu. F. Shmal'ko, M. V. Lototsky, YeV. Klochko, V. V. Solovey; *J Alloys Compds*., 231 (1995) 856-859.

261. R. Schulz, J. Huot, G. Liang, S. Boily, G. Lalande, M. C. Denis, J. P. Dodelet; *Mater Sci Eng*. A., 267 (1999) 240-245.

262. R. A Varin, S. Li, Z. Wronski, O. Morozova, T. Khomenko; *J Alloys Compds*., 390 (2005) 282-296.

263. X. H. Chen, H. S. Yang, G. T. Wu, M. Wang, F. M. Deng; *J Cryst Growth*., 218 (2000) 57-61.

264. T. S. Ong, H. Yang; *Carbon*., 38 (2000) 2077-2085.

265. M. Francke, H. Hermann, R. Wenzel, G. Seifert, K. Wetzig; *Carbon*., 43 (2005) 1204-1212.

266. J. Huot, G. Liang, S. Boily, A. van Neste, R. Schulz; *J Alloys Compds*., 495 (1995) 293-295

267. Au. Ming; *Proceedings of the Materials Research Society Symposium*., 801 (2004) BB 1.5.1-1.5.14.

268. Z. Huang, Z. Guo, A. Calka, D, Wexler, H. Liu; *J Alloys Compds*., 427 (2007) 94-100.

269. H. Imamura, N. Sakasai, T. Fujinaga; *J Alloys Compds*., 253-254 (1997) 34-37.

270. K. Nogita, S. Ockert, J. Pierce, M. C. Greaves, C. M. Gourlay, A. K. Dahle; *Int J Hydrogen Energy*., 34 (2009)7686-7691.

271. Z. Dehouche, H. A. Peretti, S. Hamoudi, Y. Yoo, K. Belkacemi; *J. Alloys Compds*., 455 (2008) 432–439.

272. N. M. Lototsky, YeV. Klochko, M. V. Lototsky, V, A. Yartys, YuF. Shmaiko; In Hydrogen materials Science and Chemistry of Carbon nanomaterials, Schur DV, Zaginaichenko SYu, Veziroglu TN,Skorokhod VV (ed). ICHMS'2007 X International Conference, Sudak, Crimea, Ukraine. AHEU;Kiev 22-28 September 2007;1094-1097.

273. Z. Dehouche, N. Grimard; *Nanoparticles Materials for Hydrogen Storage, Chapter on New Technology Research, Nova Science Publisher*, 2006, ISBN 1-60021-2131.

274. A. Jain, R. K. Jain, S. Agarwal, R. K. Sharma, S. K. Kulshrestha, I.P. Jain; *J Alloy Compds*., 454 (2008) 31-37.

275. T. Spassov, U. Köster. *J Alloys Compds*., 287 (1999) 243-250.

276. X. -L. Wang, N. Haraikawa, S. Suda;. *J Alloys Compds*., 231 (1995) 397-402.

277. M. Yamaguchi, E. Akiba; Ternary Hydrides. In: R. E. Cahn, P. Hassen, E. J. Kramer, editors. Material Science Technology. Weinheim (Germany): VCH; 1994, 333-398.

278. J. F. Fernandez, C. R. Sanchez; *J Alloys Compds*., 340 (2002) 189-198.

279. X. Liu, Z. Huang, L. Jiang, S. Wang; *Int J Hydrogen Energy*., 32 (2007) 965-968.

280. S. Bouaricha, J. P. Dodelet, D. Guay, J. Huot, R. Schulz; *J. Mater. Res*., 16 (2001) 2893-2905.

281. X. Yao, Z. H. Zhu, G. Q. Lu, C. Z. Wu, P. Wang, H. M. Cheng; *Carbon Nanomaterials In Clean Energy Hydrogen Systems*., Springer, NATO.(2007) 497-502